Planar Penning Traps with Anharmonicity Compensation for Single-Electron Qubits

A thesis presented
by

Joshua David Goldman

to
The Department of Physics
in partial fulfillment of the requirements
for the degree of
Doctor of Philosophy
in the subject of

Physics

Harvard University
Cambridge, Massachusetts
September 2011

Thesis advisor | Author

Gerald Gabrielse | **Joshua David Goldman**

Planar Penning Traps with Anharmonicity Compensation for Single-Electron Qubits

Abstract

Planar Penning traps can provide a scalable architecture for one-electron qubits only if the trapping potential can be made sufficiently harmonic to detect a single trapped electron. Our theoretical study suggests planar Penning trap geometries for which the amplitude dependence of the frequency can be vastly reduced. We propose a procedure for how such a trap with realistic imperfections can be adjusted *in situ* to reduce the broadening that arises from thermal fluctuations of the axial amplitude. We fabricate a prototype trap using the optimal geometry, taking care to minimize the exposure of insulating surfaces that can accumulate stray charge. The narrow resonances observed are consistent with having trapped one electron, though improved trap stability and detection sensitivity are needed to reach a more definite conclusion. The trap tuning procedure narrows the axial resonance much as predicted. These techniques promise to make possible the detection of a single electron in a planar Penning trap, the key first step toward realizing a one-electron qubit.

Contents

Citations to Previously Published Work

Some of the work in this thesis, particularly in Chapter 2, has appeared in print elsewhere:

- "Optimized Planar Penning Traps for Quantum Information Studies,"
  J. Goldman and G. Gabrielse, *Phys. Rev. A* **81**, 052335 (2010).

- "Optimized Planar Penning Traps for Quantum Information Studies,"
  J. Goldman and G. Gabrielse, *Hyperfine Int.* **199**, 279-289 (2011).

- "Towards Electron-Electron Entanglement in Penning Traps,"
  L. Lamata, D. Porras, J.I. Cirac, J. Goldman, and G. Gabrielse, *Phys. Rev. A* **81**, 022301 (2010).

Acknowledgments

This work would not have been possible without support from numerous people. First of all, I am deeply grateful to my advisor, Professor Gerald Gabrielse, for working closely with me on developing the theory for planar Penning trap design, providing a multitude of ideas, and always being willing to discuss even the smallest details of the apparatus. From my two semesters as a teaching fellow on Jerry's course, "Reality Physics," I am also thankful to have learned from his excellent teaching and his way of communicating science to nonspecialists.

My fellow students have been a great source of knowledge, assistance, and good company. I am especially grateful to Shannon Fogwell Hoogerheide and Josh Dorr, with whom I have worked closely ever since they had to host my trap in the cryostat and magnet designed for their experiment. I have benefitted considerably from their feedback, the parts of the apparatus they built, their running the dilution refrigerator and doing countless cryogen fills, and most of all, their limitless patience and graciousness as we brought the new system online. I am thankful for their generosity in allowing me ample time on the experiment during the last, critical stages of this work. Josh also helped run the experiment at times during that period.

I also want to thank in particular Jack DiSciacca for his generous advice on building RF amplifiers and Paul Hess for exploring possible ways to fabricate our first planar traps.

It has been a pleasure to work with and learn from each one of the other graduate students in the group—Andrew Speck, Dan Farkas, David Hanneke, David Le Sage, Phil Larochelle, Nick Guise, Steve Kolthammer, Robert McConnell, Yulia Gurevich, Phil Richerme, Ben Spaun, Rita Kalra, and Elise Novitski—as well as postdocs Ben

Levitt, Jonathan Wrubel, Irma Kuljanishvili, and Maarten Jansen. I have also enjoyed supervising several undergraduates: Armin Pourshafeie, Chris Wood, and Amol Jain.

The National Science Foundation funded this experiment, and I am grateful for support from an NSF Graduate Research Fellowship. Some computations were carried out using the Odyssey cluster of the Harvard FAS Research Computing Group.

I appreciate the helpful comments from Pavel Bushev, Fernando Galve, Ferdinand Schmidt-Kaler, and Günther Werth on our planar trap design paper (Ref. [1]), which comprises most of Chapter 2. And I valued the opportunity to collaborate with Lucas Lamata, Diego Porras, and Ignacio Cirac to refine their proposal for electron-electron entanglement in Penning traps (Ref. [2]).

The physics department at Harvard has been a welcoming home with many staff whose help I am grateful for. Stan Cotreau taught me how to machine and offered answers to my machining questions, as well as comic relief. Louis DeFeo and his machinists, particularly Al Chandler and Rich Anderson, meticulously crafted many parts of the experiment. Jim MacArthur and Al Takeda were always receptive to my questions about electronics, and Jim's reliable instruments were important components of the experiment. The staff engineers at the Center for Nanoscale Systems have been dependably helpful, and I especially valued consultations with JD Deng and Ling Xie. Jan Ragusa made everything administrative run seamlessly, and Vickie Greene and Silke Exner-Su ensured the continual flow of supplies that enabled us to do experiments.

I am grateful to many others who have made my experience at Harvard so enriching, including friends and fellow physics students; tutors, students, and faculty in Lowell House; and undergraduates in my sections of Reality Physics. Finally, I am grateful to my parents, Harriet and Steve, and my brother, Jonathan, for their constant love and support, and most of all to my wife, Courtney Peterson, for her patience, understanding, love, and humor that have made these years so positive.

Chapter 1

Introduction

A spin-1/2 particle in a magnetic field is the archetypal two-level system. Recent experiments have realized something akin to this textbook example, first by trapping a single electron in vacuum [3], then by detecting single spin transitions [4], and finally by detecting quantum jumps between the lowest cyclotron states [5], as shown in Fig. 1.1. This approach, along with a number of other new methods [6], made possible the most precise measurements of the electron magnetic moment and the fine structure constant [7].

This thesis research explores whether the methods that enabled these remarkably precise measurements can be harnessed to perform quantum information processing[1] using single-electron qubits. Decades of research have produced great advances with three-dimensional Penning traps, but these trap electrode geometries are not very scalable to a large array of nearby traps, each containing a single suspended electron. New techniques are needed to bring the same level of precise control to a scalable

[1]The terms quantum information processing and quantum computing are used interchangeably.

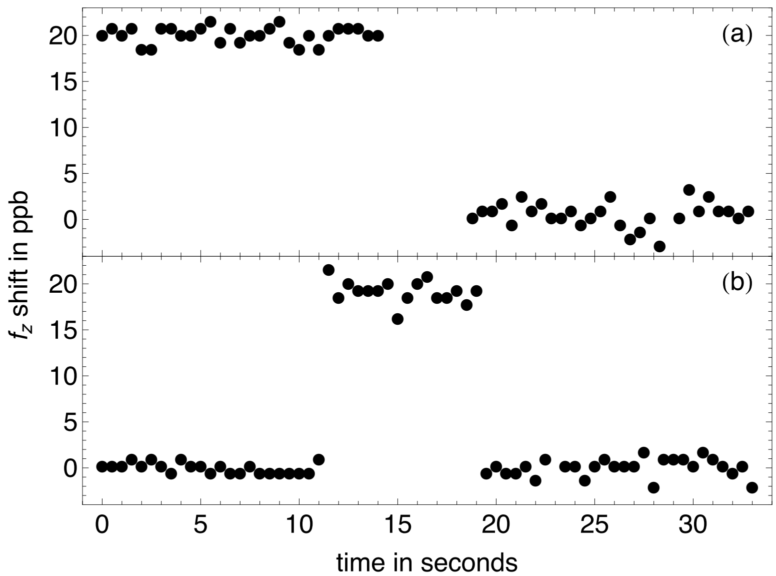

Figure 1.1: (a) QND observation of a spin flip of one trapped electron. (b) QND observation of a one-quantum cyclotron transition for one electron. Taken from Ref. [8].

architecture. This thesis reports significant progress toward that goal. We suggest planar Penning trap designs that are optimized for detecting single electrons. We fabricate a prototype trap and demonstrate experimentally that a procedure for tuning the trap reduces the anharmonic broadening. These initial tuning trials immediately enabled detection of a narrow resonance consistent with having trapped one electron, although further improvements in stability are needed for a conclusive demonstration.

1.1 Quantum Information Processing

The principle of a quantum computer is that information is stored in quantum two-level systems ("qubits") instead of classical two-level systems ("classical bits" or simply "bits"). A qubit can be represented, for example, using two continuous real variables θ and ϕ as

$$|\psi\rangle = \cos\left(\frac{\theta}{2}\right)|0\rangle + e^{i\phi}\sin\left(\frac{\theta}{2}\right)|1\rangle\,, \tag{1.1}$$

whereas a classical bit is by definition a discrete binary variable. This can be visualized by considering the possible states of a qubit as the surface of a unit sphere (the "Bloch sphere") with a point on the surface parametrized by angles θ and ϕ; by comparison, the states of a classical bit would be represented by just two points on the surface (e.g., the north and south poles). The possible states of N qubits are much richer than the possible states of N classical bits because a general N-qubit state cannot be composed of N single-qubit states. Thus the amount of information required to describe the state scales exponentially rather than linearly with the number of qubits. Computation proceeds by performing a unitary transformation on the N-qubit state. Unitary transformations in a 2^N-dimensional Hilbert space offer a vastly broader set of operations than those that can be performed on the same number of classical bits. Remarkably, quantum computations can exploit this quantum-mechanical richness even though each projective measurement performed at the end of a computation can extract only a very limited amount of the information stored in the quantum system.

The challenge of quantum algorithm design is to make an algorithm that is more efficient than an analogous algorithm on a classical computer. In 1994, Shor introduced the first quantum algorithms to solve outstanding problems of interest. He invented algorithms for computing discrete logarithms and prime factorization [9], for which the computation time is only a polynomial function of the length of the number to be factored,[2] which is exponentially faster than the best classical algo-

[2] Factoring is thus said to be performed *efficiently* on a quantum computer.

rithm.[3] The presumed difficulty of the factorization and discrete logarithm problems ensures the security of public-key cryptosystems like RSA and Diffie-Hellman. Thus, an efficient quantum algorithm threatens the security of communication over public channels like the internet [10]. After Shor [11] and Steane [12] first proposed methods of quantum error correction, quantum computation transformed from a fanciful vision to a seemingly possible though tremendously challenging experimental objective [13].

Another quantum algorithm was devised by Grover in 1995, in which a marked item in an unordered list of length N can be found in a time proportional to $\sqrt{N}$ [14, 15]. Unlike Shor's factoring algorithm, the speedup is not as spectacular relative to the best classical algorithm, but the result is still remarkable compared to the classical method of testing each item in turn, which takes on average $N/2$ queries. This also intuitively demonstrates that something is fundamentally different about quantum computing.

A different type of quantum algorithm is known as quantum simulation [10, 16, Sec. 4.7]. Conjectured by Feynman [17], the idea is to compute the evolution of a system under some specified Hamiltonian by building up the evolution out of a series of discrete gates. In many cases it is possible to approximate this evolution efficiently (i.e., with a polynomial number of gates) on a quantum computer but not a classical computer. This approach is now sometimes referred to as "digital" quantum simulation, in contrast to so-called "analog" quantum simulation in which a

[3] The runtime of Shor's algorithm scales with $n^2 \log n \log\log n$, whereas the runtime of the best classical algorithm for large numbers, the Number Field Sieve, scales as $e^{n^{1/3}(\log n)^{2/3}}$, where $n = \log_2 N$ is the number of bits in the number N [10]. It is not known whether a polynomial-time classical factoring algorithm is possible, but despite great effort, one has not been discovered. More generally, it has not been proved that an efficient quantum algorithm exists for a problem where an efficient classical algorithm is impossible.

Hamiltonian of interest is studied by constructing a model system governed by that Hamiltonian, often with tunable parameters [18].

In order to use Shor's algorithm for factoring numbers used in actual public-key communication, a quantum computer would need to have a very large number of qubits—10^4–10^5 or more, including those needed for quantum error correction [13, 19]—and gates with fidelity that surpasses the fault-tolerance threshold (error per gate below 10^{-4}–10^{-2}; see e.g. [20–23] and references therein). Both are demanding requirements that exceed (by several orders of magnitude, in the case of the number of qubits) what has been achieved in the best experimental implementations to date. This is why it still makes sense to investigate promising new qubits, as in this work. A factoring machine is still many years from fruition, so recent work has often instead emphasized applications to quantum simulation because novel results are much less difficult to achieve and more relevant to problems in physics research. A quantum simulator can yield results that are intractable on a classical computer with a far smaller number of qubits and lower fidelity than required for practical implementations of Shor's algorithm. For example, computing the evolution of n two-level systems on a classical computer requires 2^n quantum-mechanical amplitudes, so for even 30 two-level systems this becomes computationally infeasible. Although there are techniques such as Monte Carlo simulations that can yield some properties of a system, such as the ground state, a quantum simulator with relatively few qubits could yield insight into the dynamics of such systems beyond what can be achieved classically.

The attempts to make a quantum computer or quantum simulator are interesting quite apart from any algorithm such a device might be able to perform. These experiments involve quantum coherent control of an increasing number of systems; perhaps in the future, investigations with large numbers of controllably entangled particles will yield some insight into the mysteries of entanglement, decoherence, and quantum measurement. These processes differ from our classical intuition [24], as illustrated by paradoxes like Schrödinger's cat [25], and have long fascinated physicists and nonscientists alike.

1.2 Quantum Computing Devices

Many different physical systems are the subjects of ongoing research aimed at developing a practical quantum computer [26, 27]. The problem is hard, and the experimental requirements[4] are at odds with each other: a good qubit must be strongly coupled to other parts of the apparatus in order to initialize, manipulate, and read out its state as quickly as possible, yet it must be extremely well isolated from uncontrolled interactions that would change the quantum state. A quantum computer is intrinsically more susceptible to disturbance; whereas classical information can be stored in bistable systems that are essentially unaffected by small perturbations (bit flip errors are negligibly rare), quantum information processing exploits interference phenomena and entanglement and is thus subject to decoherence, even from small undesired couplings. Furthermore, these requirements must be satisfied in a system

[4] The requirements for making a physical quantum computing device were clearly distilled by DiVincenzo [28] into what are known as the DiVincenzo criteria: scalable qubits, initialization, long decoherence times relative to gate times, universal quantum gates, and measurement/readout, plus additional requirements relating to quantum communication. These criteria have also recently been restated simply as scalability, universal logic, and correctability [26].

that is practically scalable to very large numbers of qubits.

An early success of quantum computing experiments came from the implementation of a 1995 proposal [29] to use ions in a linear Paul trap as qubits, lasers to manipulate and detect them, and a center-of-mass motional mode as a bus that can be selectively coupled to each ion's internal state. A controlled-NOT gate on a pair of trapped ion qubits was achieved the same year [30]. Trapped ion systems were at the time being developed for precision metrology and spectroscopy with demonstrated long coherence times, and advances toward quantum information processing have also yielded techniques that in turn enabled extremely high-precision frequency standards [31–34]. Trapped ions are arguably the most advanced realization of quantum computing: all the methods required for quantum information processing [35], the ability to perform arbitrary unitary operations in a two-qubit space [36], ultrafast gates [37], coherence times up to 15 seconds [38], and gates at or near the fidelity required for fault-tolerant quantum computation [39, 40] have been demonstrated, though increasing the gate fidelity is challenging. By 2005, a six-ion Greenberger-Horne-Zeilinger (GHZ) [41, 42] (a.k.a. "Schrödinger Cat") state had been created in Boulder [43], and an eight-ion W state [44] had been created in Innsbruck [45]. Most recently, the Innsbruck group has entangled fourteen ions in a GHZ state [46]. When increasing the number of ions in the trap, it becomes increasingly difficult to spectroscopically address only a single motional eigenmode, so larger experiments must use techniques such as shuttling ions in multizone traps [47–49] or coupling distant ions with photons [50], perhaps via integrated optical components [51, 52]. In any case, entangling ever more qubits is difficult because the decay of coherence has been observed to scale with the square of the number of qubits [46, 53, 54]. Great advances have been made in ion trap quantum information processing (see also [55–57] among numerous reviews), but scaling to very large numbers of qubits still poses formidable technical demands.

In addition to trapped ions, early demonstrations of quantum logic gates were achieved in liquid-state NMR experiments with spin-1/2 nuclei [58–60], including implementations of Grover's search algorithm with up to three qubits [61, 62] and the celebrated realization of Shor's algorithm to factor 15 into its constituent primes, 3 and 5, using a seven-qubit NMR quantum computer [63]. Despite early successes, scalability to very large numbers seems unlikely on NMR quantum computers [64], and recent experiments have favored storing quantum information in individual systems rather than pseudo-pure states constructed from ensembles.

Experimental investigations are under way in quite a number of other systems as well. Superconducting qubits [65] have now been used to perform quantum algorithms [66–68] and to entangle three qubits [69, 70], with gate operations occurring in tens of nanoseconds, single-qubit gate fidelities exceeding 98% [71, 72], readout fidelities exceeding 90% [73, 74], and coherence times increased from 2 ns [75] to several microseconds [65, 76], which is remarkable considering that these qubits involve a macroscopic number of particles. Qubits can be stored in polarization states of photons [77, 78], with [79] or without a cavity [80], which have minimal decoherence but are difficult to couple to other photons. Photonic qubits have been used to implement Grover's algorithm [81] and Shor's algorithm [82, 83] and create GHZ states of up to ten qubits [84].

Cold atoms can be used as qubits [85, 86] and may be particularly scalable since one atom per site can be loaded into an optical lattice. Manipulating and reading out the state of individual atoms is more challenging, though recently developed techniques are enabling both operations [87–89]. Trapped atoms are a particularly useful platform for studying a variety of many-body phenomena [85, 86, 90, 91].

A different approach to scalability comes from semiconductor systems, for which there are well-established techniques for making a large number of small systems. Small quantum dots can be self-assembled or lithographically defined and easily replicated [92, 93]. Electron spin qubits in these systems have short coherence times, limited by hyperfine couplings to the nuclear spin bath, though these have been extended from nanoseconds to tens of microseconds with spin-echo techniques [94], and decoherence could be reduced by changing materials from GaAs to those with spinless nuclei, such as isotopically pure C, Si, and Ge. In other solid-state hosts, much longer decoherence times—tens of milliseconds or perhaps much longer—have been observed with electron spins and nearby nuclear spins in nitrogen-vacancy defects in diamond [95, 96]. Coherent single-electron spin rotations have been driven with microwaves in both nitrogen-vacancy centers and quantum dots [97–99], and arbitrary rotations can be performed on qubits made from two coupled electron spins in quantum dots [100].

Still other possibilities exist for quantum computation or simulation with many other systems, such as a Coulomb crystal of ions in a Penning trap [101, 102], spin and rotational states of polar molecules [103–105], trapped Rydberg atoms [106, 107], coupled optical cavities [108, 109], electrons on the surface of liquid helium [110, 111], and more. There are also entirely different paradigms, such as topological quantum computing with non-Abelian quasi-particles [112]; cluster state (a.k.a. "one-way") or other measurement-based quantum computing [113–116]; and adiabatic quantum computing, in which there are no gates and the system evolves toward a ground state that is the solution of the computational problem of interest [117–119].

There have been significant advances in coherently controlling more qubits with longer coherence times in a wide variety of physical systems. Still, a large-scale quantum processor remains a distant objective, and it is far from certain which systems, if any, could be sufficiently scaled up for that purpose. It is desirable to have many different systems under development, not only because some will prove more scalable than others, but also because different systems may be useful for different purposes. Some systems may function effectively as quantum registers (i.e., quantum memory) or quantum communication channels, and thus a quantum computer architecture might employ multiple kinds of quantum media coupled together. Some systems may be more suitable than others for particular methods of quantum error correction depending on the types of noise that are present and the way that qubits in that system are initialized, manipulated, coupled, and measured.

To this mix, we add a new and promising candidate qubit: a single trapped electron in vacuum coupled to an array of similar one-electron qubits. As mentioned, techniques developed for single trapped electron systems enabled one of the most precise measurements in physics [7], which triggered intriguing studies on using these techniques to manipulate single-electron qubits. After introducing the concept of a Penning trap, these schemes are discussed in Sec. 1.4. Trapped electrons could make extremely long coherence times possible, at least in principle.

1.3 Penning Traps

1.3.1 Ideal Penning traps

A single-electron qubit begins with an electron in a Penning trap [120], which can trap charged particles with static magnetic and electric fields. In the ideal case, an axial magnetic field

$$\mathbf{B} = B\hat{\mathbf{z}} \tag{1.2}$$

makes a charged particle placed in this field undergo cyclotron motion at frequency $\omega_c = eB/m$ in the x–y plane. A harmonic axial confining potential comes from an electrostatic quadrupole potential,

$$U \propto z^2 - \frac{1}{2}\rho^2. \tag{1.3}$$

The repulsive radial term, needed to satisfy Laplace's equation, modifies the radial equation of motion, resulting in the superposition of two harmonic circular motions: a cyclotron motion with a frequency slightly reduced from its free-space value, and a slow rotation called the magnetron motion, which can be thought of as an $\mathbf{E} \times \mathbf{B}$ drift. The magnetron motion is unstable since the motion is about a radial potential hill rather than a well. However, it is very weakly damped, so it may be treated as effectively stable.

The Hamiltonian is diagonalized into three independent harmonic oscillators, plus

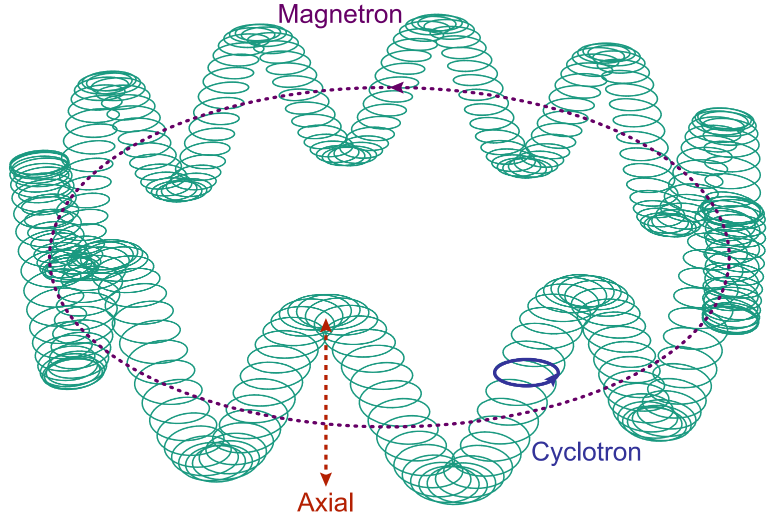

Figure 1.2: Illustration of classical particle motions in a Penning trap. The hierarchy of frequencies is compressed for easier visualization.

the interaction of the spin with the magnetic field:

$$H = \hbar\omega_c' a_c^\dagger a_c + \hbar\omega_z a_z^\dagger a_z - \hbar\omega_m a_m^\dagger a_m + \frac{1}{2}\hbar\omega_s\sigma_z, \tag{1.4}$$

where $a^\dagger$ and a are the usual creation and annihilation operators for the quantized harmonic motions, $\omega_c' = \omega_c - \omega_m \approx \omega_c$ is the modified cyclotron frequency, ω_z is the axial frequency, $\omega_m = \frac{1}{2}(\omega_c + \sqrt{\omega_c^2 - 2\omega_z^2}) \approx \omega_z^2/(2\omega_c)$ is the magnetron frequency, $\omega_s = (g/2)\omega_c$ is the spin frequency, g is the dimensionless electron magnetic moment, and σ_z is a Pauli matrix. Typically, $\omega_c' \gg \omega_z \gg \omega_m$; sample values are given in Table 1.1.

In Penning trap experiments to date, the spin and cyclotron motions are driven with microwaves broadcast into the trap volume. The spin and cyclotron states are measured using a quantum nondemolition (QND) measurement by coupling to the axial motion, which is detected as described in Secs. 2.7 and 4.5. Detection of one-quantum transitions between cyclotron and spin states is enabled by introducing a

Motion	Frequency
cyclotron	$\nu_c \approx 140.8$ GHz
axial	$\nu_z \approx 64.0$ MHz
magnetron	$\nu_m \approx 14.5$ kHz
spin	$\nu_s \approx 141.0$ GHz

Table 1.1: Typical trap frequencies used in this work. The spin and cyclotron frequencies correspond to a magnetic field of $B = 5.03$ T (Chapter 4). An axial frequency of 64 MHz is considered in Chapter 2. Axial frequencies used in the experiment are 64.5–66.5 MHz (Chapter 5).

small magnetic gradient called a magnetic bottle [120],

$$\mathbf{\Delta B} = B_2 \left[(z^2 - \frac{1}{2}\rho^2)\hat{\mathbf{z}} - \mathbf{z}\rho\hat{\rho} \right]. \tag{1.5}$$

The interaction of a particle's spin and orbital magnetic moments with the bottle, $H_{\text{bot}} = -\mu \cdot \mathbf{\Delta B}$, introduces another term proportional to z^2 in the axial Hamiltonian, which in turn means that a change in the spin or orbital state causes a change in the axial frequency, as shown in Fig. 1.1. The frequency shift due to a spin flip is given by

$$\delta\omega_z = \frac{g\mu_B B_2}{m\omega_z}, \tag{1.6}$$

where $\mu_B = e\hbar/(2m)$ is the Bohr magneton and we have assumed that $\delta\omega_z \ll \omega_z$. For the electron magnetic moment experiment [7,8], $\omega_z/(2\pi) \approx 200$ MHz and $\delta\omega_z/(2\pi) \approx 4$ Hz, as shown in Fig. 1.1. A one-quantum change in the cyclotron state produces an indistinguishable shift, differing only by a factor of $g/2 \approx 1.001$.

Unlike electrons confined in a solid-state host, here a single electron is trapped in vacuum and thus is much further away from all other particles. The vacuum produced at cryogenic temperatures is sufficiently good [121] that collisions with background gas molecules are negligible. The spin state is expected to be remarkably stable.

Spontaneous emission via a magnetic dipole transition is negligible, with a radiative damping rate

$$\Gamma_s = \frac{\alpha}{6}\left(\frac{g\hbar\omega_s}{mc^2}\right)^2 \omega_s, \tag{1.7}$$

where α is the fine structure constant, giving a decay time of $\Gamma_s^{-1} \approx 5$ years. And in a strong magnetic field, $\hbar\omega_s/k_B \approx 7$ K, much greater than the 100 mK temperature of the trap enclosure, so the spin state is unchanged by blackbody photons, provided that no higher-temperature radiation leaks into the trap volume.

1.3.2 A gallery of laboratory Penning traps

The axial magnetic field is usually generated by a superconducting solenoid, but many different configurations have been used to produce the electric quadrupole. In this manner, Penning traps have proved remarkably versatile. Some of the most precise measurements in physics have been carried out in Penning traps optimized for particular applications using trap designs from our research group.

The most straightforward way to produce an electric quadrupole is to place conducting surfaces along its equipotentials, which are hyperboloids of revolution (Fig. 1.3). This forms a hyperbolic Penning trap, which was used in the 1987 University of Washington electron/positron g-value measurement [4] and is still used in high-precision mass spectroscopy (e.g., [122, 123]). The potential produced will not be a perfect quadrupole, of course, because the electrodes cannot extend to infinity and because there will inevitably be some electrode misalignments and imperfections. Another pair of electrodes can be added along the asymptotes to compensate for the finite extent of the electrodes that lie along equipotentials; for a carefully chosen geometry, the trap will be "orthogonalized" in that the voltage applied to the compensation electrode can be adjusted to optimize the shape of the potential well while causing only very small changes in the axial frequency [124, 125].

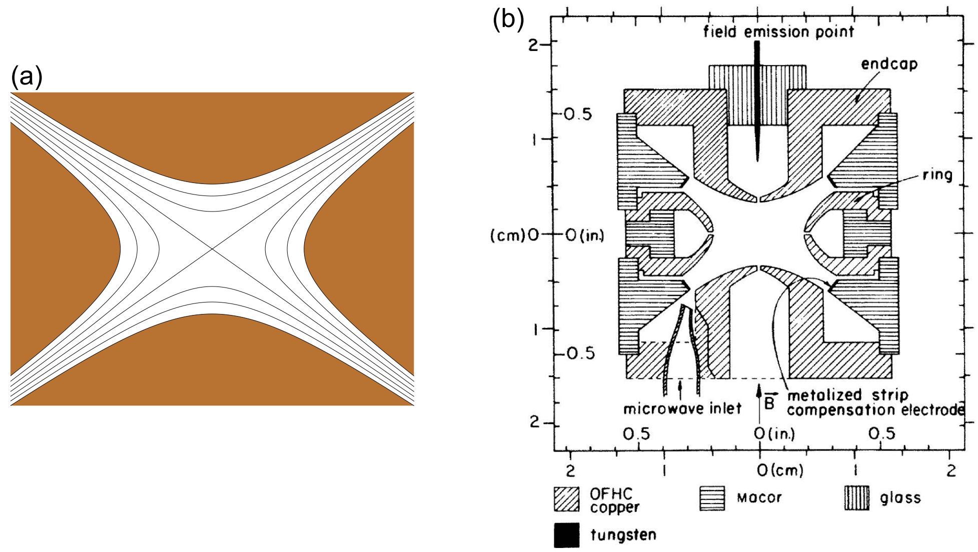

Figure 1.3: (a) Equipotentials of an ideal quadrupole potential. (b) A Penning trap with hyperbolic electrodes (right) designed to lie along the equipotentials with an "orthogonalized" geometry that makes the axial oscillation frequency largely independent of the compensation potential applied to improve the harmonicity of the trapping potential [124].

To improve the precision of the electron magnetic moment experiment, it was necessary to analyze and to control the microwave modes in the trap cavity. Thus a trap was designed with cylindrical electrodes rather than hyperbolic ones [125], and the cylindrical microwave cavity was observed to inhibit spontaneous decay of the cyclotron motion [126]. This trap design enabled the observation of one-quantum transitions [5], which then enabled the most accurate measurements of the electron magnetic moment and the fine-structure constant [7].

To allow antiprotons from an accelerator facility to enter a trap, an open-access

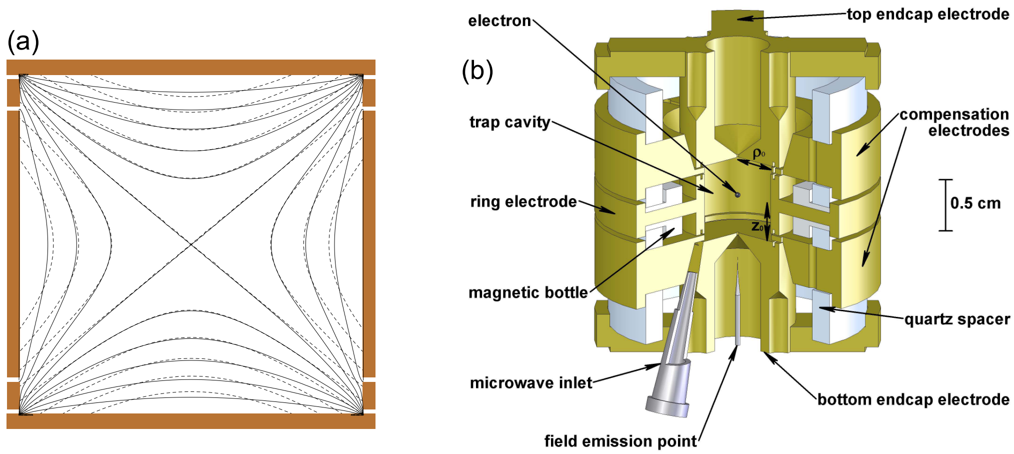

Figure 1.4: (a) Cutaway view of cylindrical Penning trap electrodes showing actual (solid) and ideal quadrupole (dashed) equipotentials. (b) Electrodes of the cylindrical Penning trap used to inhibit spontaneous emission and to make the most precise measurements of the electron magnetic moment and fine structure constant [7]. The cutaway view in (a) corresponds to the cavity in the center of the model in (b).

cylindrical trap was designed [127], in which the flat endcaps were replaced by additional cylindrical electrodes (Fig. 1.4). The most accurate comparison of q/m for an antiproton and proton [128] was carried out with a single antiproton and a single H^- ion in such a trap, as were the most accurate one-ion measurements of bound electron g values [129, 130] and the most precise measurement of the proton-to-electron mass ratio [131].

For g-factor measurements of heavier particles, a larger magnetic bottle is required to produce a measurable frequency shift, but the inhomogenous magnetic field broadens the spin and cyclotron resonances. For these applications, two open-endcap traps, one with a magnetic bottle and one without, were placed along the same magnetic field axis [129, 133]. This technique has been used with small-diameter traps to create a larger magnetic bottle for resolving a single-proton spin flip, analogous to Fig. 1.1,

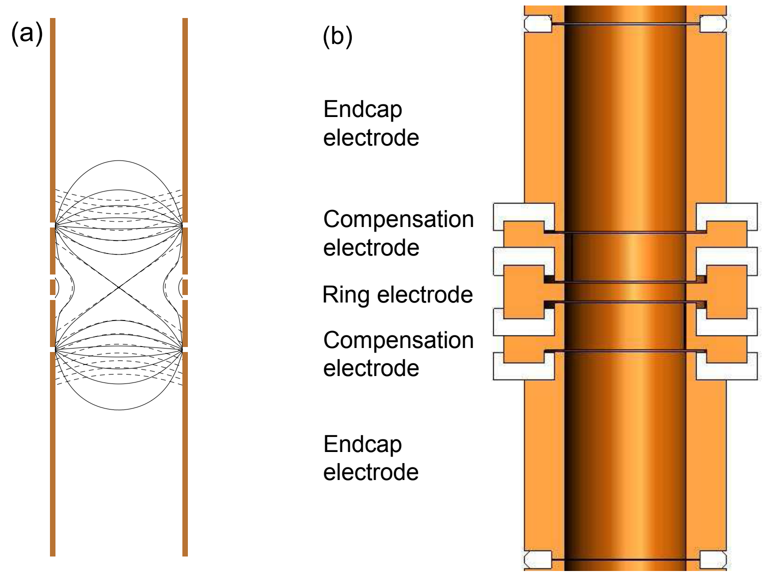

Figure 1.5: (a) Cutaway view of open-endcap cylindrical Penning trap electrodes showing actual (solid) and ideal quadrupole (dashed) equipotentials. (b) Electrodes of one of the traps used in Ref. [132]

and in turn to measure the proton and antiproton g-factors [132, 134, 135].

These designs have been well suited to their various applications, but three-dimensional, centimeter-scale trap electrodes that are machined, assembled, and wired by hand are difficult to scale to large numbers of nearby traps. Impressive progress has been made in the microfabrication of three-dimensional trap arrays [136], but it is still a formidable problem to fabricate a large array of small cylindrical traps with the properties needed to observe one-quantum transitions with one electron. For quantum computation with trapped electrons, a new kind of Penning trap design is required. A scalable array of small traps seems more feasible with traps whose electrodes are entirely in a plane [137], as in Fig. 1.6, especially if these could be fabricated on a chip using conventional lithographic methods [138]. The chip could include electrical couplings between the traps and could even include some detection electronics. Secondary advantages of a planar trap include an open structure that makes it easier to introduce microwaves to drive spin transitions and possibly also to load electrons. Suggested variations on this design include covered planar Penning traps (Sec. 2.6.1) and mirror-image Penning traps (Sec. 2.6.2), which could facilitate parallel detection and initial loading.

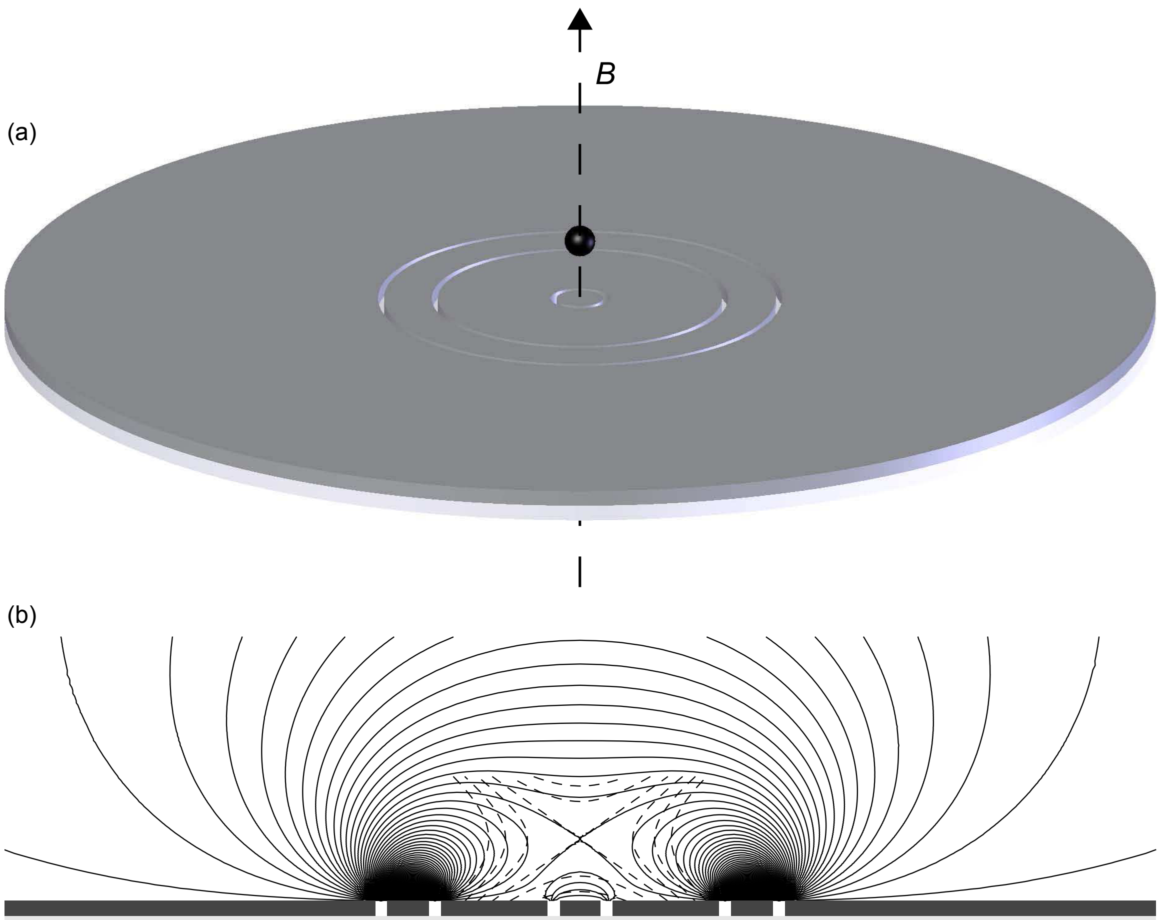

Figure 1.6: (a) A three-gap planar trap with a trapped particle suspended above an electrode plane that extends to infinity. (b) Side view of the trap electrodes showing equipotentials spaced by V_0, with the infinitesimal gaps between the electrodes widened to make them visible. The equipotentials extend into the gaps between electrodes. The dashed equipotentials of an ideal quadrupole are superimposed near the trap center.

With an eye toward scalability, other new Penning trap designs have also been proposed, including microelectromagnet traps [139], pixel traps [140], crossed-wire traps [141], and pad traps [142], though these are likely more suitable for trapping ions. For ions, the potential is not required to be harmonic because laser sideband cooling—which is not available for electrons—can force ions to the center of even an anharmonic trap. Planar Penning traps have also inspired a design for a planar Paul trap with axisymmetric, concentric electrodes just like the electrodes of planar Penning traps [143].

1.3.3 Planar Penning traps to date

One proposed planar Penning trap geometry is a round center electrode surrounded by concentric rings [137], as depicted in Fig. 1.6. This type of trap has been used for all experiments to date. A trap is formed by biasing the electrodes so that the potential along the axis of symmetry has a minimum at some height z_0 above the electrode plane. Electrons confined in a room-temperature planar Penning trap were first reported at Mainz, and the three motions have been observed [144, 145]. These experiments detected electrons destructively by dumping them from the trap to a microchannel plate.

Unlike ions, electrons have no known internal degrees of freedom aside from spin; thus, laser cooling cannot be used, and the presence and state of trapped particles cannot be detected with fluorescence. Different methods must be used instead. The axial motion is damped by a cryogenic external circuit. The cyclotron motion cools by synchrotron radiation in the cold environment of the trap electrodes. And the

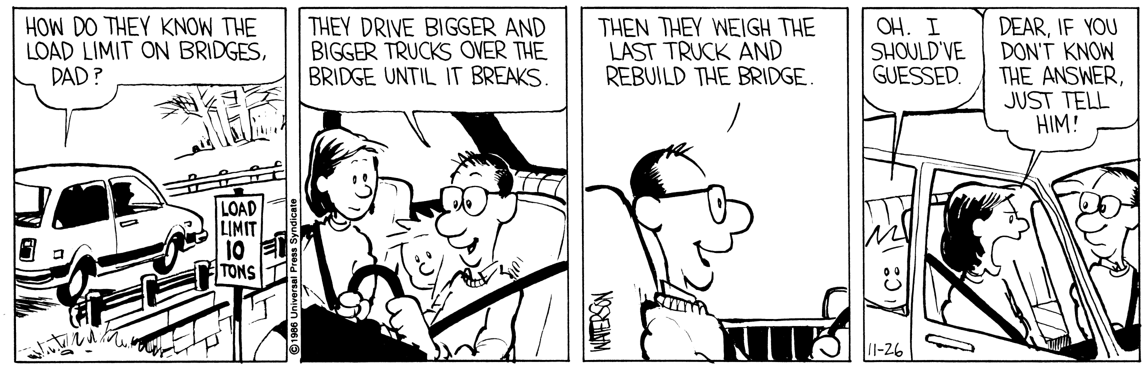

Figure 1.7: An illustration of destructive counting, in which the number of electrons in the trap is estimated by ejecting them. CALVIN AND HOBBES ©1986 Watterson. Used by permission of Universal Uclick. All rights reserved.

magnetron motion is cooled by driving a sideband of the axial motion. Also, nondestructive detection must use the translational degrees of freedom, so trapped electrons are detected by amplifying the radiofrequency image currents induced on a nearby electrode by the electrons' oscillation along the magnetic field axis, and the spin and cyclotron state of a single electron are detected via shifts in the axial frequency.

Detecting a single trapped electron is naturally a prerequisite for any quantum information processing using individual trapped electrons. The signal from a single electron is small, and the potential must be very harmonic in order for that signal to be detectable; that is, the signal must lie within a narrow range of Fourier components in order to use narrowband detection techniques that produce a sufficiently high signal-to-noise ratio. Furthermore, the axial resonance must be narrow enough and the signal-to-noise high enough to resolve the small axial frequency shifts used for detecting the spin and cyclotron states.

A second planar Penning trap experiment at Ulm attempted to detect a single electron [146]. The trap electrodes were cooled to below 100 mK, and the improved vacuum resulted in a hold time of 3.5 hours, increased from 22 seconds [144]. An RF amplifier was used to nondestructively detect trapped electrons, but both the Ulm and Mainz experiments reported axial resonances of several megahertz, broader than the tuned circuit amplifier used for detection and orders of magnitude too broad to detect a single electron. The final experimental report was not encouraging. It concluded that the "lack of mirror symmetry" makes it "impossible to create a genuinely harmonic potential" and that it is thus "impossible" to detect a single electron within a planar Penning trap. Whether the situation changes with much smaller planar traps is being considered [138].

A more optimistic conclusion is warranted. We have identified planar Penning trap geometries than can in principle produce a sufficiently harmonic potential despite the lack of mirror symmetry of the trap electrodes about the axial potential minimum, and we have proposed a method for tuning the trap *in situ* to make the potential more harmonic. We have demonstrated this tuning method with electrons in a prototype trap and observed the resonance to narrow as expected. After a first pass at tuning the trap, resonances were observed that are consistent with having trapped just one electron, although improved stability is needed to be certain. It seems likely that a single electron can indeed be trapped with the methods and apparatus presented in this work.

1.4 Quantum Information Processing with Trapped Electrons

Several proposals for quantum information processing with trapped electrons were spurred by the observations of one-quantum spin and cyclotron transitions of an electron in a cylindrical Penning trap [5]. Initial proposals were to encode qubits in the spin, cyclotron, and/or axial states of a single electron, and conditional gates between these qubits were designed based on state-dependent transition frequencies [147–150]. A subsequent scheme consisted of open-endcap traps lying along the magnetic field axis, with the axial states of electrons in neighboring traps coupled by the Coulomb interaction when their axial frequencies were brought into resonance with each other [151, 152]. A coaxial stack of cylindrical microtraps is scalable in principle, but only along one dimension, and it would be a very difficult apparatus to fabricate in light of the harmonic requirements for detecting a single electron and its spin/cyclotron state. A different architecture, however, involves Penning traps with planar electrodes [137], in which a two-dimensional array of traps could be more easily fabricated with existing methods.

For spin qubits, logical $|0\rangle$ and $|1\rangle$ simply correspond to spin states $|\downarrow\rangle$ and $|\uparrow\rangle$ relative to the static magnetic field. Single-qubit operations would then correspond to single-spin rotations driven by microwave pulses of the appropriate frequency, duration, and phase. The spin frequencies of different electrons could be differentiated by applying a magnetic gradient, in which case microwaves could be broadcast throughout the whole trapping volume,[5] or each trap could be fabricated in the near-field of a dedicated microstrip resonator.

For axial or cyclotron qubits, $|0\rangle$ and $|1\rangle$ are chosen to be the lowest two states of the harmonic oscillator. Axial transitions would be driven by pulses of oscillating voltages applied to a trap electrode. To keep the system in a linear combination of only the two computational basis states, it is necessary either to differentiate the transition frequencies by making the oscillator anharmonic or by using more complex pulse sequences to make sure that no population remains in higher energy levels [150, 157, 158]. Anharmonicity of the cyclotron motion arises from special relativity [120], which gives a difference of about 200 Hz between the frequencies for the transitions $|0\rangle_c \leftrightarrow |1\rangle_c$ and $|1\rangle_c \leftrightarrow |2\rangle_c$. This anharmonicity cannot be increased; to avoid driving unwanted transitions, the Rabi frequency must be kept much smaller than the splitting of the transition frequencies, so this puts a stringent upper bound on the speed of this type of gate. The axial potential, however, has tunable electrostatic anharmonicity. As discussed in Chapter 2, the lowest-order anharmonic terms can be tuned out for detecting the axial signal of one or more trapped electrons, but the anharmonicity could also be tuned to maximize the level spacing of the axial states. This splitting would be only of order 10 Hz for the traps fabricated in this work, but it scales inversely with the trap size squared and becomes much larger in smaller traps.

The spin and cyclotron states could be read out using the same quantum nondemolition method as the quantum jumps of Fig. 1.1, though other methods of readout,

[5] This is analogous to the ion trap systems investigated in Refs. [153–156] in which magnetic field gradients differentiate qubit transition frequencies so that the driving fields need not be focused only on a single ion, and thus microwave or RF fields can also be used instead of only lasers.

such as capacitive charge-sensing (as in semiconductor quantum dots), have also been suggested [139]. In the precision electron experiments, this readout is performed with essentially unit fidelity with 1/4 second of averaging; however, there was no need to optimize this for speed. Because a large-amplitude classical axial oscillation is used for detection, a qubit stored in the axial degree of freedom would first have to be swapped to the spin or cyclotron state in order to be read out [147].

Initialization is straightforward for the cyclotron state because it cools to the ground state via synchrotron radiation when placed in the 100 mK environment established by the dilution refrigerator [5].[6] The spin state can be initialized by driving a spin transition and observing the sign of the resulting axial frequency shift. The axial motion, however, thermalizes with the detection circuit with on average $\langle n \rangle_z \sim 1000$ phonons at the 5 K temperature of the axial amplifier. Realizing an axial qubit requires cooling the axial motion of an electron to its quantum-mechanical ground state. This may be possible by transferring quanta from the axial motion to the cyclotron motion and could be enhanced by cavity modes with the appropriate geometry; this sideband cooling technique might also enable further improvements in the measurement precision of the electron magnetic moment [6].

Finally, electrons could be coupled in various ways. Axial qubits of electrons in neighboring traps could interact directly via the Coulomb interaction if their axial frequencies are brought into resonance with each other [151, 152], though stronger coupling could be achieved by coupling two traps with a wire connected to an electrode of each trap [137, 159] (analogous to [160] for atomic systems). The latter also has the added advantage of being able to couple electrons in distant traps, and could

[6] In a magnetic field of 5 T, $\hbar\omega_c/k_B = 7$ K.

potentially even couple to a different kind of system.

Electron spins interact directly but weakly via dipole-dipole coupling. This can be greatly enhanced if the Coulomb interaction mediates the coupling. Reference [161] proposed introducing a strong linear magnetic gradient, which couples the spin of each electron to its axial motion. The axial motions then interact via the Coulomb interaction when their frequencies are matched, and the net result is an effective spin-spin interaction formally equivalent to the J-coupling in NMR.[7] This system could then use the extensive set of pulse sequences developed for manipulating NMR systems [58,60], but has the disadvantage of being relatively slow unless the gradients are made extremely strong and the traps brought very close together. Such a system could also be used to study a chain or array of interacting spins [162,163].

The promise of long coherence times motivates studies of single-electron qubits. Trapped-electron qubits could potentially even realize dense coding by using more than one quantized degree of freedom. Still, several preliminary steps must be taken to establish whether trapped electron qubits are feasible. To use an electron spin as a qubit, coherent spin manipulations must be demonstrated. Single-particle electron spin resonance has recently been achieved in solid state systems [97–99], and direct spin flips[8] have been observed for a single electron in a Penning trap [164]. But the magnetic bottle and special relativity cause thermal fluctuations in the axial energy

[7] The Hamiltonian has the same form as an ion trap system with a magnetic gradient and ions in separate traps [156], but such a system has much weaker coupling between qubits than ions in the same trap coupled by a common motional mode.

[8] "Direct" spin flips, due to a drive at ω_s, are distinct from anomaly transitions, in which a drive at $\omega_a = \omega_s - \omega_c = (g/2-1)\omega_c$ causes a simultaneous spin flip and a cyclotron jump. These transitions are driven in the electron magnetic moment experiment; because $g/2-1$ is about 0.001, it is advantageous to extract g by measuring the ratio of the anomaly frequency to the cyclotron frequency rather than the ratio of the spin frequency to the cyclotron frequency.

to generate what are essentially fluctuations in the magnetic field in the electron's rest frame (see [120, Sec. V.A]) and thus to broaden the spin resonance. To drive a coherent transition, the Rabi frequency Ω must be greater than the spin frequency spread $\delta\omega_s$, and this has not yet been achieved. This decoherence could be avoided by methods such as increasing the microwave power, using a resonant cavity mode to increase the oscillating magnetic field, turning off the magnetic bottle (see also Sec. 3.7.2), or cooling the axial motion to its ground state; the latter is also a prerequisite for using the axial motion as a qubit.

If these primary obstacles are overcome, the prospects for performing quantum logic are favorable. Theoretical studies of decoherence in trapped electron systems have concluded that many sources will be negligible at 100 mK, including the decoherence arising from coupling two traps with an ohmic wire [138, 159, 165]. Axial qubits would be particularly susceptible to heating from thermal electrical noise in the electrodes, but this noise can be reduced compared to ions' motional modes because the electron's light mass results in a higher frequency, and Penning traps have the advantage of using only DC and not RF potentials. Trapped electrons are an attractive system for these studies with many of the required features already demonstrated, but a single-electron qubit still requires developing new experimental capabilities, even if one electron can be suspended and detected in a Penning trap with planar electrode geometry.

1.5 Electrons in an Optimized Planar Penning Trap

This thesis reports progress toward realizing a one-electron qubit. We designed planar Penning traps so that it should be possible to suspend and detect one electron in a planar trap for the first time and suggested procedure for tuning a trap *in situ* to compensate for inevitable fabrication imperfections (Chapter 2). We fabricated planar Penning trap electrodes with optimized geometry and improved screening of exposed insulating surfaces (Chapter 3) and placed a protoype trap in a 100 mK environment with high-Q tuned-circuit amplifiers to detect the signal from trapped electrons (Chapter 4). We have demonstrated the anharmonicity compensation procedure and observed the axial resonance to narrow as the potential becomes more harmonic. After a first round of tuning, we observed a resonance narrow enough to be consistent with having one electron in the trap, although better stability is required to demonstrate this with certainty. These results are promising for detecting a single trapped electron with the traps and techniques presented here, which would in turn enable further progress toward developing one-electron qubits and quantum information processing with trapped electrons.

Chapter 2

Optimized Planar Penning Traps

A new design is required for a Penning trap that is scalable but still has the properties required to observe one electron. Inspired by the examples of Sec. 1.3.2, a study of planar Penning traps for one-electron applications was carried out in the hope that a similar rigorous design approach will indicate the best route to observing one electron in a planar trap [1]. This chapter is based on the work presented in Ref. [1], a summary of which can be found in Ref. [166].

The central challenge of planar Penning trap design arises because unlike hyperbolic and cylindrical Penning traps, the electrodes of a planar Penning trap are not symmetric when reflected across the x–y plane at the trap center, and hence, the electrostatic potential lacks reflection symmetry as well. Because the potential contains higher-order terms besides the ideal quadrupole (Eq. (1.3)), the frequency of a particle oscillating in this potential will depend on the amplitude of oscillation. It is thus said to be *anharmonic* because a harmonic oscillator's frequency is amplitude-independent. The axial amplitude is subject to thermal fluctuations resulting from its coupling to the detection circuit, and since the frequency is amplitude-dependent, anharmonicity will broaden the axial resonance. If this broadening is too large, it will be impossible to detect the axial signal from a small number of trapped electrons. The goal of planar Penning trap design is to minimize the amplitude-dependence of the axial oscillation frequency. This chapter focuses on calculating the relationship between the amplitude-dependent axial frequency shifts and the electrode geometry and applied potentials.

Section 2.1 describes the potential and potential expansions for a planar Penning trap. Section 2.2 relates the amplitude dependence of the particle's axial oscillation frequency to the potential expanded around the equilibrium location of the trapped particle. The axial oscillation of a trapped particle must be detected to tell that a single particle is in the trap. Small shifts in this frequency will reveal spin flips and one-quantum cyclotron transitions.

Two-gap traps (with two biased electrodes surrounded by a ground plane) are shown in Sec. 2.3 to be inadequate for the observation and the manipulation of a single electron. The considerable promise of three-gap traps (with three biased electrodes surrounded by a ground plane) is the subject of Sec. 2.4. Optimized planar trap configurations that make the particle's oscillation frequency essentially independent of oscillation amplitude are identified and discussed, along with the detection and damping of the particle's motion.

Section 2.5 estimates the size of the unavoidable deviations between ideal planar Penning traps and the actual laboratory traps. Real traps have gaps between electrodes, finite boundary conditions, and imperfections in the trap dimensions, all of which must be compensated by modifying the voltages applied to the trap electrodes.

A covered planar trap (a two-gap planar trap covered by a parallel conducting plane) is proposed in Sec. 2.6.1 as a scalable way to make planar chip traps less sensitive to nearby apparatus. An electron suspended midway between a mirror-image pair of planar electrodes is shown in Sec. 2.6.2 to be in a potential with much the same properties as is experienced by an electron centered in a cylindrical Penning trap. For an electron initially loaded and observed in an "orthogonalized" mirror-image trap, we illustrate in Sec. 2.6.3 the possibility of adiabatically changing the applied trapping potentials to move the electron into a covered planar Penning trap that is optimized.

The damping and detection of a particle in planar traps, covered planar traps, and mirror-image traps are considered in Sec. 2.7. The optimization of damping and detection is discussed, as are unique detection opportunities available with a covered planar trap.

Section 2.8 corrects an earlier calculation [137] of the crucial amplitude-dependent frequency shifts needed to characterize and optimize planar traps. Finally, Secs. 2.9 and 2.10 use the calculations of this work to analyze the properties of planar traps built earlier in Mainz and Ulm. We show that the designs used were not adequate for one-electron studies.

2.1 Planar Penning Traps

2.1.1 The ideal to be approximated

An ideal Penning trap, which we seek to approximate, starts with a spatially uniform magnetic field,

$$\mathbf{B} = B\hat{\mathbf{z}}. \tag{1.2}$$

Superimposed is an electrostatic quadrupole potential, $V_2(\rho, z)$ in cylindrical coordinates, that is a harmonic oscillator potential on the $\rho = 0$ axis,

$$V_2(0, z) = \frac{1}{2}V_0 \left(\frac{z - z_0}{\rho_1}\right)^2, \tag{2.1}$$

where ρ_1 sets the size scale for the trap and V_0 sets the potential scale.

A particle of charge q and mass m on axis then oscillates at an axial angular frequency

$$\omega_z = \sqrt{\frac{q}{m}\frac{V_0}{{\rho_1}^2}}, \tag{2.2}$$

about the potential minimum at z_0. The potential will trap a particle only if $qV_0 > 0$.

The axial oscillation frequency ω_z is the key observable for possible quantum information studies. The one-quantum cyclotron and spin-flip transitions that have been observed (e.g., Figs. 1.1a and 1.1b) were detected using the small shifts in ω_z caused by a quantum nondemolition coupling of the cyclotron and spin energies to ω_z.

For potentials that can be expressed on an axis of symmetry as a power series in $z - z_0$ (e.g., Eq. (2.1)), the general solution to Laplace's equation near the point

$(0, z_0)$ is related to the axial solution by the substitution,

$$(z - z_0)^k \rightarrow \left[\rho^2 + (z - z_0)^2\right]^{k/2} P_k\left[\cos(\theta)\right], \tag{2.3}$$

where $\cos(\theta) = (z - z_0)/\sqrt{\rho^2 + (z - z_0)^2}$ and P_k is a Legendre polynomial. We will focus upon axial potentials throughout this work since this procedure can be used to obtain the general potential in the neighborhood of any axial position when this is needed.

Applied to the harmonic axial potential of an ideal Penning trap,

$$V_2(\rho, z) = \frac{V_0}{2} \frac{\rho^2 + (z - z_0)^2}{{\rho_1}^2} P_2\left[\cos(\theta)\right]. \tag{2.4}$$

This quadrupole potential for an ideal Penning trap extends through all space.

2.1.2 Electrodes in a plane

A planar Penning trap (Figs. 1.6 and 2.1) starts with a spatially uniform magnetic field, as in Eq. (1.2). An electrostatic potential is produced by biasing N ring electrodes in a plane perpendicular to the symmetry axis of the electrodes, $\hat{\mathbf{z}}$. An electrode with an outer radius ρ_i is biased to a potential V_i, as illustrated in Fig. 2.1. Without loss of generality, the potential beyond the rings ($\rho > \rho_N$) is taken to be the zero of the potential; that is, $V_{N+1} = 0$. The N gaps between biased electrodes are taken initially to be infinitesimal, but this condition is relaxed in Sec. 2.5.1.

Two remaining boundary conditions,

$$V(\rho, z \rightarrow \infty) = 0, \tag{2.5a}$$

$$V(\rho \rightarrow \infty, z) = 0, \tag{2.5b}$$

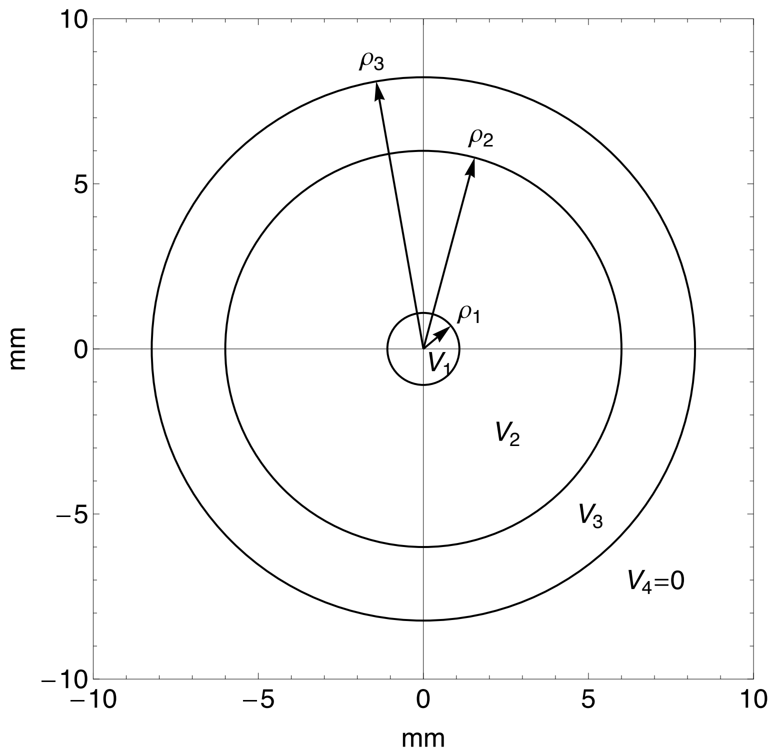

Figure 2.1: Rings of a planar Penning trap. The relative geometry of the electrodes is that of the sample trap used to illustrate the general features of planar traps. Infinitesimal gaps between electrodes are assumed until Sec. 2.5.1.

will be assumed to derive the potential for $z \geq 0$. It is not always possible in a real apparatus to keep all metal far enough away from the trap electrodes so that these boundary conditions are accurately satisfied. We consider the case of finite boundary conditions in Sec. 2.5.2.

Throughout this work, we will illustrate the basic features and challenges of a planar Penning trap using a three-gap ($N = 3$) sample trap with dimensions

$$\{\rho_i\} = \{1, 5.5, 7.5426\}\, \rho_1, \tag{2.6}$$

for reasons discussed in Sec. 2.4. Figure 2.1 shows this relative geometry (to scale).

2.1.3 Scaling distances and potentials

It is natural and often useful to scale distances in terms of the radius of the inner electrode ρ_1. We will do so, using the notation $\tilde{z} = z/\rho_1$ and $\tilde{\rho} = \rho/\rho_1$. The relative geometry of a planar Penning trap is then given by the set of dimensions $\{\tilde{\rho}_i\} = \{1, \tilde{\rho}_2, \tilde{\rho}_3, \ldots\}$, for example.

It is natural and convenient to scale the trap potential V, along with the voltages V_i applied to trap electrodes, in terms of a voltage scale, V_0, to be determined. We will then use scaled applied potentials, $\widetilde{V}_i = V_i/V_0$, and a scaled trap potential, $\widetilde{V} = V/V_0$.

2.1.4 Exact superposition

The potential produced by a planar Penning trap is a superposition

$$V(\tilde{\rho}, \tilde{z}) = \sum_{i=1}^{N} V_i\, \phi_i(\widetilde{\rho}, \widetilde{z}), \tag{2.7}$$

that is linear in the relative voltages applied to trap electrodes. The functions ϕ_i are solutions to Laplace's equation with boundary conditions such that $\phi_i = 1$ on the electrode that extends to ρ_i and is otherwise zero on the boundary. More precisely,

$$\phi_i(\tilde{\rho}, 0) = \begin{cases} 0, & \tilde{\rho} < \tilde{\rho}_{i-1} \\ 1, & \tilde{\rho}_{i-1} < \tilde{\rho} < \tilde{\rho}_i \\ 0, & \tilde{\rho} > \tilde{\rho}_i \end{cases}, \tag{2.8a}$$

$$\phi_i(\tilde{\rho}, \tilde{z} \to \infty) = 0, \tag{2.8b}$$

$$\phi_i(\tilde{\rho} \to \infty, \tilde{z}) = 0. \tag{2.8c}$$

These potentials are independent of the voltages applied to the trap and depend only upon the relative geometry of the trap electrodes.

Standard electrostatics methods [167, 168] (see details in Appendix A) give the ϕ_i that satisfy Laplace's equation for $\tilde{z} \geq 0$ and the cylindrically symmetric boundary conditions given previously,

$$\begin{aligned} \phi_i(\tilde{\rho}, \tilde{z}) = \tilde{\rho}_i & \int_0^\infty dk e^{-k\tilde{z}} J_1(k\tilde{\rho}_i) J_0(k\tilde{\rho}) \\ & - \tilde{\rho}_{i-1} \int_0^\infty dk e^{-k\tilde{z}} J_1(k\tilde{\rho}_{i-1}) J_0(k\tilde{\rho}), \end{aligned} \tag{2.9}$$

with the convention that $\tilde{\rho}_0 = 0$. The integrals are over products of Bessel functions. On axis,

$$\phi_i(0, \tilde{z}) = \frac{\tilde{z}}{\sqrt{(\tilde{\rho}_{i-1})^2 + \tilde{z}^2}} - \frac{\tilde{z}}{\sqrt{(\tilde{\rho}_i)^2 + \tilde{z}^2}}. \tag{2.10}$$

Most of the properties of a planar Penning trap can be deduced from just the potential on axis. Expressions equivalent to Eqs. (2.9) and (2.10) are in Ref. [137].

To emphasize the role of the N gaps of a planar trap, we define the gap potential across gap i as the difference $\Delta V_i \equiv V_{i+1} - V_i$. The axial potential is then given by

$$V(0, \tilde{z}) = \sum_{i=1}^{N} \Delta V_i \, \Phi_i(\tilde{z}), \tag{2.11}$$

$$\Phi_i(\tilde{z}) = \frac{\tilde{z}}{\sqrt{(\tilde{\rho}_i)^2 + \tilde{z}^2}} - 1, \tag{2.12}$$

a sum of contributions from the N gap potentials.

The axial potential can be computed exactly using Eqs. (2.7) and (2.10), or alternately from Eq. (2.11). Figure 2.2 compares an ideal harmonic axial potential to examples of axial potentials for optimized planar Penning trap configurations to be discussed. Figure 1.6b shows equipotentials spaced by V_0 for a planar Penning trap (configuration I in Table 2.1). The equipotentials are calculated for infinitesimal gaps, but the electrodes are represented with finite gaps to make them visible. The equipotentials terminate in the gaps between electrodes. The dashed equipotentials of an ideal quadrupole are superimposed near the trap center.

2.1.5 Expansion of the trap potential

To characterize the trap potential $V(\tilde{\rho}, \tilde{z})$ for $\tilde{z} \geq 0$, it suffices to focus upon expansions of the potential on the $\tilde{\rho} = 0$ axis. The potential near any expansion point $\tilde{z}_0$ on this axis can be obtained using the substitution of Eq. (2.3). The axial potential due to one electrode, Eq. (2.10), can be expanded in a Taylor series as

$$\phi_i(0, \tilde{z}) = \frac{1}{2} \sum_{k=0}^{\infty} C_{ki} (\tilde{z} - \tilde{z}_0)^k. \tag{2.13}$$

The expansion coefficients

$$C_{ki} = \frac{2}{k!} \left[\frac{\partial^k \phi_i(0, \tilde{z})}{\partial \tilde{z}^k} \right]_{\tilde{z} = \tilde{z}_0} \tag{2.14}$$

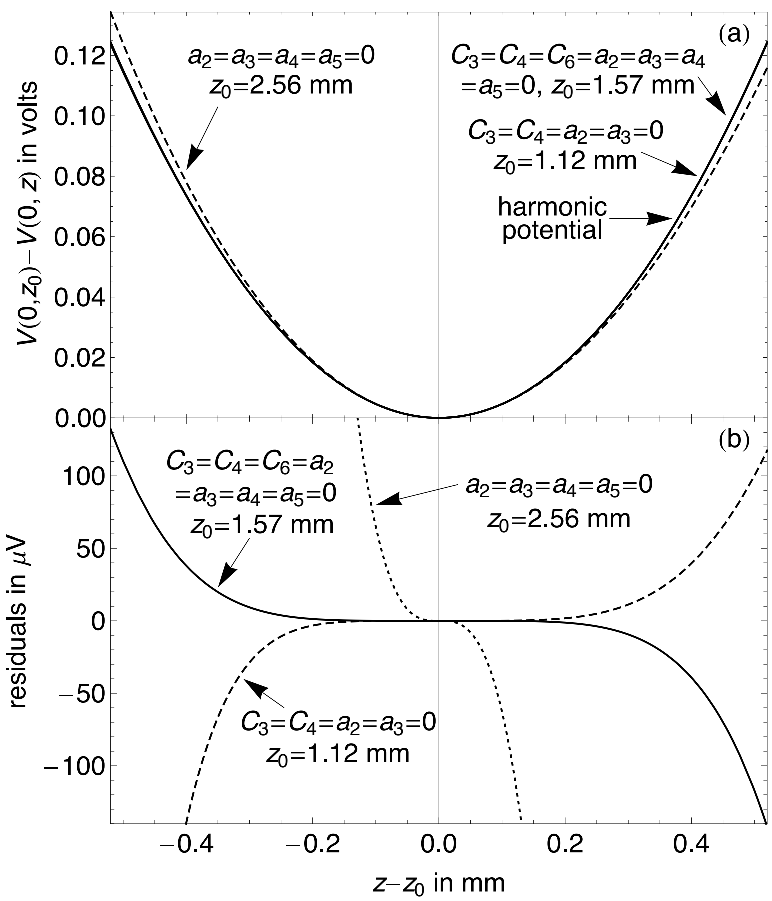

Figure 2.2: (a) Trap potential on axis. (b) Difference between the trap potential and a perfect harmonic potential on axis. The labels identify optimized configurations of the sample trap (Tables 2.1 and 2.2), using C_k from Eq. (2.15) and a_k from Eq. (2.23).

are analytic functions of the relative trap geometry, $\{\tilde{\rho}_i\}$, and the relative location of the expansion point, $\tilde{z}_0$.

The full trap potential can be similarly expanded as

$$V(0,\tilde{z}) = \frac{1}{2} V_0 \sum_{k=0}^{\infty} C_k \, (\tilde{z} - \tilde{z}_0)^k. \tag{2.15}$$

The one expansion coefficient needed for $k = 2$ is so far written as $V_0 C_2$. With no loss of generality, we are thus free to choose $C_2 = 1$. This determines V_0 and the C_k:

$$V_0 = \sum_{i=1}^{N} C_{2i} V_i, \tag{2.16}$$

$$C_k = \sum_{i=1}^{N} C_{ki} \widetilde{V}_i. \tag{2.17}$$

The latter equation, and the rest of this work, make frequent use of the scaled potentials $\widetilde{V}_i = V_i/V_0$. For the scaled potentials, Eq. (2.16) can be regarded as a constraint,

$$\sum_{i=1}^{N} C_{2i} \widetilde{V}_i = 1, \tag{2.18}$$

that an acceptable set of relative potentials must satisfy.

A trap is formed at $\tilde{z} = \tilde{z}_0$ only if there is a minimum in the potential energy $qV(0,\tilde{z})$ for a particle with charge q and mass m. The linear gradient in the potential must thus vanish at this point, whereupon

$$C_1 = \sum_{i=1}^{N} C_{1i} \widetilde{V}_i = 0. \tag{2.19}$$

Near the minimum, the potential energy will then have the form $m{\omega_z}^2(z - z_0)^2/2$, where ω_z is the angular oscillation frequency of the trapped particle in the limit of a vanishing oscillation amplitude. Comparing to the quadratic term in Eq. (2.15) gives

$${\omega_z}^2 = \frac{qV_0}{m{\rho_1}^2}, \tag{2.20}$$

the same as for the ideal case considered earlier because of our choice of V_0. Forming a trap thus requires that q and V_0 have the same sign at $\tilde{z}_0$. The sign of V_0 can be flipped if it is wrong by simply flipping the sign of all of the applied potentials.

2.1.6 Two viewpoints

Two different viewpoints of the potential expansions and equations are useful. The first is needed to analyze the performance of an N-gap trap. The second facilitates the calculation of optimized trap configurations. The point of view that we take to analyze an N-gap trap starts with the N radii $\{\rho_i\}$ and the N applied potentials $\{V_i\}$. These are the $2N$ parameters that fully characterize such a trap. No interrelations constrain the values of these parameters, so the difference of the number of parameters and constraints is $2N$.

The axial potential is then a superposition (from Eq. (2.7)) of the $\phi_i(0, \tilde{z})$ from Eq. (2.10) with scaled radii $\{\tilde{\rho}_i\} = \{\rho_i\}/\rho_1$. The extremum of $V(0, \tilde{z})$ is the $\tilde{z}_0$ needed to evaluate the expansion coefficients $C_{ki}(\tilde{\rho}_i, \tilde{z}_0)$ using Eq. (2.14). All of the properties of a trap at $\tilde{z} = \tilde{z}_0$ can then be determined. The potential scale $V_0(\rho_i, \tilde{z}_0, V_i)$ is determined using Eq. (2.16), the axial frequency from Eq. (2.2), and the expansion coefficients C_k from Eq. (2.17). An example analysis for two existing planar Penning traps is provided in Secs. 2.8–2.10.

The point of view we take to identify optimized planar trap configurations instead uses $2N+2$ parameters to characterize a planar trap. The effect of the two additional parameters is compensated by the addition of the two constraints $C_1 = 0$ and $C_2 = 1$ (from Eqs. (2.18) and (2.19)). The difference of the number of the parameters and constraints is thus $2N$, just as for our previous analysis.

We will first seek solutions for scaled trap configurations, for which there are $2N$ parameters and two constraints. The parameters are the N scaled potentials $\{\widetilde{V}_i\}$, the $N-1$ scaled radii $\{\tilde{\rho}_i\}$, and the scaled distance $\tilde{z}_0 > 0$. The two constraints, $C_1 = 0$ and $C_2 = 1$, are from Eqs. (2.18) and (2.19). The difference of the number of parameters and constraints for any scaled trap configuration is thus $2N-2$. We are thus free to specify up to $2N-2$ additional constraints on the scaled radii and scaled potentials, though not all constraints will have a set of parameters that satisfies them.

Once the $2N-2$ scaled potentials and radii are chosen, we are then free to choose two additional parameters to bring the difference of the parameters and constraints back up to $2N$. A convenient distance scale ρ_1 and a convenient potential scale V_0 can be chosen to get a desired axial frequency (using Eq. (2.20)). The radii are then $\{\rho_i\} = \rho_1\{\tilde{\rho}_i\}$, and the applied potentials are $\{V_i\} = V_0\,\{\widetilde{V}_i\}$.

Before applying these general considerations to two- and three-gap traps, we discuss amplitude-dependent frequency shifts since these will determine the additional constraint equations that we need to design optimized planar traps.

2.2 Axial Oscillations

In this section, we investigate the axial oscillation of a trapped particle near the potential energy minimum of a planar Penning trap. In the following sections, Sec. 2.3 and Sec. 2.4, we investigate optimized planar Penning traps, realized by imposing additional requirements on the design of planar traps (in addition to the two above) to make the axial oscillation of a trapped particle more harmonic.

The crucial observable for realizing a one-electron qubit is the frequency of the axial oscillation of a trapped electron. One trapped particle will be observed in the planar Penning trap only if the oscillation frequency is well enough defined to allow narrow-band radiofrequency detection methods to be used. Small changes in the particle's oscillation frequency will signal one-quantum transitions of the qubit, as has been mentioned.

For a perfect quadrupole potential, the motion of a trapped particle on the symmetry axis of the trap is perfect harmonic motion at a single oscillation frequency, ω_z, independent of the amplitude of the oscillation. For a charged particle trapped near a minimum of the nonharmonic potential expanded in Eq. (2.15), the oscillation frequency depends upon the oscillation amplitude.

2.2.1 Amplitude-dependent frequency

The oscillation frequency for a particle trapped near a potential minimum in a planar Penning trap depends upon the oscillation amplitude. A derivation of this amplitude dependence starts with applying Newton's second law to get the equation of motion. For a particle of charge q and mass m on the symmetry axis $\hat{\mathbf{z}}$ of the trap,

$$\frac{d^2}{dt^2}u + (\omega_z)^2 u + \lambda\,(\omega_z)^2 \sum_{k=3}^{\infty} \frac{kC_k}{2} u^{k-1} = 0, \tag{2.21}$$

where $u = \tilde{z} - \tilde{z}_0$. The harmonic restoring force is presumed to be larger than the additional (unwanted) terms. The latter are labeled with a dimensionless smallness parameter λ that is taken to be unity at the end of the calculation.

Solutions are sought in the form of series expansions of the amplitude and the oscillation frequency in powers of the smallness parameter,

$$u = u_0 + \lambda u_1 + \lambda^2 u_2 + \ldots, \tag{2.22a}$$

$$\omega = \omega_z + \lambda \omega_1 + \lambda^2 \omega_2 + \ldots. \tag{2.22b}$$

The lowest-order solution is a harmonic oscillation, with oscillation amplitude $\widetilde{A}\,\rho_1$, for which we chose the phase $u_0 = \widetilde{A}\cos(\omega t)$ with $\widetilde{A} > 0$.

By assumption, the lowest-frequency Fourier component of the particle's axial motion is predominant. Fourier components at harmonics of $\omega_z(\widetilde{A})$, not shown explicitly in the formula, have smaller amplitudes. The frequency contributions are determined by the requirement that no artificial driving terms resonant at angular frequency ω ("secular terms") are introduced. This well-known method [169] is sometimes called the Linstedt-Poincaré method. The result is that the oscillation frequency $\omega = \omega_z(\widetilde{A})$ is a function of oscillation amplitude $\widetilde{A}$ for the harmonic Fourier component, given by

$$\omega_z(\widetilde{A}) = \omega_z \left[1 + \sum_{k=2}^{\infty} a_k \widetilde{A}^k \right]. \tag{2.23}$$

At zero amplitude, the oscillation frequency $\omega_z(\widetilde{A}) \to \omega_z$, of course. There is no term linear in the oscillation amplitude (contrary to Ref. [137], see Sec. 2.8).

The amplitude coefficients a_k are functions of the potential expansion coefficients C_k, each of which in turn is a function of the trap dimensions ρ_i and the potentials

V_i applied to the trap electrodes.

$$a_2 = -\frac{15(C_3)^2}{16} + \frac{3C_4}{4}, \tag{2.24a}$$

$$a_3 = -\frac{15(C_3)^3}{16} + \frac{3C_3C_4}{4} \tag{2.24b}$$

$$= C_3 a_2, \tag{2.24c}$$

$$a_4 = -\frac{2565(C_3)^4}{1024} + \frac{645(C_3)^2C_4}{128} - \frac{21(C_4)^2}{64} - \frac{105C_3C_5}{32} + \frac{15C_6}{16}, \tag{2.24d}$$

$$a_5 = -\frac{2565(C_3)^5}{512} + \frac{765(C_3)^3C_4}{64} - \frac{69C_3(C_4)^2}{32} - \frac{15(C_3)^2C_5}{2} + \frac{3C_4C_5}{4} + \frac{15C_3C_6}{8} \tag{2.24e}$$

$$= (C_5 - 2C_3C_4)a_2 + 2C_3a_4, \tag{2.24f}$$

$$a_6 = -\frac{205845(C_3)^6}{16384} + \frac{159795(C_3)^4C_4}{4096} - \frac{21039(C_3)^2(C_4)^2}{1024} + \frac{81(C_4)^3}{256} - \frac{13545(C_3)^3C_5}{512} + \frac{1995C_3C_4C_5}{128} - \frac{315(C_5)^2}{128} + \frac{3015(C_3)^2C_6}{256} - \frac{57C_4C_6}{64} - \frac{315C_3C_7}{64} + \frac{35C_8}{32}, \tag{2.24g}$$

$$a_7 = 3C_3a_6 + \left[-3(C_3)^3 - 4C_3C_4 + 2C_5\right]a_4 + \left[3(C_3)^3C_4 + 4C_3(C_4)^2 - 2C_4C_5 - 3C_3C_6 + C_7\right]a_2. \tag{2.24h}$$

The exact expressions derived for a_8 and a_9 take a great deal of space to display and are not normally needed. A convention other than $C_2 = 1$ would require that each C_k in the previous equations be replaced by C_k/C_2.

Several properties of the relationships between the C_k and a_k will be exploited for designing planar traps. Two combinations of potential expansion coefficients make

$a_2 = 0$:

$$C_3 = C_4 = 0 \quad \Rightarrow \quad a_2 = 0, \tag{2.25}$$

$$C_4 = \frac{5}{4}(C_3)^2 \quad \Rightarrow \quad a_2 = 0. \tag{2.26}$$

Relationships between the a_k in Eqs. (2.24a–f) imply

$$a_2 = 0 \quad \Rightarrow \quad a_3 = 0, \tag{2.27}$$

$$a_2 = a_4 = 0 \quad \Rightarrow \quad a_2 = a_3 = a_4 = a_5 = 0. \tag{2.28}$$

One set of potential coefficients that produce this remarkable suppression of the low-order a_k is

$$\begin{aligned} &C_3 = C_4 = C_6 = 0 \\ &\quad \Rightarrow \quad a_2 = a_3 = a_4 = a_5 = 0. \end{aligned} \tag{2.29}$$

Another is

$$\begin{aligned} &C_4 = \frac{5}{4}(C_3)^2 \;\; \text{and} \;\; \mathrm{C}_6 = -\frac{7}{2}\mathrm{C}_3[(\mathrm{C}_3)^3 - \mathrm{C}_5] \\ &\quad \Rightarrow \quad a_2 = a_3 = a_4 = a_5 = 0. \end{aligned} \tag{2.30}$$

It remains to investigate whether and how any or all of these attractive combinations of C_k values can be produced by biasing a planar Penning trap.

2.2.2 Tunabilities

A change in the potential V_i applied to each electrode will change the axial frequency ω_z and will also change the amplitude dependence of the axial frequency by changing a_2. The orthogonalized hyperbolic, cylindrical, and open-access traps were designed so that the potential applied to one pair of electrodes changed the axial frequency very little while changing a_2. The potential on such compensation electrodes could then be changed to tune a_2 to zero without shifting the axial frequency out of resonance with the detectors that were needed to monitor the improvement.

We define a tunability for each electrode,

$$\gamma_i \equiv \frac{1}{\omega_z}\frac{\partial \omega_z}{\partial V_i} \Big/ \frac{\partial a_2}{\partial V_i}, \tag{2.31}$$

to quantify how useful the electrodes will be for tuning a_2. The tunabilities are defined as generalizations of the single tunability γ used to optimize the design of the orthogonalized traps.

Ideally, and this ideal was closely approximated in the orthogonalized traps, there are compensation electrodes for which $\gamma_i \approx 0$, and other electrodes for which γ_i is very large in magnitude. In Sec. 2.4.2, we will review the tunabilities that were calculated and realized for the cylindrical trap. In the sections that follow, we will compare these to what can be realized with a planar Penning trap.

2.2.3 Harmonics of the axial oscillation

The largest Fourier components for the small-amplitude motion of the trapped particle are given by

$$\tilde{z} = \tilde{z}_0 + \widetilde{A}_0 + \widetilde{A}_1 \cos(\omega t) + \widetilde{A}_2 \cos(2\omega t) + \widetilde{A}_3 \cos(3\omega t) + \ldots . \tag{2.32}$$

By assumption, the harmonic Fourier component at frequency ω has the larger amplitude $\widetilde{A}_1 \approx \widetilde{A}$, with the harmonics then given by

$$\widetilde{A}_1 = \widetilde{A} + \frac{C_3}{2}\widetilde{A}^2 + \left[\frac{29(C_3)^2}{64} - \frac{C_4}{16}\right]\widetilde{A}^3 + \ldots, \tag{2.33}$$

$$\widetilde{A}_2 = \frac{C_3}{4}\widetilde{A}^2 + \frac{(C_3)^2}{4}\widetilde{A}^3 + \ldots, \tag{2.34}$$

$$\widetilde{A}_3 = \left[\frac{3(C_3)^2}{64} + \frac{C_4}{16}\right]\widetilde{A}^3 + \ldots. \tag{2.35}$$

Insofar as $\widetilde{A} \ll 1$, these higher-order oscillation amplitudes are smaller, but they depend critically upon the low-order potential expansion coefficients as well.

2.2.4 Thermal spread in axial frequencies

The image current induced in nearby trap electrodes by a particle's axial motion is sent through the input resistance of a detection amplifier circuit. The oscillating voltage across the resistor is detected with a very sensitive cryogenic amplifier. Energy dissipated in the resistor damps the axial motion, with some damping timescale $(\gamma_z)^{-1}$. Section 2.7 shows how the damping rate γ_z is related to the resistance for a three-gap trap.

The damping brings the axial motion of a trapped particle into thermal equilibrium at the effective temperature of the amplifier. It is quite challenging to achieve a low axial temperature with an amplifier turned on. For example, the electrodes of the cylindrical Penning trap were cooled to 0.1 K with a dilution refrigerator. Even with very careful heat sinking of a Metal Semiconductor Field Effect Transistor (MESFET) amplifier that was run at an extremely low bias current, the axial temperature with the amplifier operating was still $T_z = 5.2$ K [170]. We then used feedback cooling to bring the axial temperature as low as 0.85 K [170]. A lower axial temperature was obtained, but only by switching the amplifier off during critical stages of the measurement of the electron magnetic moment. For the estimates that follow, we will assume an axial temperature of 5 K, but we stress that much higher axial temperatures are very hard to avoid.

What has prevented the observation of one electron in a planar trap so far is the large amplitude dependence of the axial frequency in such traps. Thermal fluctuations of the particle's axial energy make the particle oscillate at a range of Fourier components, $\Delta\omega_z$. In the cylindrical trap of Fig. 1.1c, this spread in frequencies is less than the damping width, $\Delta\omega_z < \gamma_z$. For earlier planar trap experiments, the thermal spread of axial oscillation frequencies was much broader than the damping width, $\Delta\omega_z \gg \gamma_z$.

As a measure of the thermal width, we will consider only the lowest-order contribution

$$\frac{\Delta\omega_z}{\omega_z} \approx |a_2| \frac{k_B T_z}{\frac{1}{2} m {\omega_z}^2 {\rho_1}^2}. \qquad (2.36)$$

It should be possible to calculate neglected higher-order contributions if correlations are considered carefully, but this lowest-order expression suffices for our purposes.

The tables that follow report the lowest-order thermal widths $\Delta f_z = \Delta\omega_z/(2\pi)$ and the damping widths $\gamma_z/(2\pi)$ in Hz. Vanishing values of Δf_z thus mean that $a_2 = 0$, whereupon there is typically not much thermal broadening of the damping width. However, higher-order contributions ensure that there is always a nonvanishing thermal width.

2.3 Two-Gap Traps

A minimal requirement for a useful trap is that it be possible to bias its electrodes to make the leading contribution to the amplitude dependence of the axial frequency vanish, $a_2 = 0$. We show here that this is not possible with a two-gap ($N = 2$) planar trap.

A scaled two-gap planar trap is characterized by $2N = 4$ parameters: $\tilde{\rho}_2$, $\widetilde{V}_1$, $\widetilde{V}_2$, and $\tilde{z}_0$. These parameters must satisfy the two constraints $C_1 = 0$ and $C_2 = 1$ (Eqs. (2.18) and (2.19)). The difference of the number of parameters and constraints is thus $2N - 2 = 2$. Consistent with this, we can solve for any two of the parameters in terms of the other two.

Unfortunately, if the additional constraint $a_2 = 0$ is added, then there are no sets of parameters that are solutions. An explicit demonstration that a_2 cannot be made to vanish comes from solving for $\widetilde{V}_1$ and $\widetilde{V}_2$ in terms of $\tilde{z}_0$ and $\tilde{\rho}_2$ using the two constraint equations. These solutions yield

$$C_3 = \frac{-9(\tilde{z}_0)^4 + (\tilde{\rho}_2)^2 - 4(\tilde{z}_0)^2\left[1 + (\tilde{\rho}_2)^2\right]}{3\left[\tilde{z}_0 + (\tilde{z}_0)^3\right]\left[(\tilde{z}_0)^2 + (\tilde{\rho}_2)^2\right]}, \tag{2.37}$$

$$C_4 = \frac{5\left\{15(\tilde{z}_0)^6 + 12(\tilde{z}_0)^4\left[1 + (\tilde{\rho}_2)^2\right] - 3\left[(\tilde{\rho}_2)^2 + (\tilde{\rho}_2)^4\right] + (\tilde{z}_0)^2\left[4 - 5(\tilde{\rho}_2)^2 + 4(\tilde{\rho}_2)^4\right]\right\}}{12\left[1 + (\tilde{z}_0)^2\right]^2\left[(\tilde{z}_0)^2 + (\tilde{\rho}_2)^2\right]^2}, \tag{2.38}$$

$$\begin{aligned} a_2 = -5 &\left\{36(\tilde{z}_0)^8 + (\tilde{\rho}_2)^4 + 36(\tilde{z}_0)^6\left[1 + (\tilde{\rho}_2)^2\right] + (\tilde{z}_0)^2\left[(\tilde{\rho}_2)^2 + (\tilde{\rho}_2)^4\right]\right. \\ &\left. + (\tilde{z}_0)^4\left[4 + 29(\tilde{\rho}_2)^2 + 4(\tilde{\rho}_2)^4\right]\right\} / \left\{48(\tilde{z}_0)^2\left[1 + (\tilde{z}_0)^2\right]^2\left[(\tilde{z}_0)^2 + (\tilde{\rho}_2)^2\right]^2\right\}. \end{aligned} \tag{2.39}$$

The amplitude coefficient a_2 is explicitly negative for all values of $\tilde{z}_0$ and $\tilde{\rho}_2$, and it only approaches zero in the not-so-useful limit that $\tilde{z}_0 \to 0$.

The best that can be done with a two-gap trap is to use $C_3 = 0$ as a third constraint on the four parameters $\widetilde{V}_1$, $\widetilde{V}_2$, $\tilde{z}_0$ and $\tilde{\rho}_2$. Only the analytic solution for $\tilde{z}_0$ is simple enough to display here,

$$\tilde{z}_0 = \frac{1}{3}\sqrt{\sqrt{4(\tilde{\rho}_2)^4 + 17(\tilde{\rho}_2)^2 + 4} - 2(\tilde{\rho}_2)^2 - 2}. \tag{2.40}$$

Figure 2.3 shows how the parameters of two-gap traps depend upon $\tilde{\rho}_2$.

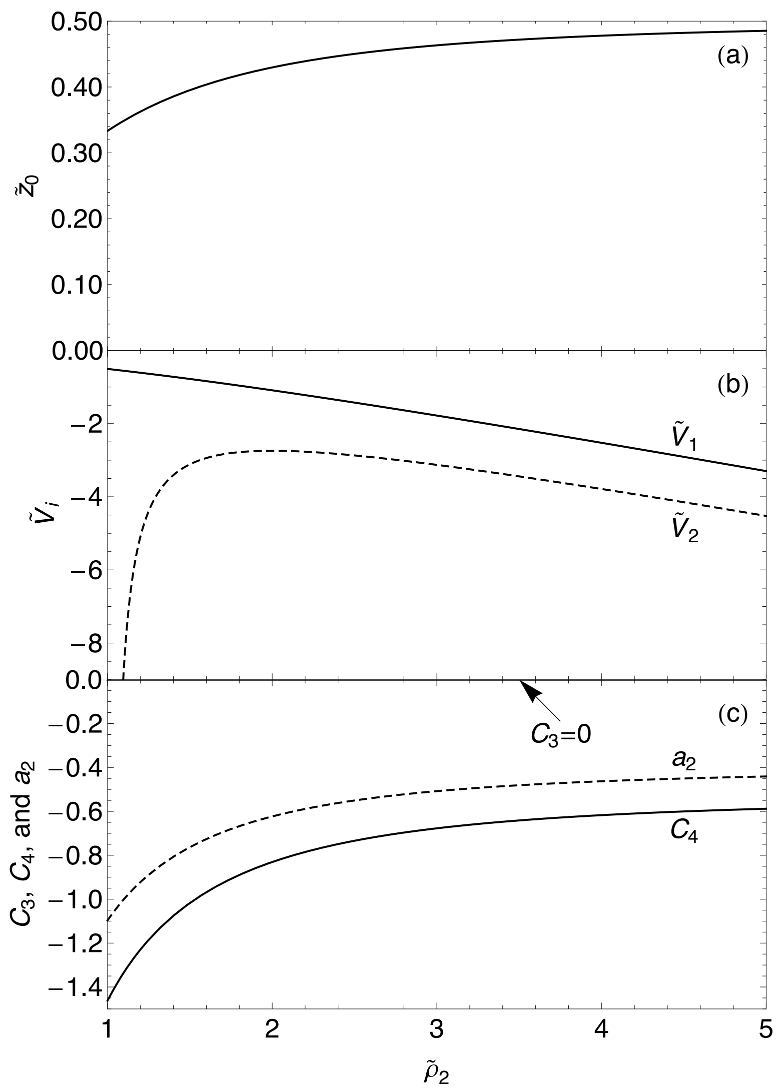

Figure 2.3: Parameters of two-gap traps that make $C_3 = 0$, as a function of $\tilde{\rho}_2$.

Two-gap traps are not so useful given that it is not possible to do better than make $C_3 = 0$. It is not possible to make $a_2 = 0$. For the remainder of our discussion of planar traps, we concentrate on three-gap traps since these have much better properties.

2.4 Optimized Three-Gap Traps

2.4.1 Overview

The goal of our optimization of a planar trap is to reduce the amplitude dependence of the axial oscillation frequency of a trapped particle to a manageable level so that the trapped particle's oscillation energy is in a narrow range of Fourier components. Otherwise, the oscillation energy will be broadened by noise-driven amplitude fluctuations to a broader range of Fourier components. The signal induced by the more harmonic axial oscillation can then be filtered with a narrow-band detector that rejects nearby noise components, making possible the good signal-to-noise ratio needed to detect the small frequency shifts that signal one-quantum transitions.

The dependence of the axial frequency $\omega_z(\widetilde{A})$ on the oscillation amplitude $\widetilde{A} = A/\rho_1$ is given by

$$\frac{\omega_z(\widetilde{A}) - \omega_z}{\omega_z} = 1 + a_2\widetilde{A}^2 + a_3\widetilde{A}^3 + a_4\widetilde{A}^4 + a_5\widetilde{A}^5 + a_6\widetilde{A}^6 + \ldots, \tag{2.41}$$

the low-order terms from Eq. (2.23). Since $\widetilde{A} \ll 1$, the lowest-order amplitude coefficient a_2 is the most important, followed by a_3, and so on. Each of the coefficients a_k is a function (given in Eq. (2.24)) of the potential expansion coefficients. Each of these is determined by the geometry and the applied trapping potentials, which must then be determined.

As discussed more generally in Sec. 2.1.6, a scaled three-gap planar Penning trap configuration is specified by $2N = 6$ parameters: $\tilde{\rho}_2$, $\tilde{\rho}_3$, $\widetilde{V}_1$, $\widetilde{V}_2$, $\widetilde{V}_3$, and $\tilde{z}_0$. These can be chosen to realize desired properties of a trap. These parameters must satisfy the two constraint equations $C_1 = 0$ and $C_2 = 1$ (Eqs. (2.18) and (2.19)). The difference of the number of parameters and the number of constraints is thus $2N - 2 = 4$. The challenge is to identify sets of up to four useful constraint equations for which solutions exist.

2.4.2 What is needed?

To estimate what is needed to observe a single trapped electron, it is natural to look to the demonstrated properties of the cylindrical trap used to observe the one-quantum transitions we seek to emulate. The electrodes of a cylindrical trap are invariant under reflections $z \to -z$ about the position of the trapped particle. This symmetry never holds for a planar Penning trap.

The first consequence of the reflection symmetry is that the odd-k expansion coefficients C_k vanish. The second is that the low-order, odd-k a_k vanish as well, since these are proportional to the C_k with odd k. For a cylindrical trap, the frequency expansion coefficients a_k of Eq. (2.24) thus simplify to

$$a_2 = \frac{3}{4} C_4, \tag{2.42a}$$

$$a_3 = 0, \tag{2.42b}$$

$$a_4 = \frac{15}{16} C_6 - \frac{21}{64} (C_4)^2, \tag{2.42c}$$

$$a_5 = 0. \tag{2.42d}$$

The odd-order a_k thus vanish naturally for an ideal cylindrical Penning trap.

Care must be taken in making quantitative comparisons between the planar traps and the cylindrical trap. Amplitudes and distances in the cylindrical trap were naturally scaled by the larger value of $d = 3.54$ mm [125,171] rather than by $\rho_1 = 1.09$ mm, as in the sample trap considered here, for trap configurations that produce the same axial frequency. The conversion between the $C_k^{(\mathrm{cyl})}$ for the cylindrical trap [120,171] and the C_k for the planar trap is given by

$$C_k = \left(\frac{\rho_1}{d} \right)^{k-2} \frac{C_k^{(\mathrm{cyl})}}{C_2^{(\mathrm{cyl})}}. \tag{2.43}$$

We apply this conversion to reported values for the cylindrical trap for the rest of this section.

The amplitude dependence of the axial frequency is reduced for the cylindrical Penning trap by adjusting a single compensation potential applied to a pair of compensation electrodes. The adjustment changes primarily C_4, but also C_6 to a lesser amount. The adjustment continues until $C_4 \approx 0$, whereupon $C_6 \approx -0.0008$. The frequency coefficients are then found using the appropriately converted C_k in Eq. (2.24). This gives $a_2 = a_3 = a_5 = 0$ and $a_4 = -0.0007$.

The resulting frequency-versus-amplitude curve is shown in Fig. 2.4 for $\omega_z/(2\pi) =$ 64 MHz, and the corresponding thermal spread of axial frequencies is $\Delta f_z = 0$ Hz since $a_2 = 0$. The compensation potential is typically then adjusted slightly away from $C_4 = 0$ to make the axial frequency insensitive to small fluctuations about a particular oscillation amplitude [172].

In practice, $C_4 = 0$ is not realized exactly, but $|C_4| < 10^{-5}$ is typically achieved. If $C_4 = -10^{-5}$ and $C_6 = -0.0008$ as before, then the amplitude coefficients are $a_2 = -8 \times 10^{-6}$, $a_4 = -0.0007$, and $a_3 = a_5 = 0$, the thermal spread of axial frequencies is 0.5 Hz, and the frequency-versus-amplitude curve is as shown in Fig. 2.4.

The cylindrical trap is designed so that the axial frequency is much more insensitive to the tuning compensation potential than to the potential applied to make the main trapping potential. If we define the endcap electrode potential to be our zero of the potential, the γ_i factors are $\gamma_{\text{ring}} = -141$ and $\gamma_{\text{comps}} = 0.032$. The latter would have the value $\gamma_{\text{comps}} = 0$ for the "orthogonalized" design for the cylindrical trap, except for the unavoidable imperfections of a real laboratory trap.

2.4.3 Previous three-gap traps

In marked contrast to the cylindrical trap within which the one-quantum transitions of a single electron were observed, the planar traps attempted so far were not designed to make $a_2 = 0$ and were not biased to make even $C_3 = 0$. It is thus not so surprising that attempts to observe one electron in a planar Penning trap have not succeeded.

In fact, Fig. 2.5 shows that the three-gap trap geometries tried so far (crosses) are

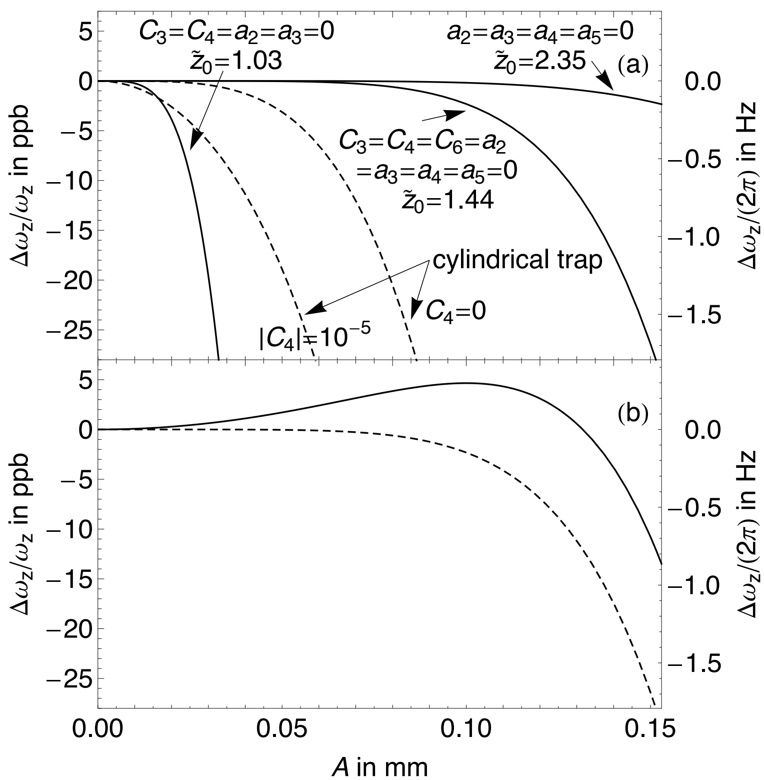

Figure 2.4: (a) The amplitude dependence of $\omega_z(A) \approx 2\pi\, 64$ MHz for optimized configurations of the sample trap (Table 2.1) is comparable to or smaller than for the cylindrical trap. (b) Slight adjustments in the applied potentials minimize the dependence of ω_z on the amplitude for fluctuations about a large oscillation amplitude (solid) rather than for small oscillation amplitudes (dashed).

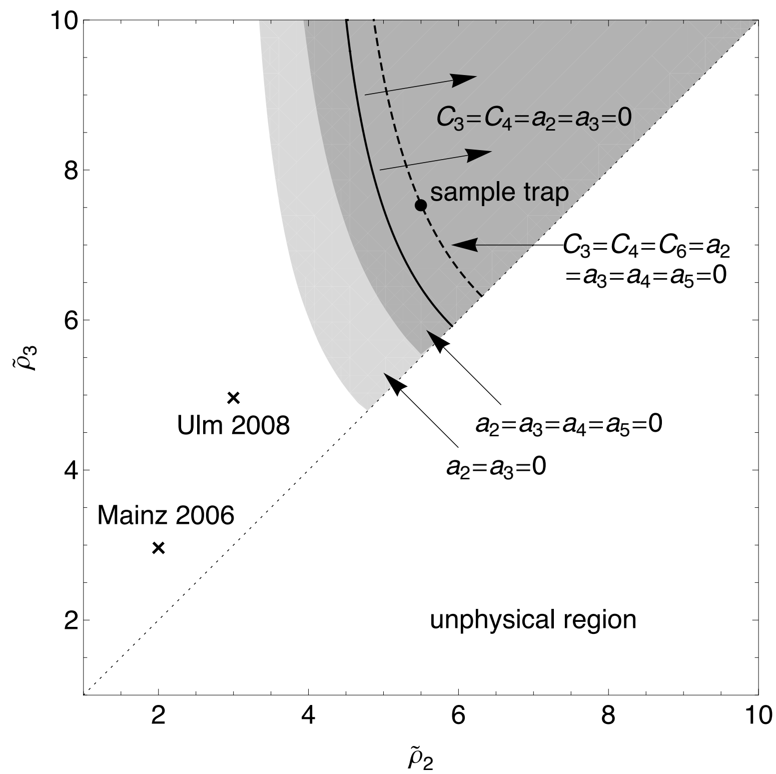

Figure 2.5: The shaded regions for which the indicated a_k can be made to vanish for a three-gap planar Penning trap, along with the region and the curve for which the indicated C_k can alternatively be made to vanish. To be avoided is the shaded area near the diagonal boundary $\tilde{\rho}_2 = \tilde{\rho}_3$ where there is a rather strong and sensitive cancellation between the effect of the potentials V_2 and V_3. No optimized traps are possible in the unshaded region, with the the earlier traps (crosses) at Mainz [144] and Ulm [146] as examples.

outside of all of the shaded regions that we use to identify optimized trap geometries. The best that could have been done for the earlier planar traps would have been to make $C_3 = 0$. In fact, any trap geometry represented in the upper triangular region of Fig. 2.5 can be tuned to make C_3 vanish. Sections 2.9 and 2.10 look more closely at the design of earlier planar Penning traps and suggest that these were not biased to make $C_3 = 0$.

2.4.4 Optimize to $a_2 = a_3 = a_4 = a_5 = 0$

For a scaled three-gap, trap we must choose six parameters ($\tilde{\rho}_2$, $\tilde{\rho}_3$, $\widetilde{V}_1$, $\widetilde{V}_2$, $\widetilde{V}_3$, and $\tilde{z}_0$) that solve the constraints of Eqs. (2.18) and (2.19). Our preferred path to optimization starts from adding the constraints

$$C_1 = 0, \tag{2.44a}$$

$$C_2 = 1, \tag{2.44b}$$

$$a_2 = a_3 = 0. \tag{2.44c}$$

What appear here to be four constraints are actually three constraints because $a_3 = 0$ follows from $a_2 = 0$ via Eq. (2.24c).

The difference of the number of parameters and constraints is three. Where solutions exist, we might thus expect them to be functions of the two parameters that specify the relative geometry and that a range of $\tilde{z}_0$ might be possible. The shaded area in Fig. 2.5 represents the relative geometries for which there are solutions. Solutions also do exist for a range of $\tilde{z}_0$ values, as illustrated in Fig. 2.6 for our sample trap geometry. The solutions are double-valued because the third constraint equation is quadratic in the scaled potentials $\widetilde{V}_1$, $\widetilde{V}_2$, and $\widetilde{V}_3$. The solid and dashed curves distinguish the two branches.

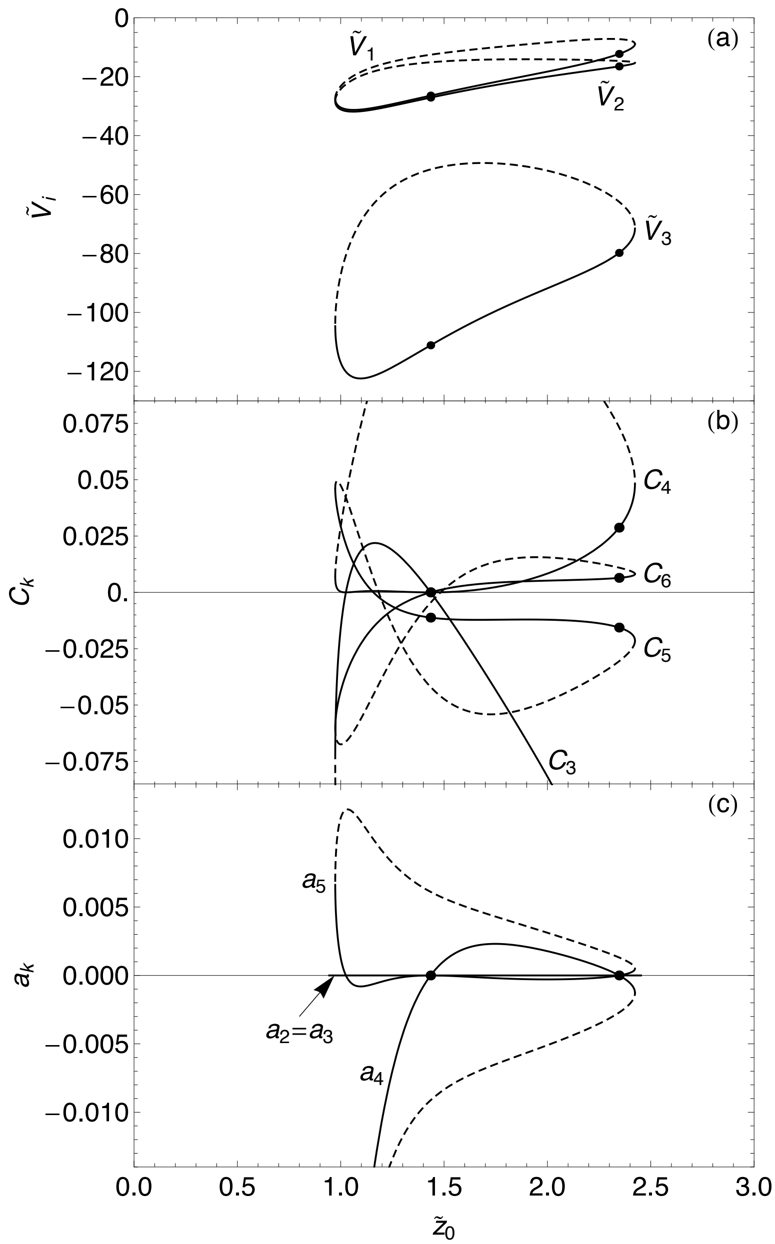

Figure 2.6: (a) Scaled potentials applied to the sample trap electrodes to make a trap with $a_2 = 0$, as a function of the position $\tilde{z}_0$ of the axial potential minimum. (b) The corresponding C_k. (c) The corresponding a_k.

The left and right points in Fig. 2.6, with detailed properties in columns I and II of Tables 2.1 and 2.2, are trap configurations that satisfy the more stringent set of constraints

$$C_1 = 0, \tag{2.45a}$$

$$C_2 = 1, \tag{2.45b}$$

$$a_2 = a_3 = a_4 = a_5 = 0. \tag{2.45c}$$

What appear to be six constraints on the six parameters are actually four constraints, in light of Eq. (2.28). The difference of the number of parameters and constraints is thus two. When solutions exist, we will thus regard them as functions of the relative geometry, $\tilde{\rho}_2$ and $\tilde{\rho}_3$, which will then determine a particular value of $\tilde{z}_0$. The darkly shaded region in Fig. 2.5 shows the relative geometries for which solutions can be found.

For the solution that is the right point in Fig. 2.6, none of the potential coefficients C_3, C_4, C_5 and C_6 vanish. The axial potential in Fig. 2.2 is thus clearly different from a harmonic oscillator potential. Since $C_3 \neq 0$, the amplitude of the second harmonic of the axial oscillation is the lowest-order term from Eq. (2.34),

$$\frac{\widetilde{A}_2}{\widetilde{A}_1} = \frac{C_3}{4}\widetilde{A} + \ldots. \tag{2.46}$$

The amplitude of this second harmonic should still be relatively small insofar as $\widetilde{A} = A/\rho_1$ is small.

We discuss the solution that is the left point in Fig. 2.6 and column II in Tables 2.1 and 2.2 in Sec. 2.4.6.

	$\{\widetilde{\rho}_i\} = \{1, 5.5, 7.5426\}$			
	$a_2 = a_4 = 0$		$C_3 = C_4 = 0$	
	I	II	III	IV
	Eq. (2.45)	Eqs. (2.45), (2.49)	Eqs. (2.47), (2.49)	Eq. (2.47)
$\widetilde{V}_1$	−12.2615	−26.4192	−26.4192	−31.0353
$\widetilde{V}_2$	−16.4972	−27.0861	−27.0861	−31.6642
$\widetilde{V}_3$	−79.7942	−111.1415	−111.1415	−120.1261
$\widetilde{z}_0$	2.3469	1.4351	1.4351	1.0250
C_3	−0.1516	0.0000	0.0000	0.0000
C_4	0.0287	0.0000	0.0000	0.0000
C_5	−0.0156	−0.0112	−0.0112	0.0213
C_6	0.0064	0.0000	0.0000	−0.0366
a_2	0.0000	0.0000	0.0000	0.0000
a_3	0.0000	0.0000	0.0000	0.0000
a_4	0.0000	0.0000	0.0000	−0.0343
a_5	0.0000	0.0000	0.0000	0.0000
a_6	−0.0003	−0.0039	−0.0039	−0.0095
C_{11}	−0.1205	−0.3737	−0.3737	−0.6810
C_{12}	−0.1625	0.0443	0.0443	0.3356
C_{13}	0.0521	0.0780	0.0789	0.0875
$C_{1d}^{(\mathrm{opt})}$	−0.3280	−0.5364	−0.5364	−0.7510
$\tilde{\rho}_d^{(\mathrm{opt})}$	3.3191	2.0295	2.0295	1.4496
γ_1	−194.15	3.45	3.45	3.50
γ_2	8.14	2.64	2.64	4.15
γ_3	−1.56	−3.12	−3.12	1.61
	Fig. 2.6 points		Fig. 2.7 points	
	Right	Left	Right	Left

Table 2.1: Scaled parameters for the sample planar trap geometry.

$\{\rho_i\} = \{1.0909, 6, 8.2283\}$ mm					
	$a_2 = a_4 = 0$		$C_3 = C_4 = 0$		
	I	II	III	IV	
	Eq. (2.45)	Eqs. (2.45), (2.49)	Eqs. (2.47), (2.49)	Eq. (2.47)	
ρ_1	1.0909	1.0909	1.0909	1.0909	mm
z_0	2.5603	1.5655	1.5655	1.1182	mm
$\rho_d^{(\text{opt})}$	3.6208	2.2140	2.2140	1.5814	mm
f_z	64	64	64	64	MHz
V_0	-1.0941	-1.0941	-1.0941	-1.0941	V
V_1	13.4158	28.9064	28.9064	33.9572	V
V_2	18.0504	29.6361	29.6361	34.6452	V
V_3	87.3065	121.6051	121.6051	131.4355	V
Δf_z	0.0	0.0	0.0	0.0	Hz
1: γ_z	$2\pi\,1.37$	$2\pi\,13.16$	$2\pi\,13.16$	$2\pi\,43.70$	s^{-1}
2: γ_z	$2\pi\,2.49$	$2\pi\,0.19$	$2\pi\,0.19$	$2\pi\,10.61$	s^{-1}
3: γ_z	$2\pi\,0.26$	$2\pi\,0.57$	$2\pi\,0.57$	$2\pi\,0.72$	s^{-1}
d: $\gamma_z^{(\text{opt})}$	$2\pi\,10.14$	$2\pi\,27.11$	$2\pi\,27.11$	$2\pi\,53.14$	s^{-1}
	Fig. 2.6 points		Fig. 2.7 points		
	Right	Left	Right	Left	

Table 2.2: One set of absolute values for the sample planar trap geometry. The broadening Δf_z is for a 5 K thermal distribution of axial energies. The damping widths $\gamma_z/(2\pi)$ are for the numbered electrode connected to $R = 100\ \text{k}\Omega$. Thermal frequency spreads Δf_z that are below 1 Hz will be very difficult to realize in practice, owing to imperfections in real traps.

2.4.5 Optimize to $C_3 = C_4 = a_2 = a_3 = 0$

A second path to optimizing the six parameters for a scaled trap configuration starts with adding the constraint $C_3 = 0$ to the two requirements for a trap, $C_1 = 0$ and $C_2 = 1$ (Eqs. (2.18) and (2.19)). All three constraint equations are then linear in the scaled potentials $\widetilde{V}_1$, $\widetilde{V}_2$, and $\widetilde{V}_3$, yielding single-valued solutions for a given $\tilde{z}_0$, $\tilde{\rho}_2$, and $\tilde{\rho}_3$. There are three more parameters than constraints. Solutions that give $C_3 = 0$ are possible for any relative geometry. The traps can be biased to make a range of $\tilde{z}_0$ values. For our sample trap geometry, the scaled potentials are plotted as a function of $\tilde{z}_0$ in Fig. 2.7. The resulting C_k and a_k are shown as well.

The axial potential is more harmonic at the two points in Fig. 2.7, both of which satisfy the more stringent set of constraints:

$$C_1 = C_3 = C_4 = 0 \tag{2.47a}$$

$$C_2 = 1 \tag{2.47b}$$

$$a_2 = a_3 = 0. \tag{2.47c}$$

What appear to be six constraints on the six parameters for the scaled trap are actually four (since Eq. (2.47c) follows from Eq. (2.47a–b) via Eq. (2.24a–c)). There are thus only two more parameters than constraints. Various relative trap geometries can thus be biased to satisfy this set of constraints, as represented by the solid boundary and arrows labeled $C_3 = C_4 = a_2 = a_3 = 0$ in Fig. 2.5, and $\tilde{z}_0$ is thus determined for each relative geometry. Note that although this region lies within the shaded area for which $a_2 = a_3 = a_4 = a_5 = 0$ can be realized, in general, it is not possible to satisfy both sets of constraints simultaneously.

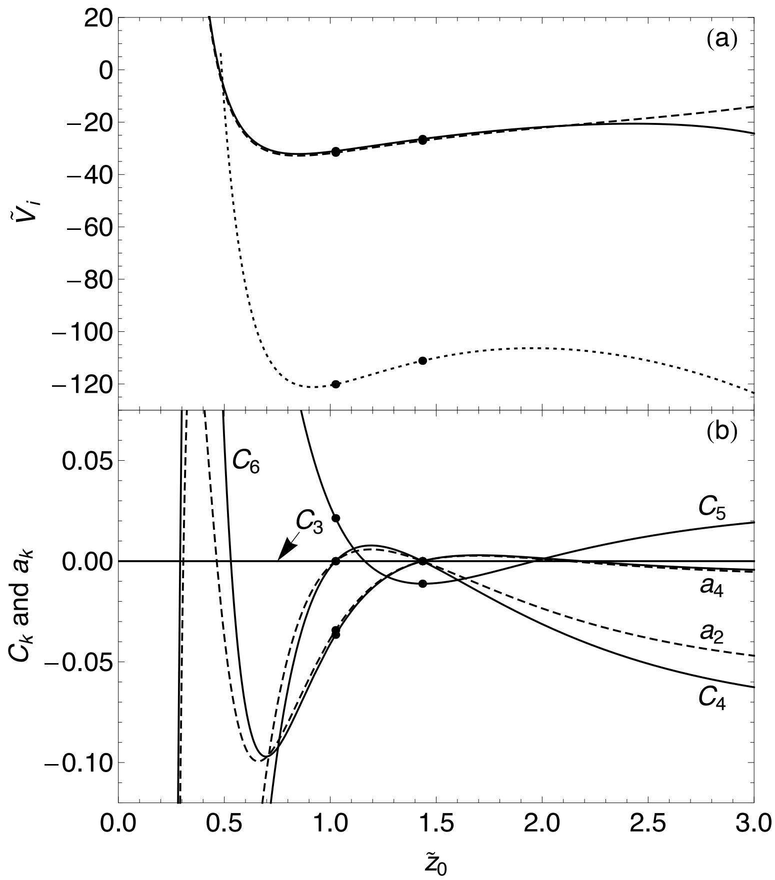

Figure 2.7: (a) Scaled potentials applied to our sample trap electrodes to produce a trap with $C_3 = 0$, as a function of $\tilde{z}_0$. (b) The resulting C_k and a_k.

For the sample trap geometry, two of the applied potentials are nearly the same, making this nearly a two-gap trap, but a slight potential difference is needed. More details about these solutions are in columns III and IV of Tables 2.1 and 2.2. Compared to the optimized configuration in Eq. (2.45), the optimization of Eq. (2.47) has a more harmonic potential (Fig. 2.2) but a less good suppression of the amplitude dependence of the axial frequency, as long as $a_4 \neq 0$ and $a_5 \neq 0$.

Any solution with $C_3 = C_4 = 0$ (including the two points in Fig. 2.7 and columns III–IV in Tables 2.1 and 2.2, as well as the left solution point in Fig. 2.6 column II in Tables 2.1 and 2.2 described in the following section) has a suppressed harmonic content compared to Eq. (2.46), with

$$\frac{\widetilde{A}_2}{\widetilde{A}_1} = \frac{5C_5}{12}\widetilde{A}^3 + \ldots, \tag{2.48}$$

from Eqs. (2.33) and (2.34). The amplitude of higher harmonics is suppressed by additional powers of $\widetilde{A}$.

We discuss the solution that is the right point in Fig. 2.7 and column III in Tables 2.1 and 2.2 in the following section.

2.4.6 Harmonic optimization

The highest level of optimization can be achieved for traps that have $C_3 = C_4 = 0$ and additionally have the remarkable suppression of the amplitude dependence of the axial frequency that comes from adding the constraint $C_6 = 0$ (Eq. (2.29)). For this optimized harmonic configuration

$$C_1 = C_3 = C_4 = C_6 = 0, \tag{2.49a}$$

$$C_2 = 1, \tag{2.49b}$$

$$a_2 = a_3 = a_4 = a_5 = 0. \tag{2.49c}$$

What appear to be nine constraints are actually five (because Eq. (2.49c) follows from Eq. (2.49a–b) via Eq. (2.24)). There is thus one more parameter to chose ($\tilde{\rho}_2$, $\tilde{\rho}_3$, $\widetilde{V}_1$, $\widetilde{V}_2$, $\widetilde{V}_3$, and $\tilde{z}_0$) than there are constraints. The free parameter leads to a range of possible relative geometries (the dashed line in Fig. 2.5). Missing from Eq. (2.49) is $C_5 = 0$, since there are no solutions when this constraint is added.

Our sample trap (filled circle in the dashed line in Fig. 2.5) is one example. For it, the left solution point in Fig. 2.6 and the right solution point in Fig. 2.7 are actually the same configuration, as is obvious from columns II and III of Tables 2.1 and 2.2. This convergence of two solutions happens only for traps with relative geometries on the dashed line in Fig. 2.5. For other traps in the shaded region where $a_2 = a_4 = 0$ can be satisfied, these two solutions remain distinct, and the highly optimized constraints of Eq. (2.49) cannot be satisfied for any choice of the trap potentials.

The optimized harmonic trap configurations (Fig. 2.8) involve only a very narrow range of scaled distances $\tilde{z}_0$ from the electrode plane to the axial potential minimum. The scaled potentials needed are shown in Fig. 2.8b. The leading departure from a harmonic potential is described by $C_5 = -0.011$ (Fig. 2.8b). As mentioned, we find no solutions to the constraint equations if a vanishing C_5 is required.

The highly optimized properties of Eq. (2.49) are an optimized harmonic configuration in that the leading departures from a harmonic axial potential vanish because

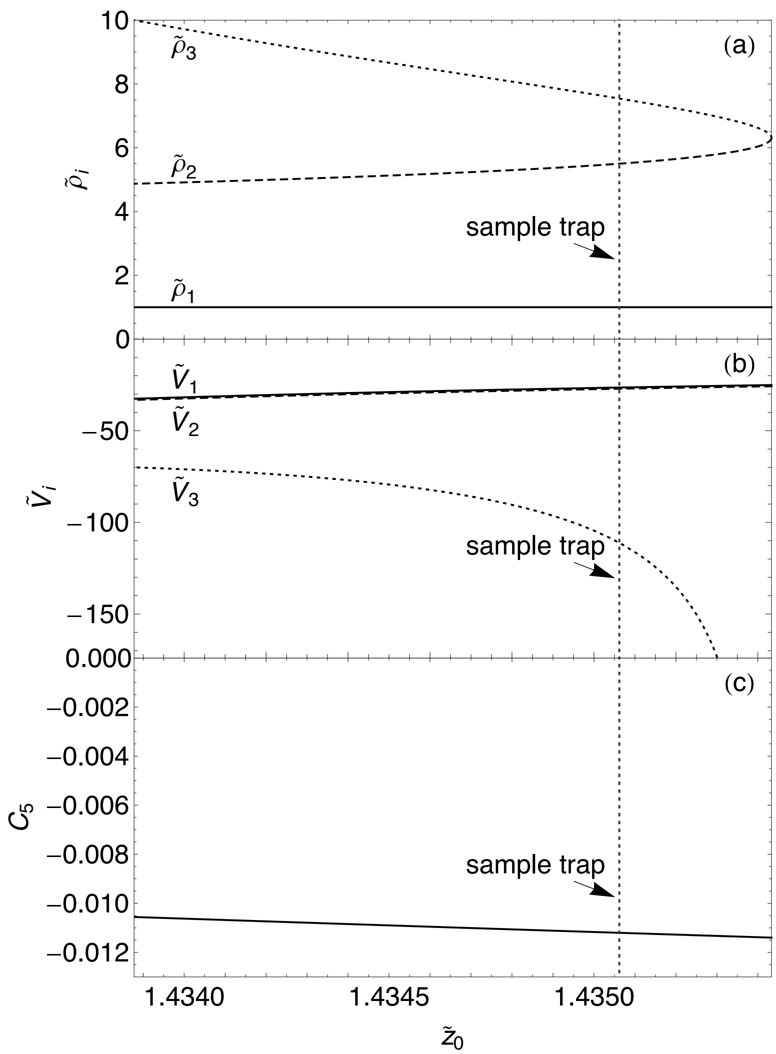

Figure 2.8: (a) An optimized harmonic trap (Eq. (2.49)), as illustrated using our sample trap geometry, is possible with only a small range of $\tilde{z}_0$ values and relative geometries. (b) The required scaled potentials. (c) The values of C_5, which remains non-zero.

$C_3 = C_4 = 0$ at the same time that the amplitude dependence of the axial frequency is strongly suppressed. A particle's axial oscillation will thus have a very small amplitude at the overtones of the fundamental harmonic, as given by Eq. (2.48), with the amplitude of higher harmonics suppressed by additional powers of $\widetilde{A}$.

2.4.7 Comparing amplitude-dependent frequency shifts

The optimized trap configurations greatly reduce the amplitude dependence of the axial oscillation frequency. Avoiding frequency fluctuations caused by noise-driven amplitude fluctuations is critical to resolving the small frequency shifts that signify one-quantum cyclotron and spin transitions.

One way to compare the optimized configurations is in Fig. 2.4. The axial frequency shift is shown as a function of oscillation amplitude for the three optimized configurations of the sample trap. For one electron in the cylindrical trap, an oscillation amplitude of 0.1 mm was large and easily detected.

Another figure of merit is the frequency broadening for the thermally driven axial motion of a trapped particle, which was discussed in Sec. 2.2.4. We use the 5 K axial temperature realized and measured for a cylindrical Penning trap cooled by a dilution refrigerator [170], though it should be noted that realizing such a low detector temperature is a challenging undertaking. Each trap configuration can thus be characterized by the thermal broadening of the axial resonance frequency, as indicated in Fig. 2.9. Imperfections in real planar traps and instabilities in applied potentials will likely make it difficult to get thermal widths much less than 1 Hz for an axial frequency of 64 MHz.

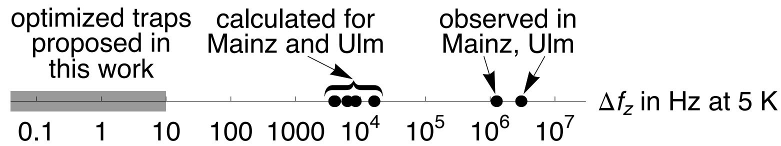

Figure 2.9: Comparison of the frequency widths calculated for optimized planar traps with a 5 K axial temperature. The imperfections of a real planar trap will likely make it difficult to realize widths that are below 1 Hz for an axial frequency of 64 MHz.

2.5 Laboratory Planar Traps

Planar Penning traps put into service in the laboratory will not have the ideal properties described in the previous sections of this work. A real trap does not have gaps of negligible width, does not have an electrode plane that extends to infinity, does not have conducting boundaries at an infinite distance above the electrode plane and at an infinite radius, and will not have exactly the ideal dimensions and the perfect cylindrical symmetry that are being approximated. None of these have large a impact on the results from an idealized calculation. However, the result is that the potentials applied to the electrodes of a real laboratory trap will need to be adjusted a bit from the ideal planar trap values to compensate for the unavoidable deviations and imperfections.

The effect of nonnegligible gaps is calculated in Sec. 2.5.1. The effect of a finite electrode plane and a finite conducting radial enclosure is discussed in Sec. 2.5.2. Imperfections in the trap dimensions and symmetry are dealt with in Sec. 2.5.3 using simple estimates that proved adequate for the design of earlier traps. These estimates are used to discuss the tuning of the trap potentials required to compensate for imperfections of this order (Sec. 2.5.4).

2.5.1 Gaps between electrodes

Small gaps of some width w between electrodes are unavoidable, of course. As long as $w \ll z_0$, the potential variation at the position of the trapped particle caused by the gaps should be small since the potential variation should diminish exponentially with an argument that goes as w/z_0. We assume that the gaps between electrodes are deeper than they are wide since this is needed to screen the effect of any stray charges on the insulators that keep the electrodes apart.

Solving exactly for the trapping potential using boundary conditions that include deep gaps between the electrodes is a challenging undertaking. Instead we use a simple and approximate boundary condition that was used to demonstrate the small effect of the gaps in a cylindrical trap [125]. We take the potential in the electrode plane across each gap to vary linearly between the potentials of the two electrodes. The potential is thus determined everywhere in the electrode plane by the potentials on the electrodes.

The basis of this approximation is illustrated by the equipotentials shown for a planar trap in Fig. 1.6b (and later in Figs. 2.10b, 2.12b, and 2.14b). All the equipotentials from the trapping volume must connect to equipotentials within the gaps. Deep within a small but deep gap, the equipotentials will be locally similar to the equipotentials between parallel plates, the plates being the vertical electrode walls within the gap. The equipotentials will remain roughly parallel until they rise above the electrode plane, whereupon they will spread. We make the approximation that in the electrode plane, the potential in the gap varies linearly with radius between the voltages applied to the two electrodes that are separated by the gap. Since the effect of the gaps is already small a better approximation should not be needed.

The completely specified electrode plane boundary is thus given by the electrode boundaries and the linear change of potential between them at the gaps of width w_i (with $\widetilde{w}_i = w_i/\rho_1$) centered at radius ρ_i. The solution to Laplace's equation on axis then becomes (see Sec. A.3)

$$V^{gap}(0,z) = \sum_{i=1}^{N} \Delta V_i \, \Phi_i(\tilde{z}), \tag{2.50}$$

$$\begin{aligned}\Phi_i(\tilde{z}) = & \frac{\tilde{z}}{\widetilde{w}_i} \sinh^{-1}\left(\frac{\tilde{\rho}_i + \widetilde{w}_i/2}{\tilde{z}}\right) \\ & - \frac{\tilde{z}}{\widetilde{w}_i} \sinh^{-1}\left(\frac{\tilde{\rho}_i - \widetilde{w}_i/2}{\tilde{z}}\right) - 1.\end{aligned} \tag{2.51}$$

In the limit of vanishing gap widths this potential becomes the potential of an ideal planar trap in Eqs. (2.11) and (2.12).

Following the procedure outlined earlier (Sec. 2.4), this potential is expanded about $\tilde{z} = \tilde{z}_0$. The sets of parameters that satisfy reasonable constraint equations identify the optimized trap configurations that greatly reduce the amplitude dependence of the axial frequency and make the trap potential more harmonic. We get four optimized configurations, as before, but with applied potentials that are slightly shifted.

Biasing a trap with a finite gap width as if it was an ideal planar trap with no gap width is one approach. Table 2.3 shows the C_k and a_k when ideal trap biases (from Tables 2.1 and 2.2) are applied to the sample trap with $w = 50$ μm gap widths. The broadening of the axial frequency Δf_z for a thermal distribution of axial frequencies is still small enough that it should not prevent observing one electron in a trap with such gaps.

	$\{\widetilde{\rho}_i\} = \{1, 5.5, 7.5426\}$				
	$a_2 = a_4 = 0$		$C_3 = C_4 = 0$		
	I	II	III	IV	
	Eq. (2.45)	Eqs. (2.45), (2.49)	Eqs. (2.47), (2.49)	Eq. (2.47)	
$\widetilde{z}_0$	2.3469	1.4351	1.4351	1.0250	
C_3	−0.1516	0.0000	0.0000	0.0000	
C_4	0.0287	0.0000	0.0000	0.0001	
C_5	−0.0156	−0.0112	−0.0112	0.0213	
C_6	0.0064	0.0000	0.0000	−0.0365	
a_2	0.0000	0.0000	0.0000	0.0000	
a_3	0.0000	0.0000	0.0000	0.0000	
a_4	0.0000	0.0000	0.0000	−0.0342	
a_5	0.0000	0.0000	0.0000	0.0000	
a_6	−0.0003	−0.0039	−0.0039	−0.0095	
Δf_z @ 5 K	0.3	0.3	0.3	2.7	Hz

Table 2.3: Finite gaps between the electrodes of the sample trap result in different C_k and a_k when the optimal potentials for the ideal trap (Tables 2.1 and 2.2) are applied. The gap width is $w = 0.002$ in $= 50$ μm.

Shifting the potentials applied to the electrodes improves the C_k and a_k, as indicated in Table 2.4. However, the predicted thermal widths then become smaller than what imperfections (discussed in Sec. 2.5.3) will likely allow us to attain, so this adjustment is not really needed.

The small size of these coefficients illustrates that realistic gaps between the electrodes of a trap as large as our sample trap pose no threat to detecting a single electron in a planar Penning trap. Simply biasing the trap as if it were a trap with vanishing gap widths suffices. However, as planar traps get smaller, the gaps will likely be relatively larger with respect to the trap dimensions. The use of Eqs. (2.50) and (2.51) will then be required.

Practical considerations associated with gaps between electrodes are considered

	$\{\widetilde{\rho}_i\} = \{1, 5.5, 7.5426\}$				
	$a_2 = a_4 = 0$		$C_3 = C_4 = 0$		
	I	II	III	IV	
	Eq. (2.45)	Eqs. (2.45), (2.49)	Eqs. (2.47), (2.49)	Eq. (2.47)	
$\delta\widetilde{V}_1$	-0.0008	0.0015	0.0015	-0.0076	
$\delta\widetilde{V}_2$	-0.0006	0.0014	0.0014	-0.0076	
$\delta\widetilde{V}_3$	0.0034	0.0048	0.0048	-0.0157	
δV_1	0.0009	-0.0016	-0.0016	0.0083	V
δV_2	0.0006	-0.0015	-0.0015	0.0083	V
δV_3	-0.0037	-0.0053	-0.0053	0.0172	V
Δf_z @ 5 K	0.0	0.0	0.0	0.0	Hz

Table 2.4: Gaps of width $w = 0.002$ in $= 50$ μm between the electrodes of our sample trap shift the scaled and absolute potentials that must be applied to obtain the optimized trap configurations. The shifts are with respect to the values calculated for a vanishing gap width in Tables 2.1 and 2.2.

in Secs. 3.4 and 3.5.

2.5.2 Finite boundaries

For laboratory traps, it is difficult to approximate an infinite electrode plane and to keep all parts of the apparatus many trap diameters away from the trapping volume. The effects of realistic finite boundary conditions are thus extremely important. For smaller planar Penning traps, the finite boundaries may be less important.

One choice of finite boundary conditions comes from locating a planar trap within a grounded conducting cylinder closed with a flat plate (Fig. 2.10). The boundary conditions in the electrode plane are still given in Fig. 2.1 for $\rho < \rho_c$. The boundary

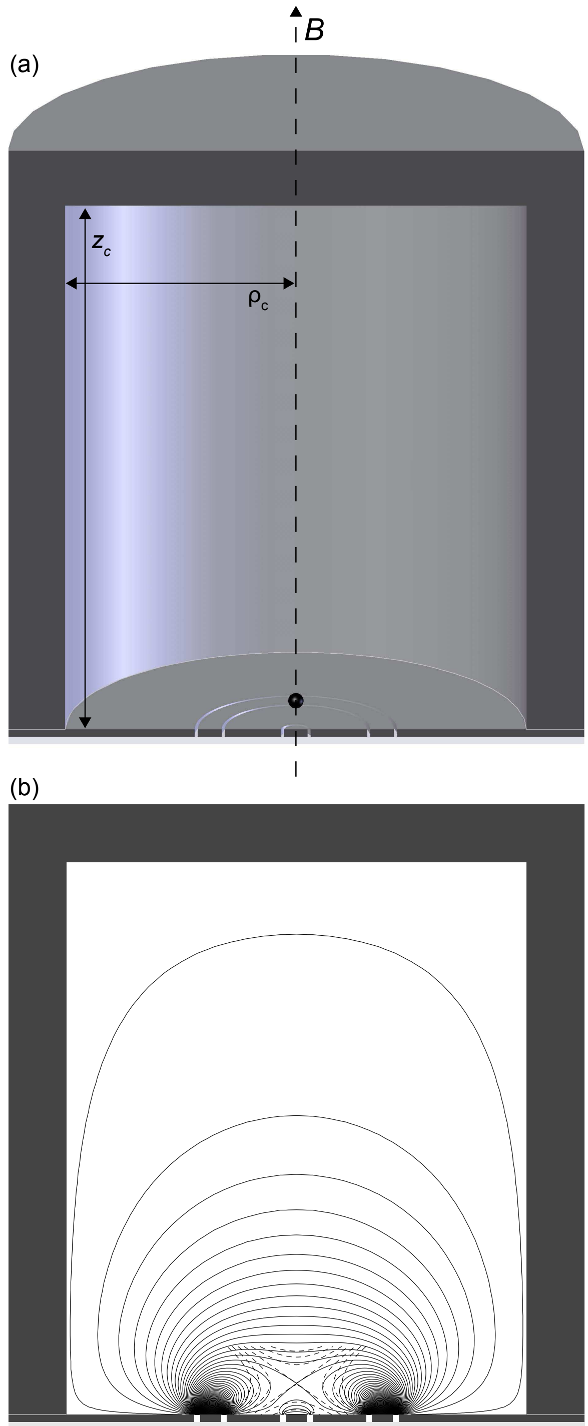

Figure 2.10: (a) Planar trap enclosed within a conducting, capped cylinder. Particles can be loaded through a tiny axial hole in the cover (not visible). (b) Side view of the trap electrodes and equipotentials spaced by V_0, with the infinitesimal gaps between the electrodes widened to make them visible. The equipotentials extend into the gaps between electrodes. The dashed equipotentials of an ideal quadrupole are superimposed near the trap center.

conditions at infinity in Eq. (2.5) are replaced by

$$V(\rho_c, z) = 0, \tag{2.52}$$

$$V(\rho, z_c) = 0. \tag{2.53}$$

Particles can be loaded into the trap through a hole through the conducting plate above that is small enough to negligibly affect the potential near the particle.

The solution to Laplace's equation for $z > 0$ that satisfies these boundary conditions can be written as (see Sec. A.6)

$$V(0, \tilde{z}) = \sum_{i=1}^{N} \Delta V_i \, \Phi_i(\tilde{z}; \tilde{\rho}_c, \tilde{z}_c). \tag{2.54}$$

Standard electrostatics methods [167, 168] give dimensionless potentials,

$$\Phi_i(\tilde{z}; \tilde{\rho}_c, \tilde{z}_c) = \frac{\tilde{\rho}_i}{\tilde{\rho}_c} \sum_{n=1}^{\infty} \frac{2J_1(\alpha_{0n} \frac{\tilde{\rho}_i}{\tilde{\rho}_c})}{\alpha_{0n} {J_1}^2(\alpha_{0n})} \frac{\sinh\left(\alpha_{0n} \frac{\tilde{z}-\tilde{z}_c}{\tilde{\rho}_c}\right)}{\sinh\left(\alpha_{0n} \frac{\tilde{z}_c}{\tilde{\rho}_c}\right)}, \tag{2.55}$$

that are functions of the zeros of the lowest-order Bessel function, with $J_0(\alpha_{0n}) = 0$. The potential off the axis is given by substituting $V(\tilde{\rho}, \tilde{z})$ for $V(0, \tilde{z})$ in Eq. (2.54) and inserting $J_0(\alpha_{0n}\tilde{\rho}/\tilde{\rho}_c)$ to the far right in Eq. (2.55). The planar trap described in Eq. (2.11) is recovered in the limit of large $\tilde{\rho}_c$ and $\tilde{z}_c$, insofar as the $\Phi_i(\tilde{z}; \tilde{\rho}_c, \tilde{z}_c)$ reduce to the $\Phi_i(\tilde{z})$ of Eq. (2.12).

The simplest approach is to bias the electrodes of the enclosed trap as if it was an ideal planar trap with no enclosure, using the potentials tabulated in Tables 2.1 and 2.2. The size of the resulting C_k and a_k coefficients are then displayed in Table 2.5 for the conducting enclosure with dimensions $\rho_c = 19.05$ mm and $z_c = 45.72$ mm (shown to scale in Fig. 2.10), both substantially larger than $\rho_3 = 8$ mm. The resulting

	$\{\widetilde{\rho}_i\} = \{1, 5.5, 7.5426\}$			
	$a_2 = a_4 = 0$		$C_3 = C_4 = 0$	
	I	II	III	IV
	Eq. (2.45)	Eqs. (2.45), (2.49)	Eqs. (2.47), (2.49)	Eq. (2.47)
$\widetilde{z}_0$	2.2406	1.2750	1.2750	0.8481
C_3	−0.1586	−0.0034	−0.0034	0.0110
C_4	0.0365	0.0082	0.0082	−0.0414
C_5	−0.0193	−0.0081	−0.0081	0.0785
C_6	0.0075	−0.0075	−0.0075	−0.0712
a_2	0.0038	0.0062	0.0062	−0.0312
a_3	−0.0006	0.0000	0.0000	−0.0003
a_4	−0.0003	−0.0072	−0.0072	−0.0701
a_5	0.0001	0.0000	0.0000	−0.0040
a_6	−0.0004	−0.0069	−0.0069	−0.0064
Δf_z @ 5 K	190 Hz	310 Hz	310 Hz	1600 Hz

Table 2.5: A conducting enclosure changes the C_k and a_k when the optimal potentials for an ideal planar trap (from Tables 2.1 and 2.2) are applied. The enclosure for the sample trap is shown to scale in Fig. 2.10, with $\rho_c = 19.05$ mm and $z_c = 45.72$ mm.

thermal frequency shifts for a 5 K axial motion are large enough that this broadening will make it hard to observe one electron and realize a one-electron qubit.

It is possible to do much better by shifting the potentials applied to the trap electrodes, without changing the relative geometry of the electrodes. Table 2.6 shows the required potential shifts and the calculated C_k and a_k that result for each of the four optimized planar trap configurations for an ideal planar trap (summarized in Tables 2.1 and 2.2). The frequency broadening is small enough that it should be possible to observe one electron within such a trap.

The configurations in columns II and III of Table 2.6 no longer coincide exactly, however, even though both trap configurations still have very attractive properties. The finite boundary conditions effectively shift the dashed line in Fig. 2.5 that represents the possible geometries for which an optimized three-gap trap can be realized, so that the relative geometry of the sample trap no longer allows this highest level of optimization. What could be done is to slightly change one of the trap radii to compensate for the calculated effect of the finite boundary conditions. However, the shift of geometry is often less than the size of the typical imprecision with which the electrode radii of a real trap can be fabricated (discussed in the next section), so in practice, this makes little sense.

2.5.3 Imprecision in trap dimensions and symmetry

A fabricated laboratory trap will not have exactly the intended dimensions and symmetry because of unavoidable fabrication imprecision. Such effects can only be estimated. The simple estimation method used here has proved itself to be adequate

	$\{\widetilde{\rho}_i\} = \{1, 5.5, 7.5426\}$				
	$a_2 = a_4 = 0$		$C_3 = C_4 = 0$		
	I	II	III	IV	
	Eq. (2.45)	Eqs. (2.45), (2.49)	Eqs. (2.47), (2.49)	Eq. (2.47)	
$\delta\widetilde{V}_1$	1.2769	1.4585	1.6122	1.6247	
$\delta\widetilde{V}_2$	1.1724	1.4626	1.6088	1.6239	
$\delta\widetilde{V}_3$	1.9777	2.2179	2.6248	2.5540	
δV_1	−1.3971	−1.5958	−1.7640	−1.7777	V
δV_2	−1.2828	−1.6003	−1.7603	−1.7768	V
δV_3	−2.1639	−2.4267	−2.8719	−2.7944	V
$\widetilde{z}_0$	2.3625	1.4333	1.4436	1.0225	
C_3	−0.1520	0.0013	0.0000	0.0000	
C_4	0.0289	0.0000	0.0000	0.0000	
C_5	−0.0155	−0.0111	−0.0113	0.0220	
C_6	0.0064	0.0000	0.0002	−0.0371	
a_2	0.0000	0.0000	0.0000	0.0000	
a_3	0.0000	0.0000	0.0000	0.0000	
a_4	0.0000	0.0000	0.0002	−0.0347	
a_5	0.0000	0.0000	0.0000	0.0000	
a_6	−0.0003	−0.0039	−0.0038	−0.0095	
Δf_z @ 5 K	0.0	0.0	0.0	0.0	Hz

Table 2.6: For a conducting enclosure around the sample trap, optimized trap configurations can be obtained by shifting the applied potentials by δV_i and $\delta\widetilde{V}_i$ from the values for an ideal planar trap in Tables 2.1 and 2.2. The enclosure for the sample trap is shown to scale in Fig. 2.10, with $\rho_c = 19.05$ mm and $z_c = 45.72$ mm. Note that configurations II and III are now distinct.

for the design of cylindrical traps [125] and open-access traps [127].

We start with an achievable fabrication tolerance of 0.001 in = 25 μm that is realistic for existing traps of the size of our sample trap. (Whether smaller traps can be constructed with better fractional tolerances is being investigated [140].) Adding and subtracting the achievable tolerance to the radii ρ_2 and ρ_3 of a three-gap planar trap makes variations (Table 2.7) from the design ideal (Tables 2.1–2.2).

These variations do not have the exact ratios of the trap radii needed to make an optimized harmonic trap configuration (Eq. (2.49)) that is specified by the dashed line in Fig. 2.5 and in Fig. 2.8a. The variations have better properties than what has been observed to date with a laboratory planar trap. However, the imprecision in the radii still makes the predicted broadening of an electron's axial resonance for a 5 K thermal distribution of axial energies be too large to observe one trapped electron very well. It would be virtually impossible to realize a one-electron qubit.

The solution must be to slightly adjust the potentials on the electrodes to recover properties closer to the ideal, if this is possible. In the cases of the gaps and the conducting enclosure, we saw that this could be done, at least in principle, by calculating what the improved set of potentials should be. For imprecision in the trap radii, however, the effective radii for the electrodes will be unknown, and hence, no such calculation is possible. What is required is a procedure for tuning the potentials of the trap to narrow the thermal broadening. In designing a trap, we must make sure that the trap potentials can be tuned to compensate for imperfections of this order. The tuning procedure and range is the subject of the next section.

Imperfections that are not axisymmetric are no doubt present. While it is pos-

$\delta\rho_2$	-25	25	0	0	μm
$\delta\rho_3$	0	0	-25	25	μm
$\widetilde{z}_0$	1.4809	1.3876	1.3966	1.4726	
C_3	0.0017	-0.0027	-0.0017	0.0012	
C_4	-0.0036	0.0038	0.0024	-0.0024	
C_5	-0.0108	-0.0112	-0.0111	-0.0110	
C_6	0.0011	-0.0016	-0.0012	0.0009	
a_2	-0.0027	0.0028	0.0018	-0.0018	
a_3	0.0000	0.0000	0.0000	0.0000	
a_4	0.0011	-0.0016	-0.0012	0.0009	
a_5	0.0000	0.0000	0.0000	0.0000	
a_6	-0.0031	-0.0048	-0.0046	-0.0033	
Δf_z @ 5 K	130	140	93	89	Hz

Table 2.7: Changes of 0.001 in = 25 μm for the electrode radii of the sample trap deteriorate its performance when the potentials for an ideal optimized harmonic configuration (from Tables 2.1 and 2.2) are applied.

sible with some effort to make calculations of potential configurations that are not cylindrically symmetric [140], the input from imperfections that should be used in such a calculation is difficult to estimate. Fortunately, the experience with earlier traps suggests that this is not necessary for trap design.

2.5.4 Tuning a laboratory trap

The point of carefully designing the optimized traps for which the lowest order a_k vanish, preferably along with C_3 and C_4, is not that we actually expect to realize this performance in a real laboratory trap. The previous section illustrates that radius imprecision alone will keep this from happening. The reason for the careful optimized designs is to make sure that imprecision alone will make these crucial coefficients differ from zero. Notice in Table 2.7, that the imperfections considered do not make either

a_3 or a_5 deviate much from zero, and a_4 stays at an acceptably low value.

To make a useful trap, we need a way to tune the trap *in situ* to make $a_2 = 0$. The other important coefficients will remain small enough because of the optimized design. For example, to tune out the effect of radius imperfections in our sample trap, the trap must be tuned to change the size of a_2 by about ± 0.003. After each adjustment, the width of the axial resonance line can be measured to see if the thermal broadening has been reduced or increased.

For the cylindrical Penning trap used to observe one-quantum transitions of one electron, tuning of the trap was essential to the observations that were made. In that trap, like every trap within which precise frequency measurements are made, the effect of imperfections could never be calculated well enough to be useful. *In situ* tuning of a compensation potential was always needed.

For a cylindrical trap, tuning is a straightforward (if a bit tedious) matter. To a good approximation, the potential applied to the compensation electrodes (Fig. 1.1c) changes a_2, while the potential applied between the endcap and ring electrodes changes V_0 and ω_z. The axial resonance line is measured after every adjustment of the compensation potential to see if the thermal broadening increased or decreased. The orthogonalized design of this trap kept the change in the compensation potential from changing the axial frequency very much at all. The axial resonance line was thus easy to keep track of during trap tuning, and the axial oscillation never comes close to going out of resonance with the detection circuit.

The tunability defined in Eq. (2.31) quantifies how much the axial frequency changes for a given change in a_2 when the potential on a particular electrode is changed. For the compensation electrodes of the cylindrical trap, the tunability was 0 for a perfect trap, and $\gamma_{\text{comps}} = 0.03$ was realized for a laboratory trap (Sec. 2.4.2). The much larger $\gamma_{\text{ring}} = -141$ indicates that this electrode is for changing the axial frequency of the trap rather than for tuning a_2.

For a planar Penning trap, such an orthogonalization is unfortunately not possible. Changing the potential on each electrode will change both a_2 and ω_z, as indicated by the tunabilities in Table 2.1, which are not small and which do not vary much from electrode to electrode in most cases (e.g., $|\gamma_i| \approx 3$ in one example). The result is that it is necessary to adjust two or three of the potentials applied to the electrodes of a three-gap trap for each step involved in tuning the trap. Adjustments of the applied potentials must be chosen to vary a_2 by a reasonable amount while keeping V_0 and ω_z fixed.

Fig. 2.11 identifies the potentials for which $a_2 = 0$ and $a_4 = 0$ for our sample trap with and without the radius imperfections of Table 2.7. For each point on this plot, V_1 has been adjusted so that V_0 and hence the axial frequency ω_z remain fixed. In this example, it would be necessary to change V_2 or V_3 (along with V_1 to keep V_0 fixed) to achieve $a_2 = 0$. However, by changing both V_2 and V_3 (along with V_1), it would be possible to make $a_2 = 0$ while at the same time making a_4 much smaller in magnitude.

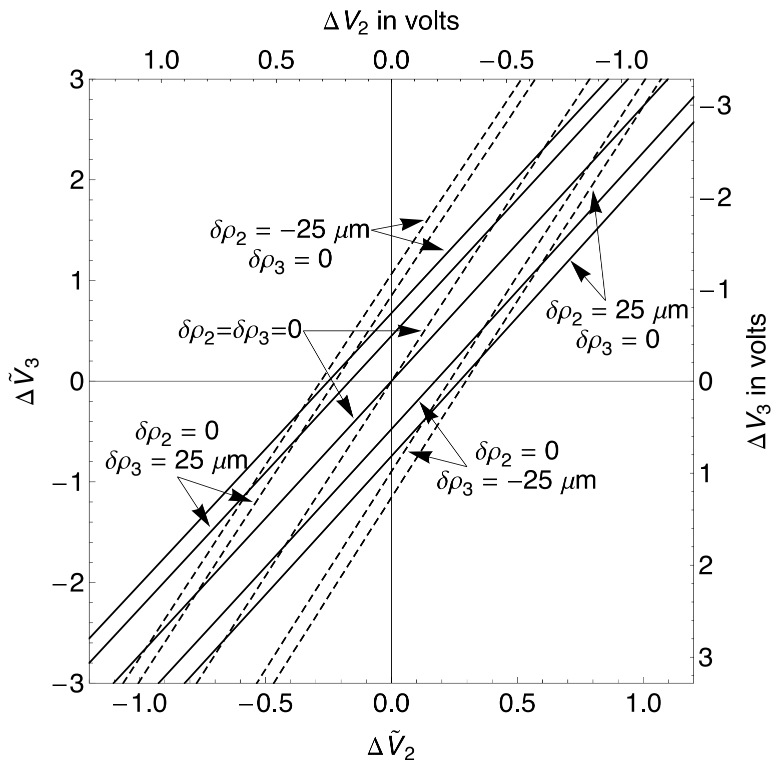

Figure 2.11: The $a_2 = 0$ (solid) and $a_4 = 0$ (dashed) contours for the sample trap with one of its radii displaced by the indicated distance as a function of the potentials applied to the electrodes. V_2 and V_3 are changed as plotted, and V_1 is adjusted to keep the axial frequency at 64 MHz.

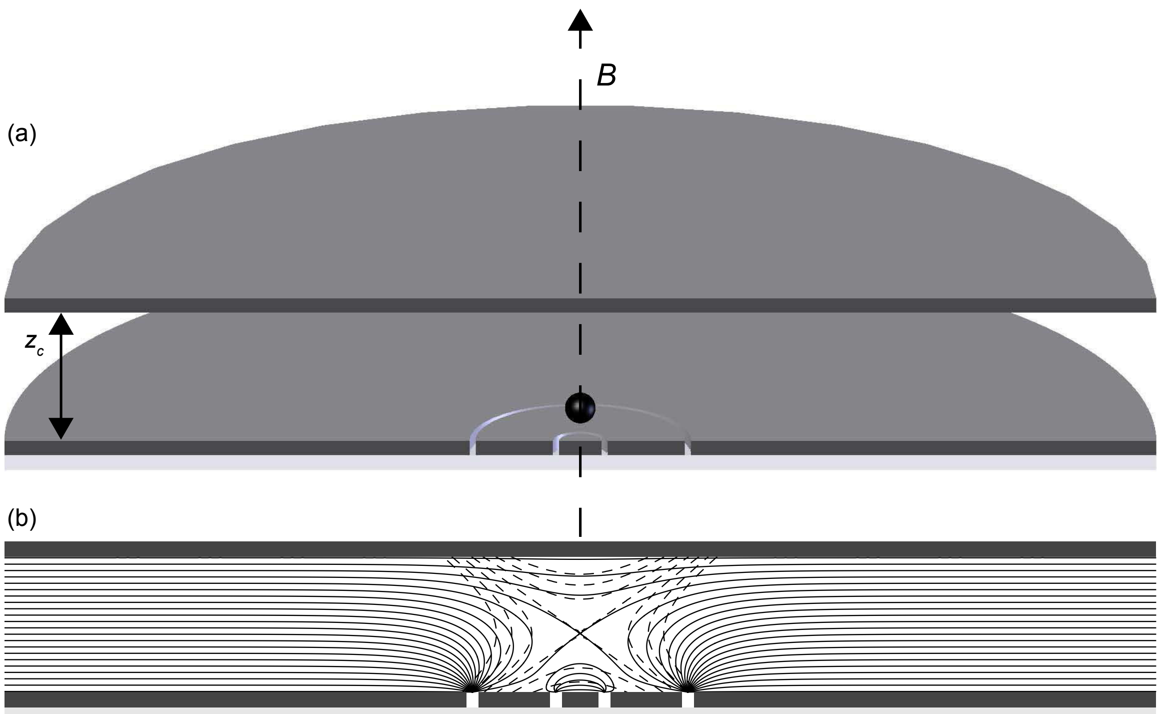

Figure 2.12: (a) A covered planar Penning trap could be loaded through a tiny axial hole in the cover (not visible). (b) Side view of the trap electrodes and equipotentials spaced by V_0, with the infinitesimal gaps between the electrodes widened to make them visible. Some equipotentials extend into the gaps between electrodes and some terminate at infinity. The dashed equipotentials of an ideal quadrupole are superimposed near the trap center.

2.6 Covers and Mirrors

2.6.1 Covered planar trap

A covered planar Penning trap (Fig. 2.12) is a planar trap that is electrically shielded by a nearby conducting plane. The covered planar trap has some very attractive features.

1. The electrodes are in a single plane that can be fabricated as part of a single chip.
2. The conducting plane provides an easily controlled boundary condition above the electrode plane that needs no special fabrication, nor any alignment beyond making the planes parallel.
3. A trap that is radially infinite is well approximated if the radial extent of the two planes beyond the electrodes is large compared to their spacing.
4. A covered planar trap is naturally scalable to an array of traps.
5. The axial motion of electrons in more than one trap could be simultaneously detected with a common detection circuit attached to the cover.
6. The axial motions of electrons in more than one trap could be coupled and uncoupled as they induce currents across a common detection resistor when the axial motions of particular electrons are tuned into and out of resonance with each other.

Three possible additional advantages emerge when the properties of the trapping potential in a covered planar trap are considered.

1. A two-gap covered planar trap can be optimized in much the same way as a three-gap infinite planar trap.

2. Smaller gap potentials can sometimes be used to achieve optimized configurations, permitting smaller gap widths and better screening of the exposed insulator between electrodes.

3. In some cases, a smaller a_6 can be realized for trap configurations with $a_2 = a_3 = a_4 = a_5 = 0$.

These possibilities are illustrated below using an example.

The secondary advantages for planar Penning traps (mentioned at the beginning of this chapter) may be diminished when a cover is used. Microwaves of small wavelength can be introduced between the electrode plane and the cover. However, the added complication of small striplines [99] is likely required for longer wavelengths. It should not be significantly more difficult to load electrons with typical methods via small holes in the electrodes, but if other loading mechanisms are used, then the electron trajectories may be obstructed by the cover.

The potential between the electrode plane and the cover plane is a superposition of terms proportional to the potentials applied to the electrodes, V_i, and the potential applied to the cover plane, V_c (see Sec. A.4),

$$\begin{aligned} V(0,\tilde{z}) = \sum_{i=1}^{N} \Delta V_i \, \Phi_i(\tilde{z};\tilde{z}_c) \\ +V_c \, \Phi_c(\tilde{z};\tilde{z}_c). \end{aligned} \tag{2.56}$$

The grounded cover plane makes the $\Phi_i(\tilde{z})$ of Eq. (2.12) dependent upon $\tilde{z}_c$,

$$\Phi_i(\tilde{z};\tilde{z}_c) = \tilde{\rho}_i \int_0^\infty dk \, \frac{\sinh[k(\tilde{z}-\tilde{z}_c)]}{\sinh(k\tilde{z}_c)} \, J_1(k\tilde{\rho}_i), \tag{2.57}$$

which approaches $\Phi_i(\tilde{z})$ for large $\tilde{z}_c$. Biasing the cover plane at a nonvanishing V_c superimposes a uniform electric field, described by

$$\Phi_c(\tilde{z};\tilde{z}_c) = \tilde{z}/\tilde{z}_c, \tag{2.58}$$

between the large electrode and cover planes.

The scaled geometry and potentials of a two-gap covered planar Penning trap are characterized by six parameters ($\tilde{\rho}_2$, $\tilde{z}_c$, $\widetilde{V}_1$, $\widetilde{V}_2$, $\widetilde{V}_c$ and $\tilde{z}_o$). This is the same number of parameters that characterize a three-gap planar trap with no cover electrode, the optimization of which was discussed in detail in Sec. 2.4.

The trap geometries that can be optimized are represented in Fig. 2.13. The six parameters can be chosen to satisfy the same set of four constraints considered in Sec. 2.4, giving the various shaded regions in Fig. 2.13. The six parameters can be chosen to satisfy the five constraints of Eq. (2.49) on the dashed curve in Fig. 2.13 for which $C_3 = C_4 = C_6 = a_2 = a_3 = a_4 = a_5 = 0$.

The optimized harmonic configuration represented by the dot in Fig. 2.13 has its scaled parameters listed in Table 2.8. One set of possible absolute parameters is listed in Table 2.9. In the following section, we discuss other attractive features of this particular configuration.

Figure 2.12b shows equipotentials spaced by V_0 for a covered planar Penning trap (configuration I in Table 2.8). The equipotentials are calculated for infinitesimal gaps, but the electrodes are represented with finite gaps to make them visible. The

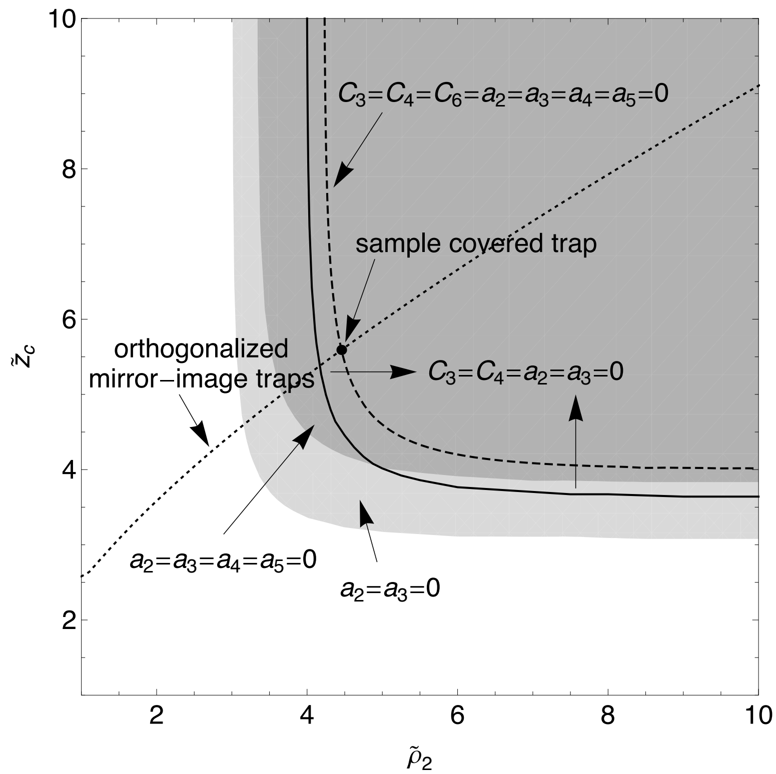

Figure 2.13: Parameter space regions for which the indicated a_k can be made to vanish for a two-gap planar trap with a cover, along with the region and the curve for which the indicated C_k can alternatively be made to vanish. No optimized traps are possible in the unshaded region. The dotted line indicates orthogonalized mirror-image traps formed from two sets of two-gap planar trap electrodes, as described in Sec. 2.6.2

equipotentials terminate in the gaps between electrodes or at infinity. The dashed equipotentials of an ideal quadrupole are superimposed near the trap center.

Covered planar traps are scalable in that an array of traps can share the same covering plane at potential V_c, with the axial frequency and the harmonic properties of each trap being tuned by the potentials applied to the other electrodes. The tuning is analogous to three-gap traps, for which a_2 can be tuned at constant frequency by changing only V_1 and V_2 while leaving V_3 fixed, as shown in Fig. 2.11.

The effect of a grounded radial boundary at $\tilde{\rho}_c$ (rather than at infinity) can also be calculated (see Sec. A.6). The superposition

$$\begin{aligned} V(0,\tilde{z}) = \sum_{i=1}^{N} \Delta V_i \, \Phi_i(\tilde{z};\tilde{\rho}_c,\tilde{z}_c) \\ + V_c \, \Phi_c(\tilde{z};\tilde{\rho}_c,\tilde{z}_c) \end{aligned} \tag{2.59}$$

has dimensionless potentials that depend upon the distance to the radial boundary, $\tilde{\rho}_c$, as well as upon $\tilde{z}_c$. The first of these,

$$\Phi_i(\tilde{z};\tilde{\rho}_c,\tilde{z}_c) = \frac{\tilde{\rho}_i}{\tilde{\rho}_c} \sum_{n=1}^{\infty} \frac{2J_1(\alpha_{0n}\frac{\tilde{\rho}_i}{\tilde{\rho}_c})}{\alpha_{0n} J_1{}^2(\alpha_{0n})} \frac{\sinh\left(\alpha_{0n}\frac{\tilde{z}-\tilde{z}_c}{\tilde{\rho}_c}\right)}{\sinh\left(\alpha_{0n}\frac{\tilde{z}_c}{\tilde{\rho}_c}\right)}, \tag{2.55}$$

was used earlier to describe a grounded enclosure around a planar trap. The second,

$$\Phi_c(\tilde{z};\tilde{\rho}_c,\tilde{z}_c) = \sum_{n=1}^{\infty} \frac{2}{\alpha_{0n} J_1(\alpha_{0n})} \frac{\sinh\left(\alpha_{0n}\frac{\tilde{z}}{\tilde{\rho}_c}\right)}{\sinh\left(\alpha_{0n}\frac{\tilde{z}_c}{\tilde{\rho}_c}\right)}, \tag{2.60}$$

goes to the uniform field limit of Eq. (2.58) in the limit of large $\tilde{\rho}_c$. These potentials can be used to investigate radial boundary effects as needed, though we will not give examples here.

	$\{\widetilde{\rho}_i\} = \{1, 4.4572\}$, $\tilde{z}_c = 5.5914$			
	$a_2 = a_4 = 0$		$C_3 = C_4 = 0$	
	I	II	III	IV
	Eq. (2.45)	Eqs. (2.45), (2.49)	Eqs. (2.47), (2.49)	Eq. (2.47)
$\widetilde{V}_1$	23.6322	23.9786	23.9786	24.2851
$\widetilde{V}_2$	19.0275	23.3251	23.3251	23.6609
$\widetilde{V}_c$	21.2413	29.8478	29.8478	32.4943
$\widetilde{z}_0$	2.4214	1.4338	1.4338	1.0306
C_3	-0.1532	0.0000	0.0000	0.0000
C_4	0.0294	0.0000	0.0000	0.0000
C_5	-0.0143	-0.0099	-0.0099	0.0208
C_6	0.0057	0.0000	0.0000	-0.0351
a_2	0.0000	0.0000	0.0000	0.0000
a_3	0.0000	0.0000	0.0000	0.0000
a_4	0.0000	0.0000	0.0000	-0.0329
a_5	0.0000	0.0000	0.0000	0.0000
a_6	-0.0003	-0.0038	-0.0038	-0.0096
C_{11}	-0.1155	-0.3781	-0.3781	-0.6789
C_{12}	-0.2558	-0.0690	-0.0690	0.2056
C_{1c}	0.3577	0.3577	0.3577	0.3577
$C_{1d}^{(\mathrm{opt})}$	-0.3715	-0.5521	-0.5521	-0.7545
γ_1	-142.78	3.37	3.37	3.47
γ_2	6.72	2.34	2.34	4.28
γ_c	7.64	0.00	0.00	0.00

Table 2.8: Scaled parameters for the sample two-gap covered planar trap geometry.

	$\{\widetilde{\rho}_i\} = \{1, 4.4572\}$, $\tilde{z}_c = 5.5914$				
	$a_2 = a_4 = 0$		$C_3 = C_4 = 0$		
	I	II	III	IV	
	Eq. (2.45)	Eqs. (2.45), (2.49)	Eqs. (2.47), (2.49)	Eq. (2.47)	
ρ_1	1	1	1	1	mm
z_0	2.4214	1.4338	1.4338	1.0306	mm
$\rho_d^{(\mathrm{opt})}$	4.6396	2.1166	2.1166	1.4797	mm
f_z	64	64	64	64	MHz
V_0	-0.9194	-0.9194	-0.9194	-0.9194	V
V_1	-21.7271	-22.0456	-22.0456	-22.3274	V
V_2	-17.4936	-21.4448	-21.4448	-21.7535	V
V_c	-19.5290	-27.4416	-27.4416	-29.8749	V
Δf_z	0.0	0.0	0.0	0.0	Hz
1: γ_z	$2\pi\, 1.50$	$2\pi\, 16.03$	$2\pi\, 16.03$	$2\pi\, 51.68$	s^{-1}
2: γ_z	$2\pi\, 7.34$	$2\pi\, 0.53$	$2\pi\, 0.53$	$2\pi\, 4.74$	s^{-1}
c: γ_z	$2\pi\, 14.35$	$2\pi\, 14.35$	$2\pi\, 14.35$	$2\pi\, 14.35$	s^{-1}
d: $\gamma_z^{(\mathrm{opt})}$	$2\pi\, 15.47$	$2\pi\, 34.18$	$2\pi\, 34.18$	$2\pi\, 63.83$	s^{-1}

Table 2.9: A set of absolute values for the sample two-gap covered planar trap geometry.

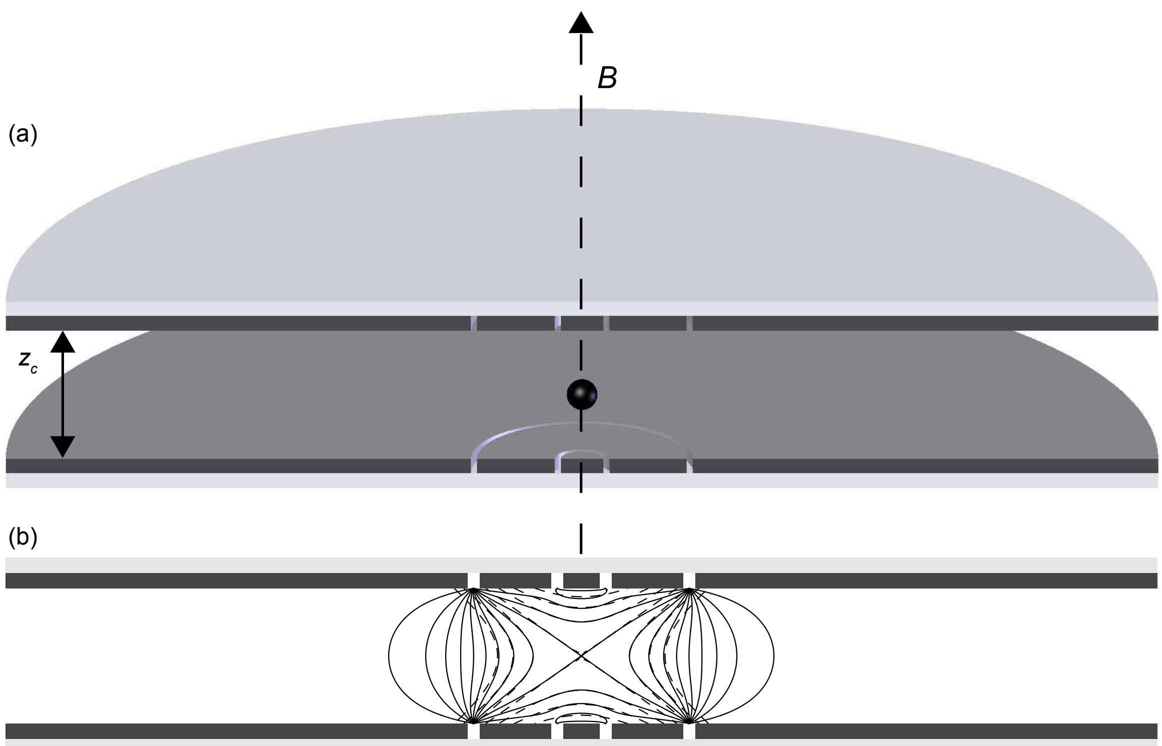

Figure 2.14: (a) A mirror-image Penning trap is formed with two sets of planar trap electrodes facing each other. Particles can be loaded through a tiny axial hole in one of the electrodes (not visible). (b) Side view of the trap electrodes and equipotentials spaced by V_0, with the infinitesimal gaps between the electrodes widened to make them visible. The equipotentials extend into the gaps between the electrodes. The dashed equipotentials of an ideal quadrupole are superimposed near the trap center.

2.6.2 Mirror-image trap

A mirror-image planar trap (Fig. 2.14) is a set of two planar electrodes that are biased identically and face each other. The axial potential (see Sec. A.5),

$$V(0,\tilde{z}) = \sum_{i=1}^{N} \Delta V_i \left[\Phi_i(\tilde{z};\tilde{z}_c) + \Phi_i(\tilde{z}_c - \tilde{z};\tilde{z}_c)\right], \tag{2.61}$$

is a function of the dimensionless potentials defined in Eq. (2.55).

For a two-gap mirror-image trap, there are only four scaled parameters to be chosen ($\tilde{\rho}_2$, $\tilde{z}_c$, $\widetilde{V}_1$, $\widetilde{V}_2$). The mirror-image symmetry of the electrodes ensures that the potential minimum is midway between the electrode planes and that all odd-order C_k vanish. The constraints are $C_2 = 1$, $C_4 = 0$, and $C_{22} = 0$, the latter giving the orthogonality property discussed in the following. With one more parameter than constraints, the possible geometries for a two-gap mirror-image trap are given by the dotted curve in Fig. 2.13. The filled circle on this curve represents the trap geometry that is used to illustrate the properties of a mirror-image trap in Fig. 2.14 and in Tables 2.10 and 2.11.

The properties of a mirror-image trap are similar to those of the cylindrical Penning trap (Fig. 1.1c) used to suspend one electron and to observe its one-quantum cyclotron transitions and spin flips. A charged particle suspended midway between the two electrode planes sees a potential that is symmetric under reflections across this midplane, in which case, all odd-order potential coefficients (C_3, C_5, etc.) vanish, as for the cylindrical trap (Sec. 2.4.2). Also, as for a cylindrical trap, we can choose the potentials applied to the trap electrodes so as to make a trap with a very small C_4, whereupon a_2 and a_3 are very small.

A useful property of mirror-image traps and cylindrical traps is that both of

$\{\widetilde{\rho}_i\} = \{1, 4.4572\}$, $\tilde{z}_c = 5.5914$	
$C_3 = C_4 = 0$, Eq. (2.47)	
$\widetilde{V}_1 = \widetilde{V}_1^{top}$	13.9582
$\widetilde{V}_2 = \widetilde{V}_2^{top}$	12.3743
$\widetilde{V}_3 = \widetilde{V}_3^{top}$	0.0000
$\widetilde{z}_0$	2.7957
C_3	0.0000
C_4	0.0000
C_5	0.0000
C_6	0.0015
a_2	0.0000
a_3	0.0000
a_4	0.0014
a_5	0.0000
a_6	0.0002
$C_{11} = -C_{11}^{top}$	-0.0811
$C_{12} = -C_{12}^{top}$	-0.2624
$C_{13} = -C_{13}^{top}$	-0.0142
$C_{1d}^{(\text{opt})}$	-0.3577
$\tilde{\rho}_d^{(\text{opt})}$	∞
$\gamma_1 = \gamma_1^{top}$	4.35
$\gamma_2 = \gamma_2^{top}$	0.00
$\gamma_3 = \gamma_3^{top}$	-33.96

Table 2.10: Scaled parameters for the sample two-gap mirror-image planar trap geometry.

$\{\widetilde{\rho}_i\} = \{1, 4.4572\}$, $\tilde{z}_c = 5.5914$		
$C_3 = C_4 = 0$, Eq. (2.47)		
ρ_1	1	mm
z_0	2.7957	mm
$\rho_d^{(\text{opt})}$	∞	mm
f_z	64	MHz
V_0	-0.9194	V
$V_1 = V_1^{top}$	-12.8330	V
$V_2 = V_2^{top}$	-11.3768	V
$V_3 = V_3^{top}$	0.0000	V
Δf_z	0.0	Hz
1: γ_z	$2\pi\, 0.74$	s^{-1}
2: γ_z	$2\pi\, 7.72$	s^{-1}
3: γ_z	$2\pi\, 0.02$	s^{-1}
d: $\gamma_z^{(\text{opt})}$	$2\pi\, 14.35$	s^{-1}

Table 2.11: A set of absolute values for the sample two-gap mirror-image planar trap geometry.

these can be "orthogonalized" in a way that a planar trap cannot. A single potential (applied to a pair of electrodes with mirror-image symmetry) is tuned to minimize the amplitude-dependence of the axial frequency. The trap is orthogonalized in that this tuning does not change the axial frequency, which in general would take it out of resonance with the detection circuit.

Figure 2.14b shows equipotentials spaced by V_0 for the mirror-image Penning trap of Table 2.10. The equipotentials are calculated for infinitesimal gaps, but the electrodes are represented with finite gaps to make them visible. The equipotentials terminate in the gaps between electrodes. The dashed equipotentials of an ideal quadrupole are superimposed near the trap center.

2.6.3 Mirror-image trap transformed to a covered trap

At least for initial studies, it may be useful first to load an electron into the center of an orthogonalized mirror-image trap. The presence of a single electron can be determined using the established methods used in cylindrical Penning trap experiments. The challenge is then to adiabatically change the potentials applied to the electrodes to turn the mirror-image trap into a covered planar trap. It is crucial that the electron not be lost. If a high-quality trapping well can be maintained throughout the transfer, then it may even be possible to monitor the electron at intermediate points between the two configurations.

We investigate the feasibility of transferring from the mirror-image trap discussed above (Tables 2.10 and 2.11) to the optimized covered planar trap discussed in the last section (Tables 2.8 and 2.9). The electrode geometry chosen for our example is the lone point in Fig. 2.13 for which it is possible to make an orthogonalized mirror-image trap and also to make the most highly optimized covered planar Penning trap. The potentials applied to achieve the mirror-image trap are those to the far right in Fig. 2.15. The potentials applied to realize the covered planar trap are those to the far left in Fig. 2.15.

For these traps, there are six parameters to choose: five relative trap potentials ($\widetilde{V}_1$, $\widetilde{V}_2$, $\widetilde{V}_1^{\rm top}$, $\widetilde{V}_2^{\rm top}$, $\widetilde{V}_3^{\rm top}$) and $\tilde{z}_0$. During the transfer, we can choose a particular $\tilde{z}_0$ as a constraint, along with four others that we have discussed earlier, $C_1 = C_3 = C_4 = 0$ and $C_2 = 1$. Since there are more parameters than constraints, there is some freedom in the choice of potentials during the transfer, provided that solutions exist. Our choice of intermediate potentials in Fig. 2.15 was made to avoid large potential

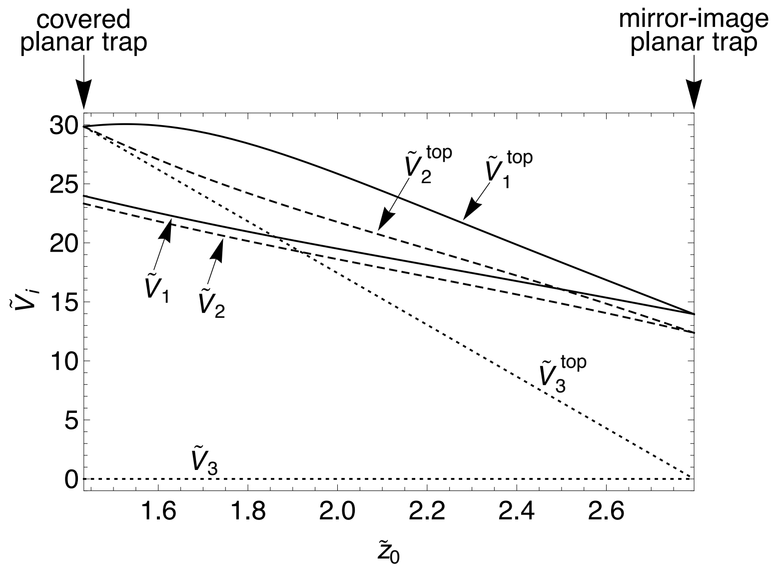

Figure 2.15: One set of applied potentials that relocates an electron centered between the electrode planes of a mirror-image planar trap (far right) to a covered planar trap (far left), while keeping the axial frequency constant and keeping $a_2 = a_3 = C_3 = C_4 = 0$.

differences between electrodes (discussed in Sec. 3.5). The axial oscillation frequency does not change during the transfer. Also, the trap remains optimized during every point in the transfer, with $a_2 = a_3 = C_3 = C_4 = 0$. It may thus be possible to detect the electron's axial oscillation at every step of the transfer.

2.7 Damping and Detecting an Axial Oscillation

2.7.1 Damping and detection in a planar trap

The damping rate γ_z for the axial motion of a trapped particle is the observed resonance linewidth for the axial motion in the limit of a vanishing oscillation amplitude. A thermal distribution of axial oscillation amplitudes broadens the observed resonance linewidth when the axial frequency is amplitude dependent. When the oscillation energy has Fourier components that extend well beyond the damping linewidth, it is difficult to detect the oscillation with the narrow-band detection methods needed to observe the small signal from a single particle. For the cylindrical Penning trap used to observe one-quantum transitions of a single trapped electron [5], this was not a problem. The thermal anharmonicity contribution to the linewidth was less than the damping linewidth. For the Ulm planar trap, the situation was very different. The thermal width was about 10^5 times larger than the damping linewidth, making it impossible to observe a single electron at all [146].

In the preceding sections, we focused on minimizing the amplitude dependence of the axial frequency so that the thermal broadening could be reduced. Just as important is increasing the axial damping linewidth. Here we discuss what is needed to maximize the electron's damping rate. Maximizing the damping maximizes the detected signal as well.

The usual method to probe the axial oscillation of a single trapped particle is to detect the current that its axial motion induces in a resistor R connected to its electrodes [3, 120]. This resistance also damps the motion. The energy dissipated in the resistor comes from the axial motion of the trapped particle, which is thereby damped to the bottom of the axial potential well. In practice, the resistor is a tuned circuit that is resonant at the axial oscillation frequency, at which frequency it acts as a pure resistance.

For a planar Penning trap, Fig. 2.16 illustrates how the AC connections between the circuit and the electrodes can be made to the same electrodes that are DC biased to form the trapping potential. Alternatively, an extra gap (e.g., the dashed circle

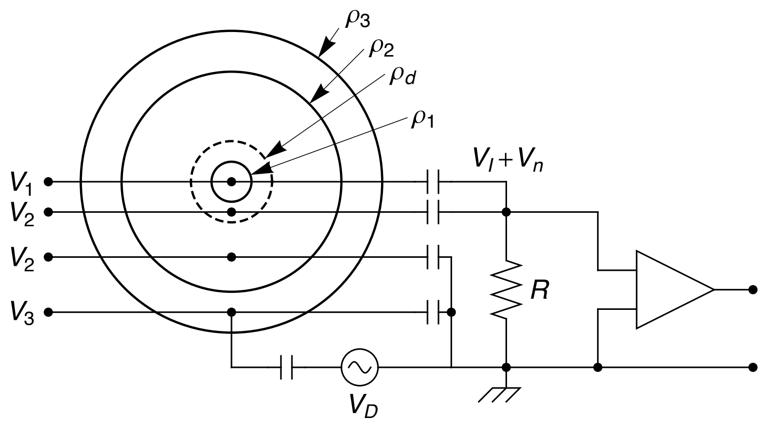

Figure 2.16: The electrical circuit used to bias, detect, damp, and drive a trapped particle's axial motion. An extra gap (dashed circle) in the electrodes of the planar trap can be added to optimize the damping and detection without changing the electrostatic properties of an optimized planar trap. The relative trap geometry is that of the sample trap.

labeled ρ_d in Fig. 2.16) can be added to one of the trap's electrodes to maximize the damping and detection, as will be discussed. This damping-detection gap can coincide with one of the gaps already chosen to minimize the amplitude dependence of the axial frequency. When the extra gap does not coincide with one of the others, the extra gap will not change the electrostatic trapping potential insofar as the same DC bias voltage is applied to either side of the additional gap.

The circuit in Fig. 2.16 represents one way to connect the detection and damping resistance, R, to the electrodes of a three-gap planar trap. The current induced by the particle's axial oscillation makes an instantaneous voltage V_I across the resistor. This induced voltage exerts a reaction force on the trapped particle. The thermal Johnson noise from random electron motions within the resistor induces an additional instantaneous noise voltage V_n across the resistor and electrodes. The oscillatory voltage $V_I + V_n$ on the effective damping electrode for which $\rho < \rho_d$ both drives the particle's axial motion and is detected.

The particle is in the near field of the potential

$$V_{osc} = (V_I + V_n)\phi_d, \tag{2.62}$$

produced by this oscillatory voltage, where the electrostatic potential

$$\phi_d(\tilde{z}) = 1 - \frac{\tilde{z}}{\sqrt{(\tilde{\rho}_d)^2 + \tilde{z}^2}} \tag{2.63}$$

follows from Eq. (2.10).

For a potential V_i applied to electrode i, the instantaneous electric field on a particle oscillating near its equilibrium position at $\tilde{z} = \tilde{z}_0$ is

$$E_i(\tilde{z}_0) \approx -\frac{D_1}{2\rho_1} V_i. \tag{2.64}$$

The factor D_1 depends upon electrodes to which a voltage is applied to make the field. For a voltage applied just to the damping and detection electrode,

$$D_1 = C_{1d} = \frac{-2(\tilde{\rho}_d)^2}{\left[(\tilde{z}_0)^2 + (\tilde{\rho}_d)^2\right]^{3/2}}, \tag{2.65}$$

where the potential expansion coefficient C_{1i} is defined in Eqs. (2.13) and (2.14).

There is a maximum coupling of the circuit and a trapped particle insofar as C_{1d} has a maximum magnitude at

$$\rho_d = \sqrt{2}\,\tilde{z}_0. \tag{2.66}$$

The coupling coefficient is then given by

$$C_{1d}^{(opt)} = \frac{-4 \times 3^{-3/2}}{\tilde{z}_0} \approx \frac{-0.77}{\tilde{z}_0}. \tag{2.67}$$

Figure 2.17a illustrates the maximum for all values of $\tilde{z}_0$.

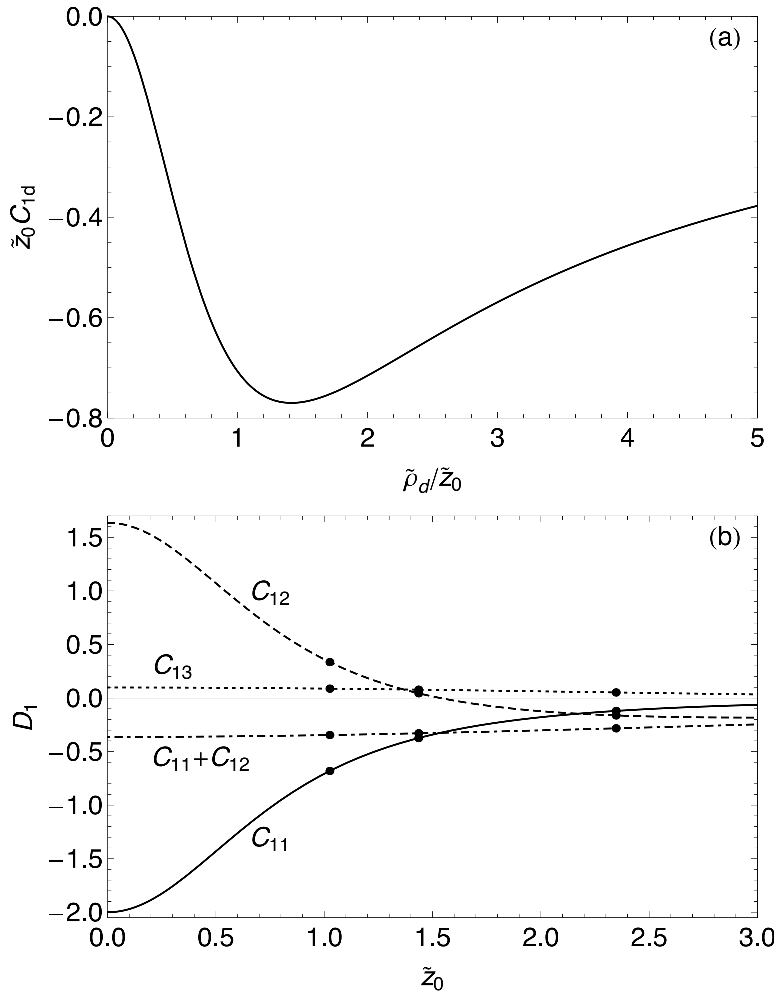

Figure 2.17: (a) The coefficient C_{1d} that describes the coupling and the plotted product $\tilde{z}_0 C_{1d}$ both have a maximum magnitude at $\tilde{\rho}_d = \sqrt{2}\tilde{z}_0$. (b) Electric field coefficients that describe the damping rates and detection efficiency for the sample trap.

If instead the electrodes of the optimized planar trap are attached to the resistor, without adding an extra gap at ρ_d, then D_1 is the sum of the C_{1i} for the electrodes attached to the resistor. If, for example, the central two electrodes are attached to the detection circuit, then $D_1 = C_{11} + C_{12}$. The coefficients C_{1i} for the optimized configurations of our sample trap are listed in Table 2.1, as is $C_{1d}^{(\mathrm{opt})}$. Figure 2.17b shows how the various possibilities for these coefficients and sums depend upon $\tilde{z}_0$.

The induced signal,

$$V_I = \frac{qD_1}{2\rho_1} R\dot{z}, \tag{2.68}$$

is proportional to the axial velocity of the oscillating particle, as well as to D_1 and R [120]. The damping force that arises from this induced potential produces the damping rate for a particle of charge q and mass m,

$$\gamma_z = \left(\frac{qD_1}{2\rho_1}\right)^2 \frac{R}{m}, \tag{2.69}$$

which goes as the square of D_1 [120]. One power of D_1 arises because the induced current is proportional to D_1. The second power arises because a potential on the electrodes induces a damping force that is also proportional to D_1. The damping rates for a resistor connected between a single electrode and ground are listed in Table 2.2 for $R = 100$ kΩ. The maximum damping rate $\gamma_z^{(\mathrm{opt})}$ that pertains for Eq. (2.66) is also tabulated for comparison. As noted previously, if the resistor is connected to more than one electrode, then the appropriate coefficients C_{1i} for the connected electrodes must be summed to make D_1 before squaring.

The thermal Johnson noise in the resistor drives a particle that is near its equilibrium location with a driving force

$$F_n \approx \frac{qD_1}{2\rho_1} V_n. \tag{2.70}$$

For the circuit shown in Fig. 2.16, we have $D_1 = C_{1d}$.

An external driving force may be added to drive the axial motion of a trapped particle. Such a driving force has the advantage that a larger oscillation amplitude and hence a larger induced signal is produced at just the frequency of the drive in the steady state. A larger oscillation amplitude, of course, makes it more important to minimize the amplitude dependence of the axial frequency. One choice is to apply an oscillatory driving voltage V_D to the third electrode, between ρ_2 and ρ_3, as indicated in Fig. 2.16. The applied driving potential, V_D, produces a driving force on a particle near its equilibrium location that is given by

$$F_D \approx \frac{qD_1}{2\rho_1} V_D. \tag{2.71}$$

For V_D applied to the third electrode, we have $D_1 = C_{13}$.

2.7.2 Damping and detection in a covered trap

For a covered planar trap, the damping and the detected signal is maximized by introducing an extra gap at radius ρ_d and connecting the damping resistor to each of the electrodes with radius $\rho \leq \rho_d$. The choice $\rho_d^{(\mathrm{opt})}$ that gives the maximum damping and detection signal, along with the corresponding $C_{1d}^{(\mathrm{opt})}$ and $\gamma_z^{(\mathrm{opt})}$, are displayed in Tables 2.8 and 2.9. This detection configuration offers an appreciable detection efficiency. For some achievable values of z_0, the detection efficiency is nearly maximized without needing to make an extra gap in the electrode plane.

As mentioned earlier, covered planar traps are scalable in that an array of traps can share the same covering plane, with the axial frequency and the harmonic properties of each trap being tuned separately by the potentials applied to the other electrodes. Multiple traps can also share the same detection circuit if the detection resistor is attached to the covering plane—a great simplification in practice. Many trapped electrons could be simultaneously detected with one circuit if their axial frequencies are tuned to be slightly different from each other but within the detector's bandwidth. A coupling between two electrons takes place during the time that their two traps are tuned to make their axial frequencies the same.

2.7.3 Damping and detection in a mirror-image trap

For a mirror-image trap, the damping and hence the signal are maximized by connecting all of the electrodes in one plane to the damping resistor (i.e., $\rho_d^{(\mathrm{opt})} \to \infty$). Choosing $\rho_d = z_c/2$ gives γ_z that is 64% of the total possible damping. Choosing $\rho_d = z_c$ gives γ_z that is 98% of the total possible damping. For the sample mirror-image planar trap (Tables 2.10 and 2.11), connecting the damping resistor to the first two electrodes of one of the planes (i.e., choosing $\tilde{\rho}_d = \tilde{\rho}_2$) results in $\gamma_z = 2\pi\, 13.23$ s^{-1}, which is 92% of the damping that would result from detecting the signal induced on the entire electrode plane.

2.8 An Earlier Calculation

Minimizing the amplitude dependence of the axial frequency is the key to designing a planar trap within which a single electron can be suspended and used to realize a one-electron qubit. An accurate description and prediction of the properties of a planar Penning trap configuration thus requires calculating the amplitude dependence of the axial frequency. Here we correct an earlier calculation [137] of the amplitude-dependent frequency shifts.

Earlier in this work, the amplitude dependence of the axial frequency was shown to have the form

$$\omega_z(\widetilde{A}) = \omega_z \left[1 + \sum_{k=2}^{\infty} a_k \widetilde{A}^k \right]. \tag{2.23}$$

Ref. [137] differs by starting this sum with $k = 1$, suggesting that the dominant axial frequency shift is first-order in the oscillation amplitude. We find no first-order shift. The substantial disagreement between the a_k in Eq. (2.24) and the expression

$$a_k = \left| \frac{C_{k+2}}{2} \right|, \tag{2.72}$$

from Ref. [137] (translated into our notation) is illustrated in Table 2.12. For example, the differing expressions for a_3 are not functions of the same C_k. Higher-order a_k differ more. (Equation (2) of Ref. [144] and also Ref. [145] repeat the Ref. [137] results.)

This work	Ref. [137]
$a_1 = 0$	$a_1 = \frac{\lvert C_3 \rvert}{2}$
$a_2 = -\frac{15(C_3)^2}{16} + \frac{3C_4}{4}$	$a_2 = \frac{\lvert C_4 \rvert}{2}$
$a_3 = -\frac{15(C_3)^3}{16} + \frac{3C_3C_4}{4}$	$a_3 = \frac{\lvert C_5 \rvert}{2}$

Table 2.12: The lowest-order coefficients that describe the amplitude dependence of the axial frequency. This work and Ref. [137] differ in both amplitude and sign, most notably in the lowest-order expressions.

The amplitude dependence of the axial frequency must be calculated by solving the equation of motion, Eq. (2.21), to get the a_k in Eq. (2.24), as outlined between these two equations. Except for the absolute value whose origin is not clear, Eq. (2.72) from Ref. [137] is instead consistent with equating $\frac{1}{2}m\omega_z^2(z-z_0)^2$ with $q[V(0,z)-V(0,z_0)]$, solving for ω_z, expanding the square root in powers of $z-z_0$, and identifying the latter with A.

Finally, the relationship between energy and amplitude in Eq. (11) of Ref. [137], repeated in Eq. (3) of Ref. [144], is missing a factor of two. It should read $A = \sqrt{2E/(m\omega_z^2)}$.

2.9 Mainz Trap

The first planar Penning trap used to store electrons was demonstrated in Mainz [144, 145]. A large number of electrons (estimated to be between 100 and 1000 electrons) were stored, and the three motions of the electrons' center of mass were observed. The trap dimensions and potentials used were

$$\rho_i = \{3.15, 6.3, 9.45\} \text{ mm}, \tag{2.73}$$

$$V_i = \{0, 16, -38.5\} \text{ V}, \tag{2.74}$$

with radii taken to extend to the center of the 0.3 mm wide gaps between electrodes. The potentials come from the caption of Fig. 8 of Ref. [144], but with signs reversed compared to what is reported since this is necessary to approximately replicate the curves in Fig. 8 of that work. Finite boundaries are not included in our analysis, even though Sec. 2.5.2 illustrates that they can be important, because the needed information is not available in the experimental accounts.

We calculate that $V_3 = -36.2$ V would make $C_3 = 0$, which seems to have been the goal, whereupon $a_2 = -0.8$ and $C_4 = -1.0$. This gives a calculated single-particle thermal frequency width of $\Delta f_z = 310$ kHz for $T_z = 300$ K. This thermal width is smaller than the calculated and measured widths of 1–6 MHz reported in Fig. 7 of Ref. [144]. Unless the calculation is corrected as described in Sec 2.8, the calculated width should not agree with what we calculate. The measured width may be wider than expected because there are more trapped electrons than was estimated. Experimental experience in our laboratory also suggests that it is likely that the observed width was broadened by charges accumulated on the insulator within the gaps, since the gaps were not deep enough to screen the potential from such charges.

A minimal requirement for a trap that could be used to observe a single electron is that a_2 be close to zero. Figure 2.5 shows that for the relative geometry used in the Mainz trap, there is no set of applied potentials that could make $a_2 = 0$. In fact, $|a_2| < 0.1$ cannot be achieved for any reasonable values of V_i and z_0. This is true even if the artificial and unnecessary constraint $V_1 = 0$ is relaxed.

2.10 Ulm Trap

The serious effort made at Ulm to try to observe a single electron trapped in a planar Penning trap [146] did not succeed. Given our conclusion above that optimized planar traps could likely be used to observe one trapped electron, we examine here the trap geometry and the applied potentials that were used. The object is to check whether the performance of the Ulm trap is consistent with our calculations. Given that the observed linewidth is broader than calculated, we also discuss some practical considerations that may have affected the performance.

The trap geometry is described in Sec. 2.1 of Ref. [146]: “The diameter of the central electrode and the width of the trapping electrodes are equal to 2 mm.” In our notation, this is

$$\{\rho_1, \rho_2, \rho_3\} = \{1, 3, 5\} \text{ mm}. \tag{2.75}$$

Several bias configurations are mentioned in Sec. 2.2 and Fig. 2 of Ref. [146]:

$$\{V_1, V_2, V_3\} = \{0, 7, 7\} \text{ V}, \tag{2.76}$$

$$\{V_1, V_2, V_3\} = \{0, 5.2, 14\} \text{ V}, \tag{2.77}$$

$$\{V_1, V_2, V_3\} = \{0, 4.8, 14\} \text{ V}. \tag{2.78}$$

The penultimate paragraph of Sec. 2.3 of Ref. [146] mentions a set of “optimized control voltages”,

$$\{V_1, V_2, V_3\} = \{0, -1, 2.611\} \text{ V}, \tag{2.79}$$

presumably for the same geometry. However, this last set of potentials seems not to have been used successfully, perhaps because of the greatly reduced trap depth that is produced.

The calculated properties for each of these four configurations are summarized in Tables 2.13 and 2.14. None of these trap configurations make a_2 close to zero, the likely minimal requirement for observing and controlling one trapped electron. The mentioned “optimized” biasing scheme is actually worse than the others. Finite boundaries are not included in our analysis, even though Sec. 2.5.2 illustrates that they can be important, because the needed information is not provided in the experimental account.

A choice was made to keep the center electrode and the plane outside the elec-

	$\{\widetilde{\rho}_i\} = \{1, 3, 5\}$ (Eq. (2.75))			
	Used			Mentioned
	Eq. (2.76)	Eq. (2.77)	Eq. (2.78)	Eq. (2.79)
$\widetilde{V}_1$	0	0	0	0
$\widetilde{V}_2$	−4.6075	−5.2815	−5.2040	22.3016
$\widetilde{V}_3$	−4.6075	−14.2194	−15.1782	−58.2296
$\widetilde{z}_0$	1.4761	1.9070	1.9493	3.9328
C_3	−0.6386	−0.4251	−0.4082	−0.3267
C_4	0.2718	0.1340	0.1211	0.0540
C_5	−0.0766	−0.0443	−0.0389	−0.0015
C_6	−0.0021	0.0141	0.0129	−0.0021
a_2	−0.1785	−0.0689	−0.0654	−0.0596
a_3	0.1140	0.0293	0.0267	0.0195
a_4	−0.0447	−0.0143	−0.0127	−0.0041
a_5	0.0088	0.0074	0.0065	0.0007
a_6	0.0026	−0.0030	−0.0026	−0.0001
C_{11}	−0.3529	−0.2003	−0.1902	−0.0299
C_{12}	−0.1287	−0.2004	−0.2029	−0.1188
C_{13}	0.1287	0.0744	0.0696	−0.0455
$C_{1d}^{(\mathrm{opt})}$	−0.5215	−0.4037	−0.3949	−0.1957
$\tilde{\rho}_d^{(\mathrm{opt})}$	2.0875	2.6969	2.7568	5.5618
γ_1	−4.89	0.47	0.07	30.26
γ_2	−5.27	−8.32	−10.05	−82.50
γ_3	−1.09	1.49	2.80	−194.34

Table 2.13: Scaled parameters for the trap used in Ulm [146].

	$\{\widetilde{\rho}_i\} = \{1,3,5\}$ (Eq. (2.75))				
	Used			Mentioned	
	Eq. (2.76)	Eq. (2.77)	Eq. (2.78)	Eq. (2.79)	
ρ_1	1	1	1	1	mm
z_0	1.4761	1.9070	1.9493	3.9328	mm
$\rho_d^{(\mathrm{opt})}$	2.0875	2.6969	2.7568	5.5618	mm
f_z	82.2714	66.2300	64.1039	14.1339	MHz
V_0	-1.5193	-0.9846	-0.9224	-0.0448	V
V_1	0	0	0	0	V
V_2	7	5.2	4.8	-1	V
V_3	7	14	14	2.611	V
Δf_z @ 5 K	8.3	4.0	3.9	16.2	kHz
Δf_z @ 300 K	500	240	235	971	kHz
$1 : \gamma_z$	$2\pi\,13.96$	$2\pi\,4.50$	$2\pi\,4.06$	$2\pi\,0.10$	s^{-1}
$2 : \gamma_z$	$2\pi\,1.86$	$2\pi\,4.50$	$2\pi\,4.61$	$2\pi\,1.58$	s^{-1}
$3 : \gamma_z$	$2\pi\,1.86$	$2\pi\,0.62$	$2\pi\,0.54$	$2\pi\,0.23$	s^{-1}
d:$\gamma_z^{(\mathrm{opt})}$	$2\pi\,30.49$	$2\pi\,18.27$	$2\pi\,17.49$	$2\pi\,4.30$	s^{-1}

Table 2.14: Absolute values for the trap used in Ulm [146]. Axial frequencies calculated here differ from those reported in Ref. [146], which claims $f_z = 62.2$ MHz and 67.97 MHz for the potentials given in columns 1 and 2, respectively, of this table.

trodes at the same potential. This is an added constraint, $\widetilde{V}_1 = 0$, on the four scaled parameters that determine the behavior of a three-gap trap: $\widetilde{V}_1$, $\widetilde{V}_2$, $\widetilde{V}_3$, and $\tilde{z}_0$. Two additional constraints, $C_1 = 0$ and $C_2 = 1$, are required to form a trap. With the optional constraint, there is one more parameter than there are constraints. If we choose $\tilde{z}_0$ as the corresponding free parameter, Fig. 2.18a shows the bias potentials that must be applied to realize each possible value of $\tilde{z}_0$. Fig. 2.18b gives the corresponding a_k and C_k. For reasonable values $\tilde{z}_0 \leq \tilde{\rho}_N$, we find that $|a_2| \geq 0.05$. Having explored what trap performance is possible with the optional constraint, we note that there is no compelling reason to make this choice. In fact, such a choice would make it impossible to identify optimized planar Penning trap configurations.

It is possible to bias the Ulm trap electrodes to make $C_3 = 0$ by choosing $V_3/V_2 = -3.533$ for any $V_2 > 0$. However, this choice also results in $C_4 = -0.77$ and $a_2 = 0.58$, the latter being worse than for the configurations in Table 2.13. For this relative trap geometry, relaxing the optional constraint $V_1 = 0$ does not improve the trap performance.

Observing a single electron will be difficult if the thermal broadening of the axial frequency, Δf_z, is very large compared to the damping linewidth, $\gamma_z/(2\pi)$. Table 2.14 shows that this is indeed the case if the axial temperature is as low as 5 K, the lowest effective axial temperature that has been achieved without feedback cooling [170]. The heat generated in the detection amplifier makes it very difficult to achieve such a temperature, even for 0.1 K surroundings, so the effective axial temperature could easily have been much higher than 5 K. The table also shows the thermal broadening for an effective axial temperature of 300 K.

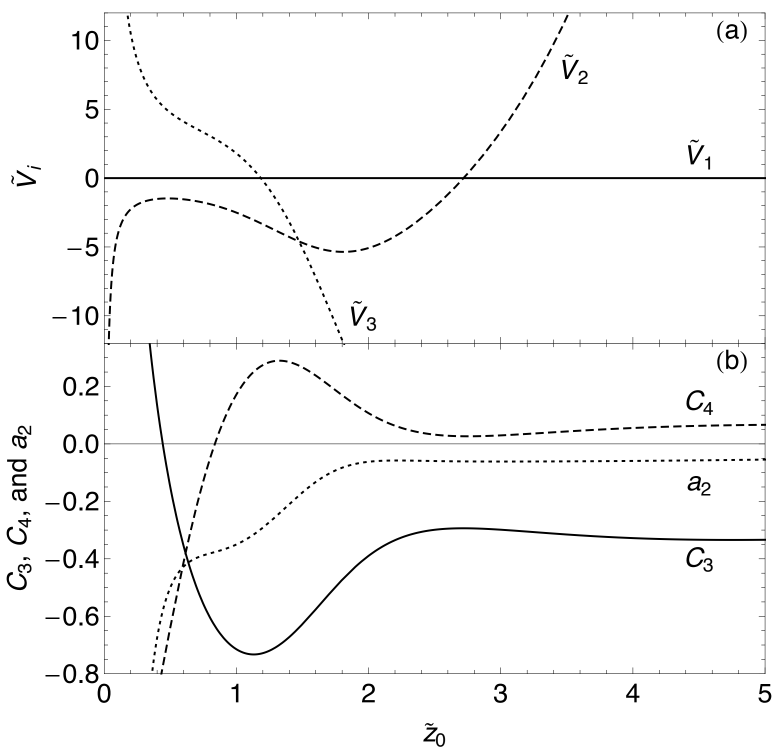

Figure 2.18: (a) The scaled potentials applied to the Ulm trap to get a particular $\tilde{z}_0$. (b) The resulting trap properties for each $\tilde{z}_0$. The trap is biased subject to the optional constraint $V_1 = \widetilde{V}_1 = 0$. For this trap design, tt is not possible to make a_2 very small.

Reference [146] says that a still broader width of 3 MHz "is expected and is in agreement with the measured data." Why this particular width should be expected is not specified. However, it is not surprising that the observed frequency width is larger than we calculate because the width grows with the large and unknown number of electrons in the trap. Experimental experience in our laboratory also suggests that it is likely that the observed width is broadened by charges accumulated on the insulator within the gaps since nothing screens the potential from such charges in the circuit board technology used to fabricate these traps.

One further item may be worth mentioning even though it is not completely understood. Many years ago, the first trap cooled with a dilution refrigerator was located on the mixing chamber of the refrigerator,[1] within the refrigerator's inner vacuum container (IVC). The vacuum was expected to be extremely good once the helium gas used to precool the IVC was pumped out. However, no good one-electron signals were ever observed, for reasons not clearly understood, but seemingly related to the cryopumped gas on the surface of the electrodes. Only when the trap vacuum was separated from the IVC vacuum did we get the clean signals used to resolve one-quantum transitions with one electron [5]. The Ulm trap was also located within the IVC vacuum. The long trapping lifetime observed with many trapped particles confirmed the expectation of a very good vacuum. Whether isolating the trap vacuum from the IVC would improve the observed signals has not been investigated at Ulm.

Ref. [146] concludes that it is not possible to observe a single electron in a planar Penning trap because the anharmonicity will always be too great, and it also reports that a thermal width narrower than 5 kHz could not be calculated for any N-gap trap,

[1] Reference [1] incorrectly states that the trap was located on the still of the refrigerator.

where N is anything between 1 and 6. The only hope offered was that a much smaller trap might make the damping rate large enough to observe one electron, despite the anharmonicity inherent in planar traps [138, 146]. Indeed, Eq. (2.69) shows that when the trap dimension is decreased, the damping rate increases as the square of dimension. With microfabrication methods, it should be possible to fabricate smaller traps that thus will have a much larger damping. What remains to be demonstrated is that the anharmonicity will not become large enough in small traps to offset the damping advantage.

Our conclusion is different and much more optimistic. It should indeed be very difficult to observe a single electron in the planar Penning trap used at Ulm. However, the fundamental problem is the relative geometry of the Ulm trap, not its size. The thermal broadening is too great as a result of choosing a trap geometry that cannot be optimized to make $a_2 = 0$. Nonetheless, the conclusion in Ref. [146] that it is "impossible" to observe a single electron in a millimeter-scale planar Penning trap now seems much too strong. The optimized geometries and applied potentials presented here for planar Penning traps of any size offer the possibility of a very large reduction in the critical amplitude dependence of the axial frequency, and Chapter 5, in fact, presents axial resonances narrower the supposed 5 kHz minimum width.

Chapter 3

Trap Electrode Fabrication

The first step toward a one-electron qubit is detecting a single electron in a scalable trap structure. In the previous chapter, we determined which electrode geometries can be biased to create a sufficiently harmonic potential. We now describe the fabrication of trap electrodes designed for detecting one electron in a planar Penning trap.

3.1 Fabrication Requirements

Besides the electrode geometry, a physical planar Penning trap must satisfy several practical requirements in order for a single electron to be detectable.

First, insulating surfaces must be well screened to avoid charges accumulating on them, which can substantially modify the trapping potential. When the trap is cooled to 4 K or below, these charges can remain for days. Such charges have made some traps in our laboratory completely unusable, but no systematic study has been undertaken. One way to mitigate this problem is to devise careful loading and operation procedures that minimize the number of charges that build up on the insulators (see Sec. 5.2). In addition, the electrode geometry must be designed to minimize the exposure of the insulators. For a planar Penning trap, that means that the gaps must be narrow compared to the thickness of the metal layer. Gaps with a large aspect ratio will make it more difficult for charges to reach the insulator at the bottom of the slits between electrodes. Any charges that do collect on the insulator will be screened by metal surfaces on either side of the gaps, with a screening factor that grows roughly exponentially with the aspect ratio of the gaps. The experiments at Mainz and Ulm used trap electrodes that did not have well-screened insulating surfaces (see Table 3.2), so stray charges may have contributed to the broader resonances observed in those experiments.

Second, in order to minimize imperfections that are not cylindrically symmetric, the biases must be applied to the electrodes without disrupting the symmetry of the trap. Non-axisymmetric imperfections are difficult to model analytically and numerically, but it is likely that such imperfections will limit the cancellation of the anharmonic coefficients that can be achieved by tuning the trap. To establish the best conditions under which a single electron's axial motion might be detectable, the trap electrodes should be as symmetric as possible.

In addition, the capacitance must be kept small enough to allow detection of the axial signal. The electrodes must not field-emit when trapping potentials are applied. And the electrodes should also have a good surface finish to minimize patch potentials.

3.2 Harvard Planar Penning Traps

We have fabricated planar Penning traps that satisfy all of the above requirements.

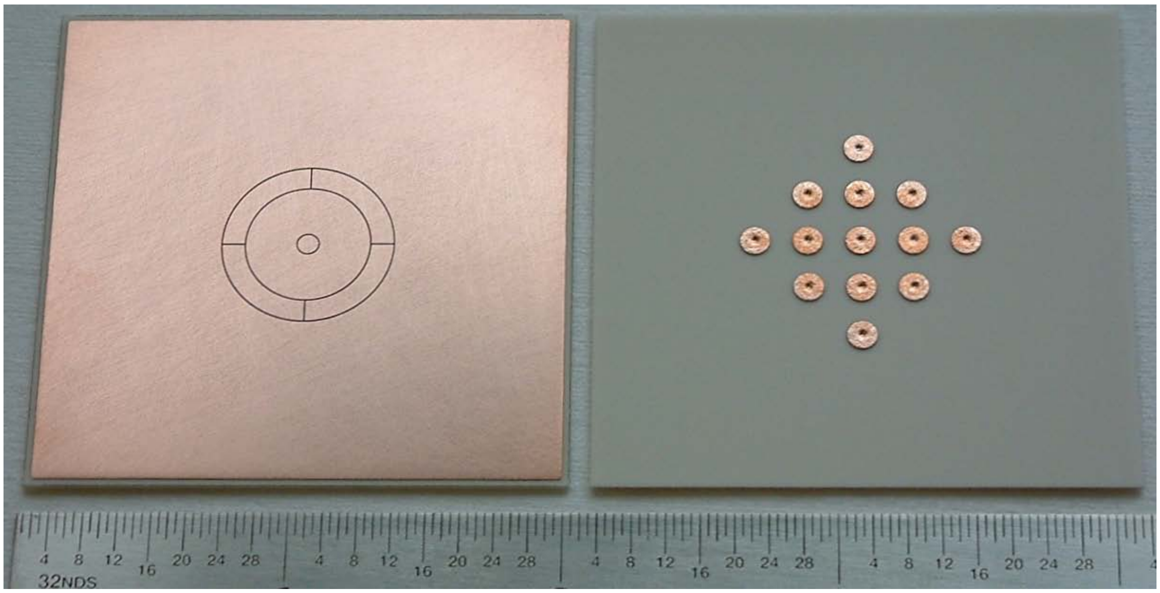

Figure 3.1: Photographs of the top of a planar trap substrate, after laser machining and deburring, and of the bottom of a substrate.

Fabrication of the trap used in the present work begins with copper-clad alumina substrates. The blank substrates[1] are composed of a $2'' \times 2'' \times 0.025''$ (50 mm × 50 mm × 0.635 mm) aluminum oxide (Al_2O_3) ceramic wafer with a $0.008''$-thick (0.2 mm) copper foil bonded to each side. The copper is bound to the alumina by a thin copper oxide layer formed at the interface when the sample is heated to a temperature above 1065°C (the copper-oxygen eutectic melting point) but below 1083°C (the melting temperature of copper) and oxygen is injected into the furnace atmosphere [173, 174, Sec. 4.7]. No additional adhesion layer is required. Such samples, with thick copper films bonded to either aluminum oxide or aluminum nitride ceramic, are referred

[1]Fabricated by Curamik Electronics, Inc.

to as "DBC" (direct-bonded copper) substrates and are often used in high-power applications because these ceramics have a higher thermal conductivity than most electrically insulating materials.

Hermetic filled vias provide electrical contact between the top and bottom copper layers (see Fig. 3.1b). The alumina wafer has via holes 1.0 mm in diameter laser-drilled prior to copper adhesion. At a high temperature, the softened copper layers are bonded by pressing a graphite tip on the bottom layer, pushing it through the hole and onto the opposite layer of copper, leaving an indentation for each via in the bottom layer. The bottom layer of copper is then etched, leaving only an array of 3.0 mm diameter contact pads centered on each via. Our samples have thirteen vias in total: one at the center of the substrate, and four on each of the other electrodes, equally spaced along circles with diameters of 5.0, 7.0, and 10.0 mm. The via holes on the 5.0 and 10.0 mm diameters are aligned with each other azimuthally; the holes on the 7.0 mm diameter are offset by 45 degrees.

The blank substrates, delivered to us in this form, next have grooves laser-cut in the top copper surface to establish the electrode pattern (Fig. 3.1a). The first step of the polishing procedure (described below) is carried out before patterning in order to create a surface with more uniform reflectivity. Before laser machining, the positions of the vias are measured using the vernier scale on an optical microscope translation stage to verify that the vias are correctly positioned relative to the substrate edges and thus that the laser machined grooves will lie between the vias. The substrate fabrication tolerance specification is ± 0.3 mm, but the via positions were all measured to be correct within 0.15 mm.

The laser machining[2] cuts three circumferential grooves to define the three electrodes and plane that can be indepedently biased, plus four radial grooves to segment the third electrode to enable magnetron sideband drives (or even rotating-wall drives, if desired). Electrical isolation is verified with a handheld multimeter ($R \gtrsim 100$ MΩ) by the laser machinists. To establish this, the laser-cut groove goes all the way through the copper layer and begins to cut into the ceramic layer; however, no change to the mechanical strength of the ceramic has been observed, and upon inspection with an 11X stereomicroscope[3] after polishing, there did not appear to be any ablated ceramic particles remaining.

Dimension	**Nominal**	**Measured**
ρ_1	1.091 mm	1.05 ± 0.02 mm
ρ_2	6.000 mm	6.04 ± 0.04 mm
ρ_3	8.228 mm	8.19 ± 0.05 mm

Table 3.1: Electrode radii as measured at the center of the gap, compared to the ideal values of Table 2.2 given as specifications to the laser machinists. Dimensions are measured with a compound microscope and CCD camera. Uncertainty arises from identifying the edge and the radius by eye. The uncertainties differ because the limited microscope field of makes it more difficult to measure the larger radii.

A kerf[4] width of $50^{+25}_{-0}\mu$m (2^{+1}_{-0} mil) was specified, with the expectation that vertical sidewalls could not be achieved. The laser machinists reported a width of approximately 50 μm at the bottom of the groove, though this was measured on test pieces rather than the machined samples. The laser machining process was developed by starting with 200 μm thick copper shim stock (the same thickness as the copper layer on the substrate), rather than the blank samples we provided, and tuning the laser

[2]Performed by Gateway Laser, Inc.
[3]Nikon SMZ1500
[4]The cut made by a saw or other cutter.

parameters until the resulting groove was measured to be 50 μm at the bottom; unlike with trap substrates, this can be easily measured by flipping over the shim stock and inspecting the bottom with an optical microscope. The same process parameters were then used on the blank trap substrates.

Upon delivery to Harvard, the laser-machined samples were viewed with a stereomicroscope, which permits the best inspection of the grooves, and a simple compound optical microscope, which permits measurement of the groove diameter and width. The groove width as a function of depth can be crudely measured by changing the working distance so that different horizontal planes come into focus; at sufficient magnification, the depth of field is inadequate to resolve all but a thin horizontal slice (see Figs. 3.2). However, because of the limited depth of field, the difficulty of getting an adequate amount of light into a deep circular trench,[5] and the near-vertical sidewalls, it is difficult to identify the bottom of the copper layer and thus to measure the width at the bottom. Using this method, the groove is estimated to be less than 70 μm wide at the bottom and approximately 105–110 μm wide at the top, which is to be compared to a film thickness that is initially 200 μm, minus some material removed in polishing.

The Harvard traps have gaps with an aspect ratio that is about six to nine times higher than planar Penning traps used in previous experiments (see Table 3.2). As mentioned in Secs. 2.9 and 2.10, both the Mainz and Ulm traps had exposed insulators in gaps that were not screened because the gaps were wider than they were deep. Charges on the insulating substrates that are exposed in the gaps of these traps may

[5] A Dolan-Jenner MI-150 Fiber Optic Illuminator was used for oblique illumination, in addition to the normal illumination through the microscope objective.

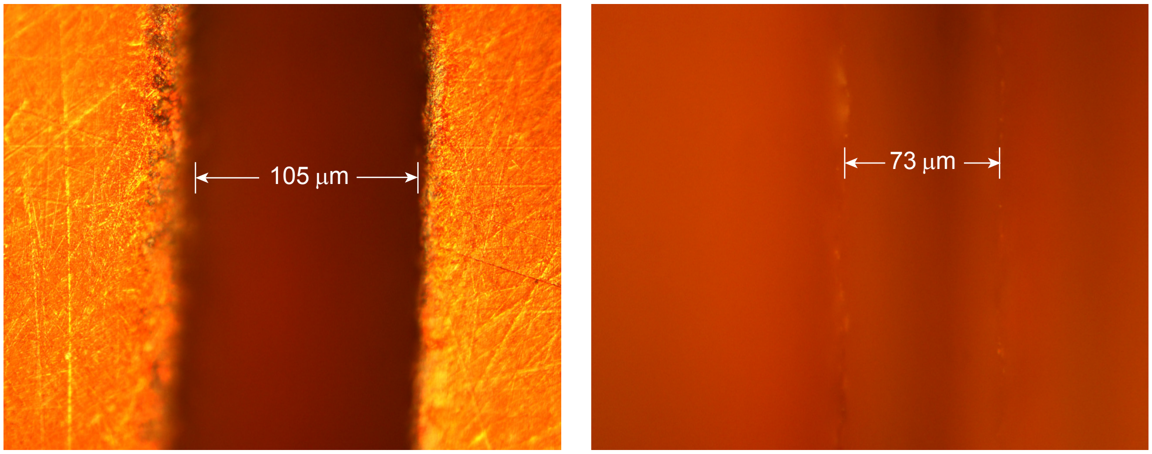

Figure 3.2: Sample optical micrographs of the groove near the top (left) and 150 μm below the top surface (right) taken with a 50X objective lens. Steeply sloping sidewalls reflect very little light to the microscope objective and the deep grooves prevent good illumination. The depth of field is limited at high power, so only a small part of the sidewall is in focus (right). A depth profile is constructed in Fig. 3.3 by measuring the width in this manner.

well have contributed to the broad frequency spreads that were observed. Our traps have much better screening of the insulator at the bottom of the gaps, which likely contributes to the narrower resonances observed in this work.

	This work	**Mainz 2006** [144]	**Ulm 2008** [146]	**Other designs** [138]	**Pixel traps** [140]
Electrodes	copper, gold-plated	silver	copper, gold-plated	gold suggested	gold
Insulator	alumina	alumina	FR-4 epoxy/ fiberglass	unspecified	sapphire
Aspect ratio	2–3	unspecified	0.35	unspecified	1
Contact side	back	back	back	front	front

Table 3.2: Comparison of the materials and aspect ratio of planar Penning traps used in experiments to date (columns 1–3) and other suggested planar Penning trap designs (columns 4–5). The latter designs lack rotational symmetry, which should make detection of a single electron even more difficult.

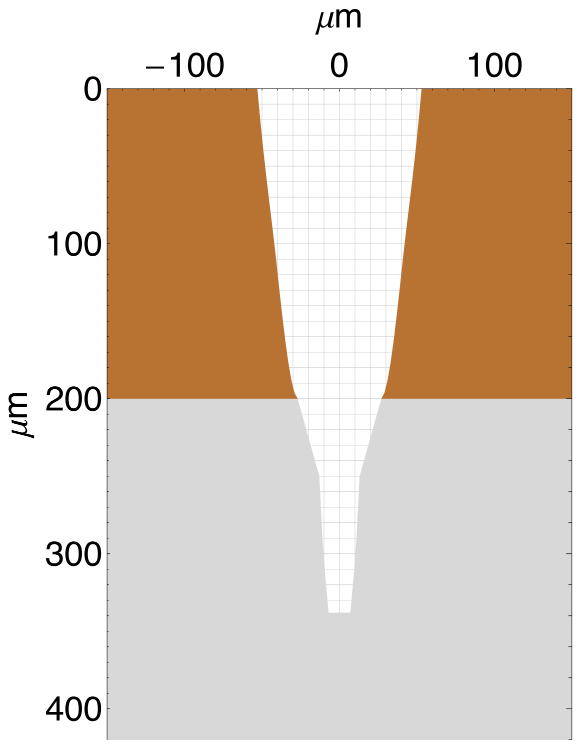

Figure 3.3: The profile of a sample laser-machined groove separating electrodes, drawn to scale. The width is measured with a microscope, as in Fig. 3.2. Vertical dimensions are measured relative to the top surface of the electrodes using the fine focus knob on the microscope. Grid lines are spaced by 10 μm. The full thickness of the alumina layer (635 μm) is not shown. The boundary between the copper and alumina is difficult to distinguish. Here the boundary is shown at the nominal depth of 200 μm, though some material is removed in polishing, and the amount of material removed is not uniform across the substrate. Further investigation with a profilometer is warranted.

3.3 Materials

The traps are constructed out of materials suitable for the low-temperature, high-magnetic-field environment and the sensitive radiofrequency methods used to detect the axial motion.

Copper is an excellent choice for electrodes since it is nonmagnetic,[6] economical, easy to work with, and has high conductivity. It has been the material of choice for cylindrical Penning traps in our group. Alumina ceramic (96%)[7] is nonmagnetic, as required; it is an excellent insulator and thus provides low leakage resistance between electrodes; and it is among the least lossy dielectric materials at RF. Although alumina and copper do not have well matched thermal contraction,[8] no deformation of the substrates was observed after repeated thermal cycling.

Resistivity	10^{13} Ω·cm
Dielectric constant	10
Dissipation factor ($\tan\delta$) at 1 MHz	0.0003

Table 3.3: Properties of Rubalit 708S (96% Al_2O_3 ceramic) at room temperature, as provided by the manufacturer. For general data on alumina and tables comparing the properties of various insulating substrates, see Refs. [174, pp. 3.6, 4.20, 4.34], [177, pp. 761, 778], and [178, App. C]. Substrates made out of 99.5% alumina or sapphire are reported to have dielectric loss smaller by about a factor of 2, with single-crystal samples having loss tangents as small as 1.0×10^{-5} [179].

Although the electronic contribution to the magnetism of copper and alumina is

[6] OFE copper, which is used to make the planar trap electrodes, has nickel and iron concentrations of ≤ 10 ppm each.

[7] The Curamik samples are made with Rubalit® 708S from CeramTec AG. The remaining composition is 3.2% SiO_2, 1.2% MgO, and <1% CaO [175].

[8] Reference [176, App. 6.4] reports $\Delta L/L = 0.3\%$ for copper from room temperature to 4 K and $\Delta L/L = 0.08\%$ for sapphire (single-crystal alumina) along the c-axis from room temperature to 40 K.

negligible, the nuclear paramagnetism is significant at low temperatures because the temperature dependence of the magnetization scales as T^{-2}. The nuclear magnetism is not a concern for the present experiments with planar traps; however, materials may not be used that would generate unwanted magnetic gradients or magnetic field fluctuations at the nearby cylindrical Penning trap used for ultrahigh-precision measurements of the electron and positron g-factors. Copper and aluminum have nuclear Curie constants two orders of magnitude larger than silver, titanium, and quartz, but the planar Penning trap is placed sufficiently far from the electron trap not to introduce unwanted fields (see also Sec. 4.2).

3.4 Capacitance

Trapped electrons are detected via the current their axial motion induces to flow through a resistor (a tuned-circuit amplifier on resonance) connected to one of the electrodes, as described in Sec. 4.5. The size of this effective resistance is inversely proportional to the capacitance between the detection electrode and its nearest neighbors in the plane. The capacitance must therefore be kept small enough to achieve adequate signal-to-noise.[9] And if the capacitance is too large, it will be impossible to tune out with a high-Q inductor at the desired frequency. These prescriptions work at cross purposes to the fabrication requirements laid out in Sec. 3.1. However, it is possible to satisfy all these conditions with judicious trap design.

First, analytical estimates are used to guide initial design decisions. Once a can-

[9] Recall that the signal size also depends on the geometric coefficient D_1 for the detection electrode introduced in Sec. 2.7. To optimize for maximum signal, one must take into account both D_1 and the capacitance.

didate trap geometry was identified, prior to fabricating the samples, a finite-element numerical calculation was used for a more precise calculation of the expected capacitance. After laser machining, the capacitance of the samples was measured with an impedance meter. And finally, the traps were connected to the detection circuit and the noise resonance was observed (Sec. 4.5).

A naive lower-bound for the capacitance can be obtained by treating the walls of the high-aspect-ratio gaps as a parallel plate capacitor. However, for thin metal layers, this estimate is much too low. If a potential is applied across the gap, many field lines will terminate on the broad electrode surfaces, not just the surfaces facing each other across the gap. Furthermore, this estimate neglects the alumina substrate beneath the electrodes, which has a dielectric constant of about 10.

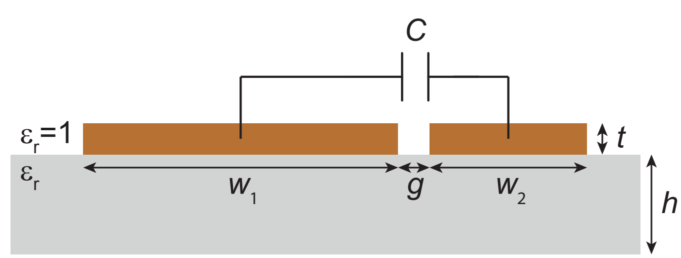

Figure 3.4: Dimensions of an asymmetric coplanar stripline for estimating the capacitance between neighboring electrodes.

A better estimate can be obtained by using formulae for the capacitance of very thin metal striplines from the literature on microwave circuits. (The capacitance between the electrodes and the contact pads of different electrodes on the backside of the substrate is small and can be neglected for these coarse estimates.) Using conformal mapping, it is possible to approximate the capacitance per unit length of an asymmetric coplanar stripline on a dielectric slab, as reported in Ref. [180, Sec. 6.2.3], quoting Ref. [181]:[10]

$$C_0^{ACPS} = 2\epsilon_0\epsilon_{\text{eff}}\frac{K(k')}{K(k)}, \tag{3.1}$$

where K is the complete elliptic integral of the first kind, w_i are the widths of the strips, g is the width of the gap, and

$$k = \sqrt{\frac{g(w_1 + w_2 + g)}{(w_1 + g)(w_2 + g)}}, \tag{3.2}$$

$$k' = \sqrt{1 - k^2}. \tag{3.3}$$

Of course, the electrodes are not simply parallel strips, but we can substitute the widths of the electrodes, $w_i \approx \rho_i - \rho_{i-1}$, to a reasonable approximation since the electrode width is large compared to the gap width. For broad electrodes, most field lines will terminate on the electrodes near the gap, so for $w_i \gg g$, the capacitance depends weakly on the width of the electrodes. The capacitance per unit length C_0 is then multiplied by the appropriate circumference $2\pi\rho_i$ to find the capacitance between adjacent electrodes. In this model, the thickness of the strips is neglected; a crude accounting of the finite thickness would be simply to add this capacitance in parallel with the parallel-plate capacitance calculated for the facing surfaces.

For two metal strips in free space, the effective relative permittivity is simply $\epsilon_{\text{eff}} = 1$. For two metal strips on a semi-infinite dielectric slab with relative permittivity ϵ_r, the effective relative permittivity is approximately $\epsilon_{\text{eff}} = (1+\epsilon_r)/2$, the average of the permittivity on the top ($\epsilon_r = 1$) and the bottom of the electrodes. For a dielectric substrate of finite thickness, the effective permittivity is given by

$$\epsilon_{\text{eff}} = 1 + \left(\frac{\epsilon_r - 1}{2}\right)\left(\frac{K(k)}{K(k')}\frac{K(k_2')}{K(k_2)}\right), \tag{3.4}$$

[10] A different solution that yields similar results is given in Refs. [182, Sec. 13.5] and [183, Sec. 7.2.2].

where

$$k_2 = \sqrt{\frac{\left(e^{2\pi(w_1+g)/h} - e^{2\pi w_1/h}\right)\left(e^{2\pi(w_1+w_2+g)/h} - 1\right)}{\left(e^{2\pi(w_1+w_2+g)/h} - e^{2\pi w_1/h}\right)\left(e^{2\pi(w_1+g)/h} - 1\right)}}, \tag{3.5}$$

$$k_2' = \sqrt{1 - k_2^2}. \tag{3.6}$$

Equation 3.4 becomes less valid for thin substrates (compared to the strip widths) [181]; still, this is sufficient for initial design guidance.

The analytical formulae were checked by computing the capacitance numerically, using commercial finite-element modeling software.[11] The method is as follows: Build and mesh a 3D model of the electrodes. Place 1 V on the electrode of choice and 0 V on other conducting surfaces, and use these boundary conditions to solve Laplace's equation for the electric potential. Find the electric field, integrate over all space, and use $U = \frac{1}{2}CV^2$ to find the capacitance. Repeat with a finer mesh size to ensure convergence. The results agreed with the analytical formulae to within about 10%, as shown in Table 3.4, demonstrating the validity of using Eqs. (3.1)–(3.6) to estimate the trap capacitance before fabricating the trap.

After laser-machining, the capacitance of the electrodes was measured with an impedance meter.[12] The results are shown in Table 3.5. One reason for the larger values is likely stray capacitance in the leads used for contacting the electrodes. Measurements were made in the same setup as the high-voltage tests described below, where the electrodes were contacted by wire bonding a 0.001″ aluminum wire between contact pads and a nearby circuit board. Wire bonds were used to avoid soldering to the contact pads until polishing was completed, so that the trap could

[11] Vector Fields Opera-3d

[12] ESI/Tegam 252

	C_1 (pF)	C_2 (pF)	C_3 (pF)
Analytical	1.0	7.0	14.5
Numerical	0.9	6.5	12.8

Table 3.4: Comparison of analytical and numerical estimates for the capacitance of each trap electrode for a sample trap with $\rho_i = \{1, 6, 8\}$ mm, gaps of 50 μm, a substrate thickness of 0.635 mm, and a metal thickness of 0.2 mm. (Note that the dimensions are slightly different than dimensions than the sample trap considered throughout most of this work.) The analytical values arise from Eqs. (3.1)–(3.6), plus the parallel plate capacitance of the gap walls, $C^{\|}_{i,i+1} = \epsilon_0 2\pi\rho_i t/g$. The single-electrode capacitances are given, for example, by $C_2 = C_{12} + C_{23}$ and $C_3 = C_{23} + C_{34}$, where C_{34} is the capacitance between electrode 3 and the grounded plane lying at $\rho > \rho_3$. The numerical calculation was for a model with a copy of the electrode pattern on both sides of the substrate, with the resulting capacitance divided by two to arrive at the numbers reported above.

still be used with a tightly-fitting polishing chuck. The measured values show that at least for the center electrode (“e1”), the capacitance is small, so the total capacitance of the detection circuit is dominated by parasitic capacitance between the electrode and the amplifier input.

C_{12}	2.2 pF
C_{23i}	2.1–2.8 pF
C_{3i4}	8.0–9.5 pF
C_{3i3j}	1.3–2.1 pF

Table 3.5: The capacitances between electrodes of a laser-machined trap substrate. C_{23i} and C_{3i4} denote the capacitance between one segment of electrode 3 and electrode 2 or electrode 4, respectively. C_{3i3j} denotes the capacitance between adjacent segments of electrode 3.

3.5 Field Emission

If the gaps between electrodes are sufficiently narrow, currents can flow directly across the gaps even when the applied potentials are much smaller than what would cause breakdown. These field emission currents must be avoided in order to establish the stable trapping potentials required to detect the signal from a single electron's axial motion and to resolve the small frequency shifts that correspond to spin or cyclotron transitions.

An applied electric field creates an electrostatic potential that decreases with distance away from the electrode surface. At a sufficient distance, the potential energy is less than the Fermi level of electrons in the metal, and electrons can tunnel across this triangular potential barrier. The stronger the electric field, the narrower the barrier, and the tunneling rate—that is, the field emission current—therefore grows exponentially with the electric field. The tunneling rate was worked out by Fowler and Nordheim in 1928 [184], one of the earliest problems solved by the then-nascent theory of Quantum Mechanics.

Using the WKB approximation, the current density is found to be [185]

$$j = 6.2\times 10^6 \frac{\sqrt{\mu/\phi}}{\mu+\phi} E^2 e^{-6.8\times 10^7 \phi^{3/2}/E} \ \mathrm{A/cm^2}, \tag{3.7}$$

where μ and ϕ, respectively, are the Fermi energy and work function in eV and E is the electric field in volts/cm. Equation (3.7) is known as the Fowler-Nordheim equation, and a plot of $\log I/E^2$ vs $1/E$, on which a field emission curve would be a straight line, is known as a Fowler-Nordheim plot. The potential due to image charges can be accounted for at lowest order by replacing E with E/α, where typically $\alpha \sim 0.8$–0.9.

At finite temperature, the current is multiplied by a correction factor, which is of order unity at room temperature or below.[13]

The Fowler-Nordheim equation matches experimental data only when the electric field is multiplied by a dimensionless fudge factor β, called the enhancement factor, typically in the range 10–2500 for polished flat or gently curved electrodes [186]. The Fowler-Nordheim derivation does not take account of any variations in the surface, so one plausible mechanism for the disagreement with theory is that the surface includes some sharp projections. The electric field around these sharp points is much higher, and these sites dominate the observed current. It has been observed that field emission from a broad surface is indeed dominated by small regions, but it is not conclusive that topographic projections are responsible. Field emission currents are also found to depend not just on the electric field but also on the total voltage (or, equivalently, upon anode-cathode separation). One explanation is that electrons dislodge positive ions from the anode surface, which are then accelerated toward the cathode, where they generate additional secondary electrons [187]. However, if this were the case, one would expect more emission from electrodes that are further apart since there is a larger potential difference to accelerate electrons, but studies demonstrate enhancement factors that variously decrease with, increase with, or do not depend upon electrode separation [186].

The field emission characteristics depend strongly on the way in which the surface is prepared. One set of recent experiments on mirror-finished OFHC copper samples has measured an enhancement factor of 56–790, with the best results coming from samples that underwent a final rinse in ultra-pure water and were not electropolished

[13] More detailed treatments can be found in Ref. [186].

[187]. Microfabricated traps may permit less control over surface preparation, but some tungsten micro-ion traps with extremely low enhancement factors ($\beta \sim 0.1$) have been fabricated at Sandia National Laboratory [188].

An initial batch of our planar trap samples were laser-machined by a different company[14] than the samples that were used to trap particles in this work. These samples manifested current that increased strongly with applied voltage, making us suspect that we were observing field emission. However, the I–V curves did not at all resemble the Fowler-Nordheim form, and the effect was much stronger than would be expected: potentials of 100 V or less induced currents of tens of microamps. It seems more likely that in fact the laser machining had not electrically isolated the electrodes, and that filaments, projections, or debris spanned the gaps resulting in both the observed values of V/I (several MΩ) and the observed intermittencies and shifts in the I–V curves from trial to trial.

These problems were resolved by improved laser machining, better trap inspection, and more effective procedures for removing debris from the gaps, as described below. The field emission characteristics were then measured by placing the sample in vacuum at room temperature and applying a voltage from a trippable high-voltage power supply. The voltage was increased until the current reached 80 nA. Each pair of adjacent electrodes was tested, and then the leads were reversed and the measurement repeated. All electrode pairs reached the current limit at 500 V or higher, with most reaching 1.5 kV without tripping the power supply. For one of the electrode pairs that tripped at around 500 V, the I–V curve was measured using an electrometer.[15]

[14]KJ Laser Micromachining

[15]Keithley 6517A

The resulting shape indicated that we could possibly be observing field emission, but this is not definitive. What matters for the experiment, however, is that the effective leakage resistance is very low. Before and after assembling the trap in its holder, the electrodes were checked with the electrometer with a 100 V source—approximately the size of the potentials applied in the planar trap experiments described in Chapter 5—and the current was observed to be at most tens of picoamps, implying a resistance of more than 1 TΩ, which is about the best limit we could measure directly with our electrometer. These leakage resistances were also verified again once the experiment was cold.

3.6 Surface Finish

The metal electrodes are not exactly equipotentials for a variety of reasons. Adsorbed gases, nonconductive surface oxides, work-function variation with crystal orientation, and material imperfections can give rise to static as well as fluctuating electric fields, known as patch potentials. The electrostatic potential near a metal surface can vary by millivolts or more [189, 190], which could disrupt the carefully produced harmonic potential. Fluctuating fields could also heat particle motions, causing decoherence of a motional qubit. It is desirable to minimize these effects by preparing smooth and clean electrode surfaces .

The cylindrical Penning traps used for detecting single particles have electrodes that are polished to a surface roughness assumed to be less than 1 micron [134]. The unwanted electric fields and electric field fluctuations associated with patch potentials are believed to scale as $1/z_0^4$ [191–195], so the surface properties of the traps will become increasingly important for smaller traps, and crucially so if the quantum limit of the axial motion is reached. In this work, electrons are trapped more than 1 mm from the electrode plane, so these issues are less critical than in micro-ion traps, where the electrode surfaces lie only tens of microns from the trapped particles.

A series of abrasive polishing and cleaning steps were used to prepare planar trap electrodes. Upon delivery, the substrates have a mottled surface with large grains. For coarse polishing, the substrate is affixed with CrystalBond 509 to a 1″-thick, machined-flat copper disk with small pockets cut out for the contact pads so that the back of the sample is supported over nearly all of its area. The substrates are then polished by sliding the chuck back and forth on abrasive paper[16] set atop a clean, flat table. This polishing step continues for about 45–60 minutes, rinsing the trap and polishing paper frequently with deionized water,[17] until the granular surface is no longer visible by eye and inspection with a low-power compound microscope reveals that there are no small pits remaining, as shown in Fig. 3.5.

The Crystalbond is then softened by heating on a hotplate, the trap is removed and cleaned with detergent and then solvents in an ultrasonic bath, and it is then sent out for laser machining. The remaining polishing steps are reserved for after the electrodes are laser-machined, both because it is desirable to have a matte finish rather than a mirror finish for laser machining and because after laser machining, the samples must be deburred and repolished. After laser machining, the trap is then inspected with a stereomicroscope. Any debris remaining in the grooves between the

[16] 3M Wetordry 481Q, with 30 μm silicon carbide grit

[17] Some polishing procedures recommend using an oxidizer since copper oxide is more easily polished away. For example, one chemical-mechanical polishing recipe has 33 mL of 30% hydrogen peroxide per liter of slurry [196].

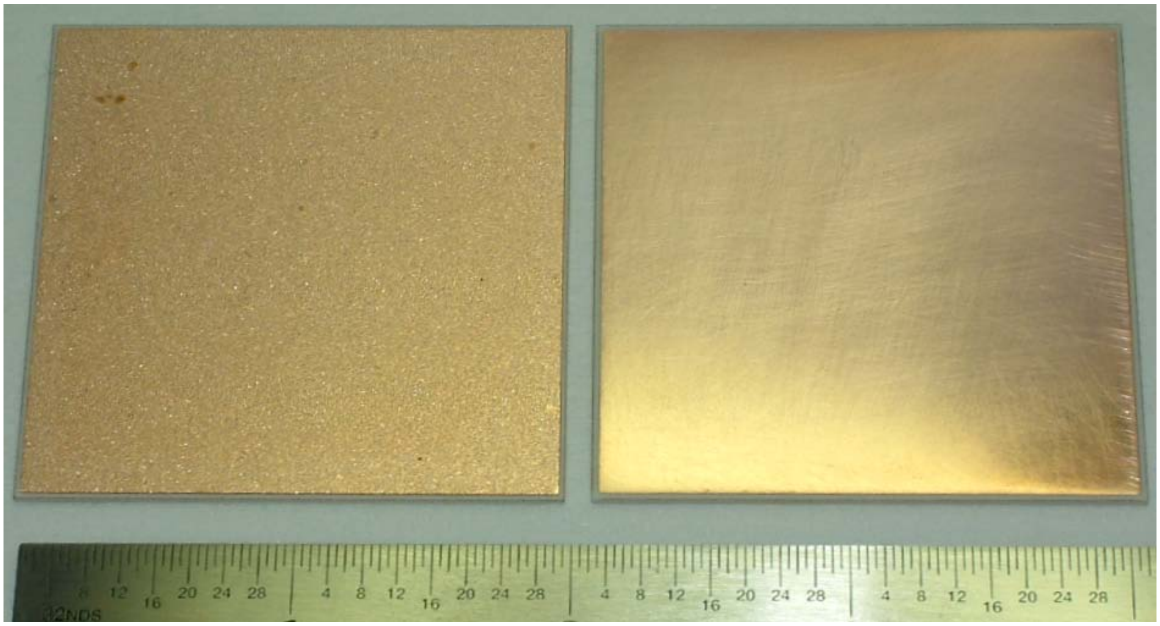

Figure 3.5: Blank DBC samples as delivered to Harvard (left) and after polishing with 30 μm paper for 45–60 min (right).

electrodes is dislodged by a high-pressure burst of CO_2 or, if necessary, with an etched tungsten tip [197, App. A].

Fine polishing requires less time, much less material is removed, and there is less friction so mounting on the polishing chuck is unnecessary. First, the contact pads are tinned with a soldering iron; this requires enough heat that oxides usually form on the electrode surface above the vias. The trap is polished with 30 μm paper for 30 seconds to remove burrs from laser machining, as well as surface oxides from the laser machining process and tinning the contact pads. The trap is subsequently polished with 9 μm, 3 μm, and 2 μm alumina grit paper[18] for 2 minutes each, with several minutes in an ultrasonic bath of deionized water in between polishing steps to remove abrasive and copper particles. The trap is again inspected with the stereomicroscope

[18] 3M Wetordry 281Q

and the grooves cleaned with high-pressure CO_2. Finally, the trap is electroplated with 50–100 nm of gold as an oxidation barrier.[19] The finished trap electrodes are displayed in Fig. 4.1.

Despite careful polishing, some fine scratches remained on the electrode surface, although they are small enough not to be visible in Fig. 4.1. A featureless mirror finish could not be obtained from this procedure, nor with other procedures attempted with various silicon carbide polishing papers, aluminum oxide polishing papers or lapping films, or abrasive slurries ranging from 6 μm diamond to 50 nm alumina. Possible explanations include scratches from chipping away pieces of copper from the edge of the substrate or the edge of the machined grooves; oxide inclusions being pulled out of the bulk copper by the abrasive; and smearing of soft copper, possibly with embedded abrasive particles [198]. Unlike copper electrodes used for cylindrical traps, the planar traps are fired in an oxygen environment, so oxide inclusions seem a likely candidate. This DBC process also anneals the copper, making it more difficult to polish compared to cylindrical copper electrodes.

As surface finish requirements become more stringent with decreasing trap size, final trap polishing will require either better abrasive polishing, etch polishing, chemical-

[19]The trap used in our first planar trap experiments at Harvard was not gold-plated and was polished using a slightly different procedure. After laser machining, the trap was polished with 15 μm silicon carbide grit paper (3M Wetordry 281Q), followed by 1200 grit (2.5 μm) SiC sandpaper (sold by PACE Technologies, metallographic.com, SIC-1200P8-100) and finished with a 1 μm polycrystalline diamond slurry (PACE Technologies, PC-1001-250) on a stiff cloth pad (PACE Technologies, DC-3008). After thermally cycling the experiment, some oxidation was observed on the surface and polished away with 2 μm and 1 μm paper, but oxidation was again observed after a subsequent cycle. Although earlier Penning trap experiments have used polished bare copper electrodes and seen the surface emerge unchanged after months or years, in this case, an oxidation barrier seems necessary, and the bare copper trap was replaced with a gold-plated one. The polishing recipe was changed due to concerns of a possible residue from either the 1200 grit paper or the diamond slurry. In the procedure reported above, the same abrasives were used as in other experiments in our laboratory, except with the finest polishing steps omitted since they seemed to increase the number of scratches on the surface.

mechanical polishing, electrolytic polishing, or diamond turning. Processing samples in a clean room may be helpful. And electroplating a thicker gold layer may also improve the surface finish.

3.7 Future Traps

The next generation of planar Penning traps poses several additional fabrication challenges: making smaller traps, detecting the spin and cyclotron states, including additional electronics on the same substrate.

3.7.1 Smaller traps

If planar Penning traps are to form the building blocks of a scalable quantum information processor, the traps must be scaled down to permit a large number of them to fit in a single experiment and possibly also to increase the coupling of one qubit to another. For planar Penning traps as currently proposed, the electrode feature size must be comparable to or smaller than the qubit spacing. In the long term, this may be a disadvantage compared to systems such as cold atoms and ion traps; for cold atoms, the trap structure can be generated with an optical lattice, and for ions several qubits can be spaced a few microns apart in one trap structure. One possible route could be to put more than one electron in each trap. We have recently investigated a method for entangling electrons held in the same Penning trap [2], though this challenging approach has not yet been pursued experimentally.

When designing experiments with smaller traps, we must consider not only fabrication challenges but intrinsic obstacles as well. Smaller gaps are more likely to result in field emission if the applied voltages are kept at about the same magnitude. However, if the same axial frequency is to be used, then Eq. (2.2) requires that the potentials $V_i \propto d^2$, where d is the characteristic linear dimension of the trap. If the electrode radii and gaps both scale with d, then the electric field across a gap goes as $E_i \propto V_i/d \propto d$, and thus a smaller trap will have weaker electric fields across the gaps and field emission will in fact be reduced. Even with small traps and high voltages, field emission would not necessarily be a limitation: field emission in the Sandia traps was truly negligible (less than 1 fA) with a trapping potential of 125 V (2.5 MV/cm electric field) in a micro-ion trap with 1 μm radius [188]. It remains to be seen, however, whether it is possible to maintain the necessary stability and harmonicity with the shallower trapping wells that would would be required in small Penning traps.

If field emission is observed to be a problem, there are several possibilities. Trap designs that limit the size of the gap potentials are one solution. For three-gap traps, $\Delta V_3 = 0 - V_3$ is generally the largest of the gap potentials. It can generally be reduced by decreasing the radial width of the second electrode, $\rho_2 - \rho_1$, and increasing the radial width of the third electrode, $\rho_3 - \rho_2$. We showed in Sec. 2.6.1 that a planar trap with a conducting plane above it will permit an optimized trap with lower gap potentials. Other solutions are to increase the gap width and to make the metal surfaces within the gap as smooth and adsorbate-free as possible, perhaps by using techniques like annealing,[20] chemical etching, electrochemical polishing, and ultrapure water rinsing.

[20] In Ref. [193], field emission was observed in silver traps when 100 V was applied across 10 μm gaps. After annealing, micrographs of the electrodes revealed a smoother surface, and no field emission was observed even with 750 V applied across the gap.

The capacitance must be considered as well, but it decreases with trap size. The gap capacitance is $C_{\text{gap}} \propto A/d \propto d$. Similarly, the strip-to-strip capacitance is derived from the capacitance per unit length of Eq. (3.1); the elliptic integrals are dimensionless, so the scaling comes only from multiplying the capacitance per unit length by the circumference of the groove, which is also proportional to d.

The main challenge, therefore, is simply to fabricate smaller traps meeting the same two requirements of high aspect ratio and backside contacts.

There is now broad experience in making small ion traps [199] including microfabricated planar traps (e.g., [178, 200]) with up to 150 zones [49], multilayer traps fabricated on a single substrate (e.g., [201]) or multiple substrates (e.g., [202, 203]), and printed circuit board traps [204, 205]. These ion traps follow on the heels of surface-electrode fabrication developed for atom chips (e.g., [206]). Recent large-scale planar ion traps have been fabricated at Sandia and Lucent (e.g., [207]) as part of the IARPA trap foundry program. Unfortunately, these fabrication methods for ion traps cannot be straightforwardly adapted to make planar Penning traps for electrons. Ion traps do not have the stringent requirements of screening insulators or preserving axial symmetry about the trap center. The motion of trapped ions can be laser-cooled, and the ions' internal states can be detected by fluorescence. Electrons, however, have no internal degrees of freedom, so we must rely on their translational degrees of freedom, particularly the axial motion since the radiofrequency signal can be detected and measured precisely. Furthermore, charge accumulation on exposed insulators can be minimized when loading ion traps by photoionizing neutral atoms with a laser focused on the trapping region. Some ion traps are designed to partially screen exposed insulators (e.g., the traps in Ref. [200] have an aspect ratio of 0.75), but this is less critical because only traps using radiofrequency detection, as required for electrons, are subject to the stringent requirements on trap harmonicity discussed in Chapter 2.

We now consider ways to make smaller planar Penning traps. For patterning the electrodes, laser micromachining can be used to make high-aspect-ratio grooves with a kerf as narrow as about 15 μm for metal films up to 100 μm thick [208]. This would permit a trap that is perhaps up to ten times smaller than the current traps. For even smaller traps, it may be possible to cut high-aspect-ratio grooves with ion beam milling, focused ion beam (FIB) milling, or reactive ion etching (RIE). Ion beam milling proceeds by masking the metal film with photoresist and then exposing it to a broad (4–15″) collimated beam of ions (typically argon) that sputter etch the metal. Copper and precious metal films up to 8 μm thick can be etched with feature sizes of a few microns or less [209]. FIB milling proceeds with a narrow beam of ions, most commonly gallium. A FIB would be useful for making only very small traps because the beam can be deflected only a small distance, unless a laser-positioned translation stage were available to increase the range of travel. Still, FIB milling would be dramatically slower than ion beam milling. RIE etches anisotropically and can produce high-aspect-ratio trenches, but only in certain materials. Aluminum, titanium, and tungsten are readily etched; copper may be possible, but Harvard's RIE apparatus is not equipped with the requisite chemistry; and gold is difficult to impossible.

Rather than etching a pattern into a conductive film, the pattern could be established by growing the metal layer through a deposition mask. Achieving a high aspect ratio is again the primary fabrication challenge.

For thick or high-aspect-ratio structures, electroplating is the deposition method of choice and is widely used in LIGA and other microfabrication processes. However, for high-aspect-ratio structures, the plating rate is limited by diffusion of ions into the narrow features; the process proceeds very slowly and may take as long as weeks [210, Sec. 16.2.3]. Some initial experiments on gold plating were conducted in our laboratory.[21] Good results were obtained for thin (∼100 nm) layers, but we have not yet developed a recipe that is optimized for plating thick layers.

Metal structures with extremely high aspect ratios (>100), smooth sidewalls, and excellent flatness and parallelism can be achieved by exposing PMMA resist to x-rays to make an electroplating mold, as used in LIGA, but this requires a sychrotron x-ray source. A good substitute would be the UV-sensitive epoxy resist, SU-8, which can produce similar structures with moderately high aspect ratios [211, 212]. Unlike PMMA, however, cross-linked SU-8 is very difficult to remove, especially from high-aspect-ratio structures, without damaging the metal deposited around it. Stripping SU-8 has been reported [213], however, with solvents, plasma ashing/RIE [214], molten salt, or laser ablation [215]. Still, efficient and economical removal of SU-8 from deep metallic trenches remains an outstanding problem, and experiments continue on new methods, such as elaborate microwave plasma etching processes [216]. Applying a layer of OmniCoat™ prior to deposition of SU-8 may make removal much easier.

[21] The electroplating solution used was Techni Gold 25 from Technic, Inc. It is sold ready-to-use (RTU), though we diluted it 3:1 DI H_2O:TG25 RTU. The recommended current density is 1–5 A/ft^2; typically 1–2 A/ft^2 gave the best results in our lab.

Although SU-8 has been most widely used for high-aspect-ratio plating molds, some other resists may be possible as well. For example, Shipley SPR 220-7 has been used to achieve structures with an aspect ratio of about 5 [217]; AZ nLOF 2070 has been used to achieve an aspect ratio of 4 with a resist layer 7 μm thick;[22] and Microresist ma-P 1275 can achieve an aspect ratio of 3–4 for a resist layer up to 40 μm thick. The photoresist must also be compatible with the chemistry of the electroplating bath, which is usually alkaline.

A small trap must also have vias that are sufficiently small to permit electrical connections to small electrodes. Planar Penning traps like those in Fig. 3.1 cannot be made much smaller since our current supplier of DBC substrates does not generally make vias with a diameter smaller than 1 mm. One possibility is to put the electrode pattern and the leads on the same side of the substrate with an insulating layer deposited between them, as used for some surface-electrode ion traps [49]. Since the layer would be very thin ($\sim$1 μm), high-aspect-ratio vias would not be required in order to have closely-spaced electrode contacts. A planarization step may be necessary after depositing the insulating layer.

Alternatively, through-wafer electrical interconnections could be fabricated in-house; these are difficult but possible to make. Again, the problem is the aspect ratio: the vias must be narrow enough to allow for small electrodes yet still must go all the way through the substrate. To minimize the required aspect ratio, a thin substrate should be used; substrates as thin as 0.1 mm are commonly available, and if necessary, the wafer could be further thinned prior to deposition. Making such a via requires etching or laser-drilling a high-aspect-ratio hole through the substrate

[22] This resist was used to attain an aspect ratio of 1 in pixel Penning trap substrates [140].

and then coating or filling it with metal. Laser-drilling could produce holes perhaps as small as 150 μm in diameter. For smaller holes, etching would be required, but a different substrate, such as quartz or silicon, may need to be used; however, silicon may be problematic because of its high RF dissipation factor, $\tan\delta = 0.005$. The metallization can be achieved by electroplating with process requirements similar to those for electrodepositing the metal electrodes. Plated-through holes have been fabricated with an aspect ratio of 17 (30 μm wide $\times$ 525 μm deep [218]) and filled vias with an aspect ratio of 7 (50–70 μm $\times$ 400 μm [219], 20 μm $\times$ 140 μm [220], or 10 μm $\times$ 70 μm [221]) or more [222] using deep reactive ion etching (DRIE) of silicon and then electroplating with copper. References [221, 222] used pulse reverse electroplating [223] and filled the small via holes within a few hours.

The tiny (1–10 μm radius) cylindrical ion traps fabricated at Sandia [136, 224] suggest an entirely different paradigm for trap fabrication that could still satisfy the two primary requirements. The electrode leads should not disrupt the axial symmetry, but need not be on the opposite side of the substrate. There could be freestanding electrodes elevated above a network of leads, though this would require a much more demanding multilayer deposition process. Finally, perhaps the cylindrical symmetry requirement could eventually be relaxed, though it may prove too difficult for precise detection of a single electron's axial motion.

3.7.2 Magnetic bottles

An electron's spin or cyclotron state can be read out by introducing a magnetic inhomogeneity, Eq. (1.5), to couple the spin and orbital magnetic moment of the electron to its axial motion. Spin and cyclotron transitions are then manifested as small shifts in the axial frequency, which is monitored via the narrowband axial detection scheme described in Section 4.5 [5]. In cylindrical Penning traps, the magnetic bottle is produced by a ring of ferromagnetic material placed symmetrically about the trap center [120]. To create a planar trap with a magnetic bottle, one possibility is to include a ring of ferromagnetic material among the electrodes of the planar trap; this is feasible since ferromagnetic materials like nickel can be readily electroplated. Unless all the electrodes are made out of the same (magnetic) material, it would be necessary to add a planarization step after depositing the magnetic electrode and the other electrodes. Because the magnetic ring would not be reflection-symmetric about the equilibrium position of the electron, there would also be a linear magnetic gradient in addition to the desired quadratic gradient; this must be checked to ensure that unwanted effects are sufficiently small.

Some proposed quantum information processing protocols assume that each electron experiences the magnetic bottle field only at the readout phase of the computation. Furthermore, it is possible to drive coherent spin or cyclotron transitions only by limiting decoherence from coupling to the axial motion, which is in thermal contact with the detection circuit.[23] One possibility would be to move the electron away from the magnetic material by varying the applied potentials to change the position of the trap center, z_0. Another possibility would be to make a magnetic bottle that could be turned on and off. The simplest implementation of a variable bottle would be a current loop, concentric with the trap axis, which could be achieved using the

[23]Even if a trapped electron could be decoupled from the amplifier during spin rotations, the axial motion would be in some unknown Fock state, and hence there would still be uncertainty in the value of ω_s.

present fabrication methods. A ring electrode with at least one radial slit and two vias would define a current path giving the necessary magnetic field pattern. This method may be limited by the heat that would be dissipated by the electrodes and the current leads when enough current is applied to generate a field gradient sufficient to produce an observable frequency shift corresponding to a spin flip or cyclotron jump. However, the quadratic field coefficient scales with the inverse square of the trap dimension [120], so for smaller traps, this method may be feasible.

Another solution to produce a variable magnetic bottle is to embed a loop of superconducting material and to induce current in the loop by changing the current in an outer normal-conducting solenoid [225], though this causes the axial frequency to be more sensitive to magnetic field fluctuations [226, Sec. 5.2]. A modified design for a variable bottle includes a second loop in order to cancel the zeroth-order contribution to the magnetic field [227]. A Penning trap with a superconducting flux transformer was used in experiments at the University of Washington, but was not adequate for further improving the precision of the electron g-factor measurement [226]. A variable bottle would be a desirable trap feature, though the ease of material deposition may be a fabrication constraint. Unlike superconducting qubits (and superconducting ion traps [228]), Penning traps require a large magnetic field, so it is necessary to select a material such as NbTi that remains superconducting in a strong field. (See Ref. [176, App. 6.6] for a table of other high-field superconductors.)

3.7.3 On-chip electronics

Ultimately, an array of traps could ideally be fabricated with on-chip detection electronics and on-chip coplanar striplines as waveguides for spin-flip pulses, as has been demonstrated with electron spin resonance in semiconductor quantum dots [99], albeit at lower frequencies than the spin and cyclotron frequencies in the high magnetic fields of the current experiments.

3.8 Trap Fabrication Summary

We have now fabricated traps designed to detect a single electron. The traps have optimized electrode radii that will allow for tuning out the lowest-order electrostatic anharmonicity. The laser-machined grooves are deep and narrow to prevent charging and to screen out any charge that reaches the insulator. The copper electrodes and alumina ceramic are suitable for operation in a high magnetic field, and the insulator has low radiofrequency dielectric loss. The electrodes do not exhibit field emission across the gaps when trapping potentials are applied. The capacitance is calculated and measured to be small enough to permit sufficient signal-to-noise. And the surface finish and oxidation barrier should minimize patch potentials. The narrow resonances we observed (Chapter 5) were made possible by using a trap that satisfies all of these requirements.

Chapter 4

Cryogenic and Electronic Apparatus

To trap and detect particles, considerable support apparatus is needed in addition to the trap electrodes. The trap is mounted in an enclosure that provides the remainder of the electrostatic boundary, which is in turn mounted inside a cryogenic vacuum vessel cooled to 100 mK by a ^{3}He–^{4}He dilution refrigerator. A 6 T superconducting magnet provides the magnetic field needed for radial confinement. High-stability voltage sources supply the trapping potentials to the electrodes. The electrons are driven with oscillating potentials applied to the electrodes. And the tiny signal from the electrons is picked up by two stages of tuned-circuit amplifiers and is further amplified, filtered, mixed down, and detected by a chain of room-temperature electronics.

4.1 Trap Mounting and Electrostatic Boundary

The electrostatic trapping potential felt by the particles is determined by the biases applied to the trap electrodes as well as the potential on the remainder of the boundary. To ensure that these potentials are well controlled, the trap electrode plane is placed at one end of a grounded titanium cylinder. A schematic is shown in Fig. 2.10, and the actual enclosure used in the experiment is represented in Fig. 4.2. To best approximate the boundary conditions of Eq. (2.5), the enclosure is made large, subject to experimental space constraints; however, the potentials are still appreciably modified from the infinite-boundary case, as discussed in Sec. 2.5.2.

The trap is glued to a rectangular frame with a small bead of glue[1] in just one spot near the center to ensure that differential thermal contraction does not stress the substrate. This frame is then clamped between two plates, one of which has a circular pocket as a register for the cylindrical enclosure. The frame is clamped, rather than the trap, to prevent fracturing the ceramic substrate. This also avoids electrical contact between the enclosure and the electrode that extends from ρ_3 to ρ_c so that drives or biases can be applied to this electrode. To ensure that the trap electrode pattern is concentric with the conducting cylinder, a microscope reticle[2] is placed in the pocket of the top plate. The trap mounting frame is moved with a translation stage until the electrode pattern is well centered[3] on the reticle pattern, as viewed through a 10X telescope mounted 12″ above the trap.

[1]STYCAST® 1266 epoxy. If necessary, the epoxy can removed without damage to the trap with stripping solutions such as Miller-Stephenson MS-111.

[2]Klarmann Rulings KR-265

[3]The trap is centered to within approximately 100 μm, the spacing of marks on the reticle. Parallax is negligible since the reticle pattern is positioned 0.02″ above the electrode plane.

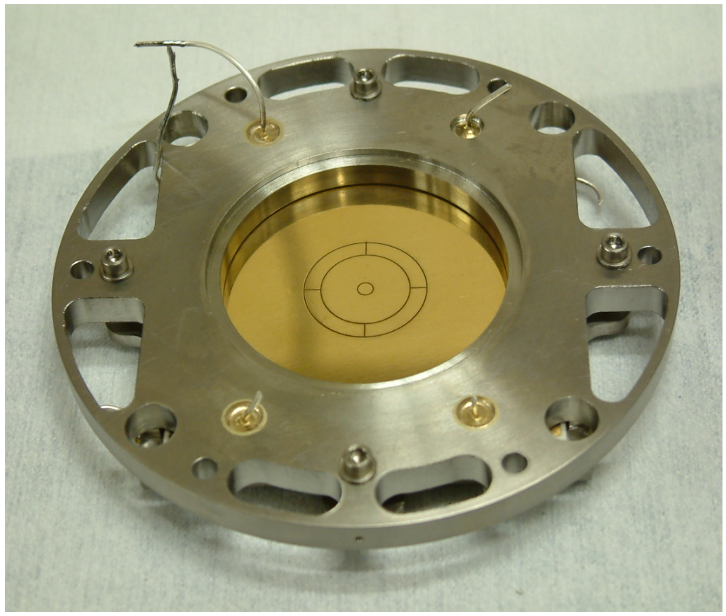

Figure 4.1: A planar trap centered in the mounting frame. The cylindrical enclosure fits tightly in the circular pocket.

Onto this trap "sandwich" are placed the side and top of the cylindrical enclosure, which has interior surfaces polished to a mirror finish.[4] Two small holes in the side walls allow the trap volume to be easily pumped out without changing the electrostatic properties. Electrons are loaded into the trap from a "field emission point" (FEP), a sharp tip made by electrochemically etching a tungsten rod [197, App. A]. When a large negative voltage is applied, the strong electric field causes electrons to tunnel out of the metal by the same process discussed in Sec. 3.5. The field emission point is mounted in a collet concentric with the trap cylinder, stood off from adjacent parts with spacers made of fused quartz. The electrons from the FEP follow magnetic

[4]The following sequence of abrasives was used for polishing titanium: P400 then P600 grit SiC sandpaper (Norton Abrasives); then 30 μm and 15 μm SiC polishing paper, followed by 9 μm alumina polishing paper (3M Wetordry 281Q); 1200 grit SiC sandpaper, 6 μm, and finally 1 μm DIAMAT diamond slurry (sold by PACE technologies). The inside of the cylindrical wall was polished by mounting it on a lathe and turning at 250-300 rpm. The flat surface of the cylinder top was polished by hand on a granite table.

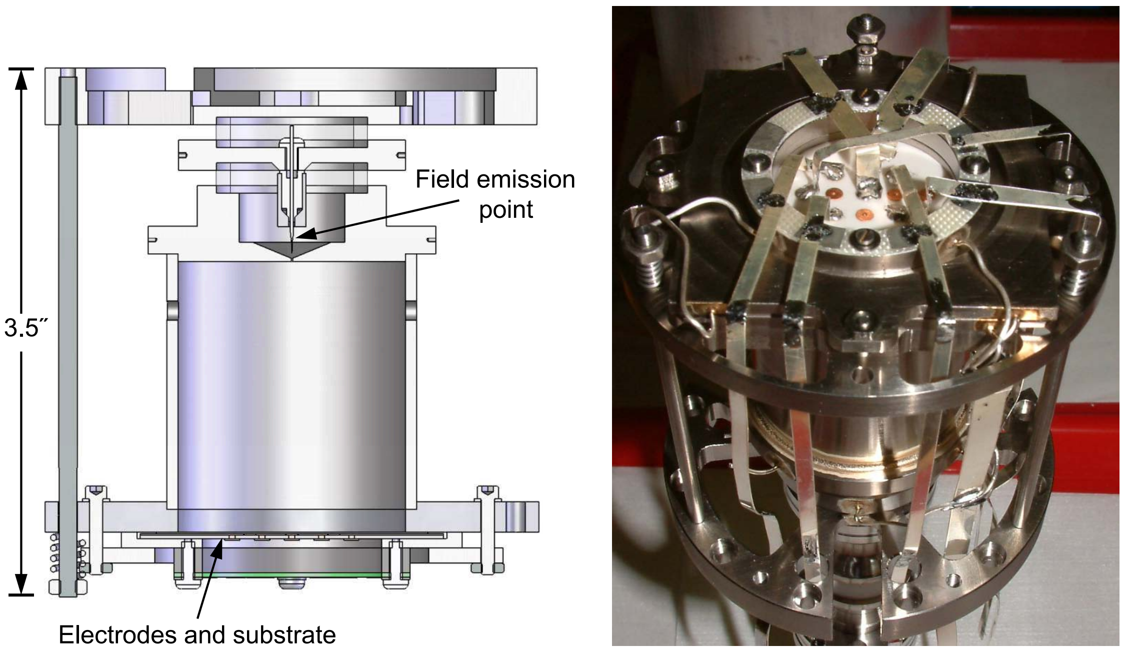

Figure 4.2: Cutaway diagram (left) and photograph (right) of the planar trap assembly. In the photograph, the cartridge is inverted to show the electrical leads and strain-relieving contact pad ring.

field lines through a 0.01″ hole in the top of the cylindrical enclosure. The electrons are highly energetic (~ 200 eV), and the trapping potential is conservative, so these electrons are not trapped. The beam of electrons strikes the electrode surface, creates secondary electrons, and desorbs gas molecules from the electrode surface. Gas ionized by the beam in the trapping region produces some electrons that fall into the trap.

To enable good RF grounding of all surfaces, all metal parts have silver wires attached by brazing[5] in a vacuum of less than 1.5×10^{-5} torr.[6]

[5] Our lab has found that silver and titanium can be joined mechanically and electrically by brazing with the same silver-copper eutectic braze alloy (72% silver/28% copper, Lucas-Milhaupt VTG-721) that we use for joining copper and silver parts, although we have found this method not to be reliable for making vacuum joints. This is consistent with reports from the literature [229], and e-beam welding has been our method of choice for silver-to-titanium (or titanium-to-titanium) vacuum joints.

[6] A good vacuum is required for brazing titanium, but estimates of the necessary pressure vary between $< 10^{-3}$ torr and $< 10^{-5}$ torr. See Refs. [230, p. 78], [231, p. 176], and [232, 233].

Electrical contact to the electrodes is made by soldering high-purity silver straps to the contact pads on the back side of the substrate, and these are strain-relieved by soldering to a pad on a piece of copper-clad teflon/glass weave circuit board mounted just beneath the trap electrodes.

The assembly is fastened together with threaded molybdenum rods and hand-wound tungsten wire springs to keep the assembly held together as the relative sizes of the parts change when cooling to low temperature.

4.2 Trap Vacuum Vessel

The trap is placed in an ultrahigh vacuum to minimize any interaction between trapped electrons and background gas molecules. To achieve this, the trap-plus-enclosure assembly is placed in a titanium vacuum container ("trap can") sealed with indium seals that is evacuated to UHV at room temperature. Then, a copper pump-out tube is "pinched off" to cold-weld the vessel shut. The entire volume is then cooled to low temperature with residual gases freezing out on the cold surfaces. A similar apparatus used the lifetime of antiprotons to set an upper bound on the pressure of 5×10^{-17} torr [121].

The entire experiment resides as a parasitic experiment in the trap can, cryostat, and magnet designed for a next-generation measurement of the electron and positron magnetic moments. Inside the trap can, the planar trap assembly hangs beneath the electron/positron trap assembly. This electron/positron trap, made with cylindrical electrodes and closed endcaps, is fastened to the underside of the top flange of the vacuum enclosure for the trap (the "pinbase"), which contains the electrical feedthroughs.

The straps leading to the electrodes pass through slots in the end plates of the planar trap and electron/positron trap assemblies to reach the feedthrough pins seven inches (18 cm) above the trap chip.

The electron g-factor measurement is so sensitive to magnetic fields that an earlier version of the experiment found that the nuclear field of copper was prohibitively large [234, 235]. Curie's law describes the nuclear paramagnetism, $M = C/T$, where C is called the Curie constant of the material. The magnetic field fluctuations scale as $dM/dT \propto T^{-2}$, so materials with large Curie constants cause unacceptably large magnetic flucutations at very low temperatures. The electron experiment therefore must be constructed of materials with small Curie constants; hence the materials used are silver electrodes and leads, quartz spacers, and titanium pinbase and trap can. When possible, all materials for the planar trap assembly were constructed from these materials as well. But the trap electrodes could not be fabricated out of these materials and still meet the demanding fabrication requirements described in Chapter 3. Copper and alumina have Curie constants [235, Table 3.1] that make them unsuitable for use in an electrode stack assembly for the electron/positron trap, but the planar trap is 4.00″ from the center of the electron/positron trap, so its effects are not problematic.[7] The resulting gradients[8] are displayed in Table 4.1. The magnetic field sensitivity to the temperature is to be compared to the approximately 3×10^{-7} T/K that results from the small nuclear paramagnetism of the electron/positron trap itself. The linear gradient is 2–3 orders of magnitude smaller than the linear gradient

[7]The planar trap lies further from the electron/positron trap center than the copper radiation shield and inner vacuum chamber.

[8]To simplify the calculation, the square electrodes are treated as axisymmetric. The magnetic field resulting from a small ring of material with a given magnetization is calculated in Ref. [120, Sec. VI].

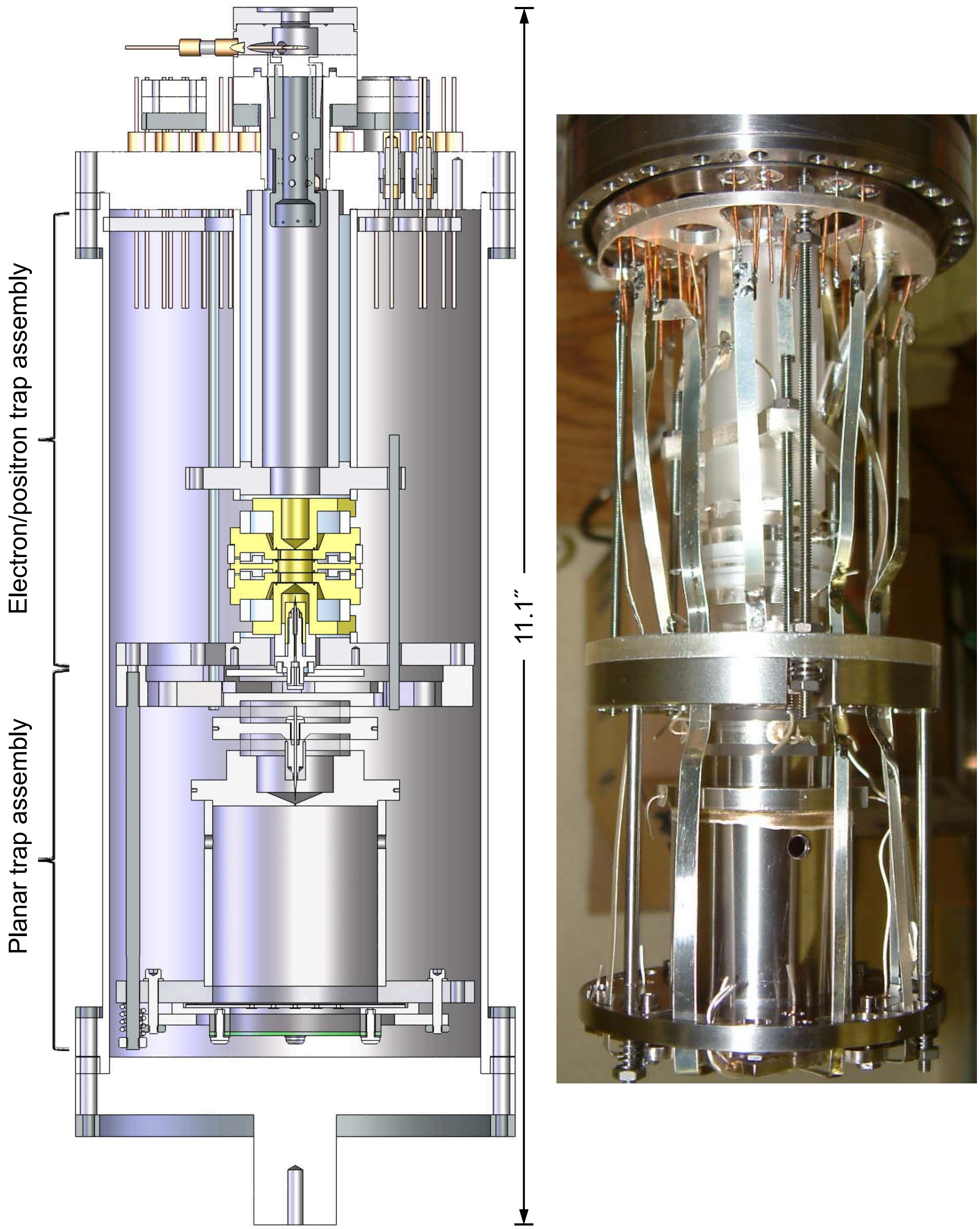

Figure 4.3: Cutaway diagram (left) and photograph (right) of the planar trap and electron/positron trap assemblies in the trap can.

from the electron trap electrodes, and the quadratic gradient is completely negligible compared to the 660 T/m^2 magnetic bottle. The contact pad ring for strain-relieving the leads to the planar trap electrodes also contains Teflon, which has a similar nuclear Curie constant to alumina, but it contains much less material than the trap electrodes and substrate and thus does not have an appreciable effect.

B_0	6×10^{-9} T
B_1	2×10^{-7} T/m
B_2	3×10^{-6} T/m^2
dB_0/dT	-1×10^{-7} T/K

Table 4.1: Calculated magnetic field gradients and temperature sensitivity of the magnetic field at the electron/positron trap center, resulting from the copper electrodes and alumina substrate of the planar trap.

The constraints on materials that can be used in the electron/positron g-factor experiment make it difficult to construct electrical feedthroughs into the trap can. We use weldable feedthrough pins[9] consisting of an OFE copper wire, a 70/30 Cu/Ni outer adapter, and an alumina ceramic insulator. Ordinarily these would be brazed directly into a copper flange, but copper is proscribed so instead the pins are brazed into a silver plug in a hydrogen atmosphere,[10] and the silver plugs are electron-beam welded to the titanium pinbase. Silver and titanium do not easily form good weld joints; forming a reliable vacuum joint requires careful selection of joint geometry and e-beam weld parameters. On separate occasions, leaks were observed to open up after thermally cycling the experiment, and twice the traps and wiring for both experiments

[9]Insulator Seal, Inc. (now part of MDC Vacuum Products, LLC), part no. 9411004.

[10]The braze alloy used is Lucas-Milhaupt VTG-721, which melts at 780 °C. The feedthrough pins are sealed with an AWS-BVAg-30 grade 1 braze alloy, Prince & Izant model PAL 5, which is composed of 68.5% Ag, 26.8% Cu, and 4.7% Pd, and has solidus and liquidus temperatures of 795 °C and 810 °C, respectively. Care must be taken when brazing pins to ensure that the braze alloy on the pin-to-plug joint melts thoroughly but the joints within the pin do not.

were removed, the leaking feedthroughs drilled out and replaced, and the apparatus reassembled. The leaks appeared intermittently at room temperature, and it is likely that a leak escaped notice for some time, resulting in a poor vacuum in the trap can when the experiment was operated at 4 K. The symptoms included an FEP failure on the planar trap experiment and an increase in the number of trapped electrons in the electron/positron trap when a detuned sideband drive was applied to a small cloud of electrons; the latter problem vanished when the experiment was cooled to 100 mK, which dramatically decreases the vapor pressure of helium (all other gases are already frozen out at 4 K). It is likely that vacuum problems also contributed to signal drifts and particle loss observed in our initial planar trap experiments. A replacement pinbase with improved welds is currently being fabricated.

4.3 Cryostat and Magnet

The experiment is cooled to 100 mK by a ^{3}He–^{4}He dilution refrigerator.[11] Beneath the mixing chamber is a region ("tripod region") in which we have placed cold electronics: the first-stage tuned-circuit amplifier and the last set of filters for DC lines. High-purity silver rods[12] brazed into silver plates thermally anchor the pinbase to the mixing chamber.

The dilution refrigerator can reach temperatures as low as 15 mK with no heat load [164], but we operate it at 100 mK. The cooling power scales quadratically with temperature [236], which can be regulated with a heater on the mixing chamber. At

[11] Janis Research Company, Inc., customized version of the JDR-500 model

[12] Experiments in smaller-bore magnets had three rods; the current experiment has six rods, though the name "tripod" is still used.

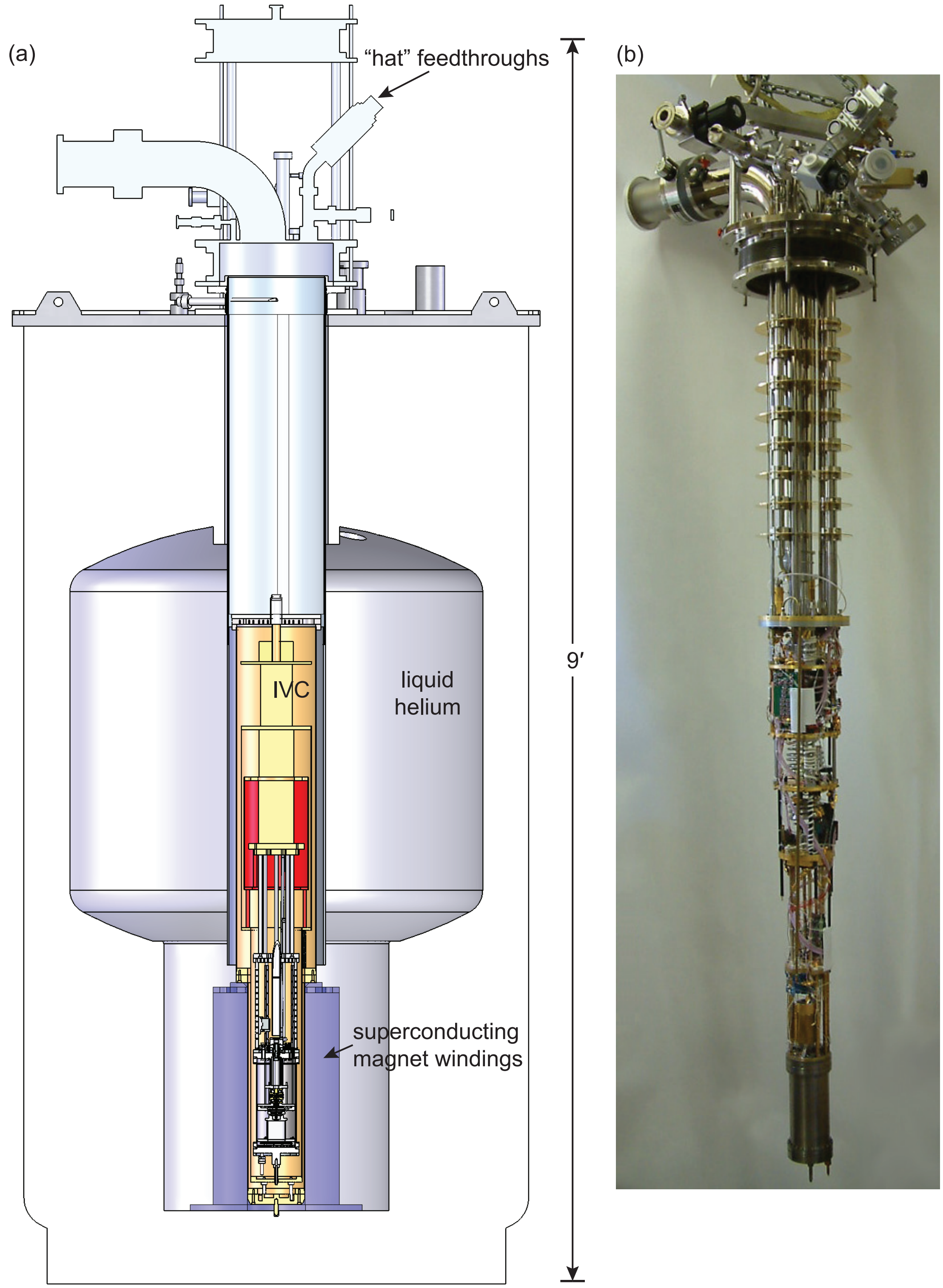

Figure 4.4: (a) Schematic section view of the magnet, dewar, and dilution refrigerator assembly. (b) Photograph of the dilution refrigerator insert.

100 mK, the dilution refrigerator has about 300 μW of cooling power [164]. Some of this power is required to cool wires coming from higher-temperature stages of the refrigerator. To minimize these loads, DC biases are applied on very thin wires[13] and heat-sunk at each temperature stage, and RF lines are applied on thin microcoax cables[14] with stainless steel sections between temperature stages and copper sections heat-sunk at each temperature stage, including two heat sinks at the still on the axial signal line, one each before and after the second-stage amplifier. The top of the dilution refrigerator assembly, referred to as the "hat", contains the feedthroughs where electrical signals pass between room temperature and the IVC.

The electrons' radial confinement results from the magnetic field produced by a 6 T superconducting magnet.[15] The magnetic field can be shimmed to a homogeneity of better than 1 part in 10^8 over a 1 cm^3 volume, and it includes a self-shielding solenoid[16] [238] that is expected to reduce fluctuations at the field center by a factor of up to 100. However, the apparatus is designed so that the electron/positron trap is positioned at the center of the magnetic field because the g-factor measurement is acutely sensitive to magnetic field gradients. The planar trap experiment is 4″ below the magnetic field center. Initial experiments with electrons in planar Penning traps are intended only to detect the axial motion, not to manipulate or detect the spin or cyclotron motion; thus, the magnetic field provides only radial confinement, and a homogenous field is not so important. At 4″ below the field center, the magnetic field

[13]0.003″ constantan wires coated with 0.003″-thick PFA insulation

[14]Microstock, Inc., UT-34-SS-SS and UT-34C. Both have a 0.034″ outer conductor diameter, a 0.026″ PTFE dielectric diameter, and a 0.008″ inner conductor diameter.

[15]Cryomagnetics, Inc.

[16]This method has in fact been used to suppress magnetic field fluctuations in a cryogenic planar ion trap by placing superconducting rings in close proximity to the trap electrodes [237].

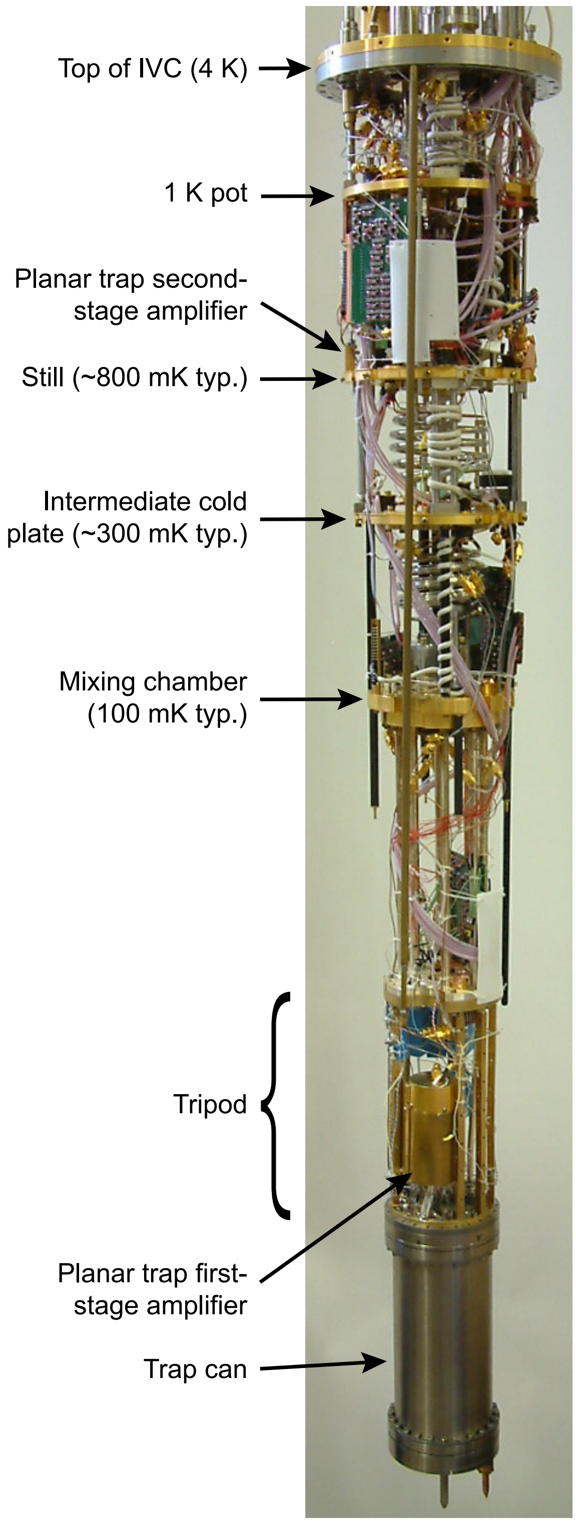

Figure 4.5: Dilution refrigerator inner vacuum chamber. Typical temperatures of each stage are indicated.

experienced by electrons in the planar trap is reduced by 3% (5.18 T at field center, 5.03 T at the planar trap electrodes).[17]

Unlike the 77 K bore NMR magnets used for other experiments in our laboratory, the magnet used in this experiment has a cold bore, and the liquid helium that bathes the magnet windings is the same volume that cools the experiment. This design was developed for the electron/positron experiment because it enables the trap to rest directly on the magnet to minimize magnetic field fluctuations arising from mechanical vibrations. Some magnetic field inhomogeneities will inevitably be present, and trap motion in a magnetic gradient can broaden the cyclotron and anomaly lineshapes. In the previous version of the electron g-factor experiment, the trap hung from a 7′-long moment arm below the flange where it attached to the magnet assembly; in the new design, the bottom section of the dilution refrigerator inner vacuum chamber (IVC), which is rigidly attached to the trap, rests directly on the magnet coilform, with flexible bellows mating to the top of the dewar.

The cost of this feature is that the experiment must be inserted directly into the liquid helium space via a 9″ diameter opening in the dewar neck. It is very difficult but imperative to minimize the amount of air admitted into the dewar because there is only 0.020″ clearance between the outer diameter of the IVC and the inner diameter of the magnet bore, so even a very small amount of nitrogen ice or water ice can prevent the experiment/refrigerator assembly from being inserted into the magnet. This happened twice as we were learning to use the new system; each time resulted in a two-week delay since the magnet had to be discharged and the system brought

[17] Unlike the electron/positron trap, the location of the planar trap center depends upon the potentials applied, as discussed in Chapter 2.

up to room temperature. The outer diameter of the refrigerator assembly mates to the dewar deck with a sliding seal.[18] However, the refrigerator assembly must be lowered into the dewar by just over 20 inches before the seal seats, and the sliding seal is imperfect, since helium can sometimes be felt venting out around it. We have found that air can be mostly hindered from entering the dewar by surrounding the refrigerator assembly with a helium-filled bag immediately before insertion, fastening it around the dewar neck as soon as the cover is removed, and flowing helium gas into the dewar from a different port to maintain a positive gas flow until the sliding seal is seated. The bag is left in place with helium gas flowing while the refrigerator is inserted in order to maintain a positive-pressure helium atmosphere so that air does not leak in around the sliding seal.

The experiment must be lowered in slowly—typically over about three hours—in order to vapor-cool it efficiently and thus to minimize boiloff of liquid helium. The outside of the IVC cools quickly, but the inside parts of the refrigerator are not efficiently cooled without some intervention: radiative cooling is slow, and the experiment and the rest of the dilution refrigerator are very weakly conductively coupled to the IVC because they must be at different temperatures when the refrigerator is operating. Thus, the IVC must be filled with an exchange gas to conduct the heat from the inside of the refrigerator to the walls, which are cooled by helium vapor; the exchange gas is then pumped out just above its boiling point once the experiment is cold. We used helium initially, until discovering the unacceptable vapor pressure in the trap can. It was thought at the time that the cause was helium permeation of the

[18] Astra Seal, a teflon-encapsulated stainless-steel spring, is rated to operate at temperatures as low as $-250\,^{\circ}$C.

glass [239] in the 200 MHz feedthrough for the electron/position experiment's axial amplifier, though a leaky e-beam weld joint is now a much likelier explanation for the observed problems. A subsequent cooldown using neon as the exchange gas was attempted, but the neon froze just a few minutes into the cooldown procedure. Even though the top plate of the IVC was still nearly at room temperature, the bottom of the IVC had already been sufficiently vapor-cooled to freeze the neon. Helium has necessarily been used thereafter, even with a known leak in the trap can. Since helium will leak into the trap can during this process, operating at 4 K will not produce an adequate vacuum, so the dilution refrigerator must be started prior to loading particles. A piece of charcoal sorb was added to the inside of the trap can because its enormous surface area increases the cryopumping of helium at low temperatures.

4.4 DC Biases

Stable trapping potentials are crucial for detecting a single electron's axial signal. For an orthogonalized trap [125], the axial frequency depends strongly upon only the potential difference between the ring and endcaps; therefore, only this potential must be held very stable. There is generally a single compensation voltage, and the axial frequency depends only weakly upon it, so it is unnecessary to go to great lengths to stabilize it. A planar trap cannot be orthogonalized (see Chapter 2), however, so each of the trap potentials, like the ring voltage in a cylindrical trap, must be kept stable in order to avoid drift or broadening of the axial resonance.

Each of the three electrode potentials originates from a floating high-stability solid-state voltage source[19] used to charge a large (10 μF) capacitor[20] in the cryostat. The potentials are applied on shielded twisted-pair cables that are further shielded within in an aluminum duct from the electronics rack to the top of the dewar. Potentials enter the IVC on high-leakage-resistance ceramic feedthroughs; because this resistance forms a voltage divider with the resistors in the bias line, a fluctuation in leakage resistance changes the potential applied to the electrode and hence also the axial frequency. Inside the IVC, the potentials are carried on constantan twisted pairs,[21] with both wires passing through LC filters thermally anchored to the 1 K pot. The voltage is applied to the pin after a final RC low-pass filter, and to avoid ground loops, the neutral lead is grounded only at the pinbase. The third electrode has four segments tied together in two pairs so that a drive applied to one half of the electrode has the correct geometry to cool (or heat) the magnetron motion (Sec. 5.4). A hand-wound inductor connected between the two pairs permits the DC bias to be applied to the whole electrode while blocking the drive applied to one side. The fourth electrode ($\rho > \rho_3$) is tied to ground at DC with a 10 kΩ resistor.

Amplifier biases from a Harvard-built computer-controlled voltage supply[22] enter the IVC on a 40-pin Fischer connector and are similarly routed through LC filter boards at the 1 K stage and (for the first-stage amplifier) the base temperature region.

---

[19] Fluke 5440B

[20] Vishay MKP-1840

[21] The four-segment e3 electrode has one lead to each segment so that we can verify *in situ* that the bias is reaching all segments. To decrease the number of lines, these leads are twisted in a bundle of six with a single ground wire.

[22] Harvard Electronics Instrument Design Lab BabyDAC, Rev. 3, Oct. 2010

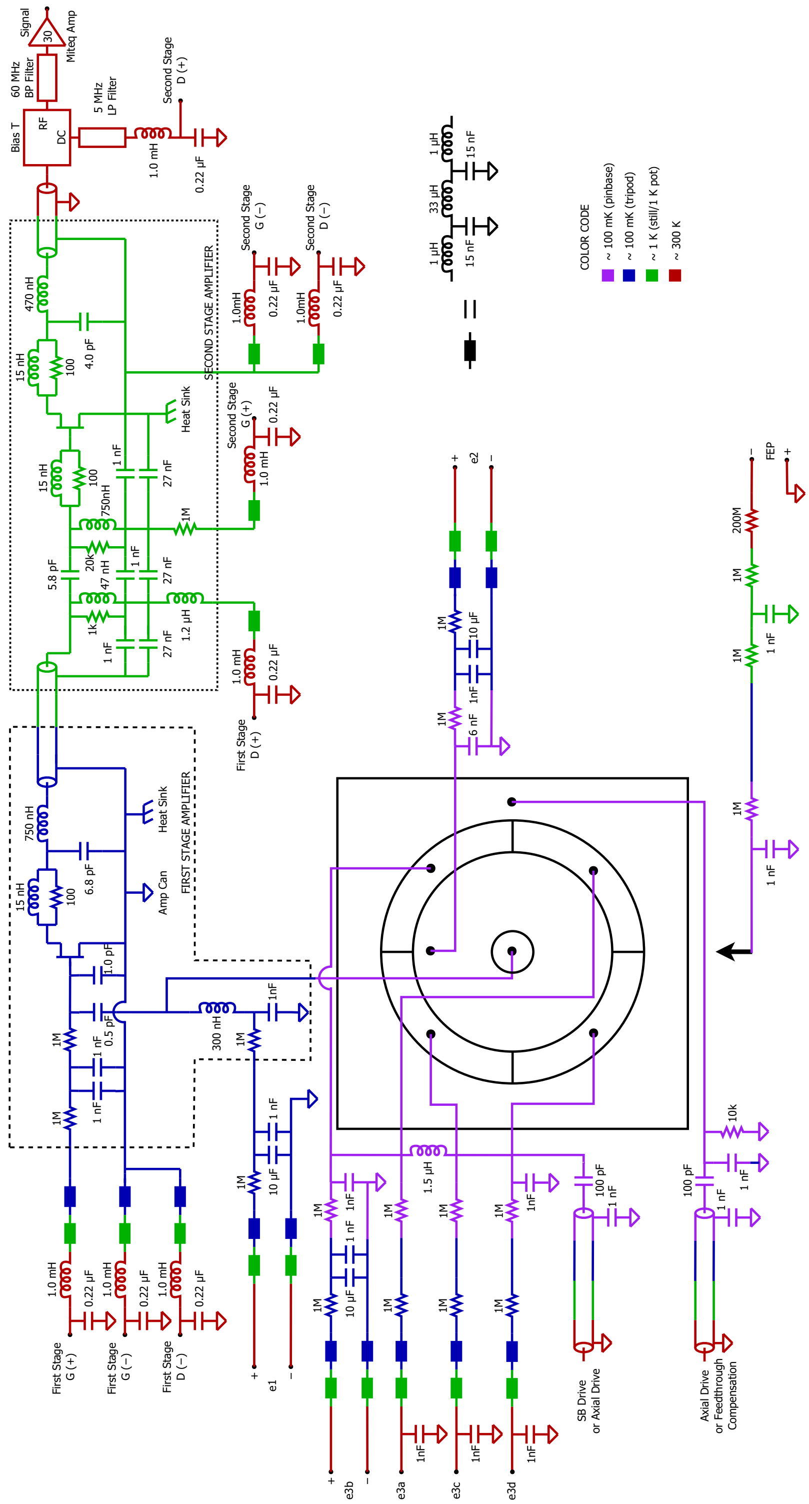

Figure 4.6: Trap electrode wiring diagram

4.5 Tuned-Circuit Amplifiers

The tiny signal from an electron's axial oscillation (a few hundred femtoamps for a large amplitude of 0.1 mm) is picked up by two stages of homemade tuned-circuit amplifiers. The capacitance between the detection electrode and adjacent electrodes provides a path to ground for the axial signal. Over a narrow frequency band, this capacitance can be canceled by an appropriately chosen inductor; at the resonant frequency of the circuit, the circuit is effectively a large parallel resistance. A trapped particle is damped by this resistance, and the energy dissipated in the resistor provides the signal that is amplified and detected, as discussed in Sec. 2.7 and depicted schematically in Fig. 2.16.

4.5.1 Parallel resonant circuit

A simplified model of the tuned circuit at the input of the first-stage amplifier is shown in Fig. 4.7a. Near resonance, the circuit of Fig. 4.7a is described to a very

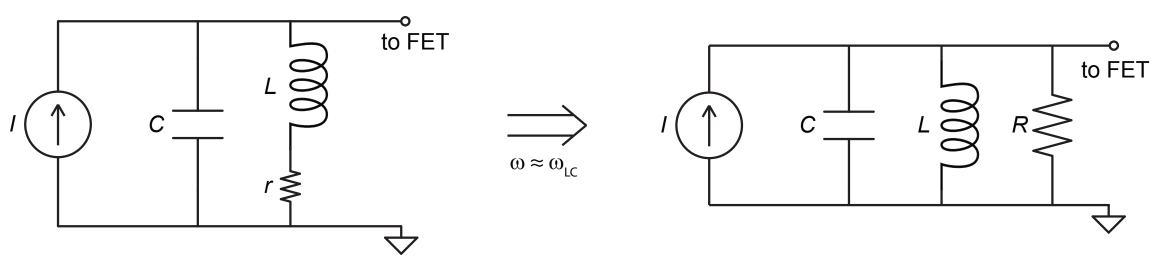

Figure 4.7: Model of the tuned circuit at the input of the first-stage amplifier (left) and impedance-transformed circuit near resonance (right).

good approximation by the RLC parallel circuit of Fig. 4.7b, and on resonance, $\omega = \omega_{LC} \equiv 1/\sqrt{LC}$, the reactance of the inductor cancels the reactance of the capacitor and the impedance is purely resistive,[23] with a value that is inversely proportional to the (unavoidable) residual series resistance,

$$R = \frac{L}{rC}. \tag{4.1}$$

The circuit is driven by a current I that has contributions from the current induced by the axial motion of trapped electrons as well as the Johnson noise in the resistor,[24]

$$I_N = \sqrt{4k_BTB/R}, \tag{4.2}$$

where k_B is the Boltzmann constant, T is the temperature, and B is the measurement bandwidth. The power dissipated in the resistor is $P = I^2(\text{Re } Z)$, where Z is the complex impedance of the parallel circuit. This has the familiar Lorentzian lineshape,

$$\text{Re } Z = R\frac{(\Gamma/2)^2}{(\omega - \omega_{LC})^2 + (\Gamma/2)^2}, \tag{4.3}$$

where Γ is the FWHM,

$$\Gamma = \frac{\omega_{LC}}{Q} = \frac{1}{RC}, \tag{4.4}$$

and the quality factor Q is simply the ratio of the parallel resistance to the (inductive or capacitive) reactance,

$$Q = \frac{R}{\omega_{LC}L} = \omega_{LC}RC = \frac{\omega_{LC}L}{r}, \tag{4.5}$$

where in the latter equality, we have used Eq. (4.1). (This expression is just the quality factor of the inductor, i.e., the ratio of its reactance to its series resistance,

[23] This is true in the limit of large Q. On resonance, the impedance of the circuit in Fig. 4.7a is actually equivalent to a resistance $L/(rC) + r = (1 + 1/Q^2)R$ in parallel with a capacitance $C/(Q^2 + 1)$. For $Q \sim 1000$, Eq. (4.1) is nearly exact.

[24] Although Johnson noise is often expressed as a voltage source in series with R, the Norton equivalent circuit is a current source in parallel with R.

at resonance, $Q_L = X_L/r = \omega_{LC} L/r$.) A more sophisticated model is described in Ref. [134, Sec. 4.1].

We can see from Eq. (4.2) that the ratio of the current induced by trapped particles to the noise current scales with $\sqrt{R}$. Thus, large R gives large signal-to-noise. From Eq. (4.1), we see that this can be achieved with high Q (i.e., minimal r), and that for a given frequency, it is desirable to minimize the capacitance.

4.5.2 First-stage amplifier construction

The first-stage tuned circuit amplifier, depicted schematically in Fig. 4.8, closely follows the design of the 64 MHz first-stage amplifier used in experiments with a single trapped electron [197], in which feedback cooling of a self-excited axial oscillator was first demonstrated [170]. The amplifier input network centers on the inductor, a hand-wound coil of high-purity silver wire surrounded by an OFE copper cylinder ("amp can"). The geometry is designed to maximize the Q [240]; in particular, the amp can was chosen to have the largest diameter that could fit in the tripod region without interfering with the tube for the positron source. This inductance tunes out the capacitance of the circuit. This capacitance is not just the capacitance between the detection electrode and the adjacent (RF-grounded) electrode ($\sim$1 pF); it also includes other contributions (15–20 pF), including the capacitance of the long lead from the electrode to the feedthrough pin inside the trap can, the capacitance between windings of the inductor, and stray capacitance of components of the circuit, particularly the coaxial lead from the feedthrough pin.

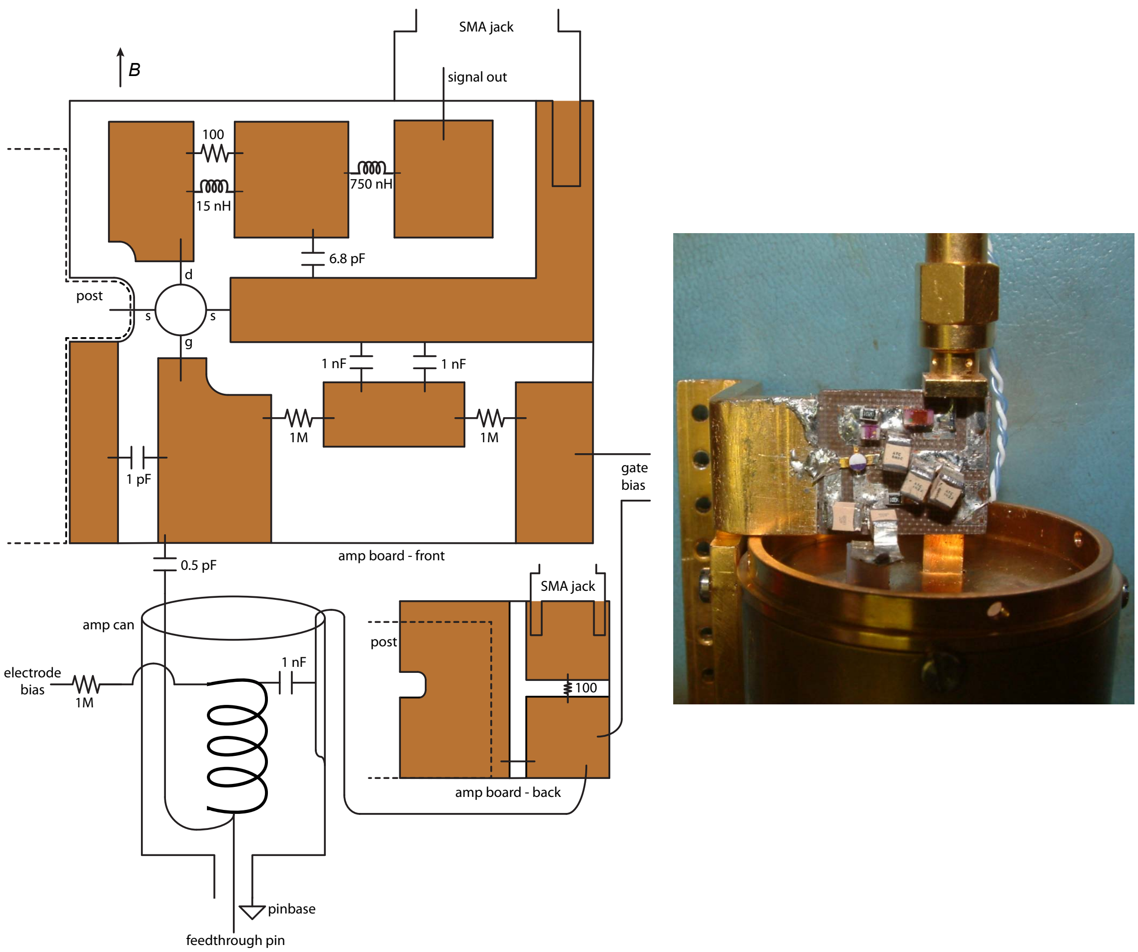

Figure 4.8: Schematics (left) and photograph (right) of the first-stage amplifier circuit board and the connections to the helical resonator and feedthrough. The entire assembly resides in an OFE copper can, of which the upper section, which encloses the circuit board, is shown. The back side of the amp board is drawn in the same orientation as the top of the board, as if seeing through the board.

Gain is provided by a high electron mobility transistor (HEMT),[25] a type of field-effect transistor (FET), and the signal from the particles is capacitively coupled to the FET input so that the electrode and FET gate can be separately biased. To achieve a large Q, Eq. (4.5) shows that it is necessary to avoid introducing any resistance in parallel with the tuned circuit that is the same order or smaller than the effective parallel resistance of the tuned circuit. A capacitive impedance transformer [241, Ch. 2] on the FET gate effectively increases the input impedance of the FET. Similar capacitive dividers are placed on drive lines so that the 50 Ω impedance of the transmission lines does not load down the tuned circuit. A suppression circuit consisting of an inductor and resistor in parallel prevents oscillation since this circuit is lossy at high frequencies [242].

The resulting front-end circuit has $Q \sim 1200$ at low temperature when connected to the trap, as shown in Fig. 4.9. It was previously suggested [197] that the Q could be limited by a long lead from the electrode, and indeed, the Q is diminished by up to a factor of 2 when placed on the trap compared to a test capacitor. However, this large Q is achieved despite having an eight-inch strap from the electrode to the feedthrough pin inside the trap can, plus another three inches of lead that includes the feedthrough and the strap to the amplifier input. The increased Q relative to the 64 MHz amplifier used on a previous electron-trapping experiment may be due primarily to the larger amp can permitted by the larger-diameter magnet bore. The circuit includes surface-mount resistors and inductors and ATC porcelain (P90) microstrip capacitors on a copper-clad teflon/glass substrate, which is less lossy at high frequencies compared to G10 epoxy/glass.

[25] Eudyna (now Sumitomo Electric Device Innovations) FHX13LG

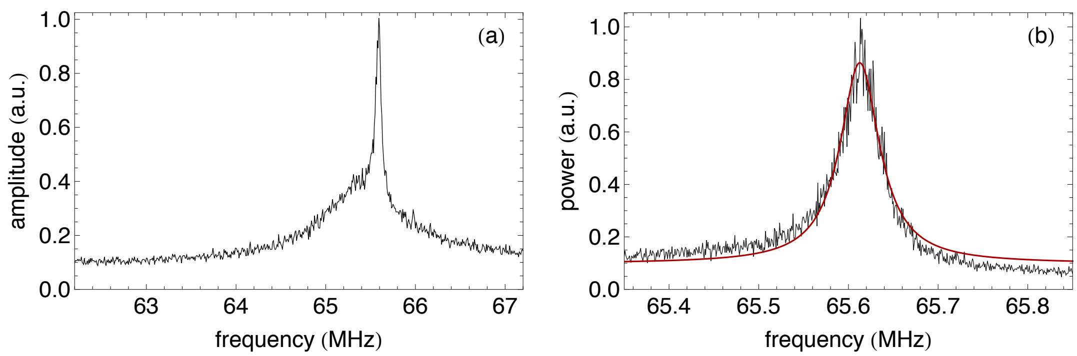

Figure 4.9: Sample amplifier noise resonances on the trap at 4 K. Here the first-stage amplifier is biased so that V_d = 0.3 V and I_d = 167 μA, and the second-stage amplifier is biased so that V_d = 1.0 V and I_d = 127 μA. The fit in (b) is to a Lorentzian with Q = 1200. The slight asymmetry arises because the first-stage front-end resonance is not exactly centered on the second-stage resonance, as is clear from (a). The shape of the noise resonance changes somewhat from 4 K to 100 mK; an example of the latter is shown in the last graph of Fig. 5.2.

The output impedance of the FET ($\sim$kΩ) is matched to a 50 Ω transmission line using a simple LC circuit called an L-network [241, Ch. 4]. The shunt capacitor transforms the real part of the load impedance to a larger value, and the series inductor resonates away the reactance added by the capacitor. The impedance matching network is designed so that its resonant frequency lies slightly below the front-end resonance (see Fig. 4.10) to avoid positive feedback to the input, which would cause regeneration [197].

The axial motion of the particle thermalizes with the detection circuit, so achieving a low temperature requires good heat-sinking to remove the heat dissipated in the FET. This is accomplished by soldering one of the FET source leads to the nearby nub of the silver "post" on which the amplifier board is mounted. Unlike all other

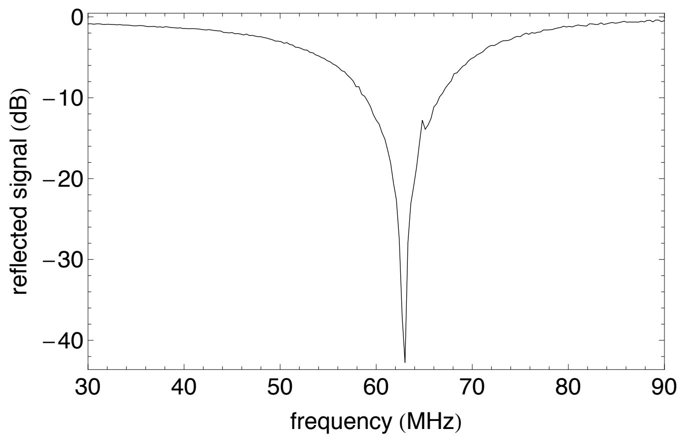

Figure 4.10: Reflection off the output network of the first-stage amplifier at nearly optimal matching, as recorded with a network analyzer. The amplifier is biased to $V_d = 0.3$ V and $I_d = 97$ μA. The front-end resonance is visible 1–2 MHz above the output resonance.

solder joints in the amplifier, this joint is made with a low-temperature solder[26] to avoid damaging the FET [197]. The post is in turn bolted to one of the legs of the tripod to provide a good thermal connection to the mixing chamber. In this case, the post is an L-shape made by twice bending a sheet of $1/8''$-thick annealed silver to enable a larger amp can to fit in the tripod region.[27]

The amp can is connected to pinbase ground via a silver tube soldered into the bottom of the amp can; this forms a coaxial lead from the feedthrough pin that is well shielded except for a small gap near the pinbase. A strap on the inside of the amp can provides a ground connection to the back side of the amp board, which is also soldered to the post.

[26] 52/48 In/Sn

[27] Since the post is large and very thermally conductive, a very large soldering iron was required to get it hot enough for soldering to the back of the amp board with ordinary tin/lead solder. A Wall Lenk LG550 soldering gun was effective for this purpose.

4.5.3 Second-stage amplifier

The axial signal is further amplified by a second cryogenic amplifier. The signal is attenuated as it travels along long stainless steel microcoax cables. The second stage amplifier counteracts this loss and boosts the signal above the noise floor of the first room-temperature amplifier. Furthermore, the second-stage amplifier reduces the effective temperature of the tuned circuit by reducing the temperature of the first-stage amplifier load [134].

The second-stage amplifier used in the present work is the same as the 64 MHz amplifier used previously; the circuit diagram is shown in Fig. 4.6, and a layout schematic and further details can be found in [197, Sec. 4.3.4]. The input network of the second-stage amplifier is a three-element impedance-matching network, known as a π-network [241], which is designed to match the 50 Ω impedance of the transmission line to the 20 kΩ resistor in parallel with the FET input. The capacitor in the input network was changed from the value used in Ref. [197] to shift the resonant frequency so that it is better aligned with the first-stage front-end resonance.

4.6 RF Detection

After the second-stage cryogenic amplifier, the signal passes through a commercial bandpass filter[28] and broadband amplifiers[29] and can then be detected on a spectrum analyzer. The signal is then mixed down to ~5 MHz, passed through narrow crystal filters and further amplified, and finally mixed down to 4965 Hz where it can be

[28] Minicircuits BBP-60
[29] Miteq AU-1464-BNC

viewed on a signal analyzer[30] and recorded with a PC data acquisition card,[31] which functions like a low-frequency lock-in amplifier. A full schematic is shown in Fig. 4.11.

Drive lines are in place to apply an oscillating voltage to an electrode; trapped particles experience an oscillating electric field that drives them to larger amplitudes, creating a larger signal. Drives originate from frequency synthesizers,[32] are controlled by RF switches,[33] and travel from the "hat" to the pinbase on microcoax lines, as described in Sec. 4.3, to minimize attenuation of high-frequency signals.

The drive can be picked up directly by the amplifier, drowning out the signal from a single electron. To limit this feedthrough, we apply drives at two different frequencies [3]: a drive at $\nu_1 = 4.995$ MHz modulates the trapping potential, and a drive on the sideband at $\nu_z - 4.995$ MHz excites the electrons' axial motion. The resulting amplitude is smaller (compared to a drive of the same strength applied directly at the axial frequency ω_z) by a factor of $\beta/2$, where

$$\beta = \frac{\epsilon\omega_z}{2\omega_1}, \tag{4.6}$$

and the modulation strength ϵ is defined by the replacement of ω_z^2 in the equation of motion by $\omega_z^2(1+\epsilon\cos(\omega_1 t))$ and is roughly proportional to the strength of the 4.995 MHz drive [120, Sec. III.C].

The feedthrough of the drive to the amplifier is greatly reduced by applying drives that are outside the passband of the front end of the amplifier. However, the non-linear response of the FET mixes together the two drives, and feedthrough at ν_z can still be seen for strong enough drives. To reduce the feedthrough further, we use a

[30] HP 3561A
[31] National Instruments PCI-4454
[32] SRS DS345 (4.995 MHz), Programmed Test Sources PTS-250 (all others)
[33] HP 8765A RF switches, controlled with an HP 87130A switch driver

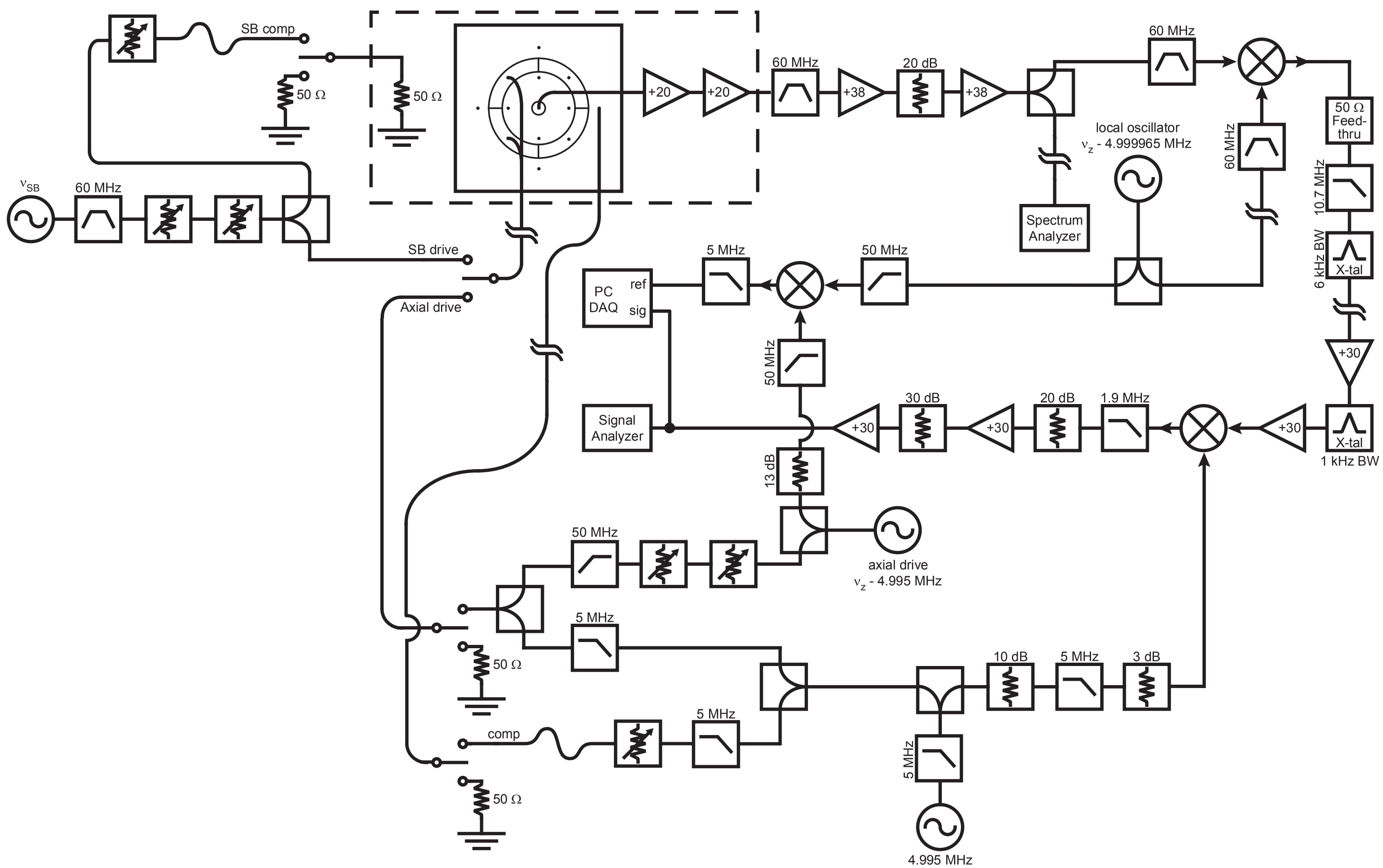

Figure 4.11: Radiofrequency schematic for driving electrons and detecting their axial motion. The dashed region indicates the cryogenic part of the experiment, which is further detailed in Fig. 4.6. The detection chain from the 50 Ω feedthrough to the DAQ and signal analyzer is shared with and identical to that used for the electron/positron experiment (see Ref. [8, Fig. 2.6]).

compensated drive scheme, in which a drive is applied to two different electrodes. The relative drive strengths and phases are adjusted so that the feedthrough from one drive to the amplifier is cancelled by the feedthrough from the other drive. It is important that the drives not cancel out at the particle, although the effective drive strength may be reduced.

In this experiment, drives can be applied either to the fourth electrode or to half of the third electrode. An axial drive applied to the fourth electrode should produce a stronger oscillating electric field at the particle (see Table 4.2), but better driven signals were achieved by driving on the third electrode. The fourth electrode was

	I	II	III	IV
e3	22.6	34.7	34.6	39.1
half of e3	11.3	17.4	17.3	19.5
e4	40.4	48.6	48.6	51.3

Table 4.2: Electric field magnitude in V/m at the trap center (for each of the four values of z_0 from Table 2.6) resulting from 1 V applied to the indicated electrode (see Eq. (2.64)). The displayed values are $C_{1i}/(2\rho_1)$, as defined in Eq. (2.14). Electrode e4 extends from ρ_3 to ρ_c.

used to apply a compensation drive at 4.995 MHz. The split third electrode is used for cooling or heating the magnetron motion. Since the magnetron frequency is smaller than the width of the amplifier front-end resonance, a sideband drive (unlike the drives at 4.995 MHz and $\nu - 4.995$ MHz) is strongly amplified. A strong sideband drive can saturate the amplifier, so it is helpful to compensate this drive line as well. The sideband compensation drive is applied to a resistor that lies in the tripod region, intended to couple to the amplifier but not to the particles. The drive and compensation lines are shown schematically in Fig. 4.11.

Chapter 5

Electrons in a Planar Penning Trap

Using the optimized design parameters of Chapter 2 and the traps fabricated as described in Chapter 3, we now present experimental evidence of what seems to be one electron in a planar Penning trap, but is certainly a very small number. Sensitive radiofrequency detection methods from cylindrical Penning traps are demonstrated for the first time in planar Penning traps. The anharmonicity of the trap is substantially reduced by applying the tuning procedure developed in Sec. 2.5.4. This produces better stability and narrower resonances that in turn enable loading a small number of particles. The measured resonances are more than four orders of magnitude narrower than resonances reported in Mainz and Ulm, which were estimated to be broader than 1 MHz [144, 146], and substantially narrower than the $\sim$5 kHz width that previous researchers had claimed was the minimum possible width for a millimeter-scale trap [138, 146].[1] The success of these techniques and the broad agreement with the behavior predicted by our theoretical study together suggest that

[1] An axial temperature of 5 K is assumed.

unambiguously detecting a single electron in this apparatus should be possible in the near future with the methods presented here. This in turn points the way toward realizing one-electron qubits in a scalable architecture.

5.1 Detecting Trapped Electrons

The principal method used for detecting trapped electrons in this work is to observe their response to the thermal noise in the detection circuit. The equation for the center-of-mass motion of N particles in a harmonic trapping potential between the plates of a capacitor (the trap capacitance) can be recast as the expression for an LC series circuit with an inductance and capacitance given by [243]

$$\ell_{\mathrm{p}} = \frac{m}{N}\left(\frac{2\rho_1}{qD_1}\right)^2, \tag{5.1}$$

$$c_{\mathrm{p}} = \frac{N}{\ell_{\mathrm{p}}\omega_z^2}. \tag{5.2}$$

Equation (5.1) can be rewritten in terms of the single-particle damping rate γ_z introduced in Eq. (2.69),

$$\ell_{\mathrm{p}} = \frac{R}{N\gamma_z}, \tag{5.3}$$

where R is the effective parallel resistance of the tuned circuit. The circuit model for the electrons interacting with the tuned circuit of Fig. 4.7 is shown in Fig. 5.1. For $\omega \approx \omega_{LC}$, the resulting power spectrum is described by the lineshape [244]

$$P(\omega) \propto \frac{\omega_{LC}^4(\omega^2-\omega_z^2)^2}{\left[(\omega^2-\omega_z^2)(\omega^2-\omega_{LC}^2)-\omega^2\Gamma N\gamma_z\right]^2+\omega^2\Gamma^2\left[(\omega^2-\omega_z^2)-\Gamma N\gamma_z\right]^2}, \tag{5.4}$$

where ω_{LC} and $\Gamma = \omega_{LC}/Q$ are the center frequency and width, respectively, of the tuned circuit (Eq. (4.4)).

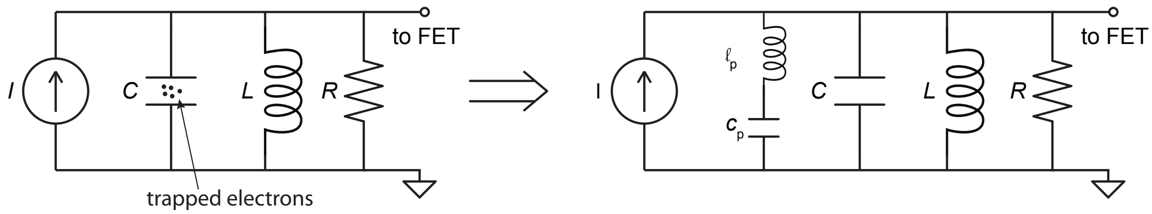

Figure 5.1: Circuit model for trapped electrons with resonant frequency $\omega_z = \sqrt{\ell_\mathrm{p} c_\mathrm{p}}$ coupled to the RLC parallel circuit of Fig. 4.7. At $\omega = \omega_z$, the particles short out the Johnson noise from the tuned circuit.

The lineshape of Eq. (5.4) describes how the amplifier resonance shape is modified by its interaction with trapped particles. The Johnson noise on the detection electrode drives the particles; near resonance, the signal induced by the particles' motion cancels out the noise. The trap potentials are adjusted so that the particles' axial frequency lies on or near the tuned circuit resonance, i.e., $\omega_z \approx \omega_{LC}$. In this case, if there are many particles in the trap, $N\gamma_z \gg \Gamma$, the noise-driven tuned circuit resonance appears not as a Lorentzian but as two peaks separated by $\sqrt{N\gamma_z\Gamma}$. For a small number of particles, the tuned-circuit response has an inverted Lorentzian "dip" centered at ω_z with width $N\gamma_z$. The particles effectively short out the noise at $\omega = \omega_z$, as can be seen intuitively from the LC series circuit model (Fig. 5.1). Since the width of a narrow dip is proportional to N, the width gives an indication of the number of particles in the trap. Dips observed in a planar Penning trap are shown in Fig. 5.2. Dips were not observed in previous experiments with planar Penning traps at Mainz and Ulm [144,146], and the first observation of trapped electrons at Harvard revealed a resonance narrower than had been observed in either of those earlier experiments.

An attractive feature of planar Penning traps is that they have a tunable damping width γ_z. The minimum of the axial potential can be moved closer to and farther away

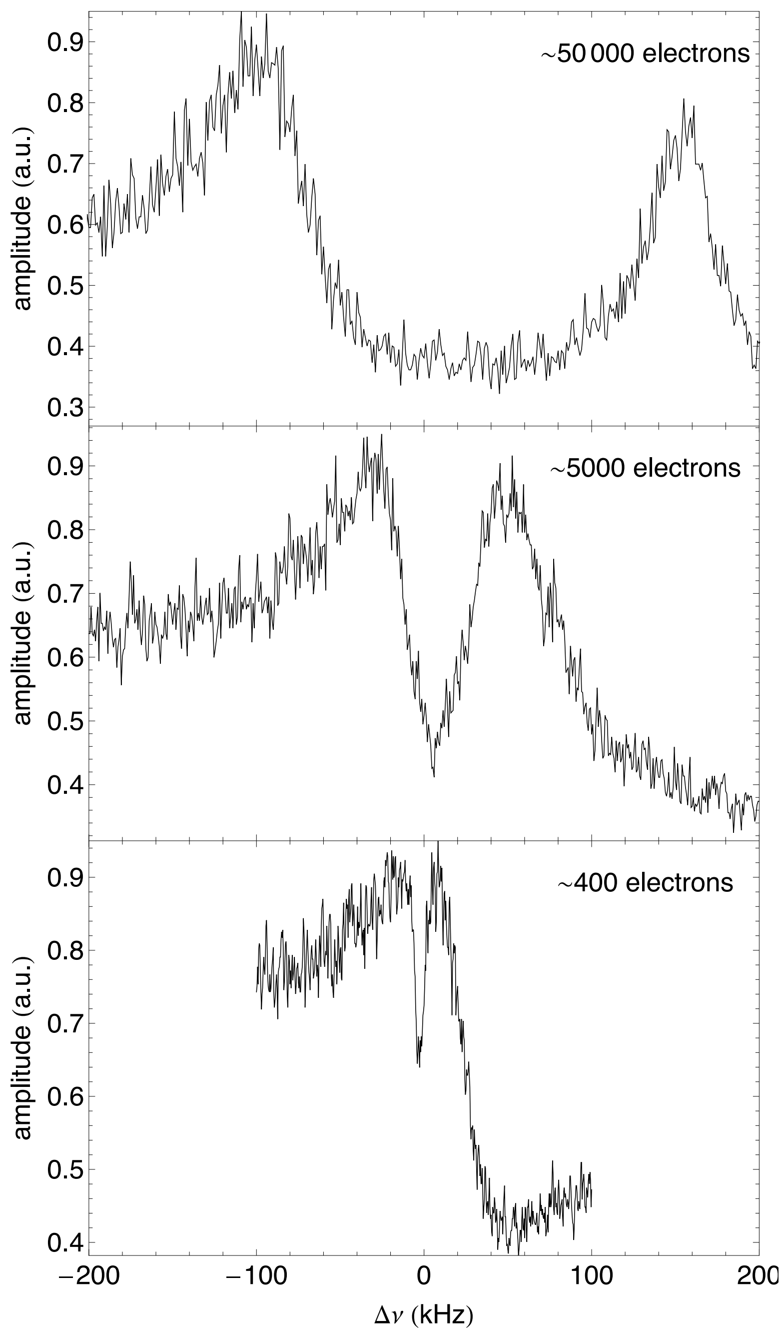

Figure 5.2: Dips from successively smaller clouds loaded into a planar Penning trap. The amplifier noise resonances differ from the $N \sim 50000$ and $N \sim 5000$ dips to the $N \sim 400$ dip because the former were recorded at 4 K while the latter was recorded at 100 mK. Narrower dips are shown in subsequent figures.

from the electrode plane, resulting in stronger or weaker coupling to the detection circuit, as shown in Fig. 2.17, and hence larger or smaller γ_z. Values of γ_z are given in Table 5.1 for the four optimized configurations from Table 2.6; however, γ_z and z_0 can be made to vary continuously between these values.

	I	II	III	IV
z_0	2.58 mm	1.56 mm	1.57 mm	1.12 mm
$\gamma_z/(2\pi)$	1.7 Hz	16.7 Hz	16.2 Hz	55.5 Hz
Trap depth	6.0 V	1.2 V	1.2 V	0.6 V

Table 5.1: Calculated properties of the four optimized potentials from Table 2.6, scaled so that $\nu_z = 66.21$ MHz. The damping width is for detection on the center electrode with a damping resistance of 126 kΩ. Dimensional changes from thermal contraction are estimated to change these values by less than 1%.

We have demonstrated this tunable damping in a planar Penning trap, varying the dip width by more than an order of magnitude for the same cloud; an example is shown in Fig. 5.3. This feature offers a possibility for detecting small numbers of particles because the damping width for a single particle could exceed the anharmonic width even when the trap is not optimally tuned. The large damping width is what enabled the detection of very small numbers of particles, as described in Sec. 5.5.

It is important to note that while increasing the damping by varying z_0 may allow improved detection by achieving a damping width that exceeds the anharmonic width Δf_z,

$$\frac{\Delta\omega_z}{\omega_z} \approx |a_2| \frac{k_B T_z}{\frac{1}{2} m {\omega_z}^2 {\rho_1}^2}, \tag{2.36}$$

it does not improve the signal-to-noise for dips because the detection bandwidth must

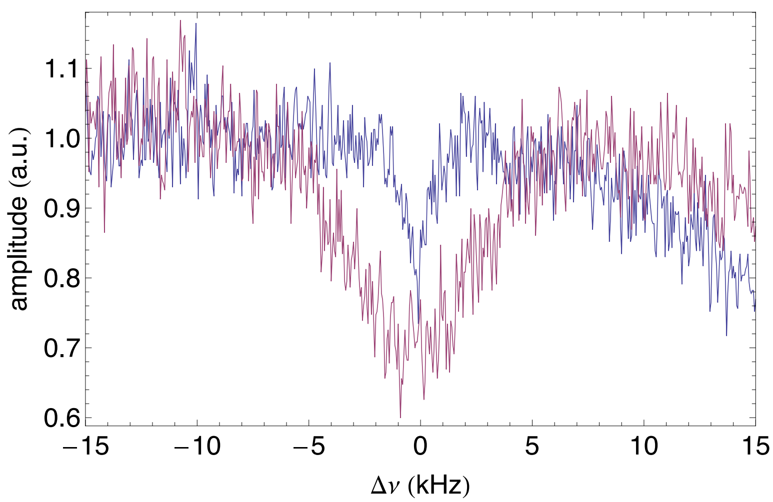

Figure 5.3: Dips from the same cloud of particles in two different potentials. The damping width changes dramatically as z_0 changes. These examples have calculated z_0 values of 1.57 mm (red curve) and 2.62 mm (blue curve), with calculated single-particle damping widths $\gamma_z/(2\pi)$ of 16.2 Hz and 1.5 Hz, respectively. Fitting the measured dips to inverted Lorentzians yields widths of 6.2 kHz and 600 Hz, respectively. The observed dip width continues to widen or narrow as the potentials are adjusted to vary z_0 over an even wider range.

be increased in order to resolve the broader dip. The induced voltage,

$$V_I = \frac{qD_1}{2\rho_1} R\dot{z}, \tag{2.68}$$

is proportional to the factor D_1 that describes the coupling to the detection electrode. The detection bandwidth B must be increased in proportion to the damping, and the damping rate

$$\gamma_z = \left(\frac{qD_1}{2\rho_1}\right)^2 \frac{R}{m} \tag{2.69}$$

is proportional to D_1^2. Thus, the Johnson noise voltage $V_N \propto \sqrt{B} \propto \sqrt{\gamma_z} \propto D_1$, and it is evident that the scaling is the same for the signal and the noise.[2]

Although dips are the primary method of detection used in this work, we also detect the particles response to an axial drive applied to one of the electrodes (Sec. 5.3.2), and we detect the axial excitation when we drive a sideband of the axial motion to cool the magnetron motion (Sec. 5.4).

5.2 Loading Electrons

Careful loading procedures are essential for stable operation of a planar Penning trap. Even though great care has been taken to fabricate trap electrodes with minimal exposed insulator, it is important to prevent stray charge from reaching the insulator in the course of loading particles into the trap or dumping them out.

Electrons are loaded by applying a large negative voltage to the FEP as described in Sec. 4.1. To avoid unwanted charging, it is important to use the lowest possible

[2] Increasing the damping by increasing the amplifier Q (and hence the effective parallel resistance R), however, does improve the signal-to-noise, as noted in Sec. 4.5.1, because $\gamma_z \propto R$; whereas for the amplifier coupling, the scaling is $\gamma_z \propto D_1^2$.

current. The axial frequency has been observed to drift after loading particles,[3] with very large drifts occurring for large clouds loaded at higher currents (tens of kHz/hour, and even more than that within the first minutes after loading) and much smaller drifts observed for very small clouds (100 Hz/hour or less).[4] The FEP current required to trap a detectable number of particles has rapidly decreased as we have gained experience trapping electrons in a planar Penning trap. Our earliest experiments used a large current (20–25 nA) for 90 seconds to load a large cloud and detect a trapped particle signal for the first time. This turns out to be much more than necessary, even to load very many particles (e.g., the 50,000-particle cloud in Fig. 5.2 was loaded at 8 nA for 10 seconds), and after loading at such large currents, the dip center drifted by 10–20 kHz/hour. The 5,000-particle cloud of Fig. 5.2 was loaded with 10 seconds at ∼100 pA, which is the lower limit of our detection sensitivity by monitoring the voltage across a 1 MΩ sense resistor with a handheld multimeter. Small clouds are loaded for 60 seconds at currents well below 100 pA. The axial frequency is adjusted by changing all of the potentials by a common scaling factor so that they remain in proportion to each other. The amount by which the potentials must be adjusted in order to observe a dip centered on the amplifier depends strongly on the cloud size, likely due to accumulated stray charges, but possibly also from space charge effects. As a single electron is desired, larger particle numbers were useful only for initially finding a resonance until smaller, more stable resonances were established.

[3] This has been observed in our group even in one experiment with a cylindrical trap that had no insulator that could be "seen" from inside the trapping volume.

[4] The drift was also observed to be greater in potentials with smaller values of z_0, although it is not known whether this is because of the proximity to stray charges on insulating surfaces or whether it is related somehow to the increased damping experienced in these potentials.

A good procedure is also essential for emptying the trap when desired.[5] We ensure that charge is not deposited on insulating surfaces by biasing all three electrodes to −10 V, creating a potential hill that the electrons roll down as they follow magnetic field lines and strike the conducting trap enclosure (Fig. 4.2). The FEP is also biased to +18 V to attract any electrons escaping through the small hole in the opposite end of the enclosure.

The loading efficiency depends on the choice of potentials used because a deep potential well collects more particles than a shallow one. For each of the four optimized harmonic potentials (Table 5.1), the potential on axis is plotted in Fig. 5.4; it is evident that configuration I produces the greatest trap depth because particles with up to about 5 V above the potential minimum can remain in the trap without striking the center electrode at $z = 0$. When doing experiments in shallow potential wells, electrons are first loaded into a deeper potential well and subsequently the potentials are changed to produce the shallower well. For example, we have observed that for a sufficiently small FEP current, loading directly into configuration III yields no trapped particles at all, but it is possible to load a small number of particles into configuration III by loading at the same FEP current into configuration I and then changing the potentials.

To further protect the gap between the center electrode and second electrode from stray charges, a few attempts were made to load into a potential for which $V_1 - V_2$ is large and positive (e.g., $V_i = \{45, 0, 165\}$ volts) and then transfer to a more harmonic potential. Even though particles could be transferred into such a potential and back,

[5] We have observed that simply setting the electrode biases to 0 V and then restoring them to their original values sometimes results in electrons remaining in the trap.

loading into this potential at the same FEP current yielded no trapped particles.

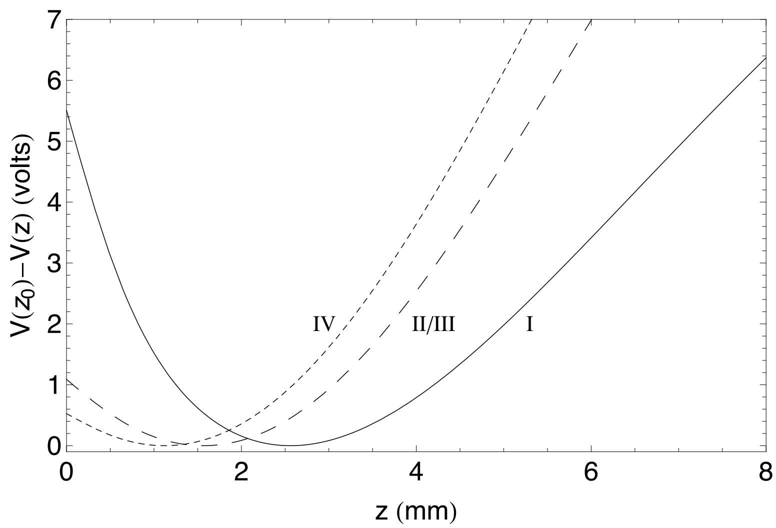

Figure 5.4: The potential on axis for the three sets of biases in Table 2.2. Any particles reaching the electrode plane at $z = 0$ are lost from the trap. The larger trap depth of configuration I is evident.

5.3 Tuning the Trap

Although the trap was carefully designed to minimize the effects of anharmonic terms in the electrostatic potential, inevitable imperfections result in some residual anharmonicity when the calculated optimized trap potentials are applied (see Sec. 2.5.3). It is necessary to tune the trap *in situ* by adjusting the potentials to make the trap more harmonic (see Sec. 2.5.4).

There are different ways of measuring how the harmonic properties of the potential change in response to adjustments in the electrode biases. In cylindrical Penning trap experiments, traps are usually tuned by exciting the axial motion of a cloud of particles with an oscillating voltage applied to an endcap or compensation electrode.

This method, discussed in Sec. 5.3.2, produces a larger-amplitude oscillation and thus produces better signal-to-noise, especially for small numbers of electrons. However, the potential in a planar Penning trap prior to tuning is likely to be substantially more anharmonic than the potential in a cylindrical trap before tuning, so large-amplitude oscillations may not produce a useful feedback signal for tuning the trap. Initial tuning can proceed with dips, in which the electrons are driven only by the thermal noise in the tuned circuit. This method, discussed in Sec. 5.3.1, is the one that has been successful in tuning our trap to date.

5.3.1 Dips

A small number of electrons in an ideal harmonic potential would produce a dip described by the lineshape of Eq. (5.4), going all the way to zero power with a width equal to $N\gamma_z$. Electrons in an anharmonic potential will produce a dip that is broader and shallower.[6] To tune a trap with dips, a cloud of electrons is loaded, and the potentials are adjusted until the dip width is minimized and the dip depth is maximized. Tuning the traps with dips has produced a sufficiently harmonic potential to observe a very small number of trapped particles despite the lack of reflection symmetry of the electrodes about the trap center.

When tuning the trap, there are three electrode biases that can be adjusted, but there are only two free parameters because the axial frequency must be held fixed in

[6] A lineshape that generalizes Eq. (5.4) has not been obtained for particles trapped in an anharmonic potential coupled to a tuned circuit. However, since the dip is caused by signal induced by the axial oscillation of particles, the amplitude dependence of the frequency $\omega_z(A)$ will be as described in Sec. 2.2. Thus, the dip due to particles in an anharmonic potential should be well approximated by considering the response to be a dip of width $N\gamma_z$ that is smeared out over Δf_z due to thermal amplitude fluctuations. For a large number of particles, the response may be affected by the coupling between the center-of-mass motion and the internal degrees of freedom.

order to keep the particles resonant with the tuned circuit and observable with the detection electronics. The two free parameters are depicted as ΔV_2 and ΔV_3 along the two axes in Fig. 2.11. Tuning the trap consists of following a path starting from the origin in this two-parameter space.

Varying the potentials will in general change z_0 and hence also γ_z. This will confound attempts to tune the trap by monitoring the dip width. In fact, this was observed in an initial attempt to tune the trap along the path $\Delta V_3 = 0$ (that is, V_1 and V_2 were varied but the axial frequency was kept constant). Starting from potentials with the same values of $\widetilde{V}_i$ as configuration I in Table 2.6, the dip width was observed to decrease monotonically, as shown in Fig. 5.5; this was attributed predominantly to z_0 increasing rather than to $|a_2|$ decreasing. The effect of increasing z_0 is that the damping decreases as the trap center is moved farther away from the detection electrode. The agreement with the expected behavior, however, gave evidence that the dip width was being limited by the damping $N\gamma_z$ rather than by the anharmonic width arising from thermal fluctuations in the axial amplitude.

To tune with dips, therefore, we must add the constraint that z_0 remain constant, which leaves just one remaining free parameter. Besides the damping width, we do not have a way to measure z_0. Thus, we must dead-reckon by relying on the calculated dependence of z_0 upon the electrode bias potentials V_i. In cylindrical traps, the value of the compensation potential V_c that gives $C_4 = 0$ in practice is quite different than the value calculated based on the nominal trap dimensions because the value of V_c that gives the cancellation $C_4 = 0$ depends on the exact dimensions. However, the slope $\partial C_4/\partial V_c$ should depend on the gross dimensions and should be changed only

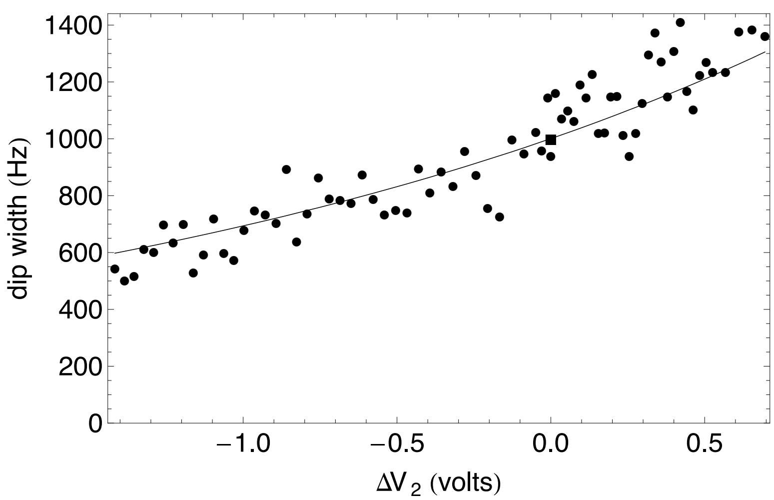

Figure 5.5: The measured dip width varies as V_1 and V_2 are adjusted while V_3 and the axial frequency are held constant. The line gives the damping width $N\gamma_z$, where γ_z is calculated for the potentials used at each point, and the single free parameter $N = 600$ is used for all points. The agreement indicates the validity of the theoretical description and suggests that the observed width is dominated by the N-particle damping width rather than the anharmonic width Δf_z. The square point has $\widetilde{V}_i$ given by column I in Table 2.6.

slightly by the imperfections; in practice, it is measured to be very nearly the same as the calculated value. Similarly, we assume that z_0 may not be the same as the calculated value but the derivatives $\partial z_0/dV_i$ are likely to be reliable. For simplicity,[7] we write the constraint equations for small changes ΔV_i as

$$\Delta\omega_z(\Delta V_1, \Delta V_2, \Delta V_3) \approx \frac{\partial\omega_z}{\partial V_1}\Delta V_1 + \frac{\partial\omega_z}{\partial V_2}\Delta V_2 + \frac{\partial\omega_z}{\partial V_3}\Delta V_3 \stackrel{!}{=} 0, \tag{5.5}$$

$$\Delta z_0(\Delta V_1, \Delta V_2, \Delta V_3) \approx \frac{\partial z_0}{\partial V_1}\Delta V_1 + \frac{\partial z_0}{\partial V_2}\Delta V_2 + \frac{\partial z_0}{\partial V_3}\Delta V_3 \stackrel{!}{=} 0. \tag{5.6}$$

These two equations may be solved to write, for example, ΔV_1 and ΔV_3 in terms of a single free parameter ΔV_2. This corresponds to a path through the parameter space given by the blue curve in Fig. 5.6. If it turned out that the constant-z_0 contour was parallel to the $a_2 = 0$ contour, it would be possible to try to tune the trap with constant z_0 without ever tuning out the lowest-order anharmonic coefficient. However, the constant-z_0 and $a_2 = 0$ contours still intersect for the various sample geometric imprecisions considered in Sec. 2.5.3, so the procedure is expected to work. Of course, by relying on the calculated values of $\partial z_0/\partial V_i$ without an independent way to measure z_0, we will inevitably still wind up changing z_0. As a result of geometric imprecisions, the actual path taken through the two-parameter space will be near but very slightly different from the constant-z_0 contour, but this should not appreciably change the tuning procedure at all. For the sample deviations of the trap radii from their nominal values, the potentials applied at each point in Figs. 5.8 and 5.9 will cause z_0 to change by only a few microns, with a resulting change in γ_z of about 1% or less.

[7] Of course, the exact expressions from Chapter 2 may be used instead of the first-order Taylor series, but for small steps, the error produced by using Eqs. (5.5) and (5.6) is negligible.

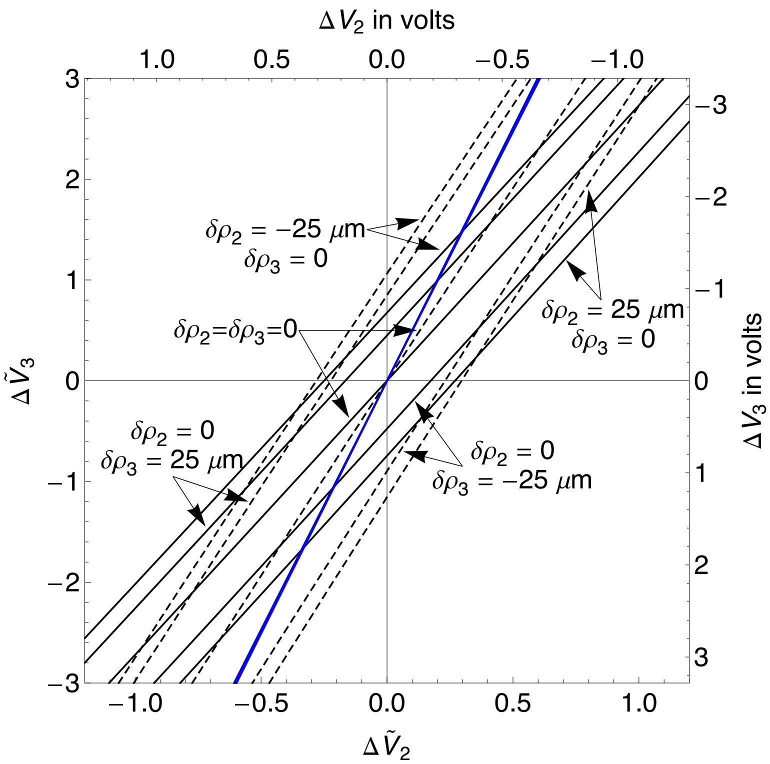

Figure 5.6: Contours of $a_2 = 0$ (black, solid) and $a_4 = 0$ (black, dashed) from Fig. 2.11, overlaid with contours of constant z_0 (blue) for various sample imperfections. The constant-z_0 contours for the sample imperfections are all contained within the thickness of the blue line, indicating that $\partial z_0/\partial V_i$ is not very sensitive to the imperfections.

Fig. 5.7 gives the predicted behavior of the lowest-order anharmonic coefficient a_2 and the corresponding thermal width Δf_z as the potentials are varied with z_0 and ν_z held constant. It is clear that imprecisions in the electrode radii are expected to shift the optimal point ($a_2 = 0$) but are expected not to change the essential behavior. The lowest-order coefficient a_2 varies smoothly, and at the point where it changes sign, the lowest-order approximation to the thermal width is zero; at this point, the width is given simply by the damping $N\gamma_z$. In practice, higher-order anharmonic terms and imperfections other than imprecise radii will result in a finite minimum thermal width, but experiments in cylindrical Penning traps have demonstrated anharmonic widths smaller than the single-particle damping. As mentioned in Sec. 2.4.2, cylindrical traps can achieve $|a_2| \sim 8\times10^{-6}$, which corresponds to a thermal spread of frequencies $\Delta f_z = 0.5$ Hz, smaller than the typical damping width $\gamma_z \sim 1$ Hz.

Tuning a laboratory trap shows results similar to those predicted in Fig. 5.7. A minimum in the axial width is indeed observed, as shown in Figs. 5.8 and 5.9.

The tuning procedure consists of choosing a step size ΔV_2, calculating ΔV_1 and ΔV_3 required to satisfy Eqs. 5.5 and 5.6,[8] and applying those potentials to the electrodes. The calculated changes to the potentials still result in a small change in the axial frequency, observed as the dip shifting on the spectrum analyzer. To correct for this, the three potentials are then scaled by a constant factor to bring the axial frequency back to its original value without further changing z_0. This procedure was carried out using two starting points, one each near configurations I and III from Table 2.6, with the results shown in Figs. 5.8 and 5.9, respectively. The narrowing

[8]The quantities $\partial\omega_z/dV_i$ and $\partial z_0/dV_i$ depend on the three potentials V_i, so they must be recalculated at each step in the tuning procedure.

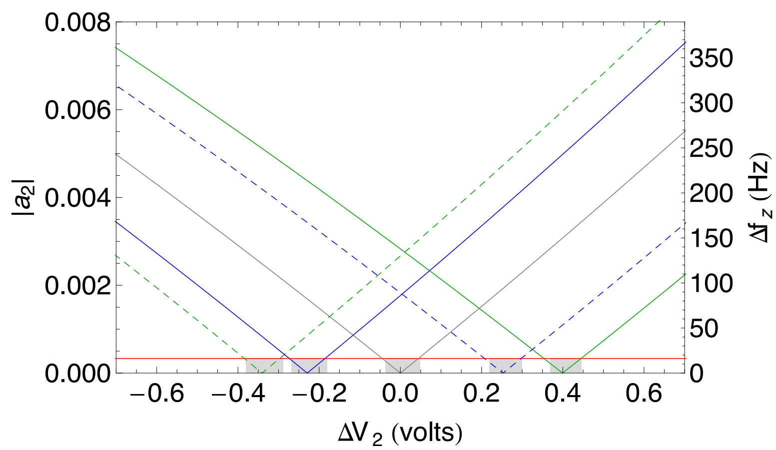

Figure 5.7: The calculated behavior of a_2 for the sample trap if all three trap potentials are varied with z_0 and ω_z held constant. The gray curve is the sample trap of Tables 2.1 and 2.2, and here we consider the potentials of column III. The other curves correspond to the sample imperfections of Table 2.7, with ρ_2 (green) or ρ_3 (blue) smaller (dashed) or larger (solid) by 25 μm. For ease of computation, the infinite boundary conditions are used. The potentials are scaled so that $\nu_z = 66.21$ MHz, and Δf_z is for a temperature of 5 K. The red line indicates the value of a_2 for which $\Delta f_z = \gamma_z/(2\pi) = 16.2$ for this set of potentials, with the shaded boxes showing the region of ΔV_2 for which a_2 is less than this value.

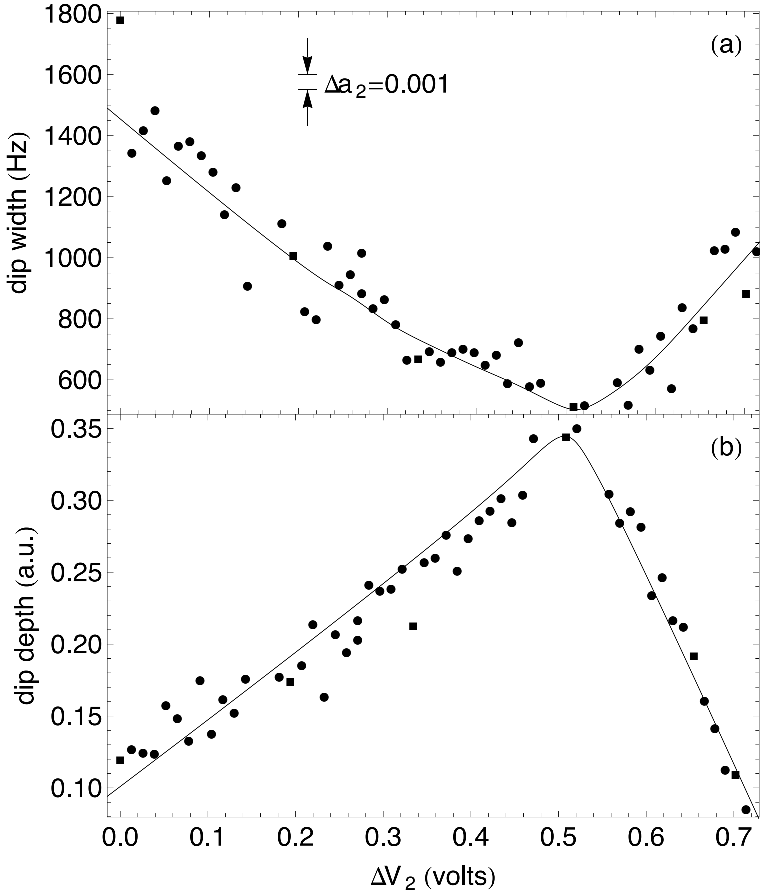

Figure 5.8: (a) Dip width and (b) dip depth for one cloud of electrons as the trap is tuned by varying the three trap potentials so that the observed axial frequency (dip center) and calculated value of z_0 remain constant. A smooth curve is drawn by hand. The starting point is a set of potentials with $\widetilde{V}_i$ near those in column I of Table 2.6. For points marked with squares, sample dips are displayed in Fig. 5.10. The y-axis units in (b) are the same as those in Fig. 5.10. The axial frequency is $\nu_z = 66.045$ MHz. The thermal frequency width arising from a given size of a_2 is indicated (Eq. (2.36)).

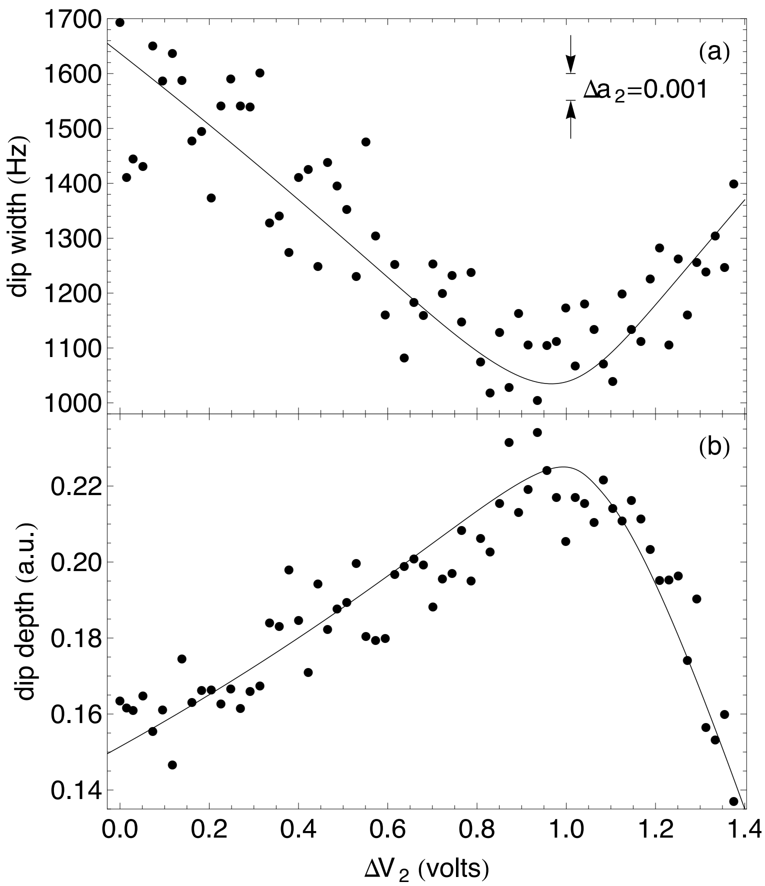

Figure 5.9: (a) Dip width and (b) dip depth as the trap is tuned starting from a set of potentials with $\widetilde{V}_i$ very nearly the same as those in column III of Table 2.6. A smooth curve is drawn by hand. The axial frequency is $\nu_z = 66.210$ MHz. The thermal frequency width arising from a given size of a_2 is indicated (Eq. (2.36)).

is clearly illustrated by the sample dips in Fig. 5.10. Tuning is best accomplished by loading the smallest cloud of electrons for which the dip can be resolved well enough that shifts can be easily followed and its center can be reliably identified by an automated fitting routine. As the trap tuning is improved, it is possible to resolve dips from smaller numbers of trapped electrons.

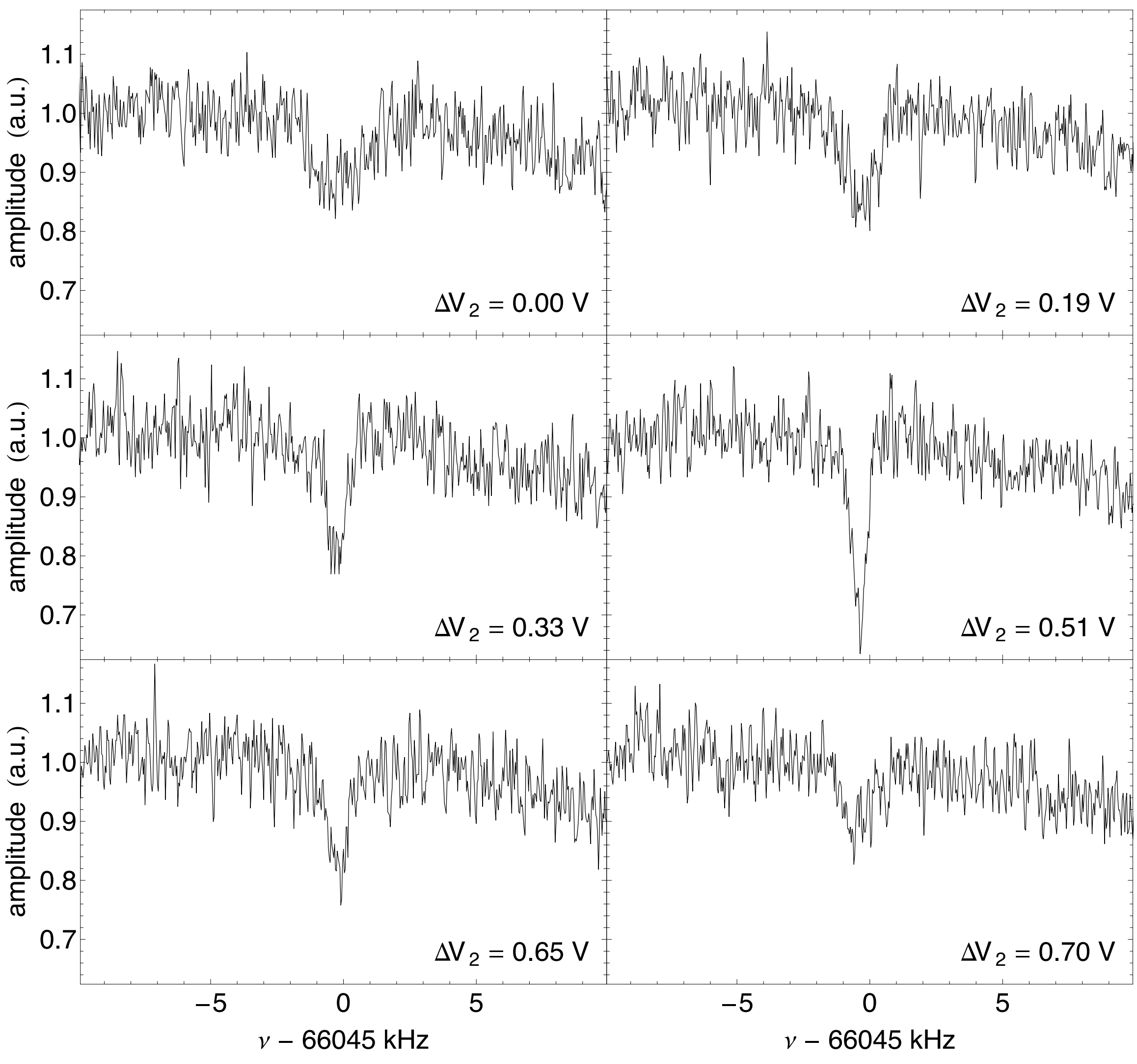

Figure 5.10: Dips are observed to narrow and deepen as the trap is tuned to reduce the anharmonic terms in the electrostatic potential. The sample dips correspond to the six points marked with squares in Fig. 5.8.

It is not known exactly how much residual anharmonicity will still permit resolving a single-electron dip, but we can expect that at a minimum, we must achieve $\Delta f_z < \gamma_z/(2\pi)$. For $\gamma_z/(2\pi) = 16.2$ Hz, we require $a_2 < 0.00033$.[9] From Fig. 5.7, we see that for the sample imperfections, this corresponds to a 75–100 mV window of ΔV_2 (shaded boxes in Fig. 5.7), with calculated ΔV_1 about the same size but with opposite sign and ΔV_3 about five times larger.

5.3.2 Driven signals

Trapped electrons can also be probed by applying an oscillating potential to one of the electrodes to increase the amplitude of oscillation. This has two principal advantages: (1) the signal-to-noise can be increased by driving the particles to large amplitudes, and (2) the shape of the driven response is sensitive to the harmonic properties of the trapping potential and thus can be used to tune out anharmonicities. This method is generally used to tune out the anharmonicity in cylindrical traps, but so far it has proven less successful for tuning planar Penning traps.

A theoretical description of the driven lineshape follows from adding forcing and damping terms to the equation of motion, Eq. (2.21),

$$\frac{d^2}{dt^2}u + \lambda\gamma_z\frac{d}{dt}u + (\omega_z)^2 u + \lambda\,(\omega_z)^2\sum_{k=3}^{\infty}\frac{kC_k}{2}u^{k-1} = \lambda f_0\cos(\omega t+\delta), \tag{5.7}$$

where f_0 is the strength of the drive applied at frequency ω and δ is the relative phase of the drive and the response. This equation of motion can then be solved perturbatively using the same method as in Sec. 2.2 (see, e.g., Ref. [169]). In the

[9] This can be compared to the tuning achieved in cylindrical traps, $|a_2| = 8\times10^{-6}$, as stated in Sec. 2.4.2. There is no discrepancy because here we are considering a damping rate γ_z that is 16 times larger, and cylindrical traps typically achieve $\Delta f_z \lesssim \frac{1}{2}\gamma_z/(2\pi)$.

absence of damping, the leading-order solution for the response curve is

$$\omega^2 = \omega_z^2 \left(1 + 2a_2 \widetilde{A}^2 - \frac{f_0}{\omega_z^2 \widetilde{A}} \right), \tag{5.8}$$

where a_2 parametrizes the lowest-order dependence of the axial frequency upon the axial amplitude and is related to the anharmonic terms in the potential by Eq. (2.24a). When damping is included, the solution has the same form except with the replacement $f_0 \to \sqrt{f_0^2 - (\omega_z \gamma_z \widetilde{A})^2}$.

Sample response curves are given in Fig. 5.11 for the axial frequency and damping used in these experiments and for various values of a_2, expressed in terms of the corresponding thermal width Δf_z (Eq. (2.36)). Due to the triple-valued region, this observed response will be different between upward and downward sweeps of the drive frequency through the resonance. The branches of the driven response curve straddle the lowest-order $\omega_z(A)$ curve for free oscillations (Eq. (2.23)), $\omega_z(\widetilde{A}) = \omega_z(1 + a_2\widetilde{A}^2)$. The dashed lines in Fig. 5.11 are essentially just the frequency-versus-amplitude curves of Fig. 2.4 with the axes transposed. Thus, the amplitude dependence of the frequency is minimized by adjusting the potentials until the driven response is made to be as symmetric as possible.

The characteristic hysteresis of an anharmonic driven response has now been observed in planar Penning traps, as shown in Fig. 5.12. However, tuning with driven resonances has not yet been investigated in sufficient detail. When cylindrical traps are tuned, the asymmetric driven resonance is observed to be tilted in one direction and then the other as the compensation voltage is varied through an optimal point and a_2 changes sign. When tuning planar Penning traps with dips, driven resonances were measured with sample potentials drawn from points that appeared well tuned

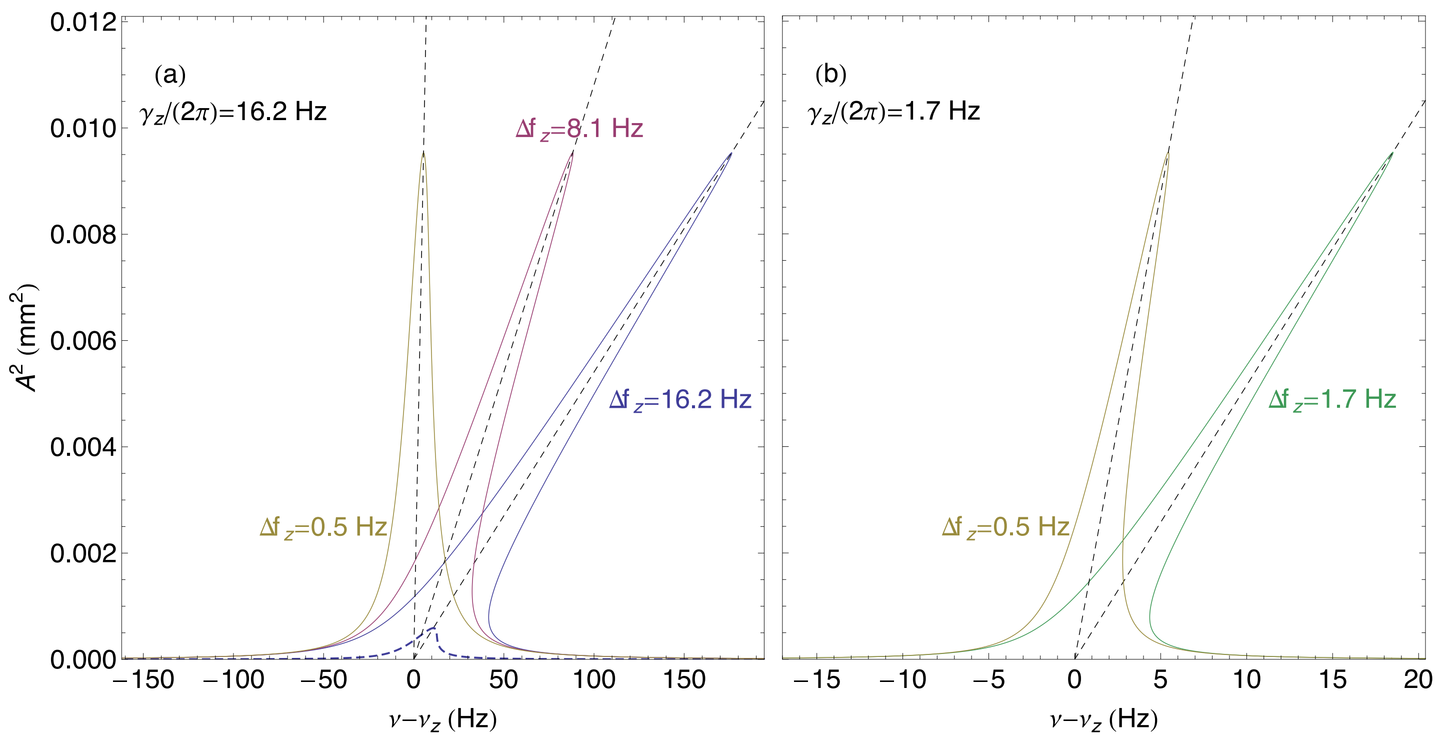

Figure 5.11: Theoretical driven lineshapes for (a) potential III and (b) potential I from Table 5.1. The thermal width Δf_z is related to the anharmonic coefficient a_2 by Eq. (2.36), assuming an axial temperature of 5 K. The dashed black curves are $\omega_z(A)$ for free oscillations, the lowest-order term from Eq. (2.23). An amplitude of 0.1 mm has been used in cylindrical trap experiments, as mentioned in Sec. 2.4.7. For comparison, the dashed blue curve gives the same size signal as the solid blue curve due to the increased damping.

or poorly tuned, as shown in Fig. 5.8. At a well-tuned point, a clear, symmetric resonance was observed with a width comparable to the measured dip width. At the poorly tuned points, however, the driven resonance did not show the expected hysteresis but was substantially broadened.

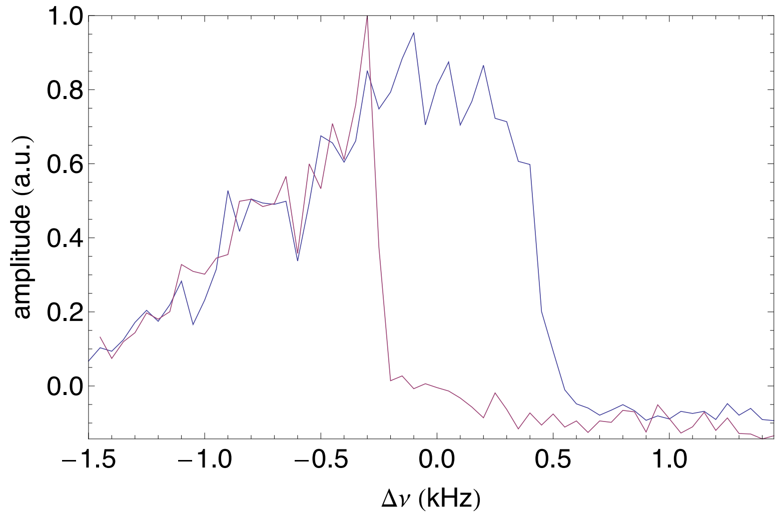

Figure 5.12: A driven resonance of trapped electrons showing the characteristic hysteresis of an anharmonic resonance. The blue and red curves are, respectively, responses to an upward sweep and a downward sweep of the drive frequency.

The driven method is experimentally more challenging when a potential is used with a larger value of D_1 and hence γ_z. It is easily seen from solving the equation of motion for a driven, damped harmonic oscillator that the oscillation amplitude at resonance is inversely proportional to γ_z. Thus, if γ_z is increased, then the drive strength must be increased by the same factor to reach the same amplitude and see the same shape of the anharmonic resonance for tuning the trap. The advantage of larger damping is that a larger signal will result from the same oscillation amplitude since the induced current (Eq. (2.68)) is proportional to D_1. The disadvantage is that it is much harder to prevent the larger drive from feeding through to the amplifier.

The feedthrough compensation was sufficiently tuned to observe resonances like those in Fig. 5.12 for potentials with an estimated single-particle damping of $\gamma_z/(2\pi) \approx 1.7$ Hz. When working with a potential with 10 times larger damping (configurations II and III from Table 5.1), a drive of 20 dB stronger is required to reach the same signal amplitude. Driven signals from very small numbers of particles can still be observed but on top of a baseline of direct feedthrough to the amplifier.

In the future, tuning with driven responses could potentially be more versatile since it is not necessarily subject to being confounded by changes in γ_z as the potentials are adjusted to tune out a_2. And if γ_z need not be kept constant while tuning, then it is possible to tune by adjusting either of two free parameters, and in principle, a more harmonic potential could be obtained. When tuning with driven signals, the sign of a_2 can be determined from the direction in which the response is skewed, so that an optimal point can be bracketed by points where the response is slanted in opposite directions. However, it may still be difficult to measure small changes in a_2: even though the shape of the free-oscillation curve does not depend on γ_z, if γ_z is varied, then a different amplitude will result for the same drive strength, and the shape of the driven resonance will consequently change as well.

5.4 Reducing the Magnetron Radius

To stabilize the axial resonance, it is imperative to ensure that electrons remain radially centered. Motion strictly along the z-axis is also assumed in protocols for quantum gates (e.g., Ref. [161]). The magnetron motion is described by the Hamiltonian of an inverted harmonic oscillator, Eq. (1.4), which corresponds to orbits around a radial potential hill. The motion is unstable, and reducing the energy of the magnetron mode increases its radius without bound. Although the radiative damping rate is negligible, noise can heat[10] the magnetron motion, and in general particles loaded into the trap are initially in some unknown and potentially large magnetron orbit. Cooling the magnetron motion is therefore required in order to detect a single electron and to realize a one-electron qubit.

Magnetron cooling is accomplished by driving a sideband of the axial motion (hereafter called simply "sideband cooling") [120, Sec. IV]. The axial and magnetron motions can be simultaneously excited by applying a drive at $\nu_z + \nu_m$ with appropriate geometry to drive both motions. In this experiment, the third electrode is segmented so that an oscillating voltage applied to an adjacent pair of the four segments (Fig. 5.13) will produce an oscillating electric field $E_d \propto xz\cos(\omega t)$ at the trap center. When the magnetron quantum number is larger than the axial quantum number, the rate for simultaneously cooling the magnetron motion and heating the axial motion exceeds the rate for the reverse process, so the magnetron radius is reduced until the quantum numbers are equal. The heated axial motion is damped by the tuned circuit.

In a planar Penning trap, sideband cooling is, if anything, even more important due to the comparatively larger anharmonicity. In this case, we must consider the radial terms in the potential, which are given by Eq. (2.15) with the substitution of

[10] Here we use "heating" to mean increasing the magnetron radius and "cooling" to mean reducing it. The magnetron energy is dominated by the potential energy, so the net energy increases when cooling the magnetron motion, but the kinetic energy decreases (as does the magnetron quantum number) as required. Since the potential hill is just an inverted potential well, zero quanta in the magnetron mode corresponds to the potential energy maximum.

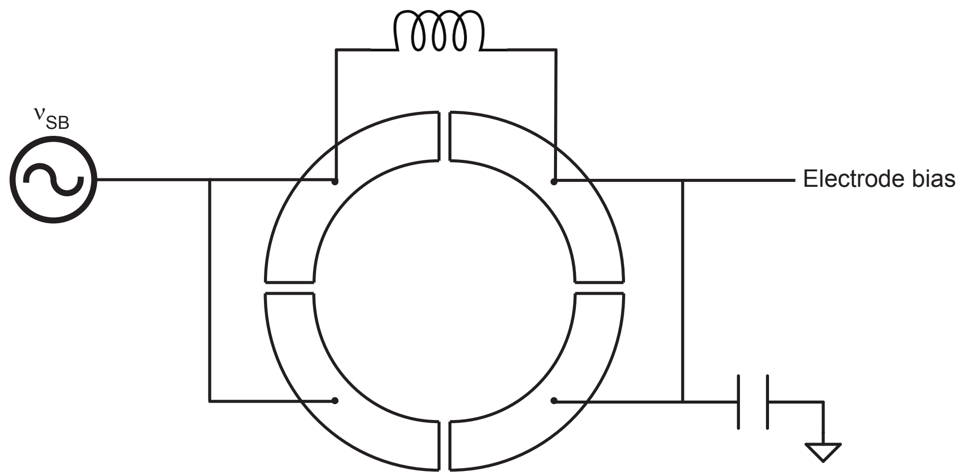

Figure 5.13: Schematic of the sideband drive applied to two segments of the third electrode. The inductor blocks the drive but passes the DC bias.

Eq. (2.3). The lowest-order terms are

$$V(\tilde{\rho},\tilde{z}) - V(0,0) = \frac{1}{2}V_0\left\{C_2\left[(\tilde{z}-\tilde{z}_0)^2 - \frac{1}{2}\tilde{\rho}^2\right] + C_3\left[(\tilde{z}-\tilde{z}_0)^3 - \frac{3}{2}(\tilde{z}-\tilde{z}_0)\tilde{\rho}^2\right]\right.$$
$$\left. + C_4\left[(\tilde{z}-\tilde{z}_0)^4 - 3(\tilde{z}-\tilde{z}_0)^2\tilde{\rho}^2 + \frac{3}{8}\tilde{\rho}^4\right]\right\}. \tag{5.9}$$

The effect of the anharmonicity is that a particle at magnetron radius ρ_m therefore has its axial frequency shifted by

$$\Delta\omega_z^{(m)} = -\frac{3}{2}C_4\tilde{\rho}_m^2\omega_z. \tag{5.10}$$

C_3 does not cause a shift to lowest order because the term proportional to z just shifts the center of the oscillation but not its frequency.

This dependence of the axial frequency upon the radius is observed as a shift in the axial frequency in response to a sideband cooling drive. For the potentials we have used, the shift is generally upward. When a sideband heating drive at $\nu_z - \nu_m$ is applied, the resonance shifts in the opposite direction. In response to either a cooling or heating drive, a narrow peak is observed at a magnetron frequency below the drive frequency (cooling) or a magnetron frequency above the drive frequency (heating), as shown in Fig. 5.14.[11] During or after the voltage ramp, the peak vanishes, which

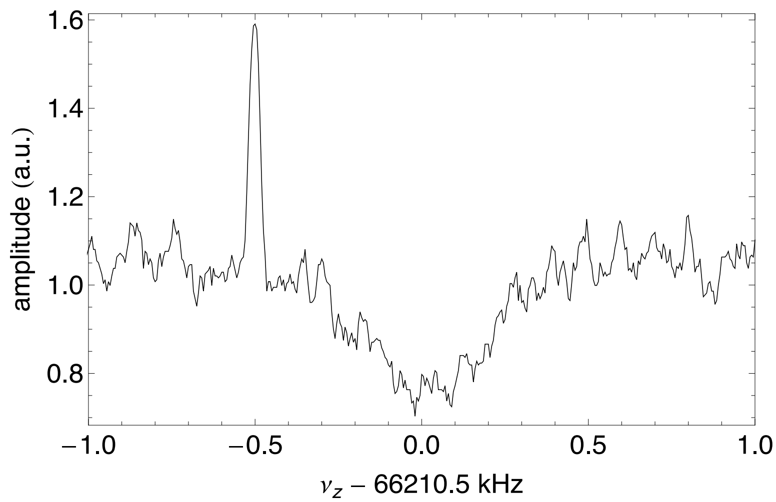

Figure 5.14: A broad dip with a narrow peak from the axial excitation of electrons during sideband cooling of the magnetron motion.

suggests that the magnetron cooling limit has been reached, and the dip does not shift further in response to the drive. This occurs only for sufficiently small clouds; with large numbers of particles, the cooling peak remains, even for strong drives.

After loading electrons into the trap and transferring them to the desired potential, a strong sideband cooling drive is applied. In general, dips narrow and move upward in response to the sideband drive. The potentials are then ramped slowly downward so that the electrons remain resonant with the drive as their axial frequency changes while cooling. Only V_0 is changed; the ratios of the potentials are kept constant so as not to change the harmonic properties of the trap. For a small cloud, typically V_0 must be changed by enough to shift the resonance by about 10 kHz. This shift is

[11] This gives a precise determination of the magnetron frequency. The observed magnetron frequency is 230 Hz smaller than the calculated frequency, most probably because of inaccuracies in estimating the magnetic field at the planar trap center, 4 inches below the center of the magnetic field.

large but not surprising; we expect C_4 to be nonzero even when the trap is well tuned because our tuning procedure leads to minimizing $a_2 = 3C_4/4 - 15C_3^2/16$, rather than C_4 alone, and particles may initially be loaded into some large magnetron orbit.

5.5 One Electron (or a Few)

The above techniques have now enabled detection of a very small number of electrons in a planar Penning trap. The FEP is fired at a low current into a deep well. Particles are then transferred into a potential where their motion will be more strongly damped. Narrow dips can then be observed with sufficient averaging using a narrow resolution bandwidth. The narrowest dip observed in our apparatus to date is shown in Fig. 5.15s. The single-particle damping width $\gamma_z/(2\pi)$ for this potential is estimated to be 16 Hz. Based on this, we would estimate that the dip in Fig. 5.15a may correspond to one electron, or perhaps two.

So far, there is still some oscillation frequency that makes the narrowest dips visible only for short averaging times. The dips become broader at times and are observed to wander within a few hundred Hz over several minutes, which would tend to smear out any narrow features and would explain the flat-bottomed shallow well surrounding the narrow trough in Fig. 5.15a. In addition, because we have no independent way to measure γ_z, conclusively demonstrating that just one electron is trapped requires more than measuring a narrow feature that is approximately the calculated single-particle damping width. A few other methods have been used to demonstrate that a resonance is due to a single electron. Once stable dips are obtained, particles could be loaded and dumped several times and the dip width measured for each trial. If narrow dips had

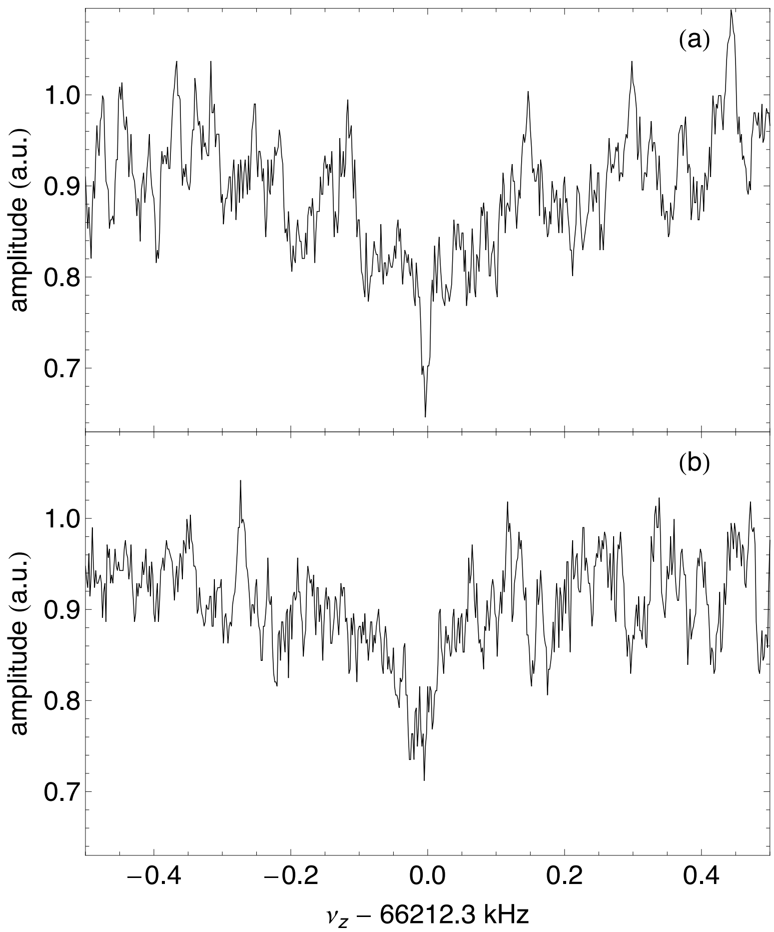

Figure 5.15: (a) The narrowest dip observed in a planar Penning trap. The feature is ∼20 Hz wide and was observed on a spectrum analyzer with 10 Hz RBW and 2 minutes of averaging. (b) A dip for the same cloud recorded with the same parameters 9 minutes later. The narrowest dips appear intermittently and are usually observed at times to become broader and shallower. The single particle damping width for this potential is $\gamma_z/(2\pi) = 16$ Hz, so the narrow dip in (a) suggests that one or perhaps two electrons may be trapped; however, consistently narrow widths of quantized values are needed to demonstrate this conclusively.

widths that were roughly integer multiples of the smallest width observed, the latter could be reasonably claimed as the single-particle damping width. Alternatively, a strong far-off-resonant axial drive could be applied and the signal observed to change in discrete steps; this method was the first used to demonstrate trapping of a single electron in a Penning trap [3].

The prospects for conclusively demonstrating a single trapped electron in the current apparatus are very bright indeed. Two avenues are likely to improve the stability and sensitivity: further tuning, and improved filtering and detection electronics. The aforesaid tuning procedure immediately produced narrower dips, enabled observation of still narrower ones, and improved the stability. Axial drifts were reduced or eliminated, either because of the reduced anharmonicity or the lower FEP currents required to load a detectable cloud of particles, and sideband cooling of the magnetron motion proceeded reliably. The tuning scans of Figs. 5.8 and 5.9 were carried out with clouds estimated to have approximately 350 and 60 particles, respectively, and were not well sideband cooled. It is reasonable to expect that further improvements may be found in the optimal range identified by these sweeps through the tuning parameter space.

We have reason to expect that straightforward improvements of DC biasing and RF driving and detection systems will improve the signal stability and reduce the noise. There is good evidence that there is a source of magnetron heating: if the sideband drive is switched off for even a time as short as one minute, when it is switched back on, an axial excitation peak becomes visible at $\nu_{\text{drive}} - \nu_m$ even when the cloud was fully cooled before shutting off the drive. And over long periods when the drive is off, the dip drifts downward; 10–100 Hz/hour is typical, though this is much less than what was observed with larger clouds and before tuning. Such a drift could be explained by magnetron heating. A likely source is room-temperature Johnson noise from the 50 Ω impedance of the sideband drive line. To avoid exactly this problem, the electron/positron magnetic moment experiment in the same cryostat has a 20 dB cold attenuator at the 1 K pot [242]. Similar attenuators were not yet incorporated into the planar Penning trap apparatus because it was not yet known what drive strength would be required. If the same drive line is to be used for axial drives, this may be a limitation on the axial oscillation amplitude that can be attained for particles in potentials with large γ_z. In addition, further improvements can be made to the axial feedthrough compensation scheme for better sensitivity. With both tuning and detection electronics, further improvements in stability will enable more sensitive adjustments to the tuning and the detection scheme. One other notable apparatus adjustment is that the pinbase will soon be replaced with one that does not have leaky electron-beam welds, removing a faint but lingering doubt about the vacuum in the trap can.

Resonances nearly as narrow as a single-electron dip have now been observed in a planar Penning trap. A very small number of electrons have been demonstrated to be trapped, far fewer than the large but unknown number of electrons, estimated to be between 100 and 1000, previously observed in planar Penning traps. There are clear steps that lead to expect that a single electron can be detected in this apparatus.

Chapter 6

Conclusion and Future Directions

6.1 Progress to Date

A single electron in a Penning trap is an attractive candidate qubit. The observations of one-quantum spin flip and cyclotron transitions of a single electron in a cylindrical trap enabled one of the most precise measurements in physics [7]. To use these methods for quantum information processing with trapped electrons, however, they must be adapted for use in a scalable trap architecture. The first, crucial step is to demonstrate that a single electron can be trapped and detected in such a scalable structure.

Earlier planar Penning trap experiments were not so encouraging. Narrowband radiofrequency detection techniques were not demonstrated, and detecting a single electron in a millimeter-scale trap was deemed "impossible" due to the unavoidable anharmonicity of the trapping potential [138]. Based on the work presented in this thesis, however, we offer a method to make a single electron detectable in a planar

Penning trap and some experimental evidence of its efficacy.

We began with a thorough theoretical study to determine whether the level of anharmonicity of the axial potential was an inevitable consequence of the lack of reflection symmetry. We concluded that it was not. For planar Penning traps with at least three concentric ring electrodes plus a grounded plane, judicious choices of trap geometry make it possible to bias the electrodes to eliminate the lowest-order amplitude dependence of the axial frequency and thus to dramatically suppress the anharmonic broadening, likely by enough to detect a single electron. The traps used in the Mainz and Ulm experiments did not have this optimized geometry, so no set of applied potentials could substantially reduce the anharmonicity. Not surprisingly, these experiments were unable to detect a single electron, but the new trap designs offered a promising way forward.

It is not enough simply to identify trap geometries and potentials that will produce a harmonic potential. Traps used in the laboratory will inevitably have radii slightly larger or smaller than expected, so the potentials must be adjusted until the anharmonicity reaches a measured minimum. Although an "orthogonalized" planar Penning trap design is not possible, we devised a procedure for tuning a planar trap while holding the axial frequency constant.

Guided by these design principles, a prototype trap was fabricated with one choice of optimized geometry. This trap also had much higher aspect ratio gaps to screen the insulating substrate from the trapping region and prevent it from accumulating stray charge. We then trapped electrons and realized the proposed tuning procedure experimentally; this enabled us to detect narrow resonances, about 10^5 times narrower than previously observed. The anharmonicity compensation in this initial implementation demonstrates the possibility of suspending a single electron, though the trap stability and detection sensitivity remain to be improved before a more definite conclusion can be reached.

6.2 Toward One-Electron Qubits and Quantum Information Processing

The promising results of this work suggest that a single electron can likely be observed using the techniques presented here with only minor modifications to the current apparatus. To realize a one-electron qubit, it would then remain to measure the state of the qubit and to manipulate it coherently.

A spin qubit state could be read out with the same QND technique used in single-electron precision measurements [5] by fabricating a trap with a magnetic bottle. This detection method introduces a source of decoherence, so a variable magnetic bottle may be required. An axial qubit is a more challenging objective because the quantum regime of the axial motion has not yet been reached. The axial motion could be cooled to its quantum-mechanical ground state by driving a sideband of the cyclotron motion, analogous to the cooling of the magnetron motion described in Sec. 5.4 [120, Sec. IV.C]. Unlike magnetron cooling and spin state detection, for example, variable magnetic bottles and axial cooling are not yet well-established Penning trap techniques. However, these techniques are also of interest for precision measurements in Penning traps and may be pursued in the near future (for example, see Ref. [8, Sec. 7.1.3]). Conversely, new methods developed for quantum information studies could have immediate applications to precision measurements as well.

After establishing one-electron qubits, the last ingredient for quantum information processing is coupling individual qubits, perhaps via the proposed methods reviewed in Sec. 1.4 or via others yet to be developed. More electrons must be trapped in the same trap structure to demonstrate the scalability of the planar trap architecture. The covered planar trap architecture introduced in Sec. 2.6.1 may facilitate parallel detection of many electrons in nearby traps using a single detection circuit. Finally, the traps can be made smaller to increase the coupling between nearby trapped electrons and to increase the number of systems that can fit in the apparatus.

The path to a one-electron qubit remains challenging, to be sure, but every system considered for quantum information processing faces considerable experimental challenges. It remains to be seen which system, if any, can be scaled up sufficiently to perform practical quantum computations. An array of electrons in planar Penning traps has attractive features. As a result of this work, one-electron qubits seem to be a feasible option for a new quantum information processing architecture.

Appendix A

Electrostatics of Planar and Cylindrical Penning Traps

To study theoretically the motion of particles in a Penning trap, we must derive the electrostatic potential by solving Laplace's equation,

$$\nabla^2 V = 0, \tag{A.1}$$

with the boundary conditions set by the potentials applied to the trap electrodes. By specifying the potential everywhere on the boundary, the solution in the bounded volume is unique.

This Appendix compiles the results for various trap geometries considered in this thesis. All solutions result from straightforward application of standard electrostatics methods [168, Ch. 11].

A.1 General Approach

We first review a general method of finding a solution to Laplace's equation, and then we apply it to various trap geometries. In general, the potential produced within a completely enclosed trap is a superposition

$$V(\rho, z, \varphi) = \sum_{i=1}^{N} V_i \phi_i(\rho, z, \varphi), \tag{A.2}$$

where V_i is the potential applied to electrode i and $\phi_i(\rho, z, \varphi)$ is the solution to Laplace's equation with the boundary condition that $\phi_i = 1$ on the surface of electrode i and $\phi_i = 0$ elsewhere on the boundary.

We now proceed to solve Laplace's equation to find the ϕ_i. We look for a separable solution to Laplace's equation in cylindrical coordinates,

$$V(\rho, z, \varphi) = R(\rho)H(\varphi)Z(z), \tag{A.3}$$

where R, H, and Z are functions to be determined. Rotational symmetry about the z-axis requires that $H(\varphi) = 1$, and the separated equations for the radial and axial functions are therefore

$$\left(\frac{\partial^2}{\partial \rho^2} + \frac{1}{\rho}\frac{\partial}{\partial \rho} + k^2\right) R(\rho) = 0, \tag{A.4}$$

$$\left(\frac{\partial^2}{\partial z^2} - k^2\right) Z(z) = 0, \tag{A.5}$$

where k is a constant. Eq. (A.4) is Bessel's equation with $\nu = 0$, as imposed by the axial symmetry. There are two classes of solutions to Eqs. (A.4) and (A.5): either the radial solution is oscillatory and the axial solution is exponential ($k^2 > 0$), or the radial solution is exponential and the axial solution is oscillatory ($k^2 \equiv -\alpha^2 < 0$).

The general solutions corresponding to these two cases are linear combinations of functions,

$$V(\rho, z) = \begin{cases} e^{-kz} \\ e^{kz} \end{cases} \begin{cases} J_0(k\rho) \\ Y_0(k\rho) \end{cases}, \tag{A.6}$$

$$\text{or} \quad \begin{cases} \sin(\alpha z) \\ \cos(\alpha z) \end{cases} \begin{cases} I_0(\alpha\rho) \\ K_0(\alpha\rho) \end{cases}. \tag{A.7}$$

The coefficients of the four possible terms in each case are determined by imposing boundary conditions. In all trap geometries considered here, we can exclude solutions containing Y_0 and K_0 since $Y_0(k\rho) \to \infty$ and $K_0(k\rho) \to \infty$ as $\rho \to 0$, and we require the potential to be finite at the origin.

A.1.1 General boundary conditions for planar Penning traps

For all variations of planar Penning traps considered in this work (but not the cylindrical traps considered in Sec. A.8), the radial boundary condition $V(\rho, z) = 0$ is imposed, either at $\rho = \rho_c$ or at $\rho \to \infty$; this can be satisfied only if the radial functions are oscillatory. The potential can then be written as a superposition of the remaining terms,

$$V(\rho, z) = \sum_k \left(A_k e^{-kz} + B_k e^{kz}\right) J_0(k\rho). \tag{A.8}$$

For a single electrode with potential 1 and all other electrodes grounded, the potential in the plane of the trap electrodes is

$$\phi_i(\rho, 0) = \begin{cases} 0, & \rho < \rho_{i-1} \\ 1, & \rho_{i-1} < \rho < \rho_i \\ 0, & \rho > \rho_i \end{cases}. \tag{A.9}$$

The potential applied to the $z = 0$ plane is therefore

$$V(\rho) \equiv \sum_{i=1}^{N} V_i \phi_i(\rho, 0). \tag{A.10}$$

Each of the planar trap variations considered below has a potential based on the form given by Eq. (A.8) and is subject to the boundary condition in Eq. (A.10).

In each of the subsequent sections, the potential is derived for different sets of boundary conditions.

A.2 Infinite Boundary

A planar Penning trap with a boundary at infinity has boundary conditions

$$V(\rho \to \infty, z) \to 0, \tag{A.11}$$

$$V(\rho, z \to \infty) \to 0, \tag{A.12}$$

$$V(\rho, 0) = V(\rho). \tag{A.13}$$

The radial boundary condition in Eq. (A.11) is satisfied for any value of $k \geq 0$, so the sum in Eq. (A.8) becomes an integral, and the solution takes the form

$$V(\rho, z) = \int_0^\infty dk \left(A_k e^{-kz} + B_k e^{kz} \right) J_0(k\rho). \tag{A.14}$$

The condition (A.12) requires that

$$B_k = 0. \tag{A.15}$$

The A_k are then determined by imposing the boundary condition in Eq. (A.13),

$$V(\rho) = \int_0^\infty dk A_k J_0(k\rho). \tag{A.16}$$

We then operate on both sides with $\int_0^\infty d\rho\rho J_0(k'\rho)$:

$$\begin{aligned}\int_0^\infty d\rho\rho J_0(k'\rho)V(\rho) &= \int_0^\infty dk A_k \int_0^\infty d\rho\rho J_0(k'\rho)J_0(k\rho),\\ &= \int_0^\infty dk A_k \frac{\delta(k-k')}{k},\\ &\Rightarrow \quad A_k = k\int_0^\infty d\rho\rho J_0(k\rho)V(\rho), \qquad \text{(A.17)}\end{aligned}$$

where in the second line we have replaced k' with k and used the orthogonality of Bessel functions,

$$\int_0^\infty d\rho\rho J_\nu(k\rho)J_\nu(k'\rho) = \frac{\delta(k-k')}{k} \quad \text{for } k,k' > 0. \qquad \text{(A.18)}$$

The integral on the RHS of Eq. (A.17) is given by

$$\begin{aligned}\int_0^\infty d\rho\rho J_0(k\rho)V(\rho) &= \sum_{i=1}^N V_i \int_0^\infty d\rho\rho J_0(k\rho)\phi_i(\rho,0)\\ &= \sum_{i=1}^N V_i \int_{\rho_{i-1}}^{\rho_i} d\rho\rho J_0(k\rho)\\ &= \frac{1}{k}\sum_{i=1}^N V_i\left[\rho_i J_1(k\rho_i) - \rho_{i-1}J_1(k\rho_{i-1})\right]\\ &= -\frac{1}{k}\sum_{i=1}^N \Delta V_i \rho_i J_1(k\rho_i), \qquad \text{(A.19)}\end{aligned}$$

where in the last step we have re-indexed $i \to i+1$ on the second term, used our conventions that $\rho_0 = 0$ and $V_{N+1} = 0$, and introduced $\Delta V_i \equiv V_{i+1} - V_i$. Inserting Eqs. (A.15), (A.17), and (A.19) into Eq. (A.14) yields the solution

$$V(\rho,z) = -\sum_{i=1}^N \Delta V_i \rho_i \int_0^\infty dk J_1(k\rho_i)e^{-kz}J_0(k\rho). \qquad \text{(A.20)}$$

On axis, the integral can be evaluated analytically [137],

$$V(z) = \sum_{i=1}^{N} \Delta V_i \left(\frac{z}{\sqrt{\rho_i^2 + z^2}} - 1 \right) \tag{A.21}$$

$$\equiv \sum_{i=1}^{N} \Delta V_i \Phi_i(z) \tag{A.22}$$

$$= V_1 + \sum_{i=1}^{N} \Delta V_i \frac{z}{\sqrt{\rho_i^2 + z^2}}. \tag{A.23}$$

This is the electrostatic potential for a planar Penning trap with infinitesimal gaps and an infinite boundary.

A.3 Finite Gaps

As was done for cylindrical Penning traps [125], finite gaps can be modeled with a potential varying linearly across the gap, as discussed in Sec. 2.5.1. The boundary conditions are still given by Eqs. (A.11)–(A.13), with the potential in the $z = 0$ plane now given by

$$V(\rho) = \sum_{i=1}^{N} V_i \phi_i(\rho, 0) + \Delta V_i \phi_i^{(\mathrm{gap})}(\rho, 0), \tag{A.24}$$

where ϕ_i are given in Eq. (A.9) and

$$\phi_i^{(\mathrm{gap})}(\rho, 0) = \begin{cases} 0, & \rho < \rho_i - w_i/2 \\ \frac{\Delta V_i}{w_i}(\rho - (\rho_i - w_i/2)), & \rho_i - w_i/2 < \rho < \rho_i \\ \frac{\Delta V_i}{w_i}(\rho - (\rho_i + w_i/2)), & \rho_i < \rho < \rho_i + w_i/2 \\ 0, & \rho > \rho_i + w_i/2 \end{cases}. \tag{A.25}$$

The solution procedure is the same as for the trap with infinitesimal gaps. From Eqs. (A.14), (A.15), and (A.17), the potential on axis is

$$V(z) = \int_0^\infty dk e^{-kz} k \int_0^\infty d\rho \rho J_0(k\rho) V(\rho). \tag{A.26}$$

The terms corresponding to the gap potential can be evaluated by using the integrals

$$\int_0^\infty dk e^{-kz} k \int_a^b d\rho \rho J_0(k\rho) = \frac{z}{\sqrt{a^2+z^2}} - \frac{z}{\sqrt{b^2+z^2}}, \tag{A.27}$$

$$\begin{aligned}\int_0^\infty dk e^{-kz} k \int_a^b d\rho \rho^2 J_0(k\rho) = z \left[\sinh^{-1}\left(\frac{b}{z}\right) - \sinh^{-1}\left(\frac{a}{z}\right)\right] \\ - \left(b\frac{z}{\sqrt{b^2+z^2}} - a\frac{z}{\sqrt{a^2+z^2}}\right).\end{aligned} \tag{A.28}$$

The contribution from the finite gaps is the sum of contributions from each gap potential,

$$V^{(\text{gap})}(z) = \sum_{i=1}^{N} \Delta V_i \Phi_i^{(\text{gap})}(z), \tag{A.29}$$

$$\Phi_i^{(\text{gap})}(z) = \frac{z}{w_i}\left[\sinh^{-1}\left(\frac{\rho_i + w_i/2}{z}\right) - \sinh^{-1}\left(\frac{\rho_i - w_i/2}{z}\right)\right] - \frac{z}{\sqrt{\rho_i^2+z^2}}, \tag{A.30}$$

and the total potential on axis is just the sum of terms due to the electrodes (Eq. (A.21)) and the finite gaps (Eqs. (A.29) and (A.30)),

$$\begin{aligned}V^{(\text{gap})}(z) &= \sum_{i=1}^{N} \Delta V_i (\Phi_i(z) + \Phi_i^{(\text{gap})}(z)) &\text{(A.31)}\\ &= \sum_{i=1}^{N} \Delta V_i \frac{z}{w_i}\left[\sinh^{-1}\left(\frac{\rho_i + w_i/2}{z}\right) - \sinh^{-1}\left(\frac{\rho_i - w_i/2}{z}\right) - 1\right]. &\text{(A.32)}\end{aligned}$$

This reduces to Eq. (A.21) in the limit $w_i \to 0$.

A.4 Covered Planar Penning Trap

Now instead of a trap with boundaries at infinity, we consider a planar trap covered by a conducting plane at potential V_p at a distance z_c from the plane containing the electrodes; the radial boundary is still at infinity. This problem can be solved by treating it as a superposition of two problems: the first has parallel plates at $z = 0$

and $z = z_c$ biased with potentials 0 and V_p, respectively. The boundary conditions are

$$V(\rho, 0) = 0, \tag{A.33}$$

$$V(\rho, z_c) = V_p. \tag{A.34}$$

And the second is a planar trap at $z = 0$ and a grounded conducting plane at $z = z_c$. The boundary conditions for this problem are

$$V(\rho \to \infty, z) \to 0, \tag{A.35}$$

$$V(\rho, z_c) = 0, \tag{A.36}$$

$$V(\rho, 0) = V(\rho). \tag{A.37}$$

These problems can be solved separately and the solutions summed to satisfy the combined boundary conditions

$$V(\rho \to \infty, z) \to 0, \tag{A.38}$$

$$V(\rho, z_c) = V_p, \tag{A.39}$$

$$V(\rho, 0) = V(\rho). \tag{A.40}$$

The first problem is simply a parallel plate capacitor. The solution to the radial equation, Eq. (A.4), is trivial, $R(\rho) = \text{constant}$. The solution to the axial equation, Eq. (A.5), has $k = 0$. The solution that satisfies the boundary conditions is thus simply

$$V(z) = V_p \frac{z}{z_c}. \tag{A.41}$$

As with the infinite-boundary trap, the solution to the second problem takes the form of Eq. (A.14), where again we have an integral over $k \geq 0$. Eq. (A.36) gives

$$0 = \int_0^\infty dk \left(A_k e^{-kz_c} + B_k e^{kz_c} \right) J_0(k\rho). \tag{A.42}$$

As above, we operate with $\int_0^\infty d\rho\rho J_0(k'\rho)$ and integrate to get

$$\begin{aligned} 0 &= \int_0^\infty dk \left(A_k e^{-kz_c} + B_k e^{kz_c} \right) \int_0^\infty d\rho\rho J_0(k'\rho) J_0(k\rho) \\ &= \frac{1}{k'} \left(A_{k'} e^{-k'z_c} + B_{k'} e^{k'z_c} \right), \\ \Rightarrow \quad & B_k = -A_k e^{-2kz_c}. \end{aligned} \tag{A.43}$$

Now we impose the boundary condition in Eq. (A.37) at the electrode plane. Following the same procedure as before, we find

$$\begin{aligned} V(\rho) &= \int_0^\infty dk J_0(k\rho) A_k \left(1 - e^{-2kz_c} \right), \\ \int_0^\infty d\rho\rho J_0(k'\rho) V(\rho) &= \int_0^\infty dk A_k \left(1 - e^{-2kz_c} \right) \int_0^\infty d\rho\rho J_0(k'\rho) J_0(k\rho) \\ &= \frac{1}{k'} A_{k'} \left(1 - e^{-2k'z_c} \right), \\ \Rightarrow \quad A_k &= \frac{k}{1 - e^{-2kz_c}} \int_0^\infty d\rho\rho J_0(k\rho) V(\rho) \\ &= -\frac{1}{1 - e^{-2kz_c}} \sum_{i=1}^{N} \Delta V_i \rho_i J_1(k\rho_i), \end{aligned} \tag{A.44}$$

where in the last step, we have used the result for the integral given in Eq. (A.19). Using Eqs. (A.43) and (A.44) in Eq. (A.8), the potential on axis is found to be

$$\begin{aligned} V(z) &= -\sum_{i=1}^{N} \Delta V_i \rho_i \int_0^\infty dk \frac{J_1(k\rho_i)}{1 - e^{-2kz_c}} \left(e^{-kz} - e^{-2kz_c} e^{kz} \right) \\ &= \sum_{i=1}^{N} \Delta V_i \rho_i \int_0^\infty dk J_1(k\rho_i) \frac{\sinh(k(z - z_c))}{\sinh(kz_c)}. \end{aligned} \tag{A.45}$$

Unlike for an infinite-boundary trap, the integral cannot be evaluated analytically, so this expression must be evaluated numerically for each choice of geometry and potentials.

Summing Eqs. (A.41) and (A.45), we arrive at

$$V(z) = V_p \frac{z}{z_c} + \sum_{i=1}^{N} \Delta V_i \rho_i \int_0^\infty dk J_1(k\rho_i) \frac{\sinh(k(z-z_c))}{\sinh(kz_c)}, \tag{A.46}$$

which gives the potential on axis for a covered planar Penning trap.

A.5 Mirror-Image Traps

We now replace the conducting covering plane with another set of planar electrodes with radii $\rho_i^{(2)}$ and potential $V^{(2)}(\rho)$. The boundary conditions for this problem are

$$V(\rho \to \infty, z) \to 0, \tag{A.47}$$

$$V(\rho, z_c) = V^{(2)}(\rho), \tag{A.48}$$

$$V(\rho, 0) = V(\rho). \tag{A.49}$$

The solution for two facing traps is just the solution for one trap in the $z = 0$ plane with a grounded plane at z_c, plus the solution for one trap in the $z = z_c$ plane with a grounded plane at $z = 0$. The former is Eq. (A.46) with $V_p = 0$, and the latter is Eq. (A.46) with $V_p = 0$ after performing the coordinate transformation $z \to z_c - z$ and replacing $V(\rho)$ with $V^{(2)}(\rho)$. The resulting potential on axis is

$$\begin{aligned} V(z) = &\sum_{i=1}^{N} \Delta V_i \rho_i \int_0^\infty dk J_1(k\rho_i) \frac{\sinh(k(z-z_c))}{\sinh(kz_c)} \\ &- \sum_{i=1}^{N_2} \Delta V_i^{(2)} \rho_i^{(2)} \int_0^\infty dk J_1(k\rho_i^{(2)}) \frac{\sinh(kz)}{\sinh(kz_c)}, \end{aligned} \tag{A.50}$$

where $\Delta V_i^{(2)}$, $\rho_i^{(2)}$, and N_2 describe the gap potentials, radii, and number of gaps for the planar electrodes lying at $z = z_c$.

We may want to bias the plane lying beyond the Nth gap on the top trap, so that eventually the potential of the mirror-image trap can become the potential of the covered planar trap. By superposition, the potential due to the entire plane biased to $V = 1$ (Eq. (A.41)) is equal to the potential due to electrode $N+1$ biased to $V_{N+1} = 1$ and the other electrodes grounded, plus the potential due to the other electrodes biased to $V_i = 1$ and electrode $N+1$ grounded. The latter case corresponds to all the ΔV_i vanishing except $\Delta V_N = -1$. That is,

$$\begin{aligned} \frac{z}{z_c} &= \phi_{N+1} + \rho_N \int_0^\infty dk J_1(k\rho_N) \frac{\sinh(kz)}{\sinh(kz_c)}, \\ \Rightarrow \quad \phi_{N+1} &= \frac{z}{z_c} - \rho_N \int_0^\infty dk J_1(k\rho_N) \frac{\sinh(kz)}{\sinh(kz_c)}. \end{aligned} \tag{A.51}$$

Then, adding this potential to Eq. (A.50) gives

$$\begin{aligned} V(z) = \sum_{i=1}^{N} \Delta V_i \rho_i \int_0^\infty dk J_1(k\rho_i) \frac{\sinh(k(z-z_c))}{\sinh(kz_c)} + V_c \frac{z}{z_c} \\ - \sum_{i=1}^{N_2} \Delta V_i^{(2)} \rho_i^{(2)} \int_0^\infty dk J_1(k\rho_i^{(2)}) \frac{\sinh(kz)}{\sinh(kz_c)}, \end{aligned} \tag{A.52}$$

where $\Delta V_N^{(2)} = V_c - V_N^{(2)}$.

A.6 Finite Cylinder

We now consider traps with a finite radial boundary. In particular, the radial boundary is a grounded conducting cylindrical wall at radius $\rho = \rho_c$, and the top of the cylinder is a conducting plane at $z = z_c$ with potential V_p as before. The boundary conditions are

$$V(\rho_c, z) = 0, \tag{A.53}$$

$$V(\rho, z_c) = V_p, \tag{A.54}$$

$$V(\rho, 0) = V(\rho). \tag{A.55}$$

As before, the solution takes the form of Eq. (A.8). The boundary condition in Eq. (A.53) is now satisfied only for a discrete set of values of k that satisfy

$$\begin{aligned} &J_0(k\rho_c) = 0, \\ \Rightarrow \quad &k = k_n = \frac{\alpha_{0n}}{\rho_c}, \end{aligned} \tag{A.56}$$

where α_{0n} is the nth zero of the Bessel function $J_0(x)$. We can then write the solution as a sum over n,

$$V(\rho, z) = \sum_{n=1}^{\infty} \left(A_n e^{-k_n z} + B_n e^{k_n z}\right) J_0(k_n \rho). \tag{A.57}$$

Now we impose the boundary condition in Eq. (A.54) to get

$$\sum_{n=1}^{\infty} \left(A_n e^{-k_n z_c} + B_n e^{k_n z_c}\right) J_0(k_n \rho) = V_p. \tag{A.58}$$

We then apply $\int_0^{\rho_c} d\rho\rho J_0(k_m\rho)$ to both sides and perform the integral over ρ:

$$\begin{aligned} \sum_{n=1}^{\infty} \left(A_n e^{-k_n z_c} + B_n e^{k_n z_c}\right) \int_0^{\rho_c} d\rho\rho J_0(k_m\rho) J_0(k_n\rho) &= V_p \int_0^{\rho_c} d\rho\rho J_0(k_m\rho) \\ \sum_{n=1}^{\infty} \left(A_n e^{-k_n z_c} + B_n e^{k_n z_c}\right) \delta_{mn} \frac{\rho_c^2}{2} J_1^2(\alpha_{0n}) &= V_p \frac{\rho_c^2}{\alpha_{0m}} J_1(\alpha_{0m}) \\ \Rightarrow \quad A_n e^{-k_n z_c} + B_n e^{k_n z_c} &= V_p \frac{2}{\alpha_{0n} J_1(\alpha_{0n})}, \end{aligned} \tag{A.59}$$

where in the second line, we have used another orthogonality property of Bessel functions [168, Eq. 11.113],

$$\int_0^{\rho_0} d\rho\rho J_\nu\left(\frac{\alpha_{\nu n}}{\rho_0}\rho\right) J_\nu\left(\frac{\alpha_{\nu m}}{\rho_0}\rho\right) = \delta_{nm} \frac{\rho_0^2}{2} J_{\nu+1}^2(\alpha_{\nu n}). \tag{A.60}$$

Finally, we impose the boundary condition in Eq. (A.55) to get

$$\sum_n \left(A_n + B_n\right) J_0(k_n\rho) = V(\rho). \tag{A.61}$$

After integrating over ρ as before, we find

$$\frac{\rho_c^2}{2} J_1^2(\alpha_{0n}) \left(A_n + B_n\right) = \int_0^{\rho_c} d\rho\rho J_0(k_n\rho) V(\rho). \tag{A.62}$$

Since $\rho_c \geq \rho_N$, the result of the integral on the RHS is the same as the result in Eq. (A.19), which gives us

$$A_n + B_n = -\frac{2}{\alpha_{0n}^2 J_1^2(\alpha_{0n})} \sum_{i=1}^{N} \Delta V_i k_n \rho_i J_1\left(k_n\rho_i\right). \tag{A.63}$$

A_n and B_n can now be found by solving Eqs. (A.59) and (A.63), yielding

$$A_n = -\frac{1}{\alpha_{0n} J_1(\alpha_{0n}) \sinh(k_n z_c)} \left(V_p + \frac{1}{\alpha_{0n} J_1(\alpha_{0n})} e^{k_n z_c} \sum_{i=1}^{N} \Delta V_i k_n \rho_i J_1\left(k_n\rho_i\right) \right), \tag{A.64}$$

$$B_n = \frac{1}{\alpha_{0n} J_1(\alpha_{0n}) \sinh(k_n z_c)} \left(V_p + \frac{1}{\alpha_{0n} J_1(\alpha_{0n})} e^{-k_n z_c} \sum_{i=1}^{N} \Delta V_i k_n \rho_i J_1\left(k_n\rho_i\right) \right). \tag{A.65}$$

Inserting Eqs. (A.64) and (A.65) into Eq. (A.57) gives the solution

$$\begin{aligned} V(\rho, z) = V_p \sum_{n=1}^{\infty} & \frac{2}{\alpha_{0n} J_1(\alpha_{0n})} \frac{\sinh(k_n z)}{\sinh(k_n z_c)} J_0(k_n\rho) \\ & + \sum_{i=1}^{N} \Delta V_i \sum_{n=1}^{\infty} k_n \rho_i \frac{2 J_1\left(k_n\rho_i\right)}{\alpha_{0n}^2 J_1^2(\alpha_{0n})} \frac{\sinh(k_n(z - z_c))}{\sinh(k_n z_c)} J_0(k_n\rho), \end{aligned} \tag{A.66}$$

which is a sum of terms arising from V_p and from each of the gap potentials ΔV_i. (The form of the first term does not make it obvious how the boundary condition in Eq. (A.54) is satisfied; however, for $z = z_c$, the sum is just the Bessel function expansion for the function $f(\rho) = 1$ [245, p. 592].)

A.7 Mirror-Image Traps with a Finite Radial Boundary

Just as with the infinite radial boundary, by the superposition principle, the solution for two traps facing each other can be written down immediately based on Eq. (A.66):

$$V(z) = \sum_{i=1}^{N} \Delta V_i \sum_{n=1}^{\infty} k_n \rho_i \frac{2J_1\left(k_n\rho_i\right)}{\alpha_{0n}^2 J_1^2(\alpha_{0n})} \frac{\sinh(k_n(z-z_c))}{\sinh(k_n z_c)}$$
$$- \sum_{i=1}^{N_2} \Delta V_i^{(2)} \sum_{n=1}^{\infty} k_n \rho_i^{(2)} \frac{2J_1\left(k_n\rho_i^{(2)}\right)}{\alpha_{0n}^2 J_1^2(\alpha_{0n})} \frac{\sinh(k_n z)}{\sinh(k_n z_c)}. \quad \text{(A.67)}$$

This is analogous to Eq. (A.52) but with a finite radial enclosure.

A.8 Single-Electrode Potentials for Cylindrical Penning Traps

We now consider Penning traps with cylindrical electrodes, both closed- and open-endcap traps. The electrostatic solutions for these traps are well documented [125,127] for applied potentials that are symmetric or antisymmetric about the trap center, but here for completeness we find the $\phi_i(z)$ for each electrode separately. These functions are useful for calculating the C_{ki} for detecting and driving axial oscillations.

We begin by considering a cylinder with closed endcaps and inside radius ρ_0. Without loss of generality, we place one endcap at $z = 0$ and the other at $z =$

L.[1] To translate the trap center to $z = 0$, one must simply perform the coordinate transformation $z \to z + \frac{L}{2}$. First, we find the potential for the endcaps of a closed-endcap trap. For $V = 1$ applied to the top endcap and all other electrodes grounded, the boundary conditions for the single-electrode potential $\phi_e(\rho, z)$ are

$$\phi_e(\rho, 0) = 0, \tag{A.68}$$

$$\phi_e(\rho, L) = 1, \tag{A.69}$$

$$\phi_e(\rho_0, z) = 0. \tag{A.70}$$

To satisfy these boundary conditions, we must choose the oscillatory radial function and exponential axial function. Thus the solution takes the form

$$\phi_e(\rho, z) = \sum_k \left(A_k^{(e)} \sinh(kz) + B_k^{(e)} \cosh(kz) \right) J_0(k\rho). \tag{A.71}$$

The boundary condition in Eq. (A.68) gives

$$B_k^{(e)} = 0. \tag{A.72}$$

The radial boundary condition in Eq. (A.70) gives

$$J_0(k\rho_0) = 0 \quad \Rightarrow \quad k = \frac{\alpha_{0n}}{\rho_0}, \tag{A.73}$$

where α_{0n} is the nth zero of the Bessel function $J_0(x)$. Thus the boundary condition as Eq. (A.70) at the top endcap can be written as

$$\sum_n A_n^{(e)} \sinh\left(\frac{\alpha_{0n}}{\rho_0} z\right) J_0\left(\frac{\alpha_{0n}}{\rho_0} \rho\right) = 1. \tag{A.74}$$

[1] For closed-endcap traps, the distance L is equal to what is often written as $2z_0$ elsewhere in the literature (e.g., [125]). Here we use different notation to avoid confusion with the position of the potential minimum, as defined in Chapter 2.

To extract $A_n^{(e)}$, as before we operate on both sides with $\int_0^{\rho_0} d\rho\rho J_0(\alpha_{0n}\rho/\rho_0)$ and use the orthogonality of Bessel functions to find

$$A_n^{(e)} = \frac{2}{\rho_0^2} \frac{1}{J_1^2(\alpha_{0n}) \sinh\left(\frac{\alpha_{0n}}{\rho_0} L\right)} \int_0^{\rho_0} d\rho\rho J_0\left(\frac{\alpha_{0n}}{\rho_0}\rho\right). \tag{A.75}$$

And the resulting potential along the z-axis is

$$\phi_e(z) = \sum_n A_n^{(e)} \sinh\left(\frac{\alpha_{0n}}{\rho_0} z\right). \tag{A.76}$$

To find the potential for the bottom endcap, we translate the coordinates $z \to z + \frac{L}{2}$ and then use that $\phi_{\text{bot}}(z) = \phi_{\text{top}}(-z)$.

Now we turn to considering an electrode that occupies part of the radial boundary, a cylindrical shell lying at radius ρ_0 and extending from $z = z_1$ to $z = z_2$ (z_1 and z_2 lie in the range 0 to L). The boundary conditions for the single-electrode potential $\phi_c(\rho_z)$ are

$$\phi_c(\rho, 0) = 0, \tag{A.77}$$

$$\phi_c(\rho, L) = 0, \tag{A.78}$$

$$\phi_c(\rho_0, z) = \begin{cases} 0, & z_2 < z \leq L \\ 1, & z_1 \leq z \leq z_2 \\ 0, & 0 \leq z < z_1 \end{cases}. \tag{A.79}$$

Since the potential must be zero at both endcaps, the axial solution must be oscillatory rather than exponential. Since the potential must be finite at $\rho = 0$, we exclude solutions containing $K_0(\alpha\rho)$. Thus the solution takes the form

$$\phi_c(\rho, z) = \sum_\alpha (A_\alpha^{(c)} \sin(\alpha z) + B_\alpha^{(c)} \cos(\alpha z)) I_0(\alpha\rho). \tag{A.80}$$

Applying the boundary conditions (A.77) and (A.78), we find

$$B_\alpha^{(c)} = 0, \tag{A.81}$$

$$\sin(\alpha L) = 0 \quad \Rightarrow \quad \alpha = \frac{n\pi}{L}, \tag{A.82}$$

where n is an integer. Thus,

$$\phi_c(\rho, z) = \sum_n A_n^{(c)} \sin\left(\frac{n\pi}{L}z\right) I_0\left(\frac{n\pi}{L}\rho\right). \tag{A.83}$$

.

We now apply the radial boundary condition, (A.79), operate on both sides with $\int_0^L dz \sin\left(\frac{m\pi}{L}z\right)$, and use the form of $\phi_c(\rho, z)$ from Eq. (A.83). The LHS is evaluated by using the orthogonality of sine functions,[2]

$$\int_0^L dz \sin\left(\frac{m\pi}{L}z\right) \sin\left(\frac{n\pi}{L}z\right) = \frac{L}{2}\delta_{mn}, \tag{A.84}$$

and the RHS is integrated trivially, yielding

$$A_n^{(c)} = \frac{2}{n\pi} \frac{1}{I_0\left(\frac{n\pi}{L}\rho_0\right)} \left[\cos\left(\frac{n\pi z_1}{L}\right) - \cos\left(\frac{n\pi z_2}{L}\right)\right]. \tag{A.85}$$

The potential on axis is

$$\phi_c(z) = \sum_n A_n^{(c)} \sin\left(\frac{n\pi}{L}z\right), \tag{A.86}$$

with $A_n^{(c)}$ given by Eq. (A.85). For the appropriate choice of z_1 and z_2, this expression gives the potential for a ring electrode or compensation electrode. For an open-endcap trap, the endcap electrode is modeled as a long cylindrical section plus a flat plate. For such an electrode, the potential is the sum of a contribution from the cylindrical and flat portions of the endcap; in practice, however, the cylindrical portion is chosen

[2]Ref. [246] leaves out the factor of $L/2$; in that work, a factor of $2/L$ belongs on the LHS of Eq. (4.9).

to be sufficiently long that the contribution from the flat part is negligible and the single-electrode potential is given by Eq. (A.86).

Bibliography

[1] Goldman, J. & Gabrielse, G. Optimized planar Penning traps for quantum information studies. *Phys. Rev. A* **81**, 052335 (2010).

[2] Lamata, L., Porras, D., Cirac, J. I., Goldman, J. & Gabrielse, G. Towards electron-electron entanglement in Penning traps. *Phys. Rev. A* **81**, 022301 (2010).

[3] Wineland, D., Ekstrom, P. & Dehmelt, H. Monoelectron oscillator. *Phys. Rev. Lett.* **31**, 1279–1282 (1973).

[4] Van Dyck, Jr., R. S., Schwinberg, P. B. & Dehmelt, H. G. New high-precision comparison of electron and positron g factors. *Phys. Rev. Lett.* **59**, 26–29 (1987).

[5] Peil, S. & Gabrielse, G. Observing the quantum limit of an electron cyclotron: QND measurements of quantum jumps between fock states. *Phys. Rev. Lett.* **83**, 1287–1290 (1999).

[6] Hanneke, D., Hoogerheide, S. F. & Gabrielse, G. Cavity control of a single-electron quantum cyclotron: Measuring the electron magnetic moment. *Phys. Rev. A* **83**, 052122 (2011).

[7] Hanneke, D., Fogwell, S. & Gabrielse, G. New measurement of the electron magnetic moment and the fine structure constant. *Phys. Rev. Lett.* **100**, 120801 (2008).

[8] Hanneke, D. *Cavity Control in a Single-Electron Quantum Cyclotron: An Improved Measurement of the Electron Magnetic Moment*. Ph.D. thesis, Harvard University (2007).

[9] Shor, P. W. Algorithms for quantum computation: Discrete logarithms and factoring. In *SFCS '94: Proceedings of the 35th Annual Symposium on Foundations of Computer Science*, 124–134 (IEEE Press, Los Alamitos, CA, 1994).

[10] Nielsen, M. A. & Chuang, I. L. *Quantum Computation and Quantum Information* (Cambridge University Press, Cambridge, U.K., 2000).

[11] Shor, P. W. Scheme for reducing decoherence in quantum computer memory. *Phys. Rev. A* **52**, R2493–R2496 (1995).

[12] Steane, A. M. Error correcting codes in quantum theory. *Phys. Rev. Lett.* **77**, 793–797 (1996).

[13] Mermin, N. D. *Quantum Computer Science: An Introduction* (Cambridge University Press, Cambridge, U.K., 2007).

[14] Grover, L. K. A fast quantum mechanical algorithm for database search. In *Proc. 28th Annual ACM Symposium on the Theory of Computing (STOC)*, 212–219 (ACM Press, New York, 1996).

[15] Grover, L. K. Quantum mechanics helps in searching for a needle in a haystack. *Phys. Rev. Lett.* **79**, 325–328 (1997).

[16] Lloyd, S. Universal quantum simulators. *Science* **273**, 1073–1078 (1996).

[17] Feynman, R. P. Simulating physics with computers. *Int. J. Theor. Phys.* **21**, 467–488 (1982).

[18] Buluta, I. & Nori, F. Quantum simulators. *Science* **326**, 108–111 (2009).

[19] Steane, A. M. How to build a 300 bit, 1 giga-operation quantum computer. *Quantum Inf. Comput.* **7**, 171–183 (2007).

[20] Steane, A. M. Overhead and noise threshold of fault-tolerant quantum error correction. *Phys. Rev. A* **68**, 042322 (2003).

[21] Reichardt, B. W. Improved ancilla preparation scheme increases fault-tolerant threshold (2004). `arXiv:0406025v1`.

[22] Knill, E. Quantum computing with realistically noisy devices. *Nature* **434**, 39–44 (2005).

[23] Raussendorf, R. & Harrington, J. Fault-tolerant quantum computation with high threshold in two dimensions. *Phys. Rev. Lett.* **98**, 190504 (2007).

[24] Leggett, A. J. Testing the limits of quantum mechanics: Motivation, state of play, prospects. *J. Phys.: Condens. Matter* **14**, R415–R451 (2002).

[25] Trimmer, J. D. The present situation in quantum mechanics: A translation of schrödinger's "cat paradox" paper. *P. Am. Philos. Soc.* **124**, 323–338 (1980).

[26] Ladd, T. D., Jelezko, F., Laflamme, R., Nakamura, Y., Monroe, C. & O'Brien, J. L. Quantum computers. *Nature* **464**, 45–53 (2010).

[27] Chen, G., Church, D. A., Englert, B.-G., Henkel, C., Rohwedder, B., Scully, M. O. & Zubairy, M. S. *Quantum Computing Devices: Principles, Designs, and Analysis* (Chapman & Hall/CRC, Boca Raton, FL, 2007).

[28] DiVincenzo, D. P. The physical implementation of quantum computation. *Fortschr. Phys.* **48**, 771–784 (2000).

[29] Cirac, J. I. & Zoller, P. Quantum computation with cold trapped ions. *Phys. Rev. Lett.* **74**, 4091–4094 (1995).

[30] Monroe, C., Meekhof, D. M., King, B. E., Itano, W. M. & Wineland, D. J. Demonstration of a fundamental quantum logic gate. *Phys. Rev. Lett.* **75**, 4714–4717 (1995).

[31] Schmidt, P. O., Rosenband, T., Langer, C., Itano, W. M., Bergquist, J. C. & Wineland, D. J. Spectroscopy using quantum logic. *Science* **309**, 749–752 (2005).

[32] Rosenband, T., Schmidt, P. O., Hume, D. B., Itano, W. M., Fortier, T. M., Stalnaker, J. E., Kim, K., Diddams, S. A., Koelemeij, J. C. J., Bergquist, J. C. & Wineland, D. J. Observation of the ${}^1S_0 \rightarrow {}^3P_0$ clock transition in ${}^{27}\mathrm{Al}^+$. *Phys. Rev. Lett.* **98**, 220801 (2007).

[33] Rosenband, T., Hume, D. B., Schmidt, P. O., Chou, C. W., Brusch, A., Lorini, L., Oskay, W. H., Drullinger, R. E., Fortier, T. M., Stalnaker, J. E., Diddams, S. A., Swann, W. C., Newbury, N. R., Itano, W. M., Wineland, D. J. & Bergquist, J. C. Frequency ratio of Al^+ and Hg^+ single-ion optical clocks; Metrology at the 17th decimal place. *Science* **319**, 1808–1812 (2008).

[34] Chwalla, M., Benhelm, J., Kim, K., Kirchmair, G., Monz, T., Riebe, M., Schindler, P., Villar, A. S., Hänsel, W., Roos, C. F., Blatt, R., Abgrall, M., Santarelli, G., Rovera, G. D. & Laurent, P. Absolute frequency measurement of the ${}^{40}\mathrm{Ca}^+ 4\mathrm{s}^2 S_{1/2} \rightarrow 3\mathrm{d}^2 D_{5/2}$ clock transition. *Phys. Rev. Lett.* **102**, 023002 (2009).

[35] Home, J. P., Hanneke, D., Jost, J. D., Amini, J. M., Leibfried, D. & Wineland, D. J. Complete methods set for scalable ion trap quantum information processing. *Science* **325**, 1227–1230 (2009).

[36] Hanneke, D., Home, J. P., Jost, J. D., Amini, J. M., Leibfried, D. & Wineland, D. J. Realization of a programmable two-qubit quantum processor. *Nature Physics* **6**, 13–16 (2009).

[37] Campbell, W. C., Mizrahi, J., Quraishi, Q., Senko, C., Hayes, D., Hucul, D., Matsukevich, D. N., Maunz, P. & Monroe, C. Ultrafast gates for single atomic qubits. *Phys. Rev. Lett.* **105**, 090502 (2010).

[38] Langer, C., Ozeri, R., Jost, J. D., Chiaverini, J., DeMarco, B., Ben-Kish, A., Blakestad, R. B., Britton, J., Hume, D. B., Itano, W. M., Leibfried, D., Reichle, R., Rosenband, T., Schaetz, T., Schmidt, P. O. & Wineland, D. J. Long-lived qubit memory using atomic ions. *Phys. Rev. Lett.* **95**, 060502 (2005).

[39] Benhelm, J., Kirchmair, G., Roos, C. F. & Blatt, R. Towards fault-tolerant quantum computing with trapped ions. *Nature Physics* **4**, 463–466 (2008).

[40] Leibfried, D., DeMarco, B., Meyer, V., Lucas, D., Barrett, M., Britton, J., Itano, W. M., Jelenković, B., Langer, C., Rosenband, T. & Wineland, D. J. Experimental demonstration of a robust, high-fidelity geometric two ion-qubit phase gate. *Nature* **422**, 412–415 (2003).

[41] Greenberger, D. M., Horne, M. & Zeilinger, A. Going beyond bell's theorem. In Kafatos, M. (ed.) *Bell's Theorem, Quantum Theory, and Conceptions of the Universe*, 73–76 (Kluwer Academic, Dordrecht, The Netherlands, 1989).

[42] Greenberger, D. M., Horne, M. A., Shimony, A. & Zeilinger, A. Bell theorem without inequalities. *Am. J. Phys.* **58**, 1131–1143 (1990).

[43] Leibfried, D., Knill, E., Seidelin, S., Britton, J., Blakestad, R. B., Chiaverini, J., Hume, D. B., Itano, W. M., Jost, J. D., Langer, C., Ozeri, R., Reichle, R. & Wineland, D. J. Creation of a six-atom 'Schrödinger cat' state. *Nature* **438**, 639–642 (2005).

[44] Dür, W., Vidal, G. & Cirac, J. I. Three qubits can be entangled in two inequivalent ways. *Phys. Rev. A* **62**, 062314 (2000).

[45] Häffner, H., Hänsel, W., Roos, C. F., Benhelm, J., Check-Al-Kar, D., Chwalla, M., Körber, T., Rapol, U. D., Riebe, M., Schmidt, P. O., Becher, C., Gühne, O., Dür, W. & Blatt, R. Scalable multiparticle entanglement of trapped ions. *Nature* **438**, 643–646 (2005).

[46] Monz, T., Schindler, P., Barreiro, J. T., Chwalla, M., Nigg, D., Coish, W. A., Harlander, M., Hänsel, W., Heinrich, M. & Blatt, R. 14-qubit entanglement: Creation and coherence. *Phys. Rev. Lett.* **106**, 130506 (2011).

[47] Kielpinski, D., Monroe, C. & Wineland, D. J. Architecture for a large-scale ion-trap quantum computer. *Nature* **417**, 709–711 (2002).

[48] Blakestad, R. B., Ospelkaus, C., VanDevender, A. P., Amini, J. M., Britton, J., Leibfried, D. & Wineland, D. J. High-fidelity transport of trapped-ion qubits through an x-junction trap array. *Phys. Rev. Lett.* **102**, 153002 (2009).

[49] Amini, J. M., Uys, H., Wesenberg, J. H., Seidelin, S., Britton, J., Bollinger, J. J., Leibfried, D., Ospelkaus, C., VanDevender, A. P. & Wineland, D. J. Towards scalable ion traps for quantum information processing. *New J. Phys.* **12**, 033031 (2010).

[50] Olmschenk, S., Matsukevich, D. N., Maunz, P., Hayes, D., Duan, L.-M. & Monroe, C. Quantum teleportation between distant matter qubits. *Science* **323**, 486–489 (2009).

[51] VanDevender, A. P., Colombe, Y., Amini, J., Leibfried, D. & Wineland, D. J. Efficient fiber optic detection of trapped ion fluorescence. *Phys. Rev. Lett.* **105**, 023001 (2010).

[52] Kim, T. H., Herskind, P. F. & Chuang, I. L. Surface-electrode ion trap with integrated light source. *Appl. Phys. Lett.* **98**, 214103 (2011).

[53] Dicke, R. H. Coherence in spontaneous radiation processes. *Phys. Rev.* **93**, 99–110 (1954).

[54] Palma, G. M., Suominen, K.-A. & Ekert, A. K. Quantum computers and dissipation. *Proc. Roy. Soc. A - Math. Phy.* **452**, 567–584 (1996).

[55] Wineland, D. J. & Leibfried, D. Quantum information processing and metrology with trapped ions. *Laser Phys. Lett.* **8**, 175–188 (2011).

[56] Blatt, R. & Wineland, D. Entangled states of trapped atomic ions. *Nature* **453**, 1008–1015 (2008).

[57] Häffner, H., Roos, C. F. & Blatt, R. Quantum computing with trapped ions. *Phys. Rep.* **469**, 155–203 (2008).

[58] Jones, J. A. NMR quantum computation. *Proc. Nucl. Mag. Res. Sp.* **38**, 325–360 (2001).

[59] Jones, J. A. Quantum computing with NMR (2010). `arXiv:1011.1382`.

[60] Vandersypen, L. M. K. & Chuang, I. L. NMR techniques for quantum control and computation. *Rev. Mod. Phys.* **76**, 1037–1069 (2004).

[61] Jones, J. A., Mosca, M. & Hansen, R. H. Implementation of a quantum search algorithm on a quantum computer. *Nature* **393**, 344–346 (1998).

[62] Vandersypen, L. M. K., Steffen, M., Sherwood, M. H., Yannoni, C. S., Breyta, G. & Chuang, I. L. Implementation of a three-quantum-bit search algorithm. *Appl. Phys. Lett.* **76**, 646–648 (2000).

[63] Vandersypen, L. M. K., Steffen, M., Breyta, G., Yannoni, C. S., Sherwood, M. H. & Chuang, I. L. Experimental realization of Shor's quantum factoring algorithm using nuclear magnetic resonance. *Nature* **414**, 883–887 (2001).

[64] Jones, J. A. NMR quantum computation: A critical evaluation. *Fortschr. Phys.* **48**, 909–924 (2000).

[65] Clarke, J. & Wilhelm, F. K. Superconducting quantum bits. *Nature* **453**, 1031–1042 (2008).

[66] DiCarlo, L., Chow, J. M., Gambetta, J. M., Bishop, L. S., Johnson, B. R., schuster, D. I., Majer, J., Blais, A., Frunzio, L., Girvin, S. M. & Schoelkopf, R. J. Demonstration of two-qubit algorithms with a superconducting quantum processor. *Nature* **460**, 240–244 (2009).

[67] Devoret, M. H. & Martinis, J. M. Implementing qubits with superconducting integrated circuits. *Quantum Inf. Process.* **3**, 163–203 (2004).

[68] Makhlin, Y., Schön, G. & Shnirman, A. Quantum-state engineering with Josephson-junction devices. *Rev. Mod. Phys.* **73**, 357–400 (2001).

[69] Neeley, M., Bialczak, R. C., Lenander, M., Lucero, E., Mariantoni, M., O'Connell, A. D., Sank, D., Wang, H., Weides, M., Wenner, J., Yin, Y., Yamamoto, T., Cleland, A. N. & Martinis, J. M. Generation of three-qubit entangled states using superconducting phase qubits. *Nature* **467**, 570–573 (2010).

[70] DiCarlo, L., Reed, M. D., Sun, L., Johnson, B. R., Chow, J. M., Gambetta, J. M., Frunzio, L., Girvin, S. M., Devoret, M. H. & Schoelkopf, R. J. Preparation and measurement of three-qubit entanglement in a superconducting circuit. *Nature* **467**, 574–578 (2010).

[71] Lucero, E., Hofheinz, M., Ansmann, M., Bialczak, R. C., Katz, N., Neeley, M., O'Connell, A. D., Wang, H., Cleland, A. N. & Martinis, J. M. High-fidelity gates in a single Josephson qubit. *Phys. Rev. Lett.* **100**, 247001 (2008).

[72] Chow, J. M., Gambetta, J. M., Tornberg, L., Koch, J., Bishop, L. S., Houck, A. A., Johnson, B. R., Frunzio, L., Girvin, S. M. & Schoelkopf, R. J. Randomized benchmarking and process tomography for gate errors in a solid-state qubit. *Phys. Rev. Lett.* **102**, 090502 (2009).

[73] Mallet, F., Ong, F. R., Palacios-Laloy, A., Nguyen, F., Bertet, P., Vion, D. & Esteve, D. Single-shot qubit readout in circuit quantum electrodynamics. *Nature Physics* **5**, 791–795 (2009).

[74] Ansmann, M., Wang, H., Bialczak, R. C., Hofheinz, M., Lucero, E., Neeley, M., O'Connell, A. D., Sank, D., Weides, M., Wenner, J., Cleland, A. N. & Martinis, J. M. Violation of Bell's inequality in Josephson phase qubits. *Nature* **461**, 504–506 (2009).

[75] Nakamura, Y., Pashkin, Y. A. & Tsai, J. S. Coherent control of macroscopic quantum states in a single-Cooper-pair box. *Nature* **398**, 786–788 (1999).

[76] Schreier, J. A., Houck, A. A., Koch, J., Schuster, D. I., Johnson, B. R., Chow, J. M., Gambetta, J. M., Majer, J., Frunzio, L., Devoret, M. H., Girvin, S. M. & Schoelkopf, R. J. Suppressing charge noise decoherence in superconducting charge qubits. *Phys. Rev. B* **77**, 180502 (2008).

[77] O'Brien, J. L. Optical quantum computing. *Science* **318**, 1567–1570 (2007).

[78] Kok, P., Munro, W. J., Nemoto, K., Ralph, T. C., Dowling, J. P. & Milburn, G. J. Linear optical quantum computing with photonic qubits. *Rev. Mod. Phys.* **79**, 135–174 (2007).

[79] Duan, L.-M. & Kimble, H. J. Scalable photonic quantum computation through cavity-assisted interactions. *Phys. Rev. Lett.* **92**, 127902 (2004).

[80] Knill, E., Laflamme, R. & Milburn, G. J. A scheme for efficient quantum computation with linear optics. *Nature* **409**, 46–52 (2001).

[81] Kwiat, P. G., Mitchell, J. R., Schwindt, P. D. D. & White, A. G. Grover's search algorithm: An optical approach. *J. Mod. Opt.* **47**, 257–266 (2000).

[82] Lu, C.-Y., Browne, D. E., Yang, T. & Pan, J.-W. Demonstration of a compiled version of Shor's quantum factoring algorithm using photonic qubits. *Phys. Rev. Lett.* **99**, 250504 (2007).

[83] Politi, A., Matthews, J. C. F. & O'Brien, J. L. Shor's quantum factoring algorithm on a photonic chip. *Science* **325**, 1221 (2009).

[84] Gao, W.-B., Lu, C.-Y., Yao, X.-C., Xu, P., Gühne, O., Goebel, A., Chen, Y.-A., Peng, C.-Z., Chen, Z.-B. & Pan, J.-W. Experimental demonstration of a hyper-entangled ten-qubit Schrödinger cat state. *Nature Physics* **6**, 331–335 (2010).

[85] Jaksch, D. & Zoller, P. The cold atom Hubbard toolbox. *Ann. Phys.* **315**, 52–79 (2005).

[86] Bloch, I. Quantum coherence and entanglement with ultracold atoms in optical lattices. *Nature* **453**, 1016–1022 (2008).

[87] Bakr, W. S., Gillen, J. I., Peng, A., Fölling, S. & Greiner, M. A quantum gas microscope for detecting single atoms in a Hubbard-regime optical lattice. *Nature* **462**, 74–77 (2011).

[88] Sherson, J. F., Weitenberg, C., Endres, M., Cheneau, M., Bloch, I. & Kuhr, S. Single-atom-resolved fluorescence imaging of an atomic Mott insulator. *Nature* **467**, 68–72 (2010).

[89] Weitenberg, C., Endres, M., Sherson, J. F., Cheneau, M., Schauß, P., Fukuhara, T., Bloch, I. & Kuhr, S. Single-spin addressing in an atomic Mott insulator. *Nature* **471**, 319–324 (2011).

[90] Lewenstein, M., Sanpera, A., Ahufinger, V., Damski, B., Sen(De), A. & Sen, U. Ultracold atomic gases in optical lattices: Mimicking condensed matter physics and beyond. *Adv. Phys.* **56**, 243–379 (2007).

[91] Bloch, I., Dalibard, J. & Zwerger, W. Many-body physics with ultracold gases. *Rev. Mod. Phys.* **80**, 885–964 (2008).

[92] Hanson, R., Kouwenhoven, L. P., Petta, J. R., Tarucha, S. & Vandersypen, L. M. K. Spins in few-electron quantum dots. *Rev. Mod. Phys.* **79**, 1217–1265 (2007).

[93] Hanson, R. & Awschalom, D. D. Coherent manipulation of single spins in semiconductors. *Nature* **453**, 1043–1049 (2008).

[94] Barthel, C., Medford, J., Marcus, C. M., Hanson, M. P. & Gossard, A. C. Interlaced dynamical decoupling and coherent operation of a singlet-triplet qubit. *Phys. Rev. Lett.* **105**, 266808 (2010).

[95] Wrachtrup, J. & Jelezko, F. Processing quantum information in diamond. *J. Phys.: Condens. Matter* **18**, S807–S824 (2006).

[96] Dutt, M. V. G., Childress, L., Jiang, L., Togan, E., Maze, J., Jelezko, F., Zibrov, A. S., Hemmer, P. R. & Lukin, M. D. Quantum register based on individual electronic and nuclear spin qubits in diamonds. *Science* **316**, 1312–1316 (2007).

[97] Jelezko, F., Gaebel, T., Popa, I., Gruber, A. & Wrachtrup, J. Observation of coherent oscillations in a single electron spin. *Phys. Rev. Lett.* **92**, 076401 (2004).

[98] Hanson, R., Gywat, O. & Awschalom, D. D. Room-temperature manipulation and decoherence of a single spin in diamond. *Phys. Rev. B* **74**, 161203 (2006).

[99] Koppens, F. H. L., Buizert, C., Tielrooij, K. J., Vink, I. T., Nowack, K. C., Meunier, T., Kouwenhoven, L. P. & Vandersypen, L. M. K. Driven coherent oscillations of a single electron spin in a quantum dot. *Nature* **442**, 766–771 (2006).

[100] Foletti, S., Bluhm, H., Mahalu, D., Umansky, V. & Yacoby, A. Universal quantum control of two-electron spin quantum bits using dynamic nuclear polarization. *Nature Physics* **5**, 903–908 (2009).

[101] Porras, D. & Cirac, J. I. Quantum manipulation of trapped ions in two dimensional Coulomb crystals. *Phys. Rev. Lett.* **96**, 250501 (2006).

[102] Biercuk, M. J., Uys, H., VanDevender, A. P., Shiga, N., Itano, W. M. & Bollinger, J. J. High-fidelity quantum control using ion crystals in a Penning trap. *Quantum Inf. Comput.* **9**, 920–949 (2009).

[103] Micheli, A., Brennen, G. K. & Zoller, P. A toolbox for lattice-spin models with polar molecules. *Nature Physics* **2**, 341–347 (2006).

[104] Rabl, P., DeMille, D., Doyle, J. M., Lukin, M. D., Schoelkopf, R. J. & Zoller, P. Hybrid quantum processors: Molecular ensembles as quantum memory for solid state circuits. *Phys. Rev. Lett.* **97**, 033003 (2006).

[105] André, A., DeMille, D., Doyle, J. M., Lukin, M. D., Maxwell, S. E., Rabl, P., Schoelkopf, R. J. & Zoller, P. A coherent all-electrical interface between polar molecules and mesoscopic superconducting resonators. *Nature Physics* **2**, 636–642 (2006).

[106] Saffman, M., Walker, T. G. & MølmerRydbergAtomQCReviewRMP2010, K. Quantum information with Rydberg atoms. *Rev. Mod. Phys.* **82**, 2313–2363 (2010).

[107] Weimer, H., Müller, M., Lesanovsky, I., Zoller, P. & Büchler, H. P. A Rydberg quantum simulator. *Nature Physics* **6**, 382–388 (2010).

[108] Hartmann, M. J., ao, F. G. S. L. B. & Plenio, M. B. Strongly interacting polaritons in coupled arrays of cavities. *Nature Physics* **2**, 849–855 (2006).

[109] Greentree, A. D., Tahan, C., Cole, J. H. & Hollenberg, L. C. Quantum phase transitions of light. *Nature Physics* **2**, 856–861 (2006).

[110] Platzman, P. M. & Dykman, M. I. Quantum computing with electrons floating on liquid helium. *Science* **284**, 1967–1969 (1999).

[111] Mostame, S. & Schützhold, R. Quantum simulator for the Ising model with electrons floating on a helium film. *Phys. Rev. Lett.* **101**, 220501 (2008).

[112] Nayak, C., Simon, S. H., Stern, A., Freedman, M. & Das Sarma, S. Non-abelian anyons and topological quantum computation. *Rev. Mod. Phys.* **80**, 1083–1159 (2008).

[113] Walther, P., Resch, K. J., Rudolph, T., Schenck, E., Weinfurther, H., Vedral, V., Aspelmeyer, M. & Zeilinger, A. Experimental one-way quantum computing. *Nature* **434**, 169–176 (2005).

[114] Tame, M. S., Prevedel, R., Paternostro, M., Böhl, P., Kim, M. S. & Zeilinger, A. Experimental realization of deutschŠs algorithm in a one-way quantum computer. *Phys. Rev. Lett.* **98**, 140501 (2007).

[115] Briegel, H. J., Browne, D. E., Dür, W., Raussendorf, R. & Van den Nest, M. Measurement-based quantum computation. *Nature Physics* **5**, 19–26 (2009).

[116] Jozsa, R. An introduction to measurement based quantum computation (2005). `arXiv:0406025v1`.

[117] Farhi, E., Goldstone, J., Gutmann, S., Lapan, J., Lundgren, A. & Preda, D. A quantum adiabatic evolution algorithm applied to random instances of an np-complete problem. *Science* **292**, 472–476 (2001).

[118] Steffen, M., van Dam, W., Hogg, T., Breyta, G. & Chuang, I. Experimental implementation of an adiabatic quantum optimization algorithm. *Phys. Rev. Lett.* **90**, 067903 (2003).

[119] Peng, X., Liao, Z., Xu, N., Qin, G., Zhou, X., Suter, D. & Duan, J. Quantum adiabatic algorithm for factorization and its experimental implementation. *Phys. Rev. Lett.* **101**, 220405 (2008).

[120] Brown, L. S. & Gabrielse, G. Geonium theory: Physics of a single electron or ion in a Penning trap. *Rev. Mod. Phys.* **58**, 233–311 (1986).

[121] Gabrielse, G., Fei, X., Orozco, L. A., Tjoelker, R. L., Haas, J., Kalinowsky, H., Trainor, T. A. & Kells, W. Thousand-fold improvement in the measured antiproton mass. *Phys. Rev. Lett.* **65**, 1317–1320 (1990).

[122] DiFilippo, F., Natarajan, V., Boyce, K. R. & Pritchard, D. E. Accurate atomic masses for fundamental metrology. *Phys. Rev. Lett.* **73**, 1481–1484 (1994).

[123] Rainville, S., Thompson, J. K. & Pritchard, D. E. An ion balance for ultra-high-precision atomic mass measurements. *Science* **303**, 334–338 (2004).

[124] Gabrielse, G. Relaxation calculation of the electrostatic properties of compensated Penning traps with hyperbolic electrodes. *Phys. Rev. A* **27**, 2277–2290 (1983).

[125] Gabrielse, G. & MacKintosh, F. C. Cylindrical Penning traps with orthogonalized anharmonicity compensation. *Intl. J. of Mass Spec. and Ion Proc.* **57**, 1–17 (1984).

[126] Gabrielse, G. & Dehmelt, H. Observation of inhibited spontaneous emission. *Phys. Rev. Lett.* **55**, 67–70 (1985).

[127] Gabrielse, G., Haarsma, L. & Rolston, S. L. Open-endcap Penning traps for high-precision experiments. *Intl. J. of Mass Spec. and Ion Proc.* **88**, 319–332 (1989).

[128] Gabrielse, G., Khabbaz, A., Hall, D. S., Heimann, C., Kalinowsky, H. & Jhe, W. Precision mass spectroscopy of the antiproton and proton using simultaneously trapped particles. *Phys. Rev. Lett.* **82**, 3198–3201 (1999).

[129] Häffner, H., Beier, T., Hermanspahn, N., H.-J. Kluge, Quint, W., Stahl, S., Verdú, J. & Werth, G. High-accuracy measurement of the magnetic moment anomaly of the electron bound in hydrogenlike carbon. *Phys. Rev. Lett.* **85**, 5308–5311 (2000).

[130] Verdú, J., Djekić, S., Stahl, S., Valenzuela, T., Vogel, M., Werth, G., Beier, T., H.-J. Kluge & Quint, W. Electronic g factor of hydrogenlike oxygen $^{16}O^{7+}$. *Phys. Rev. Lett.* **92**, 093002 (2004).

[131] Werth, G., Alonso, J., Beier, T., Blaum, K., Djekic, S., Häffner, H., Hermanspahn, N., Quint, W., Stahl, S., Verdú, J., Valenzuela, T. & Vogel, M. Highly charged ions, quantum electrodynamics, and the electron mass. *Int. J. Mass Spectrom.* **251**, 152 (2006).

[132] Guise, N. & Gabrielse, G. Self-excitation and feedback cooling of an isolated proton. *Phys. Rev. Lett.* **104**, 143001 (2010).

[133] Häffner, H., Beier, T., Djekić, S., Hermanspahn, N., Kluge, H.-J., Quint, W., Stahl, S., Verdú, J., Valenzuela, T. & Werth, G. Double Penning trap technique for precise g factor determinations in highly charged ions. *Eur. Phys. J. D* **22**, 163 (2003).

[134] Guise, N. *Spin-Flip Resolution Achieved with a One-Proton Self-Excited Oscillator*. Ph.D. thesis, Harvard University (2010).

[135] Ulmer, S., Rodegheri, C. C., Blaum, K., Kracke, H., Mooser, A., Quint, W. & Walz, J. Observation of spin flips with a single trapped proton. *Phys. Rev. Lett.* **106**, 253001 (2011).

[136] Cruz, D., Chang, J. P., Fico, M., Guymon, A. J., Austin, D. E. & Blain, M. G. Design, microfabrication, and analysis of micrometer-sized cylindrical ion trap arrays. *Rev. Sci. Instrum.* **78**, 015107 (2007).

[137] Stahl, S., Galve, F., Alonso, J., Djekic, S., Quint, W., Valenzuela, T., Verdú, J., Vogel, M. & Werth, G. A planar Penning trap. *Eur. Phys. J. D* **32**, 139–146 (2005).

[138] Marzoli, I., Tombesi, P., Ciaramicoli, G., Werth, G., Bushev, P., Stahl, S., Schmidt-Kaler, F., Hellwig, M., Henkel, C., Marx, G., Jex, I., Stachowska, E., Szawiola, G. & Walaszyk, A. Experimental and theoretical challenges for the trapped electron quantum computer. *J. Phys. B* **42**, 154010 (2009).

[139] Drndić, M., Lee, C. S. & Westervelt, R. M. Three-dimensional microelectromagnet traps for neutral and charged particles. *Phys. Rev. B* **63**, 085321 (2001).

[140] Hellwig, M., Bautista-Salvador, A., Singer, K., Werth, G. & Schmidt-Kaler, F. Fabrication of a planar micro Penning trap and numerical investigations of versatile ion positioning protocols. *New J. Phys.* **12**, 065019 (2010).

[141] Castrejón-Pita, J. R. & Thompson, R. C. Proposal for a planar Penning ion trap. *Phys. Rev. A* **72**, 013405 (2005).

[142] Castrejón-Pita, J. R., Ohadi, H., Crick, D. R., Winters, D. F. A., Segal, D. M. & Thompson, R. C. Novel designs for Penning ion traps. *J. Mod. Opt.* **54**, 1581–1594 (2007).

[143] Kim, T. H., Herskind, P. F., Kim, T., Kim, J. & Chuang, I. L. Surface-electrode point Paul trap. *Phys. Rev. A* **82**, 043412 (2010).

[144] Galve, F., Fernández, P. & Werth, G. Operation of a planar Penning trap. *Eur. Phys. J. D* **40**, 201–204 (2006).

[145] Galve, F. & Werth, G. Motional frequencies in a planar Penning trap. *Hyperfine Interact.* **174**, 41–46 (2007).

[146] Bushev, P., Stahl, S., Natali, R., Marx, G., Stachowska, E., Werth, G., Hellwig, M. & Schmidt-Kaler, F. Electrons in a cryogenic planar Penning trap and experimental challenges for quantum processing. *Eur. Phys. J. D* **50**, 97–102 (2008).

[147] Mancini, S., Martins, A. M. & Tombesi, P. Quantum logic with a single trapped electron. *Phys. Rev. A* **61**, 012303 (1999).

[148] Ciaramicoli, G., Marzoli, I. & Tombesi, P. Realization of a quantum algorithm using a trapped electron. *Phys. Rev. A* **63**, 052307 (2001).

[149] Ciaramicoli, G., Marzoli, I. & Tombesi, P. Three-qubit network with a single trapped electron. *J. Mod. Opt.* **49**, 1307–1323 (2002).

[150] Pedersen, L. H. & Rangan, C. Controllability and universal three-qubit quantum computation with trapped electron states. *Quantum Inf. Process.* **7**, 33–42 (2008).

[151] Ciaramicoli, G., Marzoli, I. & Tombesi, P. Scalable quantum processor with trapped electrons. *Phys. Rev. Lett.* **91**, 017901 (2003).

[152] Ciaramicoli, G., Marzoli, I. & Tombesi, P. Trapped electrons in vacuum for a scalable quantum processor. *Phys. Rev. A* **70**, 032301 (2004).

[153] Mintert, F. & Wunderlich, C. Ion-trap quantum logic using long-wavelength radiation. *Phys. Rev. Lett.* **87**, 257904 (2001).

[154] Johanning, M., Braun, A., Timoney, N., Elman, V., Neuhauser, W. & Wunderlich, C. Individual addressing of trapped ions and coupling of motional and spin states using rf radiation. *Phys. Rev. Lett.* **102**, 073004 (2009).

[155] Wang, S. X., Labaziewicz, J., Ge, Y., Shewmon, R. & Chuang, I. L. Individual addressing of ions using magnetic field gradients in a surface-electrode ion trap. *Appl. Phys. Lett.* **94**, 094103 (2009).

[156] Mc Hugh, D. & Twamley, J. Quantum computer using a trapped-ion spin molecule and microwave radiation. *Phys. Rev. A* **71**, 012315 (2005).

[157] Childs, A. M. & Chuang, I. L. Universal quantum computation with two-level trapped ions. *Phys. Rev. A* **63**, 012306 (2000).

[158] Stortini, S. & Marzoli, I. Composite pulses for quantum computation with trapped electrons. *Eur. Phys. J. D* **32**, 209–213 (2005).

[159] Zurita-Sánchez, J. R. & Henkel, C. Wiring up single electron traps to perform quantum gates. *New J. Phys.* **10**, 083021 (2008).

[160] Sørensen, A. S., van der Wal, C. H., Childress, L. I. & Lukin, M. D. Capacitive coupling of atomic systems to mesoscopic conductors. *Phys. Rev. Lett.* **92**, 063601 (2004).

[161] Ciaramicoli, G., Galve, F., Marzoli, I. & Tombesi, P. Array of planar Penning traps as a nuclear magnetic resonance molecule for quantum computation. *Phys. Rev. A* **72**, 042323 (2005).

[162] Ciaramicoli, G., Marzoli, I. & Tombesi, P. Spin chains with electrons in Penning traps. *Phys. Rev. A* **75**, 032348 (2007).

[163] Ciaramicoli, G., Marzoli, I. & Tombesi, P. Quantum spin models with electrons in Penning traps. *Phys. Rev. A* **78**, 012338 (2008).

[164] Hoogerheide, S. F. & Dorr, J. Private communication.

[165] Ciaramicoli, G., Marzoli, I. & Tombesi, P. Qubit decoherence in a nuclear magnetic resonance-like quantum processor with trapped particles. *Int. J. Mod. Phys. B* **20**, 1699–1710 (2006).

[166] Goldman, J. & Gabrielse, G. Optimized planar Penning traps for quantum information studies. *Hyperfine Interact.* (2011).

[167] Jackson, J. D. *Classical Electrodynamics* (John Wiley & Sons, 1999), third edn.

[168] Kusse, B. & Westwig, E. *Mathematical Physics: Applied Mathematics for Scientists and Engineers* (John Wiley & Sons, 1998).

[169] Mickens, R. E. *An Introduction to Nonlinear Oscillations* (Cambridge University Press, Cambridge, U.K., 1981).

[170] D'Urso, B., Odom, B. & Gabrielse, G. Feedback cooling of a one-electron oscillator. *Phys. Rev. Lett.* **90**, 043001 (2003).

[171] Tan, J. N. & Gabrielse, G. One electron in an orthogonalized cylindrical Penning trap. *Appl. Phys. Lett.* **55**, 2144–2146 (1989).

[172] D'Urso, B., Van Handel, R., Odom, B., Hanneke, D. & Gabrielse, G. Single-particle self-excited oscillator. *Phys. Rev. Lett.* **94**, 113002 (2005).

[173] *Curamik DBC Process (technical documentation), Curamik Electronics, Inc.* (2009).

[174] Harper, C. *Handbook Of Ceramics, Glasses, and Diamonds* (McGraw Hill Professional, 2001).

[175] Talwar, S. CeramTec AG. Private communication.

[176] Ekin, J. W. *Experimental Techniques for Low-Temperature Measurements* (Oxford University Press, Oxford, U.K., 2006).

[177] Garg, R., Bhartia, P., Bahl, I. & Ittipiboon, A. *Microstrip Antenna Design Handbook* (Artech House, 2001).

[178] Chiaverini, J., Blakestad, R. B., Britton, J., Jost, J. D., Langer, C., Leibfried, D., Ozeri, R. & Wineland, D. J. Surface-electrode architecture for ion-trap quantum information processing. *Quantum Inf. Comput.* **5**, 419–439 (2005).

[179] Alford, N. M. & Penn, S. J. Sintered alumina with low dielectric loss. *J. Appl. Phys.* **80**, 5895–5898 (1996).

[180] Simons, R. N. *Coplanar Waveguide Circuits, Components, and Systems* (Wiley-Interscience, 2001).

[181] Ghione, G. A CAD-oriented analytical model for the losses of general asymmetric coplanar lines in hybrid and monolithic MICs. *IEEE T. on Inform. Theory* **41**, 1499–1510 (1993).

[182] Hoffmann, R. K. *Handbook of Microwave Integrated Circuits* (Artech House, 1987).

[183] Gupta, K. C., Garg, R., Bahl, I. & Bhartia, P. *Microstrip Lines and Slotlines* (Artech House, 1996).

[184] Fowler, R. H. & Nordheim, L. Electron emission in intense electric fields. *Proc. Roy. Soc. A - Math. Phy.* **119**, 173–181 (1928).

[185] Gomer, R. *Field Emission and Field Ionization* (Harvard University Press, 1961).

[186] Noer, R. J. Electron field emission from broad-area electrodes. *Appl. Phys. A* **28**, 1–24 (1982).

[187] Suzuki, C., Nakanishi, T., Okumi, S., Gotou, T., Togawa, K., Furuta, F., Wada, K., Nishitani, T., Yamamoto, M., Watanabe, J., Kurahashi, S., Asano, K., Matsumoto, H., Yoshioka, M. & Kobayakawa, H. Fabrication of ultra-clean copper surface to minimize field emission dark currents. *Nucl. Instrum. Methods Phys. Res., Sect. A* **462**, 337–348 (2001).

[188] Cruz, D., Chang, J. P. & Blain, M. G. Field emission characteristics of a tungsten microelectromechanical system device. *Appl. Phys. Lett.* **86**, 153502 (2005).

[189] Camp, J. B., Darling, T. W. & Brown, R. E. Macroscopic variations of surface potentials of conductors. *J. Appl. Phys.* **69**, 7126–7129 (1991).

[190] Camp, J. B., Darling, T. W. & Brown, R. E. Effect of crystallites on surface potential variations of Au and graphite. *J. Appl. Phys.* **71**, 783–785 (1992).

[191] Turchette, Q. A., Kielpinski, D., King, B. E., Leibfried, D., Meekhof, D. M., Myatt, C. J., Rowe, M. A., Sackett, C. A., Wood, C. S., Itano, W. M., Monroe, C. & Wineland, D. J. Heating of trapped ions from the quantum ground state. *Phys. Rev. A* **61**, 063418 (2000).

[192] Deslauriers, L., Olmschenk, S., Stick, D., Hensinger, W. K., Sterk, J. & Monroe, C. Scaling and suppression of anomalous heating in ion traps. *Phys. Rev. Lett.* **97**, 103007 (2006).

[193] Labaziewicz, J., Ge, Y., Antohi, P., Leibrandt, D., Brown, K. R. & Chuang, I. L. Suppression of heating rates in cryogenic surface-electrode ion traps. *Phys. Rev. Lett.* **100**, 013001 (2008).

[194] Labaziewicz, J., Ge, Y., Leibrandt, D. R., Wang, S. X., Shewmon, R. & Chuang, I. L. Temperature dependence of electric field noise above gold surfaces. *Phys. Rev. Lett.* **101**, 180602 (2008).

[195] Henkel, C., Pötting, S. & Wilkens, M. Loss and heating of particles in small and noisy traps. *Appl. Phys. B* **69**, 379–387 (1999).

[196] White, R. Tufts University. Private communication. As recommended by Scott Rader, Fujimi Corporation.

[197] D'Urso, B. *Cooling and Self-Excitation of a One-Electron Oscillator*. Ph.D. thesis, Harvard University (2003).

[198] Zipperian, D. PACE Technologies. Private communication.

[199] Amini, J. M., Britton, J., Leibfried, D. & Wineland, D. J. Micro-fabricated chip traps for ions. In Reichel, J. & Vuletić, V. (eds.) *Atom Chips*, 395–420 (Wiley-VCH, 2008).

[200] Seidelin, S., Chiaverini, J., Reichle, R., Bollinger, J. J., Leibfried, D., Britton, J., Wesenberg, J. H., Blakestad, R. B., Epstein, R. J., Hume, D. B., Itano, W. M., Jost, J. D., Langer, C., Ozeri, R., Shiga, N., & Wineland, D. J. Microfabricated surface-electrode ion trap for scalable quantum information processing. *Phys. Rev. Lett.* **96**, 253003 (2006).

[201] Stick, D., Hensinger, W. K., Olmschenk, S., Madsen, M. J., Schwab, K. & Monroe, C. Ion trap in a semiconductor chip. *Nature Physics* **2**, 36–39 (2006).

[202] Deslauriers, L., Haljan, P. C., Lee, P. J., Brickman, K.-A., Blinov, B. B., Madsen, M. J. & Monroe, C. Zero-point cooling and low heating of trapped $^{111}Cd^{+}$ ions. *Phys. Rev. A* **70**, 043408 (2004).

[203] Schutz, S. A., Poschinger, U., Zissel, F. & Schmidt-Kaler, F. Sideband cooling and coherent dynamics in a microchip multi-segmented ion trap. *New J. Phys.* **10**, 045007 (2008).

[204] Pearson, C. E., Leibrandt, D. R., Bakr, W. S., Mallard, W. J., Brown, K. R., & Chuang, I. L. Experimental investigation of planar ion traps. *Phys. Rev. A* **73**, 032307 (2006).

[205] Brown, K. R., Clark, R. J., Labaziewicz, J., Richerme, P., Leibrandt, D. R., & Chuang, I. L. Loading and characterization of a printed-circuit-board atomic ion trap. *Phys. Rev. A* **75**, 015401 (2007).

[206] Lev, B. Fabrication of micro-magnetic traps for cold neutral atoms. *Quantum Inf. Comput.* **3**, 450–464 (2003).

[207] Leibrandt, D. R., Labaziewicz, J., Clark, R. J., Chuang, I. L., Epstein, R. J., Ospelkaus, C., Wesenberg, J. H., Bollinger, J. J., Leibfried, D., Wineland, D. J., Stick, D., Sterk, J., Monroe, C., Pai, C.-S., Low, Y., Frahm, R. & Slusher, R. E. Demonstration of a scalable multiplexed ion trap for quantum information processing. *Quantum Inf. Comput.* **9**, 901 (2009).

[208] Wall, D. Resonetics LLC. Private communication.

[209] Pergamo, R. ION Beam Milling, Inc. Private communication.

[210] Wallrabe, U. & Saile, V. LIGA technology for R&D and industrial applications. In Korvink, J. G. & Paul, O. (eds.) *MEMS: A Practical Guide to Design, Analysis, Applications*, 853–899 (William Andrew, 2006).

[211] Kouba, J., Bednarzik, M., Engelke, R., Ahrens, G., Miller, H. & Haase, D. Optimizing SU-8 resist to fabricate micro-metallic structures. *Solid State Technol.* **49**, 39–44 (2006).

[212] Kouba, J., Engelke, R., Ahrens, G., Scheunemann, H.-U., Gruetzner, G., Loechel, B., Miller, H. & Haase, D. SU-8: promising resist for advanced direct LIGA aplications for high aspect ratio mechanical microparts. *Microsyst. Technol.* **13**, 311–317 (2007).

[213] Dentinger, P. M., Clift, W. M. & Goods, S. H. Removal of SU-8 photoresist for thick film application. *Microelectron. Eng.* **61**, 993–1000 (2002).

[214] Hong, G., Holmes, A. S. & Heaton, M. E. SU8 resist plasma etching and its optimisation. *Microsyst. Technol.* **10**, 357–359 (2004).

[215] Ghantasala, M. K., Hayes, J. P., Harvey, E. C. & Sood, D. K. Patterning, electroplating and removal of SU-8 moulds by excimer laser micromachining. *J. Micromech. Microeng.* **11**, 133–139 (2001).

[216] Engelke, R., Mathuni, J., Ahrens, G., Gruetzner, G., Bednarzik, M., Schondelmaier, D. & Loechel, B. Investigations of SU-8 removal from metallic high aspect ratio microstructures with a novel plasma technique. *Microsyst. Technol.* **14**, 1607–1612 (2008).

[217] Kukharenka, E. & Kraft, M. Realization of electroplating molds with thick positive SPR 220-7 photoresist. *J. Mat. Sci.* **14**, 319–322 (2003).

[218] Soh, H. T., Yue, C. P., McCarthy, A., Ryu, C., Lee, T. H., Wong, S. S. & Quate, C. F. Ultra-low resistance, through-wafer via (TWV) technology and its applications in three dimensional structures on silicon. *Jpn. J. Appl. Phys.* **38**, 2393–2396 (1999).

[219] Leung, L. L. W. & Chen, K. J. Microwave characterization and modeling of high aspect ratio through-wafer interconnect vias in silicon substrates. *IEEE T. Microw. Theory* **53**, 2472–2480 (2005).

[220] Nguyen, N. T., Boellaard, E., Pham, N. P., Kutchoukov, V. G., Craciun, G. & Sarro, P. M. Through-wafer copper electroplating for three-dimensional interconnects. *J. Micromech. Microeng.* **12**, 395–399 (2002).

[221] Sun, J.-J., Kondo, K., Okamura, T., Oh, S., Tomisaka, M., Yonemura, H., Hoshino, M. & Takahashi, K. High-aspect-ratio copper via filling used for three-dimension chip stacking. *J. Electrochem. Soc.* **150**, G335–G358 (2003).

[222] Wang, Z., Wang, L., Nguyen, N. T., Wien, W. A. H., Schellevis, H., Sarro, P. M. & Burghartz, J. N. Silicon micromachining of high aspect ratio high-density through-wafer electrical interconnects for 3-D multichip packaging. *IEEE Trans. Antenn. Propag.* **29**, 615–622 (2006).

[223] Chandrasekar, M. S. & Pushpavanam, M. Pulse and pulse reverse plating—conceptual, advantages and applications. *Electrochimica Acta* **53**, 3313–3322 (2008).

[224] Blain, M. G., Riter, L. S., Cruz, D., Austin, D. E., Wu, G., Plass, W. R. & Cooks, R. G. Towards the hand-held mass spectrometer: Design considerations, simulation, and fabrication of micrometer-scaled cylindrical ion traps. *Int. J. Mass Spectrom.* **236**, 91–104 (2004).

[225] Schwinberg, P. B., Dyck, R. S. V. & Dehmelt, H. G. Variable magnetic bottle for geonium-1 measurements. *Bull. Am. Phys. Soc.* **24**, 1202 (1979). Abstract.

[226] Van Dyck, Jr., R. S., Schwinberg, P. B. & Dehmelt, H. G. Experiments with single electrons. In Hestenes, D. & Weingartshofer, A. (eds.) *The Electron: New Theory and Experiment*, 239–293 (Kluwer Academic, Dordrecht, The Netherlands, 1991).

[227] Dyck, R. S. V., Moore, F. L., Farnham, D. L. & Schwinberg, P. B. Variable magnetic bottle for precision geonium experiments. *Rev. Sci. Instrum.* **57**, 593–597 (1985).

[228] Wang, S. X., Ge, Y., Jaroslaw, Dauler, E., Berggren, K. & Chuang, I. L. Superconducting microfabricated ion traps. *Appl. Phys. Lett.* **97**, 244102 (2010).

[229] Smith, R. W., O'Leary, J. & Fichera, B. The fabrication of brazed, lightweight titanium plate-fin heat exchangers for aircraft applications. In Stephens, J. J. & Weil, K. S. (eds.) *Brazing and Soldering: Proceedings of the 3rd International Brazing and Soldering Conference*, 310–316 (ASM International, 2006).

[230] Donachie, Jr., M. J. *Titanium: A Technical Guide* (ASM International, 2000).

[231] Hooven III, W. T., Pierre, J. S. & Sanderow, H. Commercial practice. In Fabian, R. (ed.) *Vacuum Technology: Practical Heat Treating and Brazing*, 153–189 (ASM International, 1993).

[232] Szczurek, J. & Kowalewski, J. Issues in vacuum brazing. In Stephens, J. J. & Weil, K. S. (eds.) *Brazing and Soldering: Proceedings of the 3rd International Brazing and Soldering Conference*, 326–333 (ASM International, 2006).

[233] Schwartz, M. M. *Brazing: For the engineering technologist* (Springer, 1994).

[234] Odom, B., Hanneke, D., D'Urso, B. & Gabrielse, G. New measurement of the electron magnetic moment using a one-electron quantum cyclotron. *Phys. Rev. Lett.* **97**, 030801 (2006).

[235] Odom, B. *Fully Quantum Measurement of the Electron Magnetic Moment*. Ph.D. thesis, Harvard University (2004).

[236] Pobell, F. *Matter and Methods at Low Temperatures* (Springer-Verlag, 1992).

[237] Wang, S. X., Labaziewicz, J., Ge, Y., Shewmon, R. & Chuang, I. L. Demonstration of a quantum logic gate in a cryogenic surface-electrode ion trap. *Phys. Rev. A* **81**, 062332 (2010).

[238] Gabrielse, G. & Tan, J. Self-shielding superconducting solenoid systems. *J. Appl. Phys.* **63**, 5143–5148 (1988).

[239] Altemose, V. O. Glass vacuum systems. In Weissler, G. L. & Carlson, R. W. (eds.) *Methods of Experimental Physics, Vol. 14: Vacuum Physics and Technology*, 313–344 (Academic Press, Inc., 1979).

[240] Macalpine, W. W. & Schildknecht, R. O. Coaxial resonators with helical inner conductor. *Proc. IRE* **47**, 2099–2105 (1959).

[241] Bowick, C., Blyler, J. & Ajluni, C. *RF Circuit Design* (News, 2008).

[242] Peil, S. *Quantum Jumps Between Fock States of an Ultracold Electron Cyclotron Oscillator*. Ph.D. thesis, Harvard University (1999).

[243] Wineland, D. J. & Dehmelt, H. G. Principles of the stored ion calorimeter. *J. Appl. Phys.* **46**, 919–930 (1975).

[244] Hall, D. S. *Positrons, Antiprotons and Interactions for Cold Antihydrogen*. Ph.D. thesis, Harvard University (1997).

[245] Arfken, G. *Mathematical Methods for Physicists* (Academic Press, 1985).

[246] van Handel, R. *Self-Excited Detection in Geonium: Towards an Improved $g-2$ Measurement*. Master's thesis, Vrije Univ. (2002).